Atomic Layer Deposition of Metal Oxides for the Preparation of High Performance Zn-Air Battery Electrodes

by

Michael P. Clark

A thesis submitted in partial fulfillment of the requirements for the degree of

Doctor of Philosophy

in

MATERIALS ENGINEERING

Department of Chemical and Materials Engineering
University of Alberta

Abstract

As the world continues to implement renewable energy technologies such as wind and solar, comes the demand for grid scale energy storage. Zn-air batteries (ZABs) are a promising candidate for grid scale energy storage because of their high energy density, low cost, high safety, and low environmental impact. Current generation ZABs, however, suffer from poor efficiency due to the sluggish kinetics at the air electrode. Despite their excellent activity, noble metal catalysts such as Pt are far too expensive for widespread use; this has driven the development of inexpensive transition metal oxide (TMO) catalysts. Due to their poor electrical conductivity, TMOs are typically nanostructured and/ or mounted on a conductive support.

Atomic layer deposition (ALD) is a thin film fabrication technique capable of producing highly conformal films of a wide range of materials. Because of the highly uniform and conformal nature of ALD films, ALD is particularly well suited for coating of highly porous structures such as the air electrode used in ZABs. The purpose of this work is to develop a process to prepare high performance ZAB air electrodes by depositing MnO_x directly into the porosity of the air electrode by ALD.

The first study in this work included a thorough study of the saturation behaviour of bis(ethylcyclopentadienyl) manganese ($(EtCp)_2Mn$) and water, with and without a forming gas (FG) (5% H_2, 95% N_2) plasma step. Contrary to previously published literature, the deposition using only $(EtCp)_2Mn$ and water (W-MnO_x) did not experience saturating reactions; this deposition did not follow an ALD mechanism. A saturating ALD mechanism was achieved for depositions that used a FG plasma step between the $(EtCp)_2Mn$ and water doses (FG-MnO_x), resulting in a growth per cycle of 1.15 Å/cy within the temperature range of 100 – 200 °C. Porous carbon electrodes were coated with MnO_x following both recipes. Scanning electron

microscope (SEM), energy dispersive x-ray spectroscopy (EDX) line scans of electrode cross sections showed that the saturating mechanism FG-MnO_x resulted in deposition deeper within the porosity than the W-MnO_x. Electrochemical testing showed that the FG-MnO_x also had improved electrochemical surface area as well as activity towards the oxygen reduction reaction; this is attributed to the better porosity coverage of FG-MnO_x over W-MnO_x.

The second study in this work involved the preparation and testing of MnO_x coated electrodes in a full cell ZAB. Three types of electrodes were prepared in this work, FG-MnO_x, FG-MnO_x + CoO_x, and O_2-MnO_x. FG-MnO_x was prepared using the same procedure used in the first study and the FG-MnO_x + CoO_x sample was prepared by depositing CVD CoO_x on top of FG-MnO_x. O_2-MnO_x was prepared using an oxygen plasma and did not follow a saturating deposition mechanism. Scanning transmission electron microscopy (STEM) revealed that the gas diffusion layer (GDL) particles were successfully coated with a uniform layer of MnO_x. Electron diffraction and x-ray photoelectron spectroscopy (XPS) were used to identify FG-MnO_x and O_2-MnO_x as hausmannite, Mn_3O_4. Full cell ZAB tests showed excellent performance for MnO_x coated electrodes, out performing Pt/Ru-C at current densities larger than 100 mA cm^{-2}. FG-MnO_x and O_2-MnO_x electrodes had maximum power densities of 170 and 184 mW cm^{-2}, respectively. With the catalyst distributed within the structure of the GDL, performance limitations associated with electrolyte flooding and air diffusion are reduced, improving discharge potential and cycling behavior. FG-MnO_x + CoO_x electrodes showed good cycling stability, both in a tri-electrode configuration and bifunctionally. When cycled at 20 mA cm^{-2} for 100 h (200 cycles), FG-MnO_x + CoO_x had initial and final discharge potentials of 1.18 and 1.15 V, respectively.

Preface

This thesis is focused on the development and characterization of MnO_x depositions for use in Zn-air batteries. The work presented in Chapter 4 and Chapter 5, as well as Appendices A and B are all my original work.

Chapter 4 was conducted in collaboration with Dr. Triratna Muneshwar and Dr. Ming Xiong. Dr. Muneshwar aided in the development and analysis of the atomic layer deposition procedures and ellipsometry results. Dr. Ming Xiong helped with electrochemical testing and analysis of electrochemical results. A version of Chapter 4 has been published:

M. P. Clark, T. Muneshwar, M. Xiong, K. Cadien, and D. G. Ivey, "Saturation Behavior of Atomic Layer Deposition MnOx from Bis(Ethylcyclopentadienyl) Manganese and Water: Saturation Effect on Coverage of Porous Oxygen Reduction Electrodes for Metal−Air Batteries", *ACS Appl. Nano Mater.*, vol. 2, pp. 267-277, 2018

Chapter 5 was conducted in collaboration with Dr. Ming Xiong. Dr. Xiong helped with electrochemical testing/ analysis, developed the battery cell design, and developed the oxygen evolution catalyst used in tri-electrode tests. A version of Chapter 5 has been published:

M. P. Clark, M. Xiong, K. Cadien, and D. G. Ivey, "High Performance Oxygen Reduction/ Evolution Electrodes for Zinc-Air Batteries Prepared by Atomic Layer Deposition of MnOx", *ACS Appl. Energy Mater.,* vol. 3, pp. 603-613, 2020

In addition to the above publications, I also contributed to a number of my group members' publications:

(1) Xiong, M., **Clark, M. P**., Labbe, M., Ivey, D. G., "A horizontal zinc-air battery with physically decoupled oxygen evolution/ reduction reaction electrodes", *Journal of Power Sources,* vol. 393, no. May, pp. 108–118, 2018

(2) Costa, J., **Clark, M. P.**, de Almeida Neto, A. F., Ivey, D. G., "In-situ transformation of electrodeposited W-Co oxide to ZnCo2O4 nanoparticles as effective bifunctional catalysts in ZABs", *Electrochim. Acta,* **submitted for review**

(3) Aasen, D., **Clark, M. P.**, Ivey, D. G., "A Gas Diffusion Layer Impregnated with Mn3O4 –Decorated N-Doped Carbon Nanotubes for the Oxygen Reduction Reaction in Zinc-Air Batteries", *Batteries & Supercaps*, vol. 2, pp. 882-893, 2019

(4) Aasen, D., **Clark, M. P.**, Ivey, D. G., "(Co,Fe)3O4 Decorated Nitrogen-Doped Carbon Nanotubes in Nano-Composite Gas Diffusion Layers as Highly Stable Bifunctional Catalysts for Rechargeable Zinc-Air Batteries", *Batteries & Supercaps*, vol. 2, 2019

(5) Aasen, D., **Clark, M. P.**, Ivey, D. G., "Investigation of Transition Metal-Based (Mn, Co, Ni, Fe) Trimetallic Oxide Nanoparticles on N-doped Carbon Nanotubes as Bifunctional Catalysts for Zn-Air Batteries", *J. Electrochem. Soc.,* vol. 167, No. 4, 2020

(6) Tran, T. N. T., **Clark, M. P.**, Chung, H-J., Ivey, D. G., "A Tri-Electrode Configuration for Zinc-Air Batteries Using Gel Polymer Electrolytes", **to be submitted for review**

(7) Tran, T. N. T., **Clark, M. P.**, Chung, H-J., Ivey, D. G., "Effects of Crosslinker Concentration in Poly(Acylic Acid)-KOH Gel Electrolyte on Performance of Zinc-Air Batteries", *Batteries and Supercaps*, **accepted- awaiting publication**,
DOI: 10.1002/batt.201900199

For publication (1) my contribution included performing TEM analysis, as well as interpretation of XPS, diffraction, and electrochemical data. My contributions to paper (2) were assistance with experimental design, analysis of electrochemical results, and collection/ interpretation of SEM and TEM data. My contributions to papers (3), (4), and (5) are all very similar; I performed TEM and SEM analysis, helped with electrochemical testing/ analysis, and helped with XPS analysis. My contribution to papers (6) and (7) were to the experimental design and interpretation of electrochemical results.

Acknowledgements

I am deeply grateful to my supervisors, Dr. Douglas Ivey and Dr. Ken Cadien for their help and guidance throughout my time at the U of A, not just during my PhD but also during my undergraduate and master's degrees. Dr. Ivey has been an integral part of my growth as an engineer and as a person. Dr. Ivey has always led by example; his endless knowledge base, work ethic, patience, and empathy are an inspiration to me and many others. I hope to one day grow to be a similar person and to inspire those around me.

I am also very thankful to my fellow graduate students who have helped me in many ways, large and small, throughout my graduate studies. Ming Xiong, Aliesha Johnson, Matt Labbe, Wendy Tran, Arjun Dhiman, Drew Aasen, Josiel Costa, Neda Dalili, Elaheh Davari, Triratna Muneshwar, Mengmeng Miao, Elham Rafie Borujeny, Yingjie (Jay) He, and Yaqian Zhang: thank you all for all of your help.

Thank you to my girlfriend Zahra Abedi for all of your love and support.

Thank you Anqiang He, Shihong Xu, Peng Li, Shiraz Merali, Nathan Gerein, and Danielle Covelli for your help with sample characterization.

I would also like to thank Dr. Dennis Todoruk and Richard Dietrich. I was diagnosed with Crohn's disease in 2009 and Dr. Todoruk has helped me immeasurably over the last 10 years. Dr. Todoruk has continually gone out of his way to help me; whether it is getting me in for a short-notice procedure or simply talking on the phone or faxing a prescription. Thank you Dr. Todoruk, I am very thankful for everything you have done for me and my colon.

I am grateful for research funding provided through Natural Sciences and Engineering Research Council of Canada (NSERC) and Future Energy Systems (FES). I am also thankful for travel funding provided by the Faculty of Graduate Studies and Research (FGSR) and the Graduate Students Association (GSA).

Finally, I would like to thank my family. I am very thankful for my parents, who have always worked hard to give me every opportunity I could wish for. The continuous support and understanding of my parents have been critically important to me, not only during graduate

school but throughout life. Ben and Chris, thank you for your friendship, compassion, and understanding.

Table of Contents

Abstract ii
Preface iv
Acknowledgements vi
Table of Contents viii
List of Tables xi
List of Figures xii
Chapter 1: Introduction 1
Chapter 2: Literature Review 5
2.1 Metal-air Batteries 5
2.2 Zn-air Batteries 6
2.2.1 Zn-Air Battery Chemistry 6
2.2.2 Zn-Air Battery Design 8
2.2.2.1 Zn Electrode Design 9
2.2.2.2 Air Electrode Design 9
2.2.2.3 Challenges for Zn-Air Batteries 10
2.2.2.4 Tri-Electrode ZABs 12
2.2.2.5 Horizontal ZABs 13
2.3 Oxygen Reaction Catalysis 13
2.3.1 Catalysts for ZABs 17
2.3.1.1 Transition Metal Oxides (TMOs) 18
Manganese Oxide 18
Perovskites 20
2.3.1.2 Carbon-based materials 20
2.3.1.3 Metal-Organic Frameworks (MOFs) 21
2.4 Atomic Layer Deposition 22
2.4.1 Deposition Mechanism 22
2.4.2 ALD Reactors 26
2.4.3 Application of ALD to Renewable Energy 28
2.4.4 Precursor Selection 28
2.4.5 Nucleation and Growth 30
2.4.6 ALD on Carbon 31
2.4.7 ALD of Mn oxide 33
2.5 Characterization Techniques 37

2.5.1 Electrochemical Characterization Techniques 37
2.5.1.1 Linear Sweep Voltammetry (LSV) 37
2.5.1.2 Cyclic Voltammetry (CV) 38
2.5.1.3 Electrochemical Impedance Spectroscopy (EIS) 38
2.5.1.4 Galvanostatic Cycling 39
2.5.2 Materials Characterization Techniques 39
2.5.2.1 Scanning Electron Microscopy (SEM) 39
2.5.2.2 Transmission and Scanning Transmission Electron Microscopy (TEM/ STEM) 40
2.5.2.3 X-ray Photoelectron Spectroscopy (XPS) 42
2.5.2.4 Spectroscopic Ellipsometry 42
Chapter 3: Experimental 44
3.1 Atomic Layer Deposition 44
3.1.1 Atomic Layer Deposition Tool 44
3.1.2 ALD Precursors 46
3.1.3 Pulsed Precursor Delivery 47
3.1.4 Ellipsometry 48
3.2 Electrochemical Characterization 48
3.2.1 Half Cell Testing 48
3.2.1.1 Electrochemical Surface Area Measurements 49
3.2.2 Full Cell Testing 50
3.2.2.1 Electrodeposition of CoFe 51
3.3 Materials Characterization 51
3.3.1 Scanning Electron Microscopy 51
3.3.2 Transmission Electron Microscopy/ Scanning Transmission Electron Microscopy 51
3.3.3 X-ray Photoelectron Spectroscopy 52
Chapter 4: Saturation Behaviour of Atomic Layer Deposition MnO_x from Bis(Ethylcyclopentadienyl) Manganese and Water: Saturation Effect on Coverage of Porous Oxygen Reduction Electrodes for Metal-Air Batteries 53
4.1 Introduction 53
4.2 Experimental 55
4.3 Results and Discussion 58
4.3.1 ALD of MnO_x from $(EtCp)_2Mn$ and H_2O 58
4.3.2 ALD of MnO_x from $(EtCp)_2Mn$, FG plasma, and H_2O 60
4.3.3 Transmission Electron Microscopy 61
4.3.4 X-ray Photoelectron Spectroscopy 62

4.3.5 Scanning Electron Microscopy 64
4.3.6 Electrochemical Measurements 67
4.4 Conclusions 71
Chapter 5: High Performance Oxygen Reduction/ Evolution Electrodes for Zinc-Air Batteries Prepared by Atomic Layer Deposition of MnO_x 72
5.1 Introduction 72
5.2 Experimental 75
5.3 Results & Discussion 78
5.3.1 Electrode Characterization 78
5.3.2 Electrochemical Characterization 89
5.4 Conclusions 106
Chapter 6: Conclusions and Future Work 107
6.1 Conclusions 107
6.1.1 Chapter 4 - Conclusions 107
6.1.2 Chapter 5 - Conclusions 107
6.2 Future Work 108
References 110
Appendix A: ORR activity of Zr-, Hf-, Nb-, and Ta-based thin films 126
A.1 Introduction 126
A.2 Experimental 127
A.3 Results and Discussion 129
A.3.1 ZrO_2 and HfO_2 129
A.3.2 Reduced Oxygen Content ZrO_2 133
A.3.3 ZrN 134
A.3.4 ZrON and HfON 135
A.3.5 Ternary Oxides 136
A.3.6 TaO_x and NbO_x 139
Appendix B: Atomic Layer Deposition of La Oxide Using Pressurized Precursor Delivery 141
B.1 Introduction 141
B.2 Experimental 146
B.3 Results and Discussion 147
B.4 Deposition of La-based Perovskites 150
Appendix C: Discussion of Saturation Results Conflicting With the Literature 151

List of Tables

Table 1-1: Comparison of various battery technologies. [4]–[7] 2

Table 2-1: Summary of literature on ALD of MnO_x 35

Table 4-1: XPS deconvolution results [52], [124]–[127] 64

Table 4-2: Capacitance and V_{onset} measurement results 71

Table 5-1: Summary of TEM electron diffraction results for cycled/ uncycled electrodes 85

Table 5-2: Diffraction data for relevant M_3O_4 structures 86

Table 5-3: Capacitance measurement results 93

Table 5-4: Comparison of ZAB results 97

Table 5-5: Cycling stability results - 100 h (200 cycles) tri-electrode test at 20 mA cm^{-2} 104

Table 5-6: Bifunctional cycling results – 50 h test at 10 mA cm^{-2}. 106

Table A-1: LSV results for various thin films 120

Table B-1: Literature summary of ALD La oxide using $La(^{i}PrCp)_3$ 145

List of Figures

Figure 2-1: Comparison of various battery technologies alongside gasoline and H_2-air. [9] 6

Figure 2-2: Schematic polarization curves for a Zn-air cell. Discharge curves are shown in red and charge curves are shown in blue. Note the very large polarization/ overpotentials for the air reactions. [14]..... 8

Figure 2-3: Schematic of a typical ZAB. [14]..... 9

Figure 2-4: Schematics and cycling stability of (A) two-electrode ZAB and (B) three-electrode ZAB. The catalyst used was an N and P doped mesoporous nanocarbon. Cycling was performed at a current density of 2 mA cm^{-2}. [28] 13

Figure 2-5: A) Schematic free energy curve for a generic reaction. The free energy barrier without a catalyst is effectively reduced by the presence of stable intermediate species on the catalyst surface. [35] B) Volcano plot comparing the activity of various perovskite structures. [34] 14

Figure 2-6: A) Example four-electron ORR pathway. B) Example two-electron ORR pathway. C) Configurations of O_2 adsorption. i) On top end-on, ii) bridge end-on, iii) bridge side-on one site, iv) bridge side-on two sites. [9], [42] 17

Figure 2-7: A) Hausmannite tetragonal spinel Mn_3O_4 crystal structure, space group: I41/amd. [54] B) Ideal cubic Fm3m perovskite structure. [34] 20

Figure 2-8: Schematic of a typical ALD process. [11]..... 23

Figure 2-9: Schematic of an ALD window. [11]..... 25

Figure 2-10: Comparison of ALD and CVD film conformality within trenches. A) ALD $Ge_2Sb_2Te_5$ on patterned Si and B) CVD WSix on patterned Si. [66], [72] 26

Figure 2-11: Schematic of a continuous flow ALD reactor equip with an RF plasma source and mass spectrometer. [11]..... 27

Figure 2-12: A) Schematic of conventional precursor delivery. B) Precursor delivery utilizing a bubbler... 29

Figure 2-13: Thin film growth mechanisms: a) Island growth (Volmer-Weber), b) layer by layer growth (Frank-van der Merwe), and c) mixed growth (Stranski-Krastanov). [79] 30

Figure 2-14: SEM secondary electron (SE) images of A) smooth glassy carbon (s-GC) and B) high surface area glassy carbon (HSA-GC). C) OER activity of bare and MnOx coated electrodes. [12] 34

Figure 2-15: A) Example LSV curve for carbon-supported Fe-phthalocyanine (FePc/C) and Co-phthalocyanine (CoPc/C), compared to Pt/C. [9] B) An example of galvanostatic cycling results used to determine rate capability. [101] 38

Figure 2-16: Interaction volume simulations generated using Casino software. Simulations are for a 20 nm layer of MnO_2 on a Si substrate. The dashed line indicates the interface between MnO_2 and Si. The 4 kV electrons penetrate deeper than 200 nm, while the 2 kV electrons reach a maximum depth of ~75 nm. [102] 40

Figure 2-17: A) Schematic of BF and ADF STEM imaging modes. B) ADF STEM image of Si (110). C) BF STEM image of Si (110). D) STEM ADF and EDX maps of a CoFe alloy. [104], [108] 41

Figure 3-1: Images of the Kurt J. Lesker ALD 150LX tool used for depositions 46

Figure 3-2: ALD precursors. (A) Bis(cyclopentadienyl) manganese, (B) bis(ethylcyclopentadienyl) manganese, (C) cyclopentadienyl cobalt dicarbonyl. 47

Figure 3-3: Schematic of the pulsed precursor delivery method 48

Figure 3-4: Plots used to determine ECSA. [111] 49

Figure 3-5: Schematics of ZAB configurations used for full cell testing. 50

Figure 4-1: (a-c) Schematic of the pressurized precursor delivery method. (a) Charge, (b) dwell, and (c) dose. (d) Molecular structure of $(EtCp)_2Mn$. 56

Figure 4-2: (a) Pulse timing scheme for a single $(EtCp)_2Mn + H_2O$ ALD cycle. (b) GPC vs. precursor dose (t1) at various substrate temperatures for W-MnO_x. All depositions had a timing scheme of x/2 s/20 s/2 s/30 s. 58

Figure 4-3: GPC vs. dose and purge times for W-MnO_x (circles, Tsub = 50 °C) and FG-MnO_x (triangles, Tsub = 100 °C) systems. For all plots, the optimized timings are 3 s/2 s/20 s/2 s/30 s for $(EtCp)_2Mn$ + H_2O and 3 s/2 s/20 s/20 s/2 s/30 s for $(EtCp)_2Mn$ + FG plasma + H_2O. For each plot, only one time is varied while all other times are held constant, following the standard timing. (a) post precursor purge, (b) H_2O dose, (c) post H_2O purge, and (d) FG plasma dose. 59

Figure 4-4: (a) Pulse timing scheme for a single $(EtCp)_2Mn$ + FG plasma + H_2O ALD cycle. (b) GPC vs. precursor dose (t1) at various substrate temperatures for FG-MnO_x. All depositions had a timing scheme of x/2 s/20 s/20 s/2 s/30 s. 60

Figure 4-5: HR-TEM images of (a) W-MnO_x, and (b) FG-MnO_x films (20 nm thick) deposited on 18 nm SiO2 membranes. Diffraction patterns are inset. (c, d) STEM EDX spectra from the W-MnO_x and FG-MnO_x films as well as the bare SiO2 membrane..... 62

Figure 4-6: XPS results for W-MnO_x , FG-MnO_x , W-MnO_x-Ann , and FG-MnO_x-Ann films. (a) Mn 2p, (b) Mn 3s, (c) quantification results..... 63

Figure 4-7: XPS results for W-MnO_x (i), FG-MnO_x (ii), W-MnO_x-Ann (iii), and FG-MnO_x-Ann (iv) films. (a) O 1s, (b) N 1s, (c) C 1s..... 63

Figure 4-8: Plan view SEM secondary electron images of GDLs coated with ALD Mn oxide. (a) uncoated electrode, (b) FG-MnO_x, (c) 50C-W-MnO_x, (d) 100C-W-MnO_x, (e) 150C-W-MnO_x, (f) 200C-W-MnO_x. (g, h) EDX spectra from 50C-W-MnO_x and FG-MnOx coated GDL. 65

Figure 4-9: Cross sectional SEM results. (a) Structure of the GDL showing the microporous layer (MPL) and the backing layer (BL). (b) EDX line scan results from the regions shown in c, e, and g. (c) FG-MnO_x, (d) 50C-W-MnO_x, (e) 100C-W-MnO_x, (f) 200C-W-MnO_x. 66

Figure 4-10: (a) Cyclic voltammograms performed at a scan rate of 20 mV s^{-1} in Ar saturated 1 M KOH. The vertical line in the upper right of the plot gives the current density scale. (b, c) Linear sweep voltammetry results performed at 5 mV s^{-1} in Ar and O2 saturated 1 M KOH, respectively. (d) Double layer capacitance (CDL) measurement results. 69

Figure 4-11: (A) CV results performed in O_2 saturated 1 M KOH (20 mV s^{-1} scan rate). (B) q^{-1} vs. $v^{1/2}$ plot used for calculating total electrode capacitance. (c) Chronopotentiometry results in 1 M KOH at a current of 10 mA cm^{-2}. 70

Figure 5-1: GDL schematic showing catalyst distribution and the effect of electrolyte flooding. (a, b) Catalyst loaded on the surface of the GDL: (a) before flooding, (b) after flooding. (c, d) Catalyst distributed throughout the MPL: (c) before flooding, (d) after flooding. 73

Figure 5-2: Zn-air battery schematics for full cell tests. (a) Tri-electrode configuration and (b) bifunctional configuration. The bifunctional cell is tilted to allow O_2 bubbles to escape during OER. 76

Figure 5-3: (a-d) Plan view SEM SE images of (a) bare GDL, (b) O_2-MnO_x, (c) FG-MnO_x and (d) FG-MnO_x + CoO_x samples. (e) EDX line scan results from GDL cross sections. (f) Cross-section image of O_2-MnO_x on GDL; the red arrow indicates where the EDX line scan was taken. Plan view images (a-d) were taken at 10 kV; cross section images and EDX line scans were taken at 20 kV. 79

Figure 5-4: STEM results from O_2-MnO_x on GDL. (a) STEM bright field (BF) image. (b, c, d, g) STEM EDX maps for the region shown in (a). (b) C map, (c) Mn map, (d) O map and (g) overlain mapping results. (e) SAD pattern from O_2-MnO_x: AD. (f) SAD pattern from O_2-MnO_x after annealing. Diffracted intensity associated with GDL is marked in red, while the O_2-MnO_x film is marked in blue. (h) STEM EDX spectra from O_2-MnO_x films on GDL. 81

Figure 5-5: STEM results for FG-MnO_x on GDL. (a) STEM BF image. (b, c, d, g) STEM EDX maps for the region shown in (a). (b) C map, (c) Mn map, (d) O map and (g) overlain mapping results. (e) SAD pattern from FG-MnO_x: AD. (f) SAD pattern from FG-MnOx after annealing. Diffracted intensity associated with GDL is marked in red, while diffracted intensity from the FG-MnO_x film is marked in blue. (h) STEM EDX spectra from FG-MnO_x film on GDL. 82

Figure 5-6: STEM results for FG-MnO_x + CoO_x on GDL after annealing. (a) STEM BF image. (b, c, d, g) STEM EDX maps for the region shown in (a). (b) C map, (c) Mn map, (d) Co, (e) O map and (g) overlain mapping results. (f) SAD pattern from FG-MnO_x + CoO_x. Diffracted intensity associated with GDL is marked in red, while the diffracted intensity for the FG-MnO_x + CoO_x film is marked in blue. (h) STEM EDX spectrum from the overall area. 83

Figure 5-7: XPS results from coated electrodes after annealing. (a) Mn 3s, (b) Mn 2p, (c) Co 2p, and (d) quantification results. 88

Figure 5-8: XPS results from coated electrodes before annealing (as deposited). (a) Mn 3s, (b) Mn 2p and (d) quantification results. 88

Figure 5-9: Half-cell testing results. (a) 10th CV cycle in Ar-saturated 1 M KOH. LSV results at a scan rate of 5 mV s^{-1} in (b) O_2-saturated and (c) Ar-saturated 1 M KOH. (d) CV results used for capacitance measurements (CDL), performed between 0.1 and 0.2 V vs. Hg/HgO at varying scan rates. 90

Figure 5-10: (a) CV results at a scan rate of 20 mV s^{-1} in O_2-saturated 1 M KOH. (b) LSV results in O_2-saturated 1 M KOH. (c) Chronopotentiometry performed at -20 mA cm^{-2} in O_2-saturated KOH. (d) EDX results from samples tested in (c). (e) CV results used for capacitance measurements (CT), performed between 0.1 and 0.2 V vs. Hg/HgO at varying scan rates. 91

Figure 5-11: Full cell battery test results, performed in 6 M KOH + 0.25 M ZnO. (a) Discharge voltage at various discharge rates. (b) Electrode polarization (left axis) and power (right axis) curves (1 mA s^{-1} scan rate). (c) Electrode polarization at 1 mA s^{-1} before and after 200 cycles. (d, e, f, and g) Tri-electrode cycling results at 20 mA cm^{-2}: (d) Pt/Ru-C (ORR) and Pt/Ru-C (OER), (e) O_2-MnO_x (ORR) and CoFe (OER), (f) FG-MnO_x and CoFe, (g) FG-MnO_x + CoO_x (ORR) and CoFe (OER). 95

Figure 5-12: EIS results for cycled and uncycled electrodes performed at a cell potential of 1.2 V. (a) Pt/Ru-C, (b) FG-MnO_x, (c) O_2-MnO_x and (d) FG-MnO_x + CoO_x. Cycling was performed at 20 mA cm^{-2} for 200 cycles in a tri-electrode configuration. 96

Figure 5-13: OER performance comparison. (a) LSV in 1 M KOH at 5 mV s^{-1}. (b) Charge rate in 6 M KOH + 0.25 M ZnO. (c) Charge polarization (1 mA s^{-1}), measured after rate test shown in (b). 96

Figure 5-14: STEM results for O_2-MnO_x cycled as the ORR electrode in a tri-electrode configuration (200 cycles, 100 h at 20 mA cm^{-2}). (a) STEM annular dark field (ADF) image. (b-g) STEM EDX mapping results: (b) Mn map, (c) C map, (d) Zn map, (e) K map, (f) O map and (g) overlain Mn, Zn and C map. (h) STEM EDX spectrum from the overall area. 99

Figure 5-15: STEM results from FG-MnOx cycled as the ORR electrode in a tri-electrode configuration (200 cycles, 100 h at 20 mA cm^{-2}). (a) STEM BF image. (b) STEM ADF image. (c-g, i) STEM EDX

mapping results: (c) O map, (d) Mn map, (e) C map, (f) Zn map, (g) K map, (i) overlain Mn, Zn and C map. (h) SAD pattern. (j) STEM EDX spectrum from overall area. 101

Figure 5-16: TEM/ STEM results from FG-MnO_x + CoO_x cycled as the ORR electrode in a tri-electrode configuration (200 cycles, 100 h at 20 mA cm^{-2}). (a) TEM BF image. (b) STEM ADF image. (c) SAD pattern. Diffracted intensity associated with GDL is marked in red, while the diffracted intensity for the FG-MnO_x + CoO_x film is marked in blue. (d-j) STEM EDX mapping results: (d) Mn map, (e) K map, (f) O map, (g) Zn map, (h) Co map, (i) C map and (j) overlain Mn, Co and C maps. (k) STEM EDX spectrum from the overall area. 102

Figure 5-17: TEM/ STEM results for FG-MnO_x + CoO_x cycled in a bifunctional configuration (100 cycles, 50 h at 10 mA cm^{-2}). (a) TEM BF image. (b) STEM ADF image. (c) STEM BF image. (d-h, j) STEM EDX mapping results: (d) Mn map, (e) Co map, (f) C map, (g) Zn map, (h) O map, (j) overlain Co and Mn maps. (i) SAD pattern. Diffracted intensity associated with GDL is marked in red, while the diffracted intensity for the FG-MnO_x + CoO_x film is marked in blue. (k) STEM EDX spectrum of the overall area. 103

Figure 5-18: Bifunctional cycling results. (a) Charge and discharge polarization before and after cycling. (b) EIS before and after cycling. (c) Bifunctional cycling test for 100 cycles (50 h) at 10 mA cm^{-2}. 105

Figure A-1: TEM Results for ZrO_2 films deposited on GDL. A), B), and C) are 25 cycles; D), E), and F) are 50 cycles; G), H), and I) are 100 cycles. A) D) and G) are bright field images, B), E) and H) are dark field images, C), F), and I) are selected area diffraction patterns. 131

Figure A-2: LSV results from various ALD films prepared on GDL: A) ZrO_2, B) HfO2, C) reduced oxygen content ZrOx , and D) ZrN 132

Figure A-3: TEM results from 50 cycles ZrO_x(3.5sO_2). A) Bright field image, B) dark field image, and C) selected areas diffraction pattern. 134

Figure A-4: TEM results from 50 cycle ZrN on holey carbon, A) bright field image, B) dark field image, C) selected area diffraction pattern. 135

Figure A-5: LSV for various ALD and sputtered films. A) ALD oxynitrides, B) ALD ternary oxides, C) sputtered Ta based films, and D) sputtered Nb based films. 136

Figure A-6: TEM results from 50 cycles $HfZrO_x$ on GDL. A) Bright field image, B) dark field image, and C) diffraction pattern. 138

Figure A-7: STEM EDX mapping results for 50 cycles $HfZrO_x$ on GDL. A) ADF image, B) C-K map, C) O-K map, D) Zr-L map, E) Hf-M map, and F) overlain C, Hf, and Zr map. 138

Figure A-8: TEM results from TaO_x (A, B, E) and NbO_x films (C, D, G). A and C are bright field images, while B and D are dark field images. E, F, and G are diffraction patterns. F is a diffraction pattern taken from a sample of bare GDL and is shown for comparison. 140

Figure B-1: Schematics of A) conventional precursor delivery, and B) precursor delivery using a bubbler 141

Figure B-2: Schematic of pressurized precursor delivery steps. A) Charge, B) dwell, C) discharge. D) Pulse timing scheme. 147

Figure B-3: ALD temperature window, depositions were performed with a pulse timing of 10 s–10 s–20 s–10 s. 148

Figure B-4: Saturation curves. A) Precursor saturation curve, prepared with timing scheme: 10 s–10 s–20 s–10 s. B) Plasma dose saturation curve, prepared with timing scheme 10 s–10 s– x – (30 s-x). 150

Figure C-1: Saturation plots for the $(EtCp)_2Mn + H_2O$ ALD system presented in literature. (A) Burton *et al.*[80], (B) Pickrahn *et al.*,[76] (C) Siddiqi *et al.*[120] 151

Chapter 1: Introduction

In recent decades, the effects of greenhouse gases from fossil fuels have become increasingly apparent. The vast majority (~72%) of greenhouse gas emissions come from energy generation (eg., electrical energy, transportation, heating, etc.). [1] In order to slow the effects of climate change, alternative methods of energy generation and storage are necessary. Wind and solar technologies have seen vast improvements in recent years, and now, in most parts of the world, have become the lowest cost source of power. [2] This is very exciting for climate proponents and is critical step towards the elimination of fossil fuels. Despite the dropping costs of renewable power generation, the intermittent nature of wind and solar remains problematic. Because wind and solar cannot generate power on demand, energy needs to be storage during periods of high generation and released when demand is high. Inexpensive, safe, and efficient grid-scale energy storage is mandatory for a renewable energy economy.

Pumped hydro storage (PHS) is by far the most widely used technology for grid scale energy storage, accounting for 96% of the world's energy storage power capacity. [3] PHS requires two large reservoirs for water, separated in elevation. Energy is stored in the form of gravitational potential energy by pumping water from the lower reservoir to the higher reservoir. Energy is then drawn from the system by flowing the water through a turbine, back into the lower reservoir. The largest drawback of PHS is the need for specific geographic features, making PHS more of a niche storage solution. Some other grid scale storage solutions are compressed air, flywheel, electrochemical (batteries, supercapacitors), and thermal. These other storage solutions are much more versatile in their implementation than PHS but are more expensive and generally have lower total capacity. [3]

Batteries are an appealing option for grid scale storage because of their versatility, safety, and low maintenance. The modular nature of batteries facilitates easy installation of grid scale energy storage solutions ranging from tens of kWh to hundreds of MWh, even in areas with poor infrastructure or geography. There are many types of batteries commercially available, with varying chemistry, cost, energy density, power density, cycle life, and safety characteristics. A comparison of battery technologies is shown in Table 1-1. [4]–[7] Since most batteries have historically been designed for use in portable applications, many of the mature battery technologies are not very well suited for grid-scale applications. For example, lead-acid batteries

(invented in 1859) are considered the most mature and widely used battery technology but are not applicable to grid-scale storage because of their low depth of discharge, low energy density, and short cycle life. For grid-scale applications, the most important design considerations are cost, cycle life, safety, and, to a lesser extent, energy density. [3]

Table 1-1: Comparison of various battery technologies. [4]–[7]

Battery Type	Power Density W kg^{-1}	Energy Density Wh kg^{-1}	Cycle life Cycles	Efficiency %	Cost \$ kWh^{-1}
Ni-MH	150-300	50-70	500-3000	50-80	150-200
Pb-acid	200-400	30-50	2000-4500	70-90	120-150
Na-S	120	100	2500-4500	75-90	250-500
Redox-flow	100	30-50	>12000	60-85	150-1000
Li-ion	315	155	>1200	80-90	250-350
Zn-air	105	230	100-300	50-65	90-120

Metal-air batteries are a technology that has received a lot of research interest in recent years because of their very high theoretical energy densities. Metal-air batteries have a metal electrode (Zn, Al, Fe, Mg, Li, etc.), which dissolves during discharge, and a porous carbon electrode which reduces oxygen during discharge. The use of atmospheric oxygen is what enables the high energy densities of metal-air batteries; oxygen is used as a reactant but is not contained/ carried within the cell, reducing battery mass. The main challenges hindering commercialization of metal-air batteries are the poor reaction kinetics at the air electrode and instability of the metal electrode. The use of atmospheric air necessitates a complicated air electrode structure which maintains three phase boundaries between the air, electrolyte, and catalyst. Of the metal-air batteries examined in the literature, ZABs are the most promising for grid scale energy storage. Compared with Mg, Al, and Li, dissolution and deposition of Zn is easily controlled in aqueous electrolytes. Because of their reactivity with water Mg-, Al-, and Li-air batteries generally require non-aqueous electrolytes which are flammable, expensive, and harmful to the environment. Additionally, Zn is abundant, inexpensive, and environmentally benign. [8], [9]

Although ZABs have many attractive properties, their performance is still limited by a number of technical challenges. Passivation and shape change of the Zn electrode result in poor depth of discharge and cycle life. Problems with the air electrode result in low discharge/ charge efficiencies, typically ~50-60%. ZAB efficiency can be improved by using an effective

electrocatalyst. Platinum is widely known as a very active catalyst for oxygen reduction, but is far too expensive for widespread use. In recent years, there has been much research into inexpensive transition metal oxides for use in ZABs, demonstrating the good activity and stability of transition metal oxides such as MnO_x and CoO_x in ZAB applications. In addition to the inherent activity of a catalyst, its morphology and distribution are critically important. The distribution of catalyst throughout the structure of the air electrode maximizes three phase boundary area and reduces the effects of electrolyte soaking into/ through the electrode. Catalysts with a nanoscale morphology tend to exhibit improved catalytic activity over their micro- or macroscale counterparts, because of shorter paths for electron conduction and increased surface area to volume ratios. New innovative methods of catalyst synthesis and electrode preparation are needed to improve ZAB efficiency before widespread commercialization is feasible. [9], [10]

Atomic layer deposition (ALD) is a thin film deposition technique capable of depositing high quality films of a wide variety of materials. ALD is performed by exposing the substrate to alternating pulses of reactant gases such that the substrate surface is saturated with reactant after each pulse. The saturating nature of the reactions gives ALD films their unique set of properties including high uniformity, high conformity, very fine thickness control, and high purity. ALD is very good at depositing conformal films on porous substrates; high surface area substrates can be coated, producing a high surface area deposit. [11] This property of ALD films is particularly attractive for the preparation of catalysts because it allows the catalyst to be deposited directly onto conductive high surface area substrates, producing high catalyst surface area with excellent electrical conductivity. [12]

The purpose of this work is to develop an ALD procedure for the deposition of MnO_x and to use this procedure to prepare high performance ZAB electrodes. Chapter 2 is a literature review, summarizing background information and current research in the areas of ZABs and ALD. Experimental details are given in Chapter 3. Chapter 4 reports the process development and growth behaviour of MnO_x films prepared by ALD. Chapter 5 characterizes ALD MnO_x films on gas diffusion layers (GDL) and examines their performance in full-cell ZAB tests. Conclusions and recommendations for future work are given in Chapter 6. Appendix A examines Zr, Hf, Nb, and Ta based films deposited onto carbon based substrates and characterized using electron

microscopy and electrochemical half-cell tests. Appendix B gives the growth behaviour of ALD LaO_x using $La(^iPrCp)_3$ and oxygen plasma.

Chapter 2: Literature Review

2.1 Metal-air Batteries

With the drive to eliminate the world's reliance on fossil fuels, comes the need for new energy storage solutions. Since many renewable energy sources like wind and solar do not provide energy on demand, the energy must be stored when the wind is blowing or the sun is shining and released when the energy is needed. There are a number of proposed solutions to grid scale energy storage such as pumped hydro or compressed air. However, these solutions often rely on specific geographic features that many areas of the world do not have access to. Electrochemical energy storage, i.e., batteries, are an attractive option for grid scale renewable energy storage for a number of reasons. Firstly, batteries have a high conversion efficiency (~80%) compared to other technologies. Battery technology can also be implemented anywhere and their modular nature allows for easy implementation in both large and small scale applications; from a single home to a large wind or solar farm. Batteries are typically constructed in self-contained cells that are assembled off sight, making installation quite simple. Most battery technologies are also very low maintenance, having no moving parts and little to no additional auxiliary equipment is required. Apart from grid scale storage, battery development is also largely driven by consumer electronics such as mobile phones and hybrid/ electric vehicles. [3], [13]

For many applications the most important performance metrics are energy density (Wh/cm^3) and specific energy (Wh/kg). Metal-air batteries have exceptional theoretical energy densities because their use of air as a reactant eliminates the need for an on board oxygen source. Metals used for metal-air batteries include Fe, Zn, Al, Mg, and Li. Mg-, Al-, and Li-air batteries all have very high specific energies, exceeding 5000 Wh/kg. Figure 2-1 compares the specific energy of various battery technologies along with gasoline and H_2-air. Although Mg, Al, and Li-air technologies can theoretically out perform Zn-air batteries, there are some serious challenges facing their development. It is possible to operate Al- and Mg-air batteries using aqueous electrolytes; however, Al and Mg experience severe corrosion in aqueous environments. Li-air batteries necessitate the use of non-aqueous electrolytes. Non-aqueous electrolytes are expensive and are often dangerous. Of the metal-air battery systems, Zn-air is the most promising option for wide spread implementation. [9], [14]–[16]

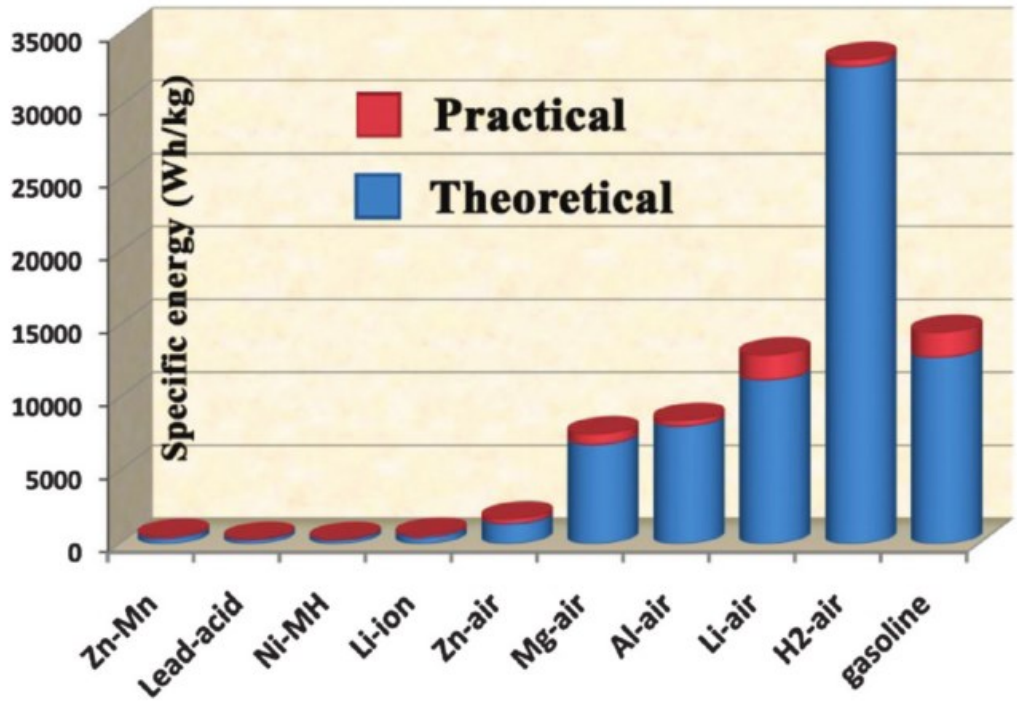

Figure 2-1: Comparison of various battery technologies alongside gasoline and H_2-air. [9]

2.2 Zn-air Batteries

Zn-air batteries (ZABs) are an attractive option to Li-ion batteries because of their low cost, high safety, high specific energy, environmental compatibility, and abundance of raw materials. There are three types of ZABs: primary, secondary, and mechanically rechargeable. Primary ZABs are non-rechargeable and have been commercialized for many years as hearing-aid batteries. Secondary ZABs are rechargeable, but more development is required to improve cycle efficiency and cycle life before wide spread commercialization can be implemented. Some companies have already begun commercialization of ZABs including Fluidic Energy, Revolt, and Eos Energy Storage. Mechanically rechargeable ZABs are recharged by physically replacing the spent Zn and electrolyte. [9], [17]

2.2.1 Zn-Air Battery Chemistry

The electrodes used in a ZAB are a metallic Zn electrode and a porous air electrode. Zn readily dissolves and produces hydrogen in acidic environments; this necessitates the use of an alkaline electrolyte. Oxygen reduction and oxygen evolution reactions occur at the air electrode. During discharge, the following reactions occur (SHE is the standard hydrogen electrode): [9], [14]

Zn electrode:

$$Zn \rightarrow Zn^{2+} + 2e^- \quad (1)$$

$$Zn + 4OH^- \rightarrow Zn(OH)_4^{2-} + 2e^- \quad E^0 = -1.25 \text{ V vs. SHE} \quad (2)$$

$$Zn(OH)_4^{2-} \rightarrow ZnO + H_2O + 2OH^- \quad (3)$$

$$Zn + 2H_2O \rightarrow Zn(OH)_2 + \uparrow H_2 \quad \text{Hydrogen evolution} \quad (4)$$

Air electrode:

$$O_2 + H_2O + 4e^- \rightarrow 4OH^- \quad E^0 = 0.401 \text{ V vs. SHE} \quad (5)$$

$$2KOH + CO_2 \rightarrow K_2CO_3 + H_2O \quad \text{Parasitic carbonate formation} \quad (6)$$

Overall reaction, (1) + (2) + (3) + (5):

$$2Zn + O_2 \rightarrow 2ZnO \quad E^0 = 1.65 \text{ V} \quad (7)$$

(1) During discharge at the Zn electrode, the reaction begins with the oxidation of Zn to Zn^{2+}. (2) Zn^{2+} then combines with hydroxyl ions in the electrolyte to form zincate ions. (3) Once the concentration of zincate ions reaches saturation, they begin to decompose into Zn oxide. Zn oxide coats the electrode and is electrically insulating, which can cause non-uniform dissolution/ deposition of Zn during cycling. During recharge, the reverse of these reactions takes place. Because the degree of zincate supersaturation is time-dependent, the chemistry of rechargeable ZABs is complicated and not fully understood. Zincate chemistry is a very important consideration in the development of secondary ZABs; a more thorough understanding of the zincate ion will help in the development of Zn electrodes for ZABs. [9], [14], [18]

At the air electrode during discharge, as shown in equation (5), oxygen is reduced into hydroxide ions. This is called the oxygen reduction reaction (ORR). During charge, hydroxyl ions are converted into oxygen gas, which is known as the oxygen evolution reaction (OER). Both of these reactions suffer from significant polarization effects, which necessitates the need for effective electrocatalysts. Slow kinetics resulting in large polarization for ORR and OER is considered one of the main challenges in the development of ZABs. Equation (6) is the parasitic formation of K_2CO_3 from KOH and CO_2. CO_2 is present as an impurity in the feed air or as a product of carbon corrosion. The K_2CO_3 formed from this reaction is poorly soluble in alkaline solutions and has a tendency to clog porosity within the GDL, reducing electrode performance and lifetime. [9], [14], [18]

Polarization curves for the Zn and air reactions are shown schematically in Figure 2-2. The anodic reaction potential is -1.25 V vs. SHE and the cathodic reaction potential is 0.40 V vs. SHE, resulting in a total cell potential of 1.65 V. However due to the sluggish kinetics of ORR, the discharge potential is lowered in order to obtain sufficient current. Typical working voltages for ZABs are < 1.2 V. Kinetic limitations are also experienced during charge cycles; OER requires a large overpotential before significant current is achieved. Electrocatalysts are used to reduce the overpotential at the air electrode by improving the kinetics of the ORR and OER. Despite the use of electrocatalysts, most ZABs have an efficiency somewhat less than 60%. Efficiency is calculated from the ratio of discharge to charge potentials. [19]

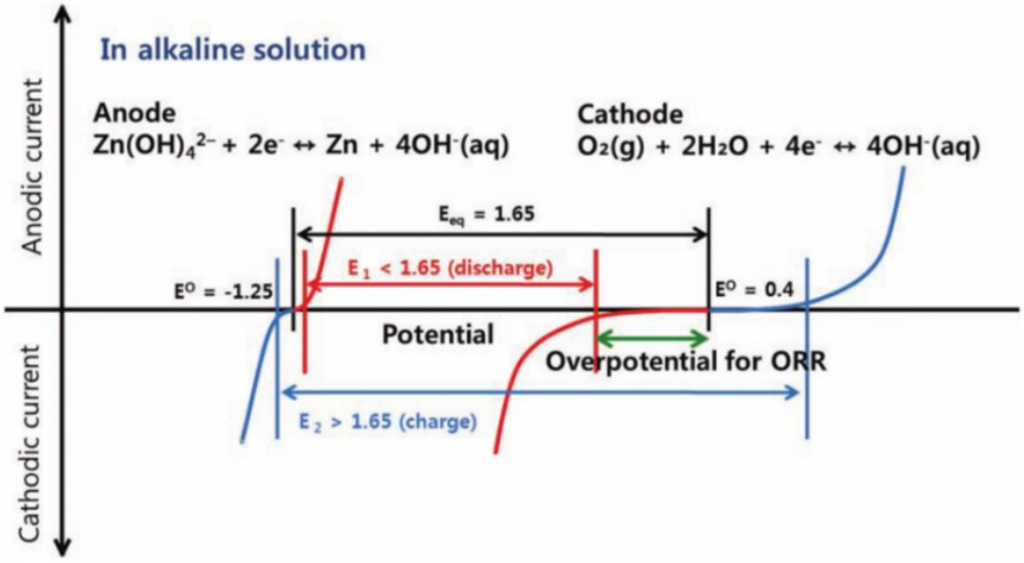

Figure 2-2: Schematic polarization curves for a Zn-air cell. Discharge curves are shown in red and charge curves are shown in blue. Note the very large polarization/ overpotentials for the air reactions. [14]

2.2.2 Zn-Air Battery Design

A schematic of a typical ZAB is shown in Figure 2-3. [14] ZABs are composed of four main components: a Zn electrode, a porous air electrode, an electrolyte, and a separator. Zn foil, or a Zn plate, is commonly used as the Zn electrode. Zn dissolves during discharge and is redeposited during charging. To prevent hydrogen evolution and Zn corrosion, the electrolytes used in ZABs are highly alkaline; 6 M KOH is commonly used. The purpose of the separator is to facilitate the

transport of hydroxide ions (OH^-) from the air electrode to the Zn electrode; not all ZAB designs require a separator. The separator should be electronically insulating and have good ionic conductivity. Separators are typically polymers such as polyethylene, polyvinyl alcohol, polyolefin, and polypropylene. [14]

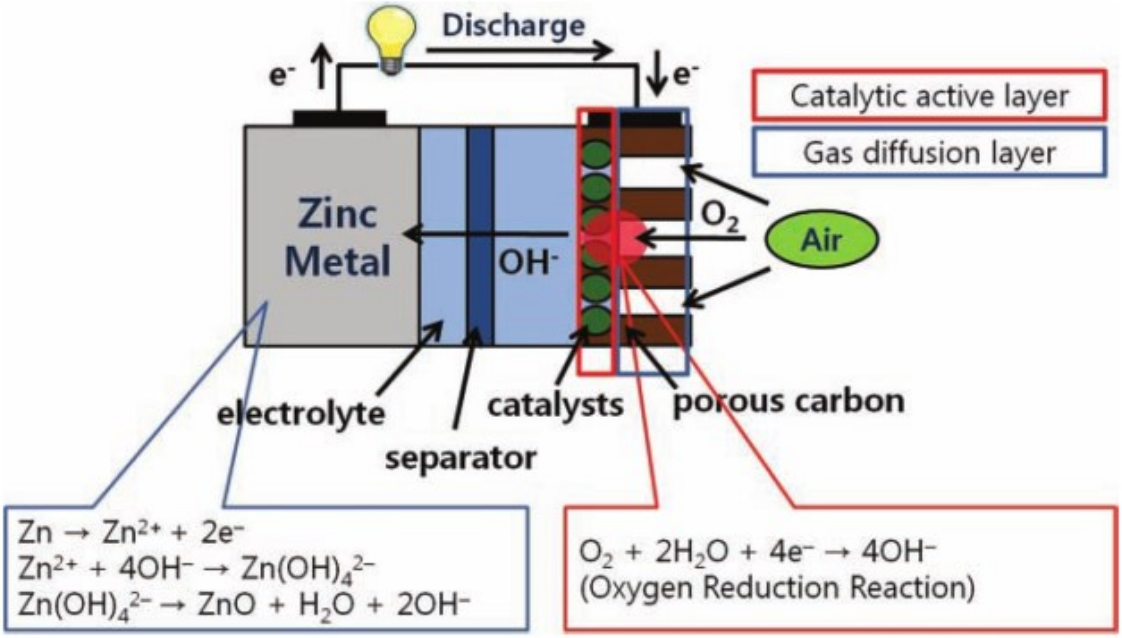

Figure 2-3: Schematic of a typical ZAB. [14]

2.2.2.1 Zn Electrode Design

Since ZABs utilize oxygen from the air, the capacity of a ZAB is determined entirely by the Zn electrode. As the battery is discharged, a layer of ZnO will begin to form on the Zn electrode surface. Over time the ZnO layer continues to grow and eventually causes complete passivation of the Zn surface; at this point the battery is completely discharged. Although a Zn plate or foil is commonly used in ZABs, these simple electrodes have limited surface area, resulting in poor battery capacity. Some alternative Zn electrode structures are powders, fibres, sponges, and composites. These high surface area structures increase battery capacity, as well as improve Zn electrode cyclability [17], [20]

2.2.2.2 Air Electrode Design

The performance of a ZAB is largely determined by the design of the air electrode. The air electrode is commonly referred to as the gas diffusion layer (GDL). Most air electrodes used in

ZABs have two layers; a backing layer and a microporous layer. The backing layer is composed of carbon fibres with a high weight fraction of polytetrafluoroethylene (PTFE, >10 wt%). The backing layer provides mechanical support, acts as a current collector, and enhances electrode hydrophobicity. On top of the backing layer is the microporous layer (MPL). The MPL is composed of activated carbon nanoparticles (~50 nm in size) bound together with PTFE (~5 wt%). Catalyst is loaded onto or within the MPL. The air electrode must allow for gas diffusion; this is achieved by the highly porous structure of the GDL. ORR occurs at three phase regions between oxygen gas, electrolyte, and catalyst. In order to maximize the three phase boundary area, the MPL should be highly porous and contain well dispersed catalyst. Effective catalyst dispersion can be difficult to achieve, as most catalyst preparation techniques only deposit catalyst in the near surface region of the electrode. [19]

Another requirement of the air electrode is stability in the highly alkaline electrolyte and within the wide potential window of the charge and discharge reactions. The high surface area carbon is quite susceptible to corrosion under these conditions. One method of decreasing corrosion of carbon is to increase the graphite content; graphite is more resistant to corrosion than amorphous carbon. [19] The air side of the electrode must be hydrophobic to prevent leakage of electrolyte; PTFE is used to achieve this. The concentration of PTFE is varied through the structure of the GDL, with the catalyst side being relatively hydrophilic and the air side being very hydrophobic. The intention of the hydrophobicity gradient is to maintain the position of the electrolyte/ air within the GDL structure. However, during extended cycling, it is possible for the PTFE to begin losing its hydrophobic nature. If this occurs, electrolyte will wet through the GDL and leak through the GDL, severely degrading performance of the cell. Electrolyte leaking from the cell is also potentially dangerous, since 6 M KOH has a pH of 14 and can cause chemical burns.

2.2.2.3 Challenges for Zn-Air Batteries

For the development of ZABs, there are a number of materials problems that must be addressed. The most pressing issue with ZABs is the poor kinetics of the reactions utilizing air. Both the charge and discharge reactions that take place at the air electrode require large overpotentials, resulting in poor charge/ discharge efficiency (<60%). In order to improve the efficiency of ZABs, the overpotential at the air electrode must be reduced by finding suitable electrocatalysts for the charge and discharge reactions. [9], [21], [22]

Finding a suitable electrocatalysts for ZABs is not a trivial exercise. Apart from the factors of cost, safety, catalytic activity, and ease of manufacturing, catalyst stability is a very important consideration. Due to the high pH (>14) and wide potential window used in ZABs, most materials are not stable during cycling. Many materials will corrode under these conditions, while others will agglomerate or undergo phase changes which lead to mechanical degradation due to cyclic volume changes. Catalysts used in ZABs are discussed in Section 2.3.1. [23]

Changes in the Zn electrode structure during cycling is also a significant problem facing ZABs. Zn oxide produced during discharge will deposit on the Zn electrode and can cause inconsistencies in conductivity along the surface. Over the course of multiple charge/ discharge cycles, the morphology of the Zn electrode can change dramatically due to non-uniform dissolution and deposition of Zn. In order to fully understand the mechanisms behind Zn and ZnO deposition, a more thorough understanding of the chemistry of the Zn reactions is needed, specifically for the zincate ion. Electrodeposited Zn also has a tendency to form dendrites. During extended cycling these dendrites grow and can become large enough to puncture the separator or even cause a short circuit. There has been a large amount of work done in prevention of Zn dendrite formation and there are three main methods of prevention: separator modification, additives to the electrode/ electrolyte, and AC or pulsed charging. [17], [18], [20], [24]

The use of atmospheric air as a reactant in ZABs presents its own challenges; one major concern is that air contains 0.03% CO_2. When dissolved in the electrolyte, CO_2 can reduce the pH by forming carbonic acid. If CO_2 is present in the electrolyte, K_2CO_3 can precipitate out of solution, clogging electrode porosity and degrading performance. [19] Eos Energy Storage claim that their use of a neutral pH electrolyte does not absorb CO_2, avoiding carbonate clogging issues. [25] The humidity of the feed air is also an important consideration. If the feed air has a low humidity, electrolyte will evaporate. Over time, evaporation will change the electrolyte composition and cause instabilities within the cell. The carbon dioxide and evaporation problems can both be solved through treating the air before introducing it to the cell. By bubbling feed air through a hydroxide solution, CO_2 is removed and the humidity of the feed air will increase. Another solution to the feed air problem is to remove old electrolyte and replace it with fresh electrolyte once CO_2 has accumulated and/ or significant electrolyte evaporation has occurred. [19], [25]

The harsh conditions of high pH and large applied potential during charge can cause corrosion of the carbon GDL. Carbon corrosion damages the substrate, causing morphological changes and producing K_2CO_3 as well as CO_2. As discussed previously, these species are detrimental to performance. Ross and Sattler [18] showed that the corrosion rate of carbon black in 30% KOH was much higher for amorphous carbon compared with graphitic carbon. This result indicates that the corrosion of carbon is very dependent on its structure. [9], [14], [19], [26]

2.2.2.4 Tri-Electrode ZABs

The cycling stability of a ZAB can be greatly enhanced by utilizing separate electrodes for the charge and discharge reactions. The discharge reaction (ORR) occurs under reducing conditions and requires an electrode that is not flooded by electrolyte. The charge reaction (OER) occurs under oxidizing potentials and favours an electrode that is fully wet by the electrolyte. Large potential differences between charge and discharge reactions can cause fast degradation of most catalysts due to a number of effects such as corrosion, carbonate formation, or volume expansion/ contraction associated with phase changes. It is, therefore, advantageous to use separate electrodes for ORR and OER. [27]–[31] The incorporation of an additional electrode into a ZAB battery will inevitably increase the weight and volume of the cell, reducing the overall energy density and specific energy. However, the improvement to efficiency and stability may be drastic enough to justify the weight increase. Also, the main application for ZABs is stationary storage, where cell size and weight are only minor design considerations. Figure 2-4 shows the electrode configuration and cycling stability for a two-electrode and a tri-electrode ZAB. The catalyst used was an N and P doped mesoporous nanocarbon. Note that the tri-electrode configuration greatly enhances charge and discharge potentials as well as cycling stability. [28]

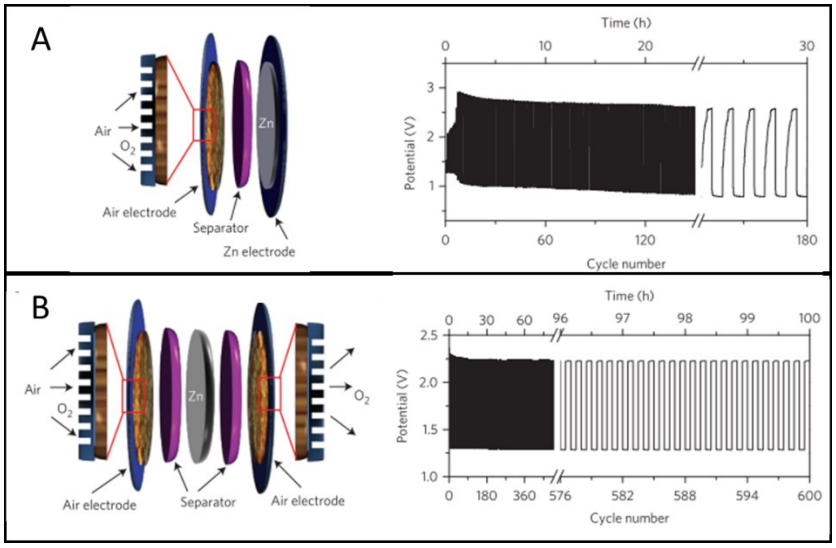

Figure 2-4: Schematics and cycling stability of (A) two-electrode ZAB and (B) three-electrode ZAB. The catalyst used was an N and P doped mesoporous nanocarbon. Cycling was performed at a current density of 2 mA cm^{-2}. [28]

2.2.2.5 Horizontal ZABs

Another modification to the ZAB design is the use of horizontal electrodes. In a vertical configuration, the bottom of the GDL experiences elevated pressure from the electrolyte. This pressure pushes electrolyte into the GDL and exacerbates flooding. The vertical configuration can also cause problems with the Zn electrode. Due to gravity effects, Zn deposition tends to concentrate near the bottom of the electrode leading to dendrite formation and potential short-circuits. ZABs with a horizontal configuration have been shown to have improved cycle life over vertical cells. [27], [31], [32]

2.3 Oxygen Reaction Catalysis

The kinetics of the oxygen reduction (discharge) and oxygen evolution (charge) reactions are one of the main challenges facing the development of metal-air batteries as well as many other electrochemical devices such as fuel cells and electrolysis cells. Catalysts improve the kinetics of ORR and OER by providing alternate pathways for the reaction to take, reducing the energy barrier (i.e., overpotential) required. Catalysts provide active sites where intermediate species are relatively stable, allowing a reaction to occur over a few intermediate steps that each have a relatively small energy barrier. A schematic free energy curve is shown in Figure 2-5A; this

schematic shows that the energy barrier for the reaction is drastically smaller when the reaction proceeds via intermediates. [33]–[35]

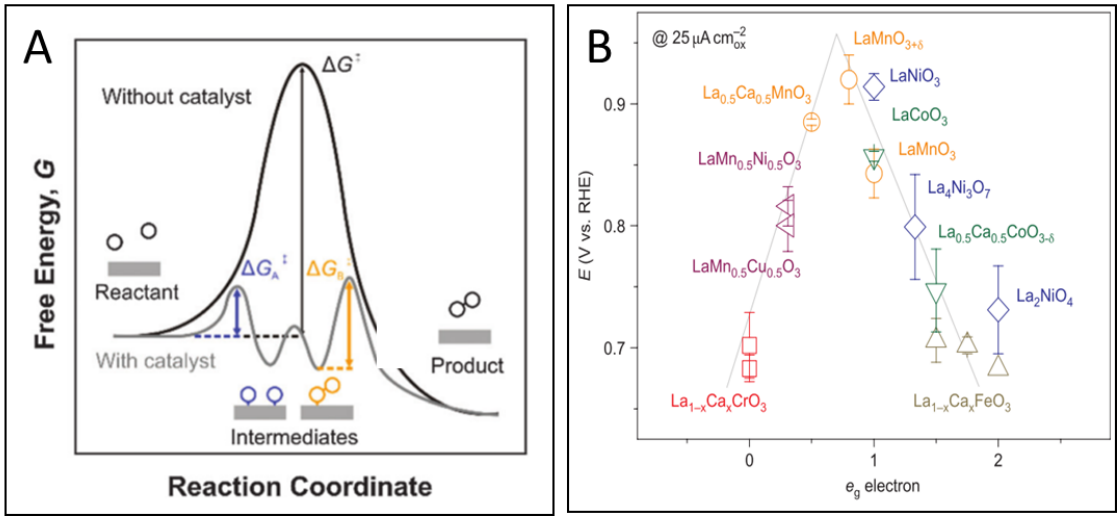

Figure 2-5: A) Schematic free energy curve for a generic reaction. The free energy barrier without a catalyst is effectively reduced by the presence of stable intermediate species on the catalyst surface. [35] B) Volcano plot comparing the activity of various perovskite structures. [34]

The reaction pathways for ORR and OER are a series of complex electrochemical reactions and the exact path depends on the catalyst used. These electrochemical reactions involve a number of intermediate species such as OOH*, OH*, and O* (* denotes a surface species). The affinity of the catalytic site to bond to the intermediate species is the main factor affecting catalytic activity. The active site must bond strongly enough to allow for the reaction to take place, but also weak enough to allow for removal of the intermediate and regeneration of the active site. In order to obtain a good electrocatalyst, there needs to be a precise balance of bond energies for each of the intermediate species. Due to the non-ideal scaling between the bond energies of OOH* and OH* species, there is a nonzero theoretical overpotential of 0.3 – 0.4 V for ORR. OER also has a similar theoretical limit due to bond energy relations. [33]–[35]

Over the years there has been much work in trying to find material properties that can be directly related to catalytic activity, so-called activity descriptors. As discussed above, the activity of a catalyst is dependent on the bond strength of intermediate species; most activity descriptors are related to oxygen bond energy. Some activity descriptors that have been proposed are the enthalpy (or electrochemical potential) of transition between oxidation states, enthalpy of

formation for metal hydroxides, pH of zero charge, and electron orbital filling. [35]–[37] In recent years, computer simulations using density functional theory (DFT) have enabled a deeper understanding of the underlying mechanisms of ORR and OER. By modeling the free energy changes for each intermediate step in oxygen reactions, the activity of catalysts can be predicted. It should be noted that the results of DFT calculations can only be as accurate as the reaction model/ mechanism used. ORR/ OER can occur via many different reaction pathways and determination of the exact pathway a catalyst utilizes can be extremely difficult. The combination of DFT calculations and experimental studies have given rise to an activity descriptor for oxide surfaces; the d-band center relative to the Fermi level. Ultimately what the position of the d-band center describes is the balance in oxygen bond strength. A high d-band bonds too strongly and a low d-band bonds too weakly. DFT calculations give rise to a figure commonly seen in the literature on oxygen catalysis, the volcano plot. Volcano plots show the relation of catalytic activity to an activity descriptor; an example volcano plot is shown in Figure 2-5B. Volcano plots get their name from the shape that the data takes, the maximum activity occurs some where in the middle, with linear decreases in activity on either side of the maximum giving the shape of a volcano. The maximum represents the best balance of intermediate bonding strength, while the sloped sides of the volcano represent binding energies that are either too strong or too weak. [34], [35], [38]–[40]

In general there are two mechanisms for ORR catalysis, the direct four-electron pathway and the two-electron pathway via a peroxide intermediate. The two-electron pathway occurs in two steps; peroxide generation followed by either peroxide reduction or decomposition. The reduction/ decomposition of peroxide is typically quite slow. However, some materials are able to quickly catalyze peroxide decomposition, resulting in two consecutive two-electron reactions. This process can be viewed as an apparent four-electron mechanism known as a serial 2 x $2e^-$ pathway. In alkaline media, the two-electron pathway is more common, but the four-electron pathway is more desirable as it is generally faster and avoids peroxide generation. Peroxide is a strong oxidizer and can cause corrosion of the carbon based GDL. In alkaline media, the general reaction mechanisms for ORR are: [9], [14], [41]

Four-electron:

$$O_2 + 2H_2O + 4e^- \rightarrow 4OH^- \quad (8)$$

Two-electron:

$O_2 + H_2O + 2e^- \rightarrow HO_2^- + OH^-$ Peroxide generation (9)

$HO_2^- + H_2O + 2e^- \rightarrow 3OH^-$ Peroxide reduction (10)

$2HO_2^- \rightarrow 2OH^- + O_2$ Peroxide decomposition (11)

Example reaction pathways are shown in Figure 2-6A and Figure 2-6B for four-electron and two-electron mechanisms, respectively. The precise steps taken for ORR vary between catalysts; the pathways shown in Figure 2-6 are not applicable to all catalysts. The four-electron mechanism shown in Figure 2-6A follows a four step pathway: 1) Molecular oxygen gains an electron and adsorbs to the catalyst, displacing a surface hydroxide group. 2) An electron is gained as water donates a proton to the surface OO* group, producing a surface peroxide group (OOH*) and releasing a hydroxide ion. 3) The OOH* group is then reduced by an electron, producing a hydroxide ion and a surface O* group. 4) Another proton is donated from a water molecule as an electron is gained, producing a hydroxide ion and regenerating the surface OH* group. The two electron pathway in Figure 2-6B essentially follows the same first two steps as the four-electron pathway: 1) Molecular oxygen gains an electron and adsorbs to the catalyst, displacing a surface hydroxide group. 2) An electron is gained as water donates a proton to the surface OO* group, producing a surface hydroxide group (OH*) and a peroxide ion The difference between the two- and four-electron mechanisms is whether the peroxide group produced after step 2 remains on the surface, or if it is released into the electrolyte. For these example pathways shown in Figure 2-6, whether ORR follows a two- or four-electron mechanism is dependent on the surface affinity for peroxide species (OOH*). [34], [42]

The preferred reaction pathway for a specific catalyst is dependent on the binding energies for the reaction intermediates as well as the configuration of the active sites. How active sites are configured on a catalyst surface is dependent on the crystal structure, exposed crystallographic plane(s), and the presence of defects. Active site configuration determines how O_2 molecules are able to adsorb to the catalyst surface. Figure 2-6C shows different configurations for oxygen adsorption. [9] For end-on configurations (Figure 2-6C i, ii), only one oxygen atom is adsorbed to the surface. These configurations contribute mainly to the two-electron path. Parallel configurations (Figure 2-6C iii, iv) have two oxygen atoms adsorbed to the surface, promoting the direct four-electron pathway. [9], [41]

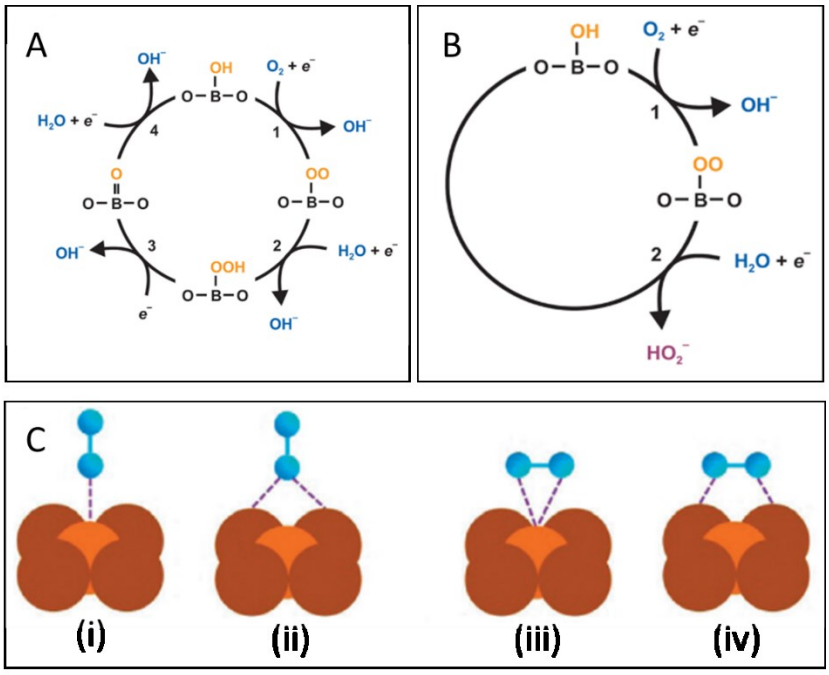

Figure 2-6: A) Example four-electron ORR pathway. B) Example two-electron ORR pathway. C) Configurations of O_2 adsorption. i) On top end-on, ii) bridge end-on, iii) bridge side-on one site, iv) bridge side-on two sites. [9], [42]

2.3.1 Catalysts for ZABs

For many years, ORR electrocatalysts have been investigated for use in a variety of applications. For a catalyst to be suitable for use in ZABs, it must be sufficiently active towards to ORR and/ or OER, stable, inexpensive, and abundant enough for widespread use. The stability of catalysts in ZABs is a major challenge due to the harsh conditions within the cell. Not only does the catalyst need to be stable in the highly alkaline electrolyte, it must be stable within the potential range used. The use of a tri-electrode configuration reduces the potential window that each catalyst is exposed to (see Section 2.2.2.4). Catalyst stability limits the cycle life of ZABs and is one of the main challenges for ZAB development. [9]

There are four main categories of ORR catalyst: noble metals, transition metal oxides (TMOs), carbon based materials, and metal-organic frameworks (MOFs). Noble metal catalysts are known for their excellent catalytic performance and reasonable stability. Because of this, Pt is commonly used as a benchmark for comparing ORR catalysts. However, the high cost and scarcity of noble metals makes them impractical for wide spread application. Transition metal

oxides, carbonaceous materials, and MOFs all show promise as possible alternatives to noble metals. [43]

2.3.1.1 Transition Metal Oxides (TMOs)

Transition metal oxides are a very promising alternative to noble metal catalysts because of their abundance, low cost, catalytic activity, and environmental friendliness. The most common TMOs used for ORR are CoO_x, NiO_x, FeO_x, and MnO_x. In addition to their catalytic activity, many TMOs are also stable in alkaline solutions, making them attractive for use in ZABs. However, most TMOs suffer from poor electronic conductivity. In order to improve their conductivity, there has been much work in developing composites and nanostructured oxides. [9], [10], [19], [35], [41]

Most transition metals have multiple stable oxidation states. This allows TMOs to have a range of possible stoichiometries and crystal structures. As discussed in Section 2.3, the ORR/ OER activity of a material is determined by the surface's binding energy to intermediate compounds (i.e., OOH*, OH*, and O*). The variable stoichiometry and crystal structures of TMOs allow their surface binding energies to be tuned in order to achieve optimal performance. The electronic structure and subsequent oxygen affinity of TMOs can be further tuned by the introduction of additional transition metal elements; ternary and higher order oxides have been demonstrated to improve catalytic performance and stability. Ternary and higher order TMOs are also commonly used to improve the bifunctional performance of a TMO. For example, MnO_x catalyzes ORR well, but is a poor OER catalyst. Adding Co to MnO_x results in dramatically increased OER performance, while causing little to no change in the ORR activity. [10], [23]

Manganese Oxide

Mn oxide is a widely used ORR catalyst because of its well documented activity, as well as its low cost, abundance, low toxicity, and environmental friendliness. Mn oxide has a wide variety of stable phases with different oxidation states (Mn^{2+}, Mn^{3+}, Mn^{4+}) and over 30 possible crystal structures. [10] Although there have been many reports in the literature on the ORR activity of various Mn oxide phases, direct comparison of quantitative data can be difficult and/ or misleading. The catalytic activity of MnO_x is dependent on many factors besides the oxidation state and crystal structure. Some of these factors are crystal size, particle size, shape, porosity,

and electronic conductivity. Not only do these factors affect the specific surface area of the catalyst, they can also affect the electronic structure. [42] The complex relationships between all these factors make it impractical to label a single MnO_x phase as the "best" for ORR. Stoerzinger *et al.* compiled literature results on the ORR activity of Mn oxides and Mn containing perovskite/ spinel oxides. [42] Stoerzinger *et al.* found that octahedral-coordinated Mn^{3+} sites are critical to ORR performance; the electron transfer number approaches four as Mn^{3+} content increases. Mn^{2+} was found to promote oxygen reduction via the two-electron pathway, causing peroxide formation. Mn^{4+} was found to catalyze peroxide reduction, resulting in a serial $2x2e^-$ mechanism. Stoerzinger *et al.* report that the optimal oxidation state for a MnO_x ORR catalyst is mostly Mn^{3+} with a small amount of Mn^{4+}. [42]

One Mn oxide phase that is of particular interest is hausmannite (Mn_3O_4). Hausmannite has a tetragonal spinel crystal structure, with Mn^{3+} occupying octahedral sites and Mn^{2+} occupying tetrahedral sites (Figure 2-7A). [44] It is possible, however, for Mn_3O_4 to contain some amount of Mn^{4+}. [45] The reported activity of Mn_3O_4 varies substantially throughout the literature. Some report that Mn_3O_4 is the lowest activity MnO_x phase [46], while others report very high activity for Mn_3O_4. [42], [47]–[49] The discrepancies in the literature are likely due to the poor conductivity of Mn_3O_4 or because of differences in $Mn^{2+}/Mn^{3+}/Mn^{4+}$ content. Fan *et al.* [49] and Duan *et al.* [48] both found that Mn_3O_4 nanoparticles mounted on conductive carbon exhibited an apparent four-electron ORR mechanism. The nanostructured catalysts reported by Fan *et al.* and Duan *et al.* utilized carbon nanotubes and graphene, respectively, to provide a conductive support for the Mn_3O_4 nanoparticles. In addition to its catalytic activity, Mn_3O_4 also has desirable electrochemical behaviour in alkaline electrolytes. Mn_3O_4 does not dissolve chemically, whereas other Mn oxides such as Mn_2O_3 will passively dissolve when exposed to high pH. [50] Mn_3O_4 is also electrochemically stable within the voltage window used in ZABs. At cathodic potentials experienced during discharge (-0.3 to 0 V vs. Hg/HgO), Mn_3O_4 is the thermodynamically stable phase. [50] At anodic potentials, oxidation of Mn_3O_4 is kinetically difficult; some reports state that Mn_3O_4 cannot be electrochemically oxidized [51] and some reports state that oxidation of Mn_3O_4 to birnessite will occur at fairly high potentials (~0.9 V vs. Hg/HgO). [52] If Mn_3O_4 is to be used as a bifunctional catalyst and formation of birnessite occurs during OER, a second transition metal element such as Co or Fe can be introduced to reduce the OER potential and improve catalyst stability. [53]

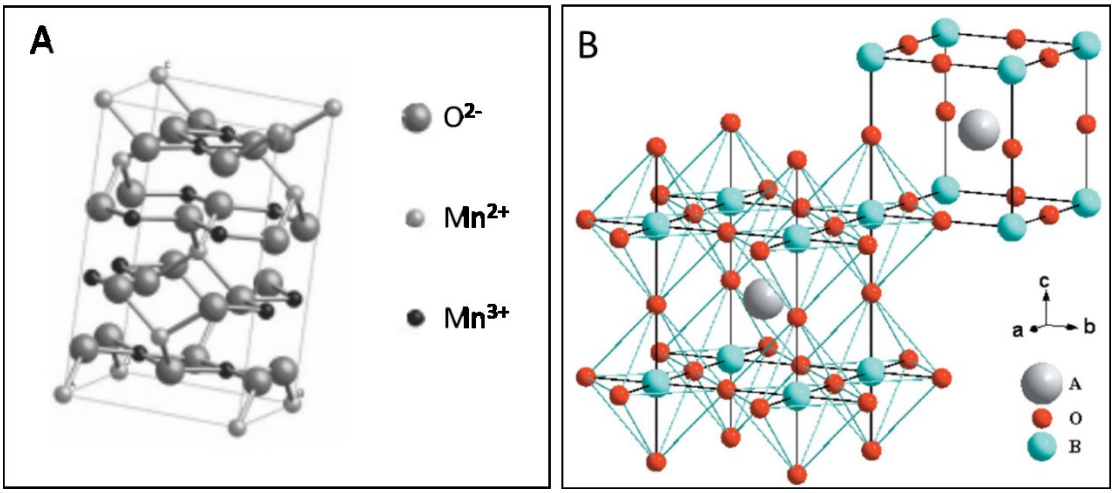

Figure 2-7: A) Hausmannite tetragonal spinel Mn_3O_4 crystal structure, space group: $I4_1/amd$. [54] B) Ideal cubic Pm3m perovskite structure. [34]

Perovskites

Perovskites are metal oxides of the form ABO_3, where A and B are transition metal cations. Due to their crystal structure, perovskites have been shown to have a wide variety of useful materials properties such as ferroelectricity, piezoelectricity, catalytic activity, superconductivity, and many more. The ideal perovskite crystal structure belongs to the cubic space group Pm3m. The A cation is in a 12-fold coordination site and the B cation is in a 6-fold coordination site. A schematic of the cubic perovskite structure is shown in Figure 2-7B. It is possible to form perovskites with multiple A or B site species, allowing for fine control of the physical, electrical, and chemical properties. Suntivich *et al.* [34] performed DFT calculations to determine the catalytic activity of perovskites with a wide range of compositions. They showed that the ORR activity of perovskites is a function of filling of the e_g electron orbital. The e_g orbital consists of the components of the 3d electron shell responsible for σ/σ^* bonding (d_{x2-y2} and d_{z2}). The orientation of the e_g orbital allows it to easily overlap and hybridize with the 2p orbital of an oxygen molecule; the filling of this orbital governs B-O_2 bond strength. An e_g filling slightly less than one results in the optimum B-O_2 bond strength for ORR catalysis. A volcano plot summarizing Suntivich *et al.*'s findings is shown in Figure 2-5B. [34], [35], [55], [56]

2.3.1.2 Carbon-based materials

Carbon-based materials are an attractive option for ZAB catalysts because of their conductivity, abundance, low cost, chemical and environmental safety, and ease of manufacturing. Most

carbon materials catalyze ORR via the less desirable two electron mechanism, producing peroxide species. Carbon can readily react with peroxide, causing corrosion. The activity of carbon materials can be improved by doping with heteroatoms such as N, P, S, or B. Heteroatoms improve the activity of carbon by modifying the electron structure and by introducing defects. Carbon nanostructures like graphene and CNTs have been widely investigated as catalysts for ORR/ OER. As with other carbon materials, the activity of nanocarbons relies on heteroatom doping and/ or defects to modify their electronic structure. The main issues facing carbon-based catalysts for ZABs are their poor stability at oxidizing potentials (OER) and their limited activity compared to other classes of materials. [9], [23], [43], [57]–[60]

2.3.1.3 Metal-Organic Frameworks (MOFs)

Metal-organic frameworks (MOFs), also called porous coordination polymers, are highly crystalline materials consisting of metal clusters and organic linkers. MOFs have very tunable structures, enabling them to be modified in order to achieve desired properties. Since early studies began in the 1990's, there have been over 20,000 different MOF structures reported in the literature (as of 2013). When applied to ORR catalysis, MOFs are typically used as precursors to prepare high surface area materials. [61] By heating MOFs, the organic linkers carburize, producing very high surface area conductive structures. Liu *et al.* carburized a Zn based MOF (MOF-5) after a treatment using furfuyl alcohol vapour, resulting in a very large BET surface area of 2872 m^2/g. [62] During carburization of MOFs, it is common for non-metal atoms (B, N, P, S, etc.) to become incorporated into the carbon structure, resulting in heteroatom doping. Heteroatom doping can greatly improve the ORR performance of carbon materials. MOF structures can also facilitate the formation of more complicated metal-coordination sites. Recent studies in the literature have demonstrated the excellent catalytic performance of MOF-derived M-N-C sites, some achieving performance exceeding that of Pt/C. Despite their promising catalytic performance, MOF-derived catalysts suffer from poor cycling stability due to corrosion, dissolution, and agglomeration. [61], [63]

2.4 Atomic Layer Deposition

Atomic layer deposition is a vapor phase deposition technique similar to chemical vapor deposition (CVD). ALD was introduced by two different groups in the 1960's; Suntola and Antson, as well as a group from the former Soviet Union.[64], [65] Much of the development of ALD techniques was driven by the strict materials requirements of the semiconductor industry. One example of a current use of ALD is the deposition of high-k gate oxides for transistors. Gate oxides need to be highly conformal, uniform, pinhole free, and very thin. In recent years, the applications for ALD have expanded away from the semiconductor industry; in particular, there has been much interest in its application to renewable energy. ALD has been used to produce photovoltaics, fuel cells, batteries, supercapacitors, and many other energy related devices. [11], [66]–[69]

ALD films are known to have excellent properties; many of these properties are achieved by the use of sequential self-limiting reactions. In CVD, like ALD, gas phase molecules react to form a solid film of material. The distinguishing factor between ALD and conventional CVD is that in ALD the reactants are introduced to the substrate one at a time, separating the deposition into multiple steps. In conventional CVD all reactants are introduced to the substrate simultaneously. ALD reactions are self-limiting, which means that a maximum of a single monolayer of material is deposited with each deposition cycle. [11], [66], [67], [70]

2.4.1 Deposition Mechanism

ALD is performed by introducing the reactant gases to the substrate one at a time, typically utilizing an inert carrier gas (Ar or N_2). A schematic of a generic ALD reaction is shown in Figure 2-8. [11] A typical ALD process for a binary material AB using molecular species AL_y and BX_z (L and X are sacrificial ligands) is as follows: First, AL_y is introduced to the substrate where it reacts at reactive sites, either on the substrate or at BX* sites (* denotes a surface species) deposited from the previous cycle. When AL_y reacts with the surface it loses one or more of its L ligands and produces AL* reactive sites. A purge step of inert gas flow is then used to remove any reaction by-products and excess precursor molecules. After the purge step, BX_z is introduced to the sample where it reacts with the AL* sites, losing one or more X ligand and removing the L ligand, forming A-BX*. Another purge step is then used to remove by-products and excess precursor. These four steps are then repeated until the desired film thickness is

achieved. For the deposition of metal oxides, the AL_y species is the metal containing species and is commonly referred to as the precursor. BX_z is the oxygen containing species and is often referred to as the reactant; common oxygen reactants are H_2O, O_2, O_2 plasma, and O_3. [11], [71]

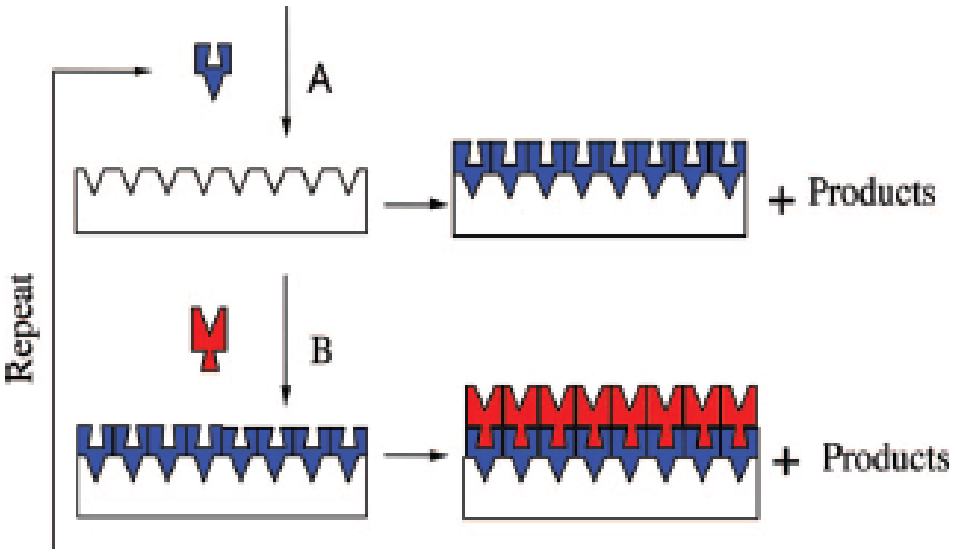

Figure 2-8: Schematic of a typical ALD process. [11]

The substrate surface will have a finite number of reactions sites. The self-limiting nature of ALD relies on the fact that deposition will stop once these reaction sites have been consumed, regardless of how large the precursor dose is. With each dose, the maximum amount of material that can be deposited is a single monolayer. In practice, most ALD reactions have a growth per cycle (GPC) of significantly less than a monolayer. If a substrate has a low density of active sites, then there may not be enough active sites for the precursor to form a complete monolayer on the surface. This will result in a GPC less than the monolayer thickness and causes a phenomena known as nucleation delay. If the substrate has a low density of active sites, very little material will be deposited in the first cycles of the deposition. As the film is deposited, more and more of the surface changes from the initial substrate to the deposited film, causing a gradual increase in the number of reaction sites and subsequently the GPC. Once the entire substrate surface is covered with deposit, the GPC will level off and become a constant value. Another effect that causes a sub monolayer GPC is known as steric hindrance. Steric hindrance is when the size of a precursor molecule is large enough that when adsorbed to the surface, it blocks more than one active site. This prevents adsorption of additional precursor molecules at these sites until the bulky ligands are removed. [11], [71]–[73]

When precursor molecules are introduced to the sample surface, the surface reaction occurs in two steps, physisorption and chemisorption. First, the molecule physisorbs to the surface, retaining all of its ligands. A physisorbed molecule is only attracted by weak Van der Waals forces and can easily diffuse across the surface, finding a preferred site for deposition. The physisorbed molecule will then either desorb back into the gas phase or it will chemisorb to the surface, losing one or more ligands in the process. Because a physisorbed molecule still has all its ligands it is larger than a chemisorbed species, causing a larger degree of steric hindrance. The rates of physisorption, desorption, and chemisorption depend on the molecular species, the substrate type, and the temperature. Because of the finite time needed for these steps it is some times advantageous to break a single precursor dose into multiple shorter doses with purge times between. The purge time between sequential precursor doses allows time for the chemisorption step to occur, reducing waste of precursor molecules. [71]

There are a number of temperature dependent phenomena governing how a precursor molecule will interact when exposed to a sample surface. In order to achieve a true ALD mechanism, the substrate temperature needs to be chosen carefully such that self-limiting surface reactions occur. The temperature regime where an ALD mechanism occurs is called the ALD window. An ALD window is constructed by plotting the GPC vs. substrate temperature; a schematic of an ALD window is shown in Figure 2-9. [11] At temperatures below the ALD window the self limiting reactions can be disturbed by either condensation or kinetic limitations. Condensation occurs when the substrate is cold enough such that precursor molecules undergo a phase change from the gas phase to a liquid or solid phase on the substrate surface. Condensation is not self limiting and results in a large amount of precursor being deposited with each cycle, resulting in a high GPC. Kinetic limitations occur if the substrate is cold enough such that there is not enough thermal energy to overcome the energy barrier required for chemisorption, resulting in incomplete reactions and a reduced GPC. If the substrate temperature is above the ALD window, decomposition and desorption can cause deviations from ideal ALD behavior. Decomposition occurs if the substrate temperature is high enough such that the precursor molecules undergo thermal decomposition on the surface, resulting in a CVD type of deposition. Decomposition causes excess material to be deposited with each cycle, increasing the GPC. At high temperatures it is also possible for desorption to limit deposition, reducing GPC. Physisorbed molecules always have some probability of desorbing before they are able to chemically bond to the surface

(chemisorption); this probability increases with temperature. At sufficiently high temperatures, precursor molecules have a very high probability of desorbing before they chemisorb; the thermal energy essentially causes precursor molecules to bounce off of the substrate surface instead of sticking to it. The mechanisms on either side of the ALD window are dependent on the chemical system; the ALD window can take a variety of shapes. [11]

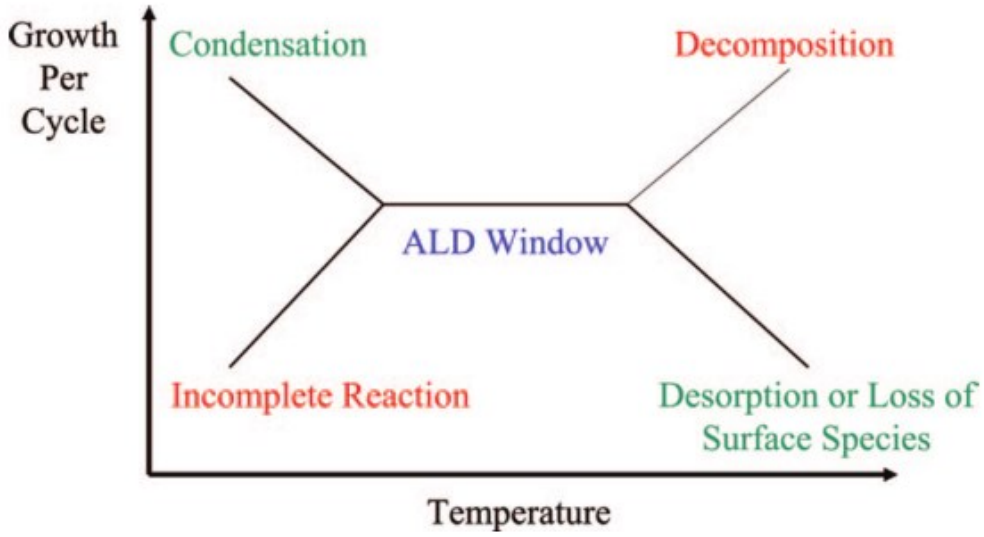

Figure 2-9: Schematic of an ALD window. [11]

The self-limiting reactions characteristic of ALD allow for a combination of film properties that would not be possible through any other method. During ALD, only a single monolayer can be deposited with each cycle. Because the reactions are self-limiting, long exposure times can be used without causing excessive deposition. Long exposure times can be used to allow gas species to diffuse and deposit within high aspect ratio structures or deep within porosity. Figure 2-10 shows a comparison of ALD and CVD films deposited within a trench. [66], [74] Since CVD reactions have continuous exposure to both reactants, areas with better exposure to the gas will experience more deposition while areas with poor gas access will receive little to no deposition. The ALD deposit conformally coats each surface of the trench evenly; sufficient time can be given to allow for diffusion to the bottom of the trench without causing excessive deposition at the top of the trench. Another significant advantage of ALD over CVD is the low deposition temperature. ALD is typically performed at temperatures less than 350°C, while most CVD reactions are performed at temperatures in excess of 700°C. [11], [66]

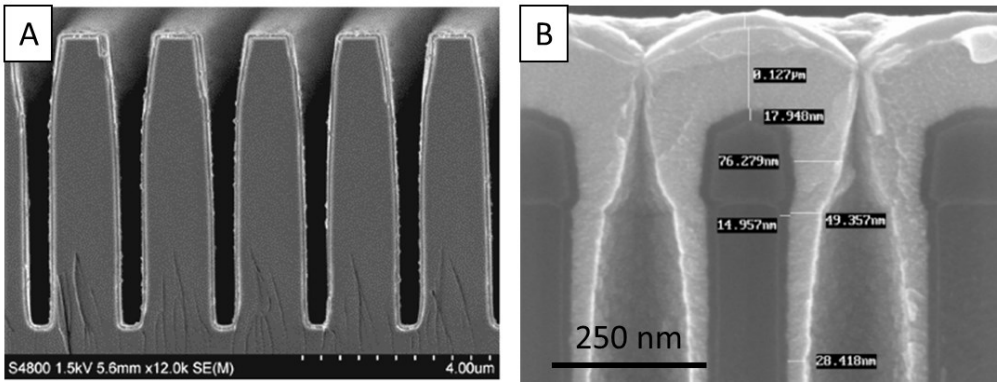

Figure 2-10: Comparison of ALD and CVD film conformality within trenches. A) ALD $Ge_2Sb_2Te_5$ on patterned Si and B) CVD WSi_x on patterned Si. [66], [74]

2.4.2 ALD Reactors

There are multiple designs used for ALD reactors and each reactor can be placed in one of two main categories. The two main types of reactors are defined by their use of a carrier gas and their pumping scheme. The first type of reactor does not use a carrier gas and uses little to no pumping during precursor exposure. In this type of reactor, after each precursor dose the pump is opened and the reactor is completely evacuated before the next dose is introduced. These types of reactors require long purge times, but improve precursor utilization. [11]

The second type of reactor is the continuous flow reactor. A schematic of a continuous flow reactor is shown in Figure 2-11. [11] A continuous flow reactor utilizes a continuous carrier gas flow and continuous pumping. Precursor vapours can be introduced by flowing the carrier gas in the head space above a solid or liquid precursor. If the solid/ liquid precursor has sufficient vapor pressure, gaseous precursor is transported to the substrate by the carrier gas. Continuous flow reactors have much shorter cycle times than reactors that do not use a carrier gas because of reduced purge times. Most ALD reactors utilize continuous flow and are operated in the viscous flow regime at a pressure of ~1 Torr. A pressure of 1 Torr is considered the optimum pressure for an ALD reactor, because it enables fast diffusion while still effectively transporting reactants/ products. [11]

The reactor shown in Figure 2-11 is equipped with an RF (radio frequency) coil to generate plasma species. [11] This reactor also has a quadrupole mass spectrometer (QMS) to analyze the gas composition within the reactor. A variety of other equipment, such as a spectroscopic

ellipsometer (SE) or an x-ray photoelectron spectrometer (XPS), can be installed in an ALD reactor for in-situ studies. [75], [76]

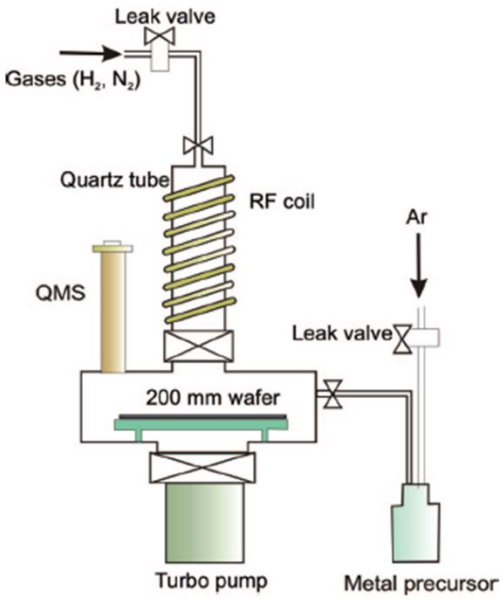

Figure 2-11: Schematic of a continuous flow ALD reactor equip with an RF plasma source and mass spectrometer. [11]

Many ALD reactions utilize plasma to generate high energy species for deposition, either as a reactant or to condition the sample surface. Plasma enhanced ALD (PEALD) allows for deposition of many materials that cannot be deposited through conventional thermal ALD (e.g., single element films). Single element film depositions are performed by using a plasma that will remove precursor ligands adsorbed to the surface, but will not become incorporated in the film. To perform PEALD, a plasma source is required. Inductively coupled plasma (ICP) systems are becoming an increasingly more common feature of ALD reactors because they are able to generate a high flux of plasma species. [11]

One main limitation of ALD is the slow deposition rate. Typical GPCs for ALD processes are on the order of 1 Å. If an ALD process is to be applied to large scale manufacturing, the slow deposition rate needs to be addressed. One method of increasing throughput is the use of large batch reactors. By depositing on many samples at once, the average time to coat one sample can be drastically reduced. Although the dose and purge times in large batch reactors are long, depositing on many substrates simultaneously offsets the increase in cycle time. Another method of increasing throughput is spatial ALD, which increases throughput by eliminating the need for

individual dose/ purge steps. Using a specialized head, streams of precursor are introduced to the sample simultaneously. Streams of carrier gas between the precursor streams prevent the precursors from mixing. The sample is moved relative to the head, exposing the sample to alternating streams of precursor and reactant. [11], [66]

2.4.3 Application of ALD to Renewable Energy

The unique properties of ALD films makes them very attractive in the development of renewable energy devices including fuel cells, batteries, supercapacitors, photovoltaics, and photoelectrochemical systems. There are a number of review articles on the use of ALD for renewable energy devices. [67]–[70], [77], [78] In the application of solid oxide fuel cells (SOFCs), ALD can be used to prepare the solid electrolyte. In SOFCs, diffusion of oxygen ions through the solid electrolyte occurs quite slowly and limits performance. Using ALD to prepare the electrolyte as a thin, pin hole free film drastically reduces diffusion distances required while also avoiding short circuits between anode and cathode. ALD has also been used to prepare catalysts for SOFCs. [66], [67], [78]

For many electrochemical devices such as batteries and supercapacitors, high surface area between the electrode and electrolyte is critical to achieving high performance. ALD can be used to coat high surface area conductive substrates with very thin layers of active material, maximizing surface area while minimizing the use of active material. ALD has also been used extensively to fabricate protective layers in batteries. The electrolytes and high potential range of many batteries result in a very harsh environment in which many materials are not stable. By depositing a thin film of protective material, the conductive support can be protected without drastically reducing the conductivity of the electrode. [67], [69], [78]

2.4.4 Precursor Selection

There are a number of requirements for a chemical to be used as an effective precursor in an ALD reaction. The first requirement is that the precursor needs to have sufficient vapor pressure. Most ALD systems require the precursor to inject itself into a carrier gas stream when a valve is opened; this is referred to as conventional precursor delivery. A schematic of precursor delivery methods is shown in Figure 2-12. If a solid/ liquid phase precursor has a low vapor pressure, then the pressure in the ampule will not be high enough to permit precursor flow into the carrier gas.

It is also possible for a precursor to have excessive vapor pressure. If the vapor pressure is too high, than a large amount of precursor molecules will be introduced with each pulse, many of them going to waste. A precursor with too high of vapor pressure can drastically reduce precursor utilization. A vapor pressure of 1 Torr is typically sufficient for a precursor to be effective, as this is the same as the operating pressure of the reactor. Many precursors need to be heated to obtain sufficient vapor pressure, but temperature constraints on the ALD equipment limit the maximum operating temperature for a precursor. One way to achieve deposition with a low vapor pressure precursor is through the use of a bubbler. The name bubbler is a bit misleading, as not all bubblers "bubble" gas through the precursor. Instead of having the carrier gas flow above the ampule, the carrier gas stream is diverted such that it enters the ampule through one valve and exits through another. Even if the vapor pressure is low, there will still be some amount of gaseous precursor molecules in the ampule. The use of a bubbler allows for transport of these molecules to the reactor.

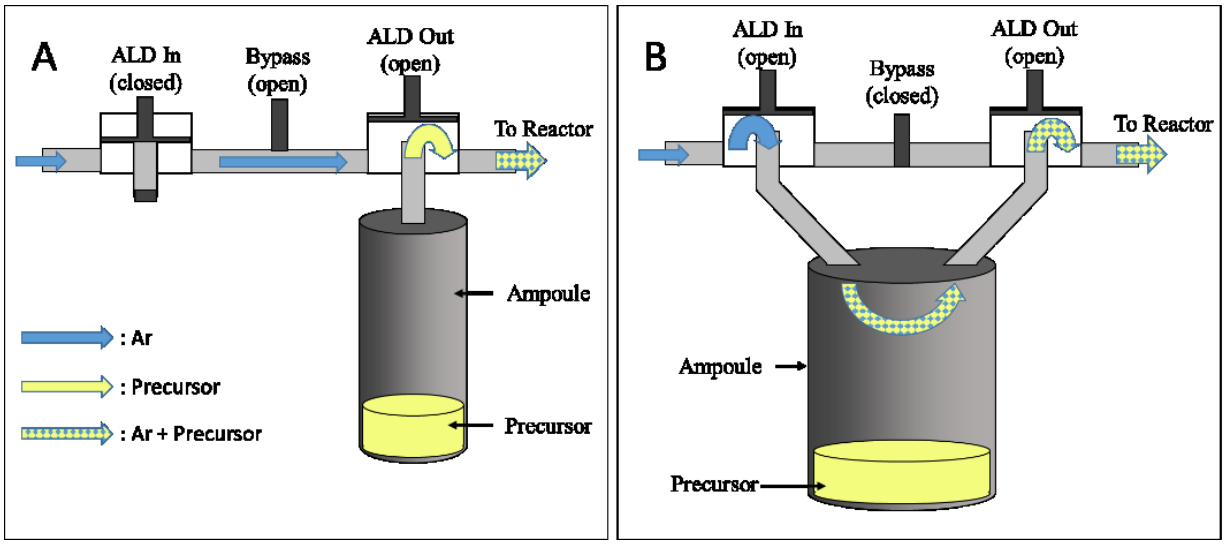

Figure 2-12: A) Schematic of conventional precursor delivery. B) Precursor delivery utilizing a bubbler.

The decomposition temperature of the precursor is another factor that needs to be considered. Many organometallics will decompose at elevated temperatures, resulting in CVD like growth. The precursor must also be reactive towards the other reactant utilized to obtain the desired film (i.e., H_2, NH_3, N_2, O_2, etc.). The composition of the precursor is important, not just the metallic component of the precursor but also the composition of the ligands. For example, if a nitride is to be deposited, the precursor should not contain oxygen. Steric hindrance is another consideration

when selecting a precursor. If the precursor has many bulky ligands, there will be significant steric hindrance, which may or may not be problematic depending on the application. In some applications the valence of the metal atom in the precursor may be of concern. Many metals have multiple stable valence states and the valence of the metal in the precursor molecule can effect the valence obtained in the deposited film. Cost is another consideration, as many of the organometallic compounds used for ALD can cost hundreds of dollars per gram. [72]

2.4.5 Nucleation and Growth

The nucleation stage of an ALD process has a large impact on the growth and resulting properties of a film. The mechanism of growth for a given film and substrate depends on the surface energy (or wettability), density of the lattice sites, and lattice misfit. In the context of ALD, wettability refers to the ability of the precursor to adsorb to the substrate surface. The wettability of a substrate depends on the atomic structure of the surface (surface species) and the chemistry of the precursor. Lattice misfit is a measure of the percent difference in lattice spacing between a film and substrate. If the lattice misfit is zero, the lattice planes in the film are able to perfectly align with the lattice planes in the substrate; this is known as epitaxy. Epitaxial growth can occur for misfit values ranging from around 0-15%. For any misfit >0%, strain is introduced into the film which causes defects and can promote island growth. There are three possible growth mechanisms: layer by layer growth, island growth, and mixed growth. Schematics of the three mechanisms are shown in Figure 2-13. [79]

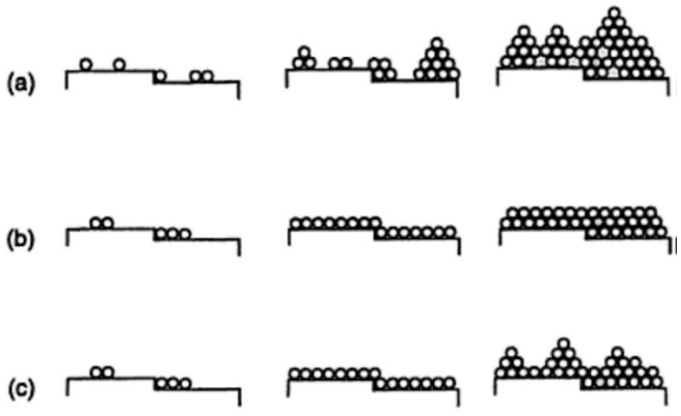

Figure 2-13: Thin film growth mechanisms: a) Island growth (Volmer-Weber), b) layer by layer growth (Frank-van der Merwe), and c) mixed growth (Stranski-Krastanov). [79]

The first mechanism is Volmer-Weber or island growth. Growth occurs when there is significant mismatch between the film and substrate, causing large lattice strains and high surface energy between the film and substrate. The precursor does not readily nucleate on the substrate because of this high surface energy; only a few nuclei are deposited with the first ALD cycle. With subsequent cycles the precursor continues to poorly nucleate on the substrate surface; however, the precursor is able to deposit readily on nuclei deposited during previous cycles. The lower surface energy of the particles causes preferential growth of nuclei, leading to the formation of individual particles. Given enough cycles, the particles of an island growth film can fuse together to form a continuous film. However, these films tend to be highly defective and lack many other properties that define ALD films, such as fine thickness control, uniformity, and conformality. Although island growth films are generally considered low quality, this mechanism can be utilized to prepare quantum dots or nanoparticles. [66], [79], [80]

Frank-van der Merwe, or layer by layer, growth is considered the ideal growth mode for ALD films. This growth mode occurs when there are sufficient active sites and good lattice match between the film and substrate. Under these conditions, the surface energy of the substrate/ deposit interface is very low, promoting good wettability. The gaseous precursor readily adsorbs and nucleates across the entirety of the substrate surface, depositing a complete monolayer of material with each cycle. Layer by layer growth produces high quality ALD films that are highly uniform and conformal. [11], [79]

Stranski-Krastanov or mixed growth occurs when the wettability and lattice mismatch have intermediate values. Mixed growth begins as a layer by layer mechanism. As the film grows thicker, strain caused by the lattice misfit accumulates. Once the film reaches a critical thickness, the elastic strain energy becomes too large and growth switches to an island growth mechanism. [79]

2.4.6 ALD on Carbon

Carbon based nanostructures like carbon nanotubes (CNTs), graphene, and carbon aerogels are attractive substrates for a variety of applications because of their high surface area, high thermal and electronic conductivities, and stability, both chemical and mechanical. ALD is an attractive technique for coating carbon materials because of the unique ability of ALD films to uniformly

and conformally coat highly porous structures with very thin layers of high purity materials. ALD films on carbon substrates have been used for catalysis, gas sensing, energy storage, and electronic applications. [81]

Obtaining ideal ALD behavior on carbon substrates can be difficult due to the inert nature of graphitic carbon. ALD on unfunctionalized carbon commonly experiences island growth, resulting in nanoparticle formation. Many ALD reactions do not readily nucleate on a pristine graphite surface; these reactions require surface functional groups and/ or defects for nucleation to occur. Functionalization of carbon involves modifying the surface by introducing functional groups which promote nucleation. Most functionalization procedures rely on oxygen containing functional groups (e.g., OH, COOH, CO) covalently bonded to the carbon surface. Because of the bonding involved, these functional groups modify the intrinsic properties of the carbon which may be detrimental in some applications such as electronics. To help avoid modification of the properties of carbon substrates, alternative functionalization procedures have been developed. These procedures rely on other bonding mechanisms like Van der Waals, π-π interactions, hydrogen bonding, and electrostatic forces to add functional groups to the surface. Non-covalent functionalization still alters the electronic properties of the carbon, but not as dramatically as covalent functionalization. [81]

There have been many studies in the literature that involve ALD on carbon substrates, with most work involving CNTs or graphene. CNTs and graphene have an sp^2-hybridized electronic structure which does not promote nucleation. Other carbon materials such as aerogels or carbon black contain amorphous carbon which promotes nucleation because of its high density of defects and functional groups. [81] One carbon of particular interest in electrochemistry is glassy carbon. Glassy carbon is a common electrode material used in electrochemical testing. Contrary to its name, glassy carbon is actually not amorphous. The structure of glassy carbon is not fully understood, but it has been proposed that it is composed of fullerene-like closed particles. A fullerene-like structure explains many of glassy carbon's properties including its relatively low reactivity, impermeability to gases, and absence of observable structure with a transmission electron microscope. [82] Pickrahn *et al.* performed ALD of MnO_x on glassy carbon electrodes and made no mention of difficulties with nucleation; this is an indication that glassy carbon has sufficient active sites on its surface to facilitate good nucleation. [81]

2.4.7 ALD of Mn oxide

There have been several studies in the literature concerning ALD of Mn oxide. [12], [49], [75], [76], [80], [83]–[100] Table 2-1 presents a summary of the work on ALD Mn oxide presented in the literature. Nilsen *et al.* [98], [99] were the first to report on ALD of Mn oxide. In their work Mn oxide was prepared from precursors of $(thd)_3Mn$ and O_3 on a wide variety of substrates. Depending on the substrate, a number of different MnO_2 phases were deposited (α-, β-, β'-, and ε-MnO_2). A thorough crystallographic analysis using XRD to generate reciprocal space maps was done and showed that many of the MnO_2 films were grown epitaxially. As discussed in Section 2.3.1, the performance of an Mn oxide as an electrocatalyst is dependent on its crystal structure. This work by Nilsen *et al.* indicates that by using a carefully selected seed layer to encourage epitaxial growth, the phase of ALD Mn oxide may be controlled. [98], [99]

Pickrahn *et al.* [12], [76] investigated ALD Mn oxide as an electrocatalyst for OER and ORR. In their work, Mn oxide was prepared from $(EtCp)_2Mn$ and H_2O and deposited onto substrates of glassy carbon, Si, and SiO_2. The as deposited ALD Mn oxide had the structure of MnO (NaCl-type). Select films were annealed in air for 10 h at 480°C to yield films of Mn_2O_3. For use in electrochemical analysis, depositions were performed directly onto glassy carbon electrodes. Catalytic studies of the Mn oxide films showed that annealed films (Mn_2O_3) had good activity towards ORR and OER, while as-deposited films (MnO) only had good activity towards OER. [76] Pickrahn *et al.* [12] demonstrated the importance of electrode surface area in catalytic performance by comparing depositions on smooth and high surface area glassy carbon. Figure 2-14 compares the microstructure and OER performance of films prepared in Pickrahn's study. The films prepared on high surface area glassy carbon showed improved activity towards OER in terms of onset potential as well as current density. This indicates that the morphology of the substrate has a large impact on catalyst performance. [12]

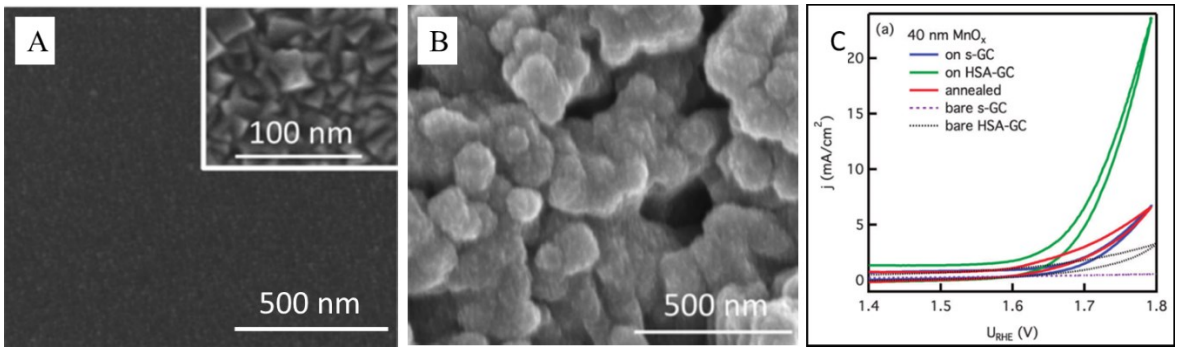

Figure 2-14: SEM secondary electron (SE) images of A) smooth glassy carbon (s-GC) and B) high surface area glassy carbon (HSA-GC). C) OER activity of bare and MnO_x coated electrodes. [12]

Reported growth rates were around 1 Å/cycle for studies using $(CpEt)_2Mn$ as the Mn source, [12], [76], [80], [85], [87], [96], [100] while studies using $(thd)_3Mn$ reported GPC values of 0.2 Å/cycle. [84], [97]–[99] This discrepancy in growth rates between precursors is likely due to the large size of the $(thd)_3Mn$ molecule, which causes a large degree of steric hindrance. Burton *et al.* observed a GPC of 1.2 Å/cycle using an $(EtCp)_2Mn$ precursor at ~100°C. [80] Lu *et al.* [96] reported growth rates ranging from 0.24-0.42 Å/cycle using $(EtCp)_2Mn$ at temperatures ranging from 150 to 300°C. For both Burton *et al.* [80] and Lu *et al.* [96], higher growth rates were achieved at lower temperatures, suggesting that the $(EtCp)_2Mn$ precursor had difficulty adsorbing on the substrate at elevated temperatures. Young *et al.* [100] reported a GPC of 5.7 Å/cycle using $(EtCp)_2Mn$ and O_3. A GPC of 5.7 Å/cycle is very high and suggests that growth does not follow an ALD mechanism. However, Young *et al.* claim that growth is self-limiting and explain the anomalously high GPC by proposing a new mechanism that involves Mn diffusion to the surface during O_3 exposure and Mn diffusion into the bulk during $(CpEt)_2Mn$ exposure. They call this mechanism self-limited multilayer deposition. [100]

Mattelaer *et al.* [97] investigated the use of different plasma species on the deposition of MnO_x from the $(thd)_3Mn$ precursor. Depending on the plasma used, a number of different Mn oxide phases were obtained. In their subsequent work, Mattelaer *et al.* [84] used a number of annealing conditions and in-situ XRD for ALD MnO and MnO_2 films to obtain every oxidation state of MnO_x (i.e., MnO, Mn_3O_4, Mn_2O_3, and MnO_2). This work shows that the phase of ALD MnO_x can quite easily be controlled through deposition conditions and/ or post deposition annealing.

Table 2-1: Summary of literature on ALD of MnO_x

	Reactants	Deposition Temperature	Substrate	Composition	Growth Per Cycle (Å)	Characterization	Notes
[88], [89]	$(acac)_3Mn + H_2O$	300-360 °C	α-Al_2O_3 (0001)	Not determined	Not reported	SIMS, XRD, EPMA	Investigated magnetic properties of ZnMnO, very little ALD analysis.
	$(thd)_3Mn + H_2O$						
[98], [99]	$(thd)_3Mn + O_3$	138-210 °C	NaCl (100), KCl (100), KBr (100)	α-MnO_2	0.2	XRD, AFM, Resistivity, SEM	Very thorough crystallographic analysis, many films grown epitaxially.
			α-Al_2O_3 (012), muscovite (001), α-SiO_2 (001), MgO (100), Kapton™	β-MnO_2			
			Soda lime glass, n-SiO_x/S i(100)	β-MnO_2 + β'-MnO_2			
			α-Al_2O_3 (001)	ε-MnO_2			
[84], [97]	$(thd)_3Mn + NH_3$*	140-275 °C	SiO_2, TiN	MnO	0.22	SE, AFM, SEM, XRD, XPS, XRR, XRF	Uniformity could not be achieved using O_2* films. Investigated for use in Li-ion batteries. [97] In-situ XRD during annealing in various atmospheres; obtained every oxidation state between MnO-MnO_2. [84]
	$(thd)_3Mn + H_2$*	180 °C	SiO_2, TiN	MnO/Mn_3O_4	0.2		
	$(thd)_3Mn + H_2O$*	180 °C	SiO_2, TiN	Mn_3O_4	0.2		
	$(thd)_3Mn + O_3$	140-275 °C	SiO_2, TiN	MnO_2	0.12		
[90]	$(thd)_3Mn + O_3$	225 °C	Stainless Steel, Si (100)	β-MnO_2	0.2	SE, XRD, XRR, XPS, TOF-ERDA, AFM, CV	Prepared $Li_xMn_2O_4$ for Li-ion batteries.
	$(EtCp)_2Mn + H_2O$	200-250 °C	Stainless Steel, Si (100)	Not determined	1.1		
[80]	$(EtCp)_2Mn + H_2O$	100-300 °C	ALD Al_2O_3 on Si (100)	MnO	1.2	RBS, XRD, XRR, FTIR, QCM	Proposed a growth mechanism.
[91]	$(EtCp)_2Mn + H_2O$	125-200 °C	SiO_2, SiOCH, Cu	Not determined	0.6-1.0	XRF, TEM, XPS	Used as a Cu diffusion barrier.
[92]	$(EtCp)_2Mn + H_2O$	250 °C	Fe_2O_3	Mn_2O_3 (annealed)	1	XPS, LSV, EIS	Catalyst for photoelectrochemical water splitting.
[96]	$(EtCp)_2Mn + H_2O$	150-300 °C	SiO_2	MnO	0.24-0.42	XRR, XRD, FTIR	Films prepared using O_3 had poor adhesion.

[12], [76], [93]	$(EtCp)_2Mn + H_2O$	170 °C	Glassy carbon, SiO_2	MnO, Mn_2O_3 (annealed)	0.84	SE, SEM, XRD, XPS, XAS, CV, LSV	Investigated as catalyst for ORR and OER and syngas conversion.
[94], [100]	$(EtCp)_2Mn + O_3$	150-180 °C	n-SiO_2/Si	Mn_5O_8	5.7	QCM, XRR, XRD, XPS, RBS	Claim deposition with O_3 follows a self-limited multilayer deposition mechanism.
	$(EtCp)_2Mn + H_2O$	150-180 °C	n-SiO_2/Si	MnO	1.2		
[87]	$(EtCp)_2Mn + H_2O$	150 °C	Cu	MnO	1	AFM, SEM	Prepared for use as a Li-ion battery anode.
[85]	$(Et_2Cp)_2Mn + H_2O$	150-200 °C	Si (HF pretreatment)	MnO	1	SE, XPS	Followed Burton et al.'s recipe. Very brief ALD analysis.
[75]	$MeCpMn(CO)_3 + N_2O$ $MeCpMn(CO)_3 + H_2$	350 °C	n-SiO_x/Si (100)	$MnO_x + SiO_2$	Not reported	XPS	In-situ XPS measurements.
[49], [86]	$MeCpMn(CO)_3 + O_3$	200 °C	Glass, CNT, Inconel	Mn_3O_4	0.45	XRD, XPS, Raman, SEM, TEM	Prepared as a supercapacitor and ORR catalyst.
[83]	$Mn_2(CO)_{10} + O_3$	80-100 °C	n-SiO_2	α-Mn_2O_3	1.2	XRD, XRF	Investigated for magnetic properties.
		120-160 °C	n-SiO_2	Mn_3O_4	1.2-1.5		
[95]	Mn(tBu-MeAMD)2 + H_2O	150-275 °C	SiO_2	$MnO + Mn_2O_3$	2.1	XRD, Raman, XPS, SEM, AFM	Home made precursor. Thorough saturation analysis.

Abbreviations: ***** denotes a plasma activated species, **n-SiO_2** is native oxide on Si, **$MeCpMn(CO)_3$** is methycyclopentadienyl manganese tricorbonyl ($C_5H_4CH_3Mn(CO)_3$), **$(CpEt)_2Mn$** is bis(ethylcyclopentadienyl) manganese ($Mn(C_7H_9)_2$), **$(thd)_3Mn$** is tris(2,2,6,6-tetramethyl-3,5-heptanedionato)manganese ($Mn(C_{11}H_{19}O_2)_3$), **Mn(tBu-MeAMD)$_2$** is bis(N,N'-di-tert-butylacetamidinato)manganese ($C_{20}H_{42}N_4Mn$), **SIMS** is secondary ion mass spectroscopy, **EPMA** is electron probe micro analysis, **XPS** is x-ray photoelectron spectroscopy, **RBS** is Rutherford back scattering spectrometry, **XRD** is x-ray diffraction, **XRR** is x-ray reflectivity, **XAS** is x-ray absorption spectroscopy, **XRF** is x-ray fluorescence, **FTIR** is Fourier transform infrared spectroscopy, **QCM** is quartz crystal microbalance, **AFM** is atomic force microscopy, **SEM** is scanning electron microscopy, **SE** is spectroscopic ellipsometry, **XAS** is x-ray absorption spectroscopy, **TOF-ERDA** is time-of-flight elastic recoil detection analysis, **CV** is cyclic voltammetry, **LSV** is linear sweep voltammetry.

2.5 Characterization Techniques

2.5.1 Electrochemical Characterization Techniques

In order to quantify the behaviour and performance of prepared catalysts, a number of electrochemical techniques are employed. Properties of interest that can be measured through electrochemical techniques are onset potential, cycle life, charge transfer resistance, electrode resistance, and rate capability.

2.5.1.1 Linear Sweep Voltammetry (LSV)

Linear sweep voltammetry (LSV) is performed by scanning the potential between two limits and measuring the resulting current. The current produced at the electrode is dependent on a number of factors including surface area, electron transfer rate, chemical reactivity, diffusion in the electrolyte, and scan rate. LSV is commonly used to determine the catalytic activity of ORR catalysts. A typical experiment to determine ORR activity is performed by scanning from 0.2 to -0.7 V vs. Hg/HgO at a scan rate of 5 mV/s. The electrolyte used is a solution of KOH (0.1 – 6 M) saturated with oxygen. Example LSV curves are shown in Figure 2-15A. [9] As the potential is scanned from positive to negative, the measured current is near zero until a potential is reached where ORR can take place. This potential is referred to as the onset potential and is a common figure of merit used to compare ORR catalysts. Ideally, the onset potential for ORR should be as positive as possible. Since there is no strict definition for how onset potential is to be measured from an LSV curve, it is important to be cautious when comparing data from the literature. It is common for catalysts to be compared directly to a benchmark catalyst such as Pt/C, so that relative performance can easily be assessed. [26]

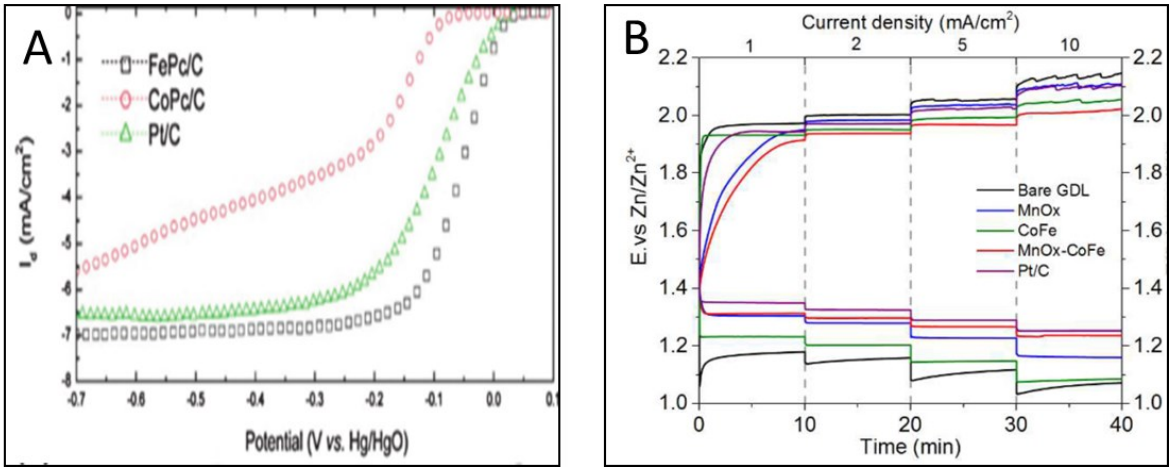

Figure 2-15: A) Example LSV curve for carbon-supported Fe-phthalocyanine (FePc/C) and Co-phthalocyanine (CoPc/C), compared to Pt/C. [9] B) An example of galvanostatic cycling results used to determine rate capability. [101]

2.5.1.2 Cyclic Voltammetry (CV)

Cyclic voltammetry is commonly used to investigate electrochemical reactions occurring at the electrode. CV is similar to LSV in that the potential is swept between two potentials while measuring the resultant current. However, unlike LSV, the potential is swept in the reverse direction once one of the limits is reached. When performing CV, it is common to do multiple cycles in a single test. If a reaction is taking place at the electrode during CV the obtained curve will show a peak at a specific potential; this peak can be used to characterize the reaction. In the context of ZABs, CV is performed in a KOH solution saturated with either O_2 or an inert gas (Ar or N_2). In O_2 saturated KOH, the CV data is usually dominated by ORR. CV cycling in an electrolyte saturated with an inert gas reveals the electrochemical behaviour of the electrode in the absence of ORR. This can give insight into the stability of the electrode and whether or not any redox reactions are occurring to the catalyst. [26]

2.5.1.3 Electrochemical Impedance Spectroscopy (EIS)

Electrochemical impedance spectroscopy (EIS) is performed by imposing a small alternating current (AC) signal on a finite direct current (DC). The frequency of the AC current is varied and the resultant impedance values are measured. EIS data is commonly displayed as a Nyquist plot which displays the imaginary component of the impedance (Z_i) vs. the real component (Z_r). By fitting an equivalent circuit to the Nyquist plot, it is possible to quantify a number of

electrochemical parameters including electrode resistance, charge transfer resistance, and diffusion behaviour. [26]

2.5.1.4 Galvanostatic Cycling

Galvanostatic cycling is performed by measuring the potential required to obtain a constant current. In the context of ZABs, galvanostatic cycling is used for determining the rate capability of an electrode, as well as for charge/ discharge cycling tests. For rate capability tests, the charge/ discharge potential for an electrode is measured for a range of current densities and plotted alongside one another to display how potential varies with charge/ discharge rate. An example of these plots is shown in Figure 2-15B.

2.5.2 Materials Characterization Techniques

Materials characterization techniques are used to determine the composition, structure, morphology, and chemical state of a material. These techniques provide insight into material properties and are invaluable for understanding material fabrication, performance, and stability. Because ALD films are extremely thin, they typically have a very small total material volume which makes characterization very difficult. ALD films present challenges for characterization and techniques must be selected and used with care.

2.5.2.1 Scanning Electron Microscopy (SEM)

Scanning electron microscopy (SEM) is performed by directing a focused beam of electrons onto a sample surface and measuring the signals generated by the sample. The beam is digitally scanned across the sample surface and the signal intensity at each point is measured. The measured intensity is then translated into a relative brightness and used to generate an image. The most common signals measured in SEM are secondary electrons, backscattered electrons, and x-rays. Secondary electrons have fairly low energy and give information about the topography of the sample. Backscattered electrons are higher energy and give information about the atomic number of the sample (Z contrast). X-rays are collected when performing energy dispersive x-ray (EDX) analysis. In EDX, x-rays energies are measured and used to identify the composition of a sample using their characteristic x-ray emissions. EDX spectra are commonly obtained from a single point, but can also be used to plot composition along a line or used to generate a map of element distribution.

The resolution limitations of SEM make analysis of ALD films difficult if not impossible (depending on the film). When the electron beam hits the sample, it spreads out under the sample surface, generating signal from this entire volume. This interaction volume is the main limitation with SEM. Since ALD films are so thin, the majority of the measured signal originates from the underlying substrate. Figure 2-16 shows how the interaction volume of an electron beam is affected by the energy of the electron beam. In order to achieve an interaction volume on the same scale as an ALD film, a very low accelerating voltage is required. However, at low accelerating potentials, the x-ray yield is significantly reduced.

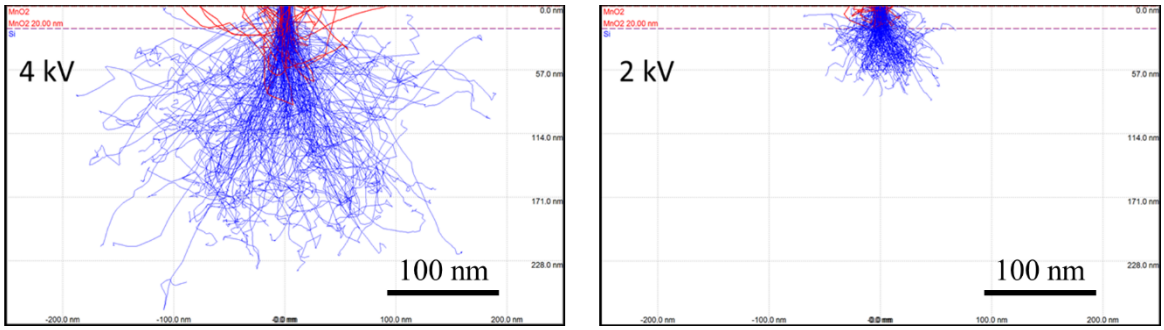

Figure 2-16: Interaction volume simulations generated using Casino software. Simulations are for a 20 nm layer of MnO_2 on a Si substrate. The dashed line indicates the interface between MnO_2 and Si. The 4 kV electrons penetrate deeper than 200 nm, while the 2 kV electrons reach a maximum depth of ~75 nm. [102]

2.5.2.2 Transmission and Scanning Transmission Electron Microscopy (TEM/ STEM)

Transmission electron microscopy (TEM) is a very powerful materials characterization technique capable of imaging and structural analysis on the atomic scale. TEM is performed by transmitting a beam of electrons through a very thin sample (<200 nm). As the electrons pass through the sample, the electrons interact in a number of ways; they can be scattered, reflected, absorbed, or pass through uninterrupted. Electrons that pass through the sample are focused and used to form an image. Modern TEMs, such as the JEOL JEM-ARM200F, are capable of imaging at a resolution of 0.08 nm, which is smaller than the atomic spacing for many materials. [103] The sub-atomic resolution of TEM allows for characterization of materials and structures on size scales not possible through any other technique. Crystallographic information can be collected from very small and specific areas using techniques such as convergent beam electron diffraction (CBED) and selected area diffraction (SAD), which is one of the main uses for TEM. [104]

A useful variation of TEM is scanning transmission electron microscopy (STEM); shown schematically in Figure 2-17A. When performing STEM, the electron beam is focused to a point and scanned across the sample, similar to an SEM. The electrons that pass through the sample are then collected and translated into an intensity for that specific pixel. There are two commonly used imaging modes in STEM, bright field (BF, Figure 2-17B) and annular dark field (ADF, Figure 2-17C). BF STEM images are generated by collecting the unscattered electrons that pass through the sample. The mechanisms of contrast in BF STEM mass-thickness and diffraction contrast effects. ADF STEM images are produced using electrons that have been scattered away from the optic axis. Contrast in ADF images is almost entirely due to mass-thickness effects; this allows for easy interpretation of high resolution ADF images. [104]–[106] STEM EDX is a very useful technique for composition analysis of nanomaterials. Because STEM utilizes high beam energy (~200 kV) and thin samples, STEM EDX resolution is not limited by the interaction volume as it is in SEM. STEM EDX is capable of very high spatial resolution elemental mapping; an example of atomic resolution EDX maps is shown in Figure 2-17D. [104], [107] Resolution limitations in STEM mode (BF, ADF, and EDX) are mainly governed by the precision of the electromagnetic lenses. Modern aberration-corrected STEMs are capable of resolutions of 50 pm. [106]

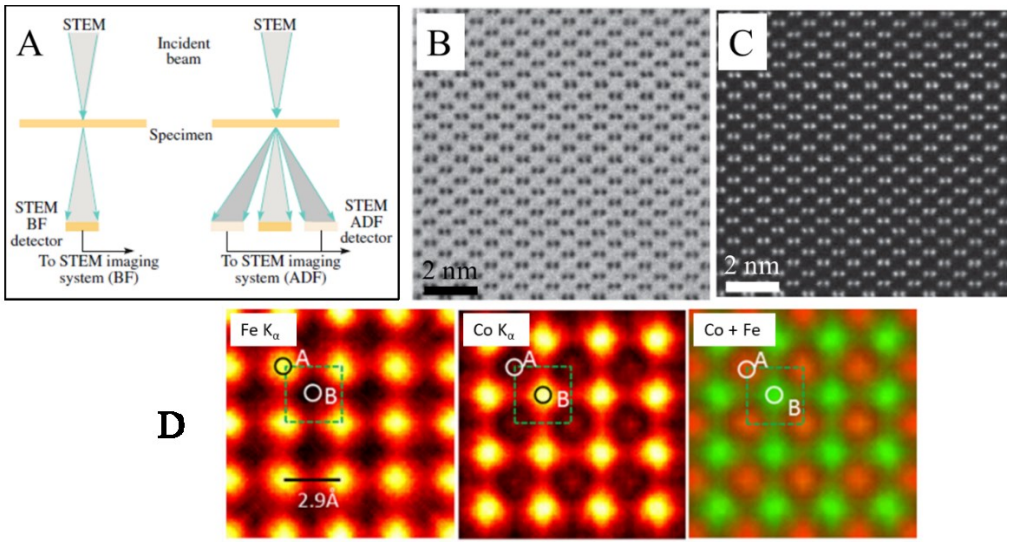

Figure 2-17: A) Schematic of BF and ADF STEM imaging modes. B) ADF STEM image of Si (110). C) BF STEM image of Si (110). D) STEM ADF and EDX maps of a CoFe alloy. [104], [108]

The main limitations of TEM are sample preparation and the small sample volume. Depending on the sample, TEM sample preparation can be trivial, or it can be virtually impossible. TEM requires that electrons pass through the sample, so they must be very thin. A thickness of 200 nm is typically regarded as the upper limit for TEM samples; high resolution imaging requires samples significantly thinner than 200 nm. Preparing samples this thin can be extremely challenging and is likely to alter the structure of the sample. One technique to prepare TEM samples of nanostructures is to use a focused ion beam (FIB). Because TEM images are taken at extremely high magnification, the amount of material actually imaged is very small, so that a single TEM image may not be representative of the entire sample. [104]

2.5.2.3 X-ray Photoelectron Spectroscopy (XPS)

X-ray photoelectron spectroscopy (XPS) is used for characterization of the chemical composition and valence state of a material at the surface. XPS is performed by exciting a sample with a monochromatic beam of x-rays. These x-rays excite the electrons within the material and some of them are ejected from the surface. The electrons are called photoelectrons and their energy is characteristic of the electronic structure of the sample atoms. Differences in electronic structure caused by bonding or differences in valences cause shifts in the electron binding energy. These shifts can be measured and used to determine chemical and electronic information about the sample. One important consideration when using XPS is that it is very sensitive to the surface condition of the sample. Photoelectrons are low energy and can only travel through a small amount of material before they are absorbed. This means that photoelectrons are only emitted from the near surface region of the sample (~5 nm). A sputtering step is commonly conducted before XPS measurements to remove any surface contamination. For ALD films, because they are only nanometers thick, this sputtering step can damage the thin film, so that composition analysis of ALD films through XPS may not be valid. XPS quantification results should be validated with other techniques. [79]

2.5.2.4 Spectroscopic Ellipsometry

Spectroscopic ellipsometry (SE) is a technique commonly used to characterize the growth of thin films. SE is performed by shining a beam of polarized light onto the sample surface and measuring the polarization of the reflected light. The photon-sample interactions probed by SE

include reflection, refraction, and absorption; the effects of these interactions can become quite complex. Photon-sample interactions are governed by the dielectric function of the material. SE utilizes models to determine the dielectric function(s) for a given sample. Data analysis in SE is done by building a model and curve fitting to experimental data. There are a number of models used to analyze SE data; they include the Lorentz model, Sellmeier model, Cauchy model, Drude model, and Tauc-Lorentz model. These different models each apply to certain types of materials. SE is an excellent technique for characterizing ALD films because of its high precision, fast in-situ measurement, and ability to measure various film properties. [109]

Chapter 3: Experimental

3.1 Atomic Layer Deposition

Atomic Layer Deposition (ALD) is performed by exposing a substrate to alternating pulses of gas phase molecules. A more detailed explanation of ALD is given in Section 2.4. Most ALD recipes utilize an organometallic compound containing the metal atom to be deposited (e.g., $Al(CH_3)_3$ for Al); this is frequently called the precursor. The second compound used will usually contain the anion for the film (e.g., O_2, NH_3, H_2S, for oxides, nitrides, and sulfides, respectively); this is frequently called the reactant. The precursor and reactant react with each other after adsorbing to the substrate surface, depositing a maximum of a single monolayer of material with each cycle. In order for ALD to be performed properly, the precursor and reactant pulses must be separated by an inert gas flow, commonly referred to as a purge step. A single ALD cycle follows the steps of precursor dose/ purge/ reactant dose/ purge. These steps are then repeated tens, hundreds, or even thousands of times until the desired film thickness is achieved.

3.1.1 Atomic Layer Deposition Tool

Atomic layer deposition (ALD) was performed using a Kurt J. Lesker ALD 150LX system, shown in Figure 3-1. This ALD system was designed as a tool for research and development. It is able to simultaneously hold up to four organometallic precursors and is capable of both thermal and plasma-enhanced depositions. The available ALD tool (ALD 150LX) accommodates up to 4” (100 mm) wafers and is equipped with a load lock which allows for transport between sputtering and ALD tools without exposing the sample to atmosphere. A spectroscopic ellipsometer (SE) is mounted to the tool, allowing for in-situ measurement of film properties during deposition.

The ALD 150LX tool is a continuous flow type design, meaning that carrier gas is constantly flowing through the reaction chamber. The reactor pressure is maintained by constant pumping. During idle times (when the tool is not in use), N_2 (99.998%) is flowed through the reactor, maintaining a pressure of ~0.25 Torr. When depositions are being performed, the carrier gas used is Ar (99.999%) and the reactor has a pressure of ~1 Torr. 1 Torr was selected as the optimum operating pressure because it is low enough to enhance diffusion while high enough to achieve

proper flow characteristics. The Ar carrier gas serves a few main purposes. Firstly, it helps to transport precursor vapours through the reactor to the substrate; hence, the name carrier gas. The second purpose of the carrier gas is to maintain proper fluid flow properties within the reactor. The carrier gas flow rate and pressure are carefully selected to achieve laminar flow. Laminar flow ensures that reaction by-products and excess precursor molecules are efficiently removed from the reactor without mixing caused by turbulent flow. The carrier gas also provides a protective "curtain" of gas around the reactor walls. This inert gas curtain helps prevent reactor contamination by preventing precursor molecules from reaching the reactor walls.

Thermocouples and heaters are used to control the temperature of the reactor, valves, lines, and precursor ampules. Temperature control is very important in ALD in order to prevent condensation and/ or decomposition of the precursor. The reaction chamber itself has numerous independently controlled temperature regions, including the substrate holder, reactor walls, and gas inlets. Precursor ampule, valve, and gas line temperatures are carefully selected to ensure that vapour phase molecules are transported to the substrate without condensation or decomposition. Precursor condensation is commonly prevented by ensuring that the precursor vapour experience a positive temperature gradient as it approaches the reactor. This is done by setting temperatures such that $T_{ampule} < T_{valve} < T_{line}$.

The ALD system is also equipped with an inductively coupled plasma system, typically operated at a power of 600 W. The plasma is generated in a quartz tube above the substrate. This remote plasma produces gas-phase radicals which then flow/ diffuse towards the sample surface and react. A number of plasma gases can be used in this system including O_2, forming gas (95% N_2, 5% H_2), H_2, and CH_4.

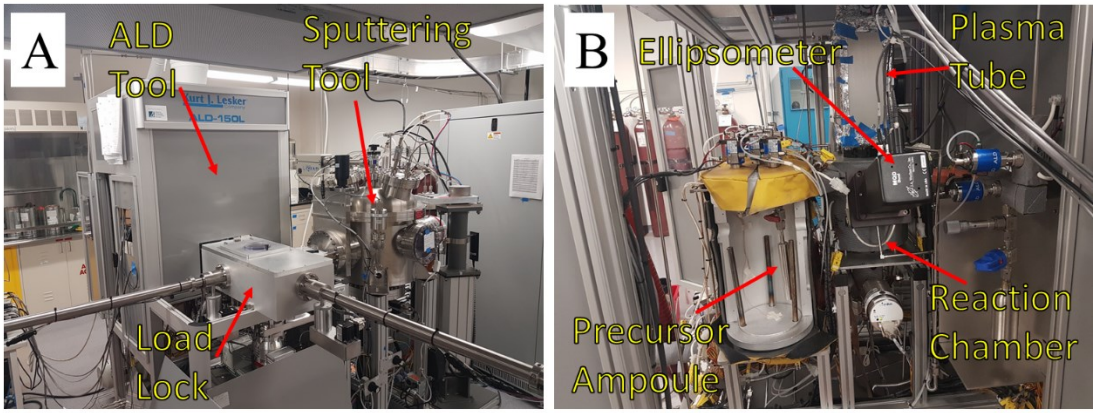

Figure 3-1: Images of the Kurt J. Lesker ALD 150LX tool used for depositions.

3.1.2 ALD Precursors

Metal organic precursors were purchased from STREM, pre-packaged in 50 mL Swagelok ampules filled with Ar and equipped with a ball valve. Many of the precursors used in ALD are air sensitive; the ampule allows for a precursor to be installed/ removed from the ALD tool without exposing the precursor to the atmosphere. When a new precursor is received, it is important to perform a number of cycles before depositions are performed. From our experience with a variety of precursors, the deposition behaviour of the first cycles from a new precursor ampule is not consistent or repeatable. As the precursor is pulsed/ cycled more and more, the deposition behaviour eventually stabilizes. It is suspected that the anomalous behaviour is due to volatile impurities. Over time these impurities become depleted and eventually are completely removed. Stabilization of the precursor can take a few hundred cycles to thousands of cycles, depending on the precursor being used.

Two Mn precursors were examined in this work; their molecular structures are shown in Figure 3-2. Bis(cyclopentadienyl) manganese (manganocene, $(Cp)_2Mn$) was the first Mn precursor to be examined. This precursor, however, caused serious problems during deposition. The manganocene condensed in the lines and valves of the ALD system, causing severe contamination. Many line/ valve/ ampule heating schemes were used in an attempt to avoid condensation, but no effective scheme was found. Because of the condensation problem, manganocene was determined to be an unsuitable precursor for ALD of MnO_x. The second Mn precursor examined was bis(ethylcyclopentadienyl) manganese ($(EtCp)_2Mn$). This precursor has

been used in a number of reports in literature and has been reported to deposit MnO_x via an ALD mechanism with H_2O as the oxygen source. [76], [80], [85] The cobalt precursor used was cyclopentadienyl cobalt dicarbonyl (Figure 3-2C).

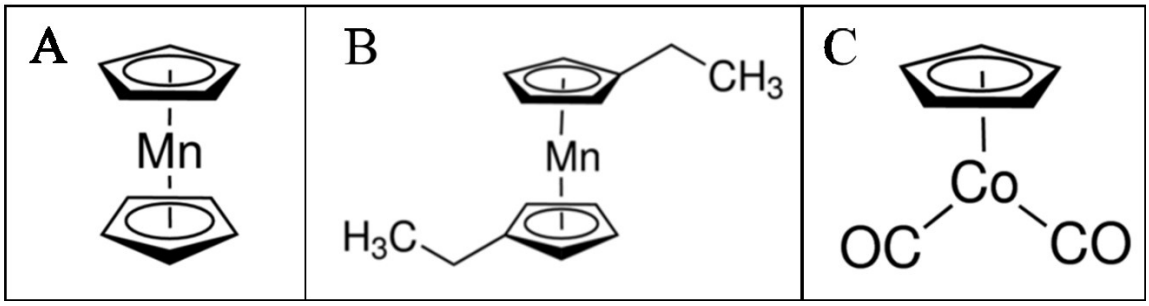

Figure 3-2: ALD precursors. (A) Bis(cyclopentadienyl) manganese, (B) bis(ethylcyclopentadienyl) manganese, (C) cyclopentadienyl cobalt dicarbonyl.

3.1.3 Pulsed Precursor Delivery

As discussed in Section 2.4.4, some of the precursors used in ALD do not produce a high enough vapour pressure to utilize conventional precursor delivery. Reports in the literature using $(EtCp)_2Mn$ held the precursor at 75 – 100 °C, with some using conventional precursor delivery and some using a bubbler. [12], [76], [80], [87], [90], [91], [93], [96], [100] During experiments in this work, sufficient $(EtCp)_2Mn$ doses were not attainable when using conventional precursor delivery. However, there was reluctance to buy a bubbler because of the cost and potential complications in transferring the air sensitive precursor from the 50 mL ampule into the bubbler.

A 2011 patent by Cambridge Nanotech describes a procedure for delivery of low vapour pressure precursors using an inert gas boost to increase the pressure within the ampule which can then transport precursor molecules to the substrate. [110] This procedure was adapted for use in the ALD system, and is referred to as “pulsed precursor delivery” or colloquially as a “poor man’s bubbler”. A precursor pulse using this method is broken into three steps: charge, dwell, and discharge (summarized schematically in Figure 3-3). During the charge step the ALD bypass valve is closed, allowing Ar to flow into the ampule, increasing the pressure relative to the ALD reactor. Once pressurized, the ampule is isolated (ALD in valve closed) and given some time to allow for the precursor partial pressure to equilibrate. This is the dwell step and it occurs in conjunction with the precursor purge, reactant dose, and reactant purge. The dwell step is an important consideration when using low vapor pressure precursors, because the precursors tend

to have slow evaporation rates and require some time to regenerate gas phase precursor molecules within the ampule. When it is time for the precursor dose, the ampule is discharged. The ampule is opened to the reactor, allowing the positive pressure inside the ampule to carry precursor molecules to the substrate. Consistent $(EtCp)_2Mn$ dosing was achieved using the pulsed precursor delivery method.

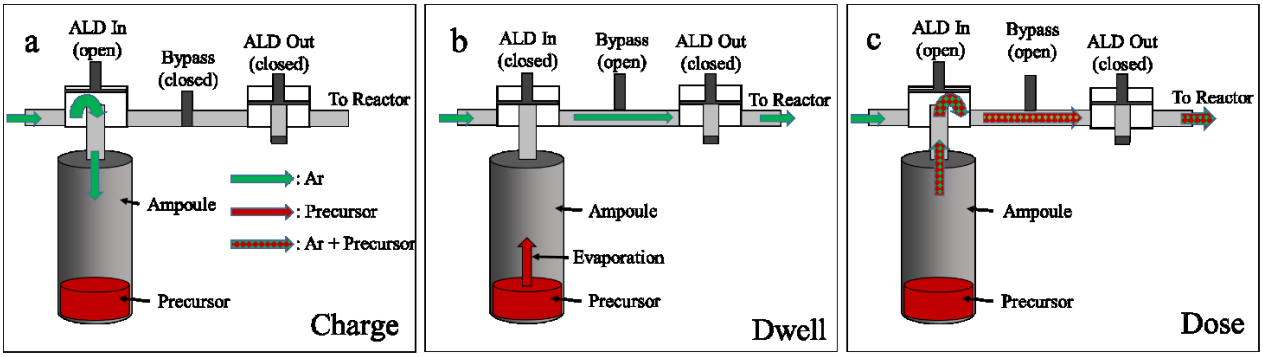

Figure 3-3: Schematic of the pulsed precursor delivery method.

3.1.4 Ellipsometry

In-situ spectroscopic ellipsometry (SE) was used to monitor film properties (e.g., thickness) during ALD processes. The ellipsometer used was a Woollam M-2000DI and results were analyzed using the CompleteEASE software. The ellipsometer data for MnO_x films were fit using a two oscillator Tauc-Lorentz model.

3.2 Electrochemical Characterization

All electrochemical measurements were performing using Biologic SP-300 and VSP-300 potentiostats. Chemicals were acquired from Fisher Scientific and used without further purification. The substrates used were carbon gas diffusion layers (GDL, Sigracet 35/39 BC) purchased from the Fuel Cell Store.

3.2.1 Half Cell Testing

Half cell tests were performed in an electrolyte of 1 M KOH, saturated with either O_2 or Ar. The reference and counter electrodes used were Hg/HgO (0.098 V vs. SHE) and a Pt coil, respectively. All half cell tests were IR corrected. Cyclic voltammetry (CV) was performed from -0.5 to 0.2 V vs. Hg/HgO using a scan rate of 20 mV s^{-1}. Linear sweep voltammetry was

performed from -0.5 to 0.2 V vs. Hg/HgO at a sweep rate of 5 mV s^{-1}. Chronopotentiometry was performed at either -10 or -20 mA cm^{-2} utilizing a graphite counter electrode in O_2 saturated 1 M KOH. Graphite was used instead of Pt during chronopotentiometry to avoid oxidation of the Pt.

3.2.1.1 Electrochemical Surface Area Measurements

The electrochemical surface areas (ECSA) of the electrodes were determined using a method described by Lee *et al.* [111] Cyclic voltammetry was performed at a variety of scan rates in Ar saturated 1 M KOH. It is important that the potential range used for ECSA measurement is free of faradaic reactions; ideally the range scanned should only contain current from the double layer. If faradaic reactions occur in the potential window used, the resulting measurement will not be accurate. The potential range used in this work was 0.1 – 0.2 V vs. Hg/HgO.

Once the CV data was collected, the charge passed (q) at each scan rate (ν) was then calculated and plotted. These plots allow for deconvolution of double layer and faradaic effects. Since faradaic processes occur more slowly than double layer processes, an increase in scan rate will cause a drop in faradaic charge (q_F), while double layer charge (q_{DL}) remains relatively constant. Capacitance (C) was calculated by dividing the charge passed by the voltage window ($C = q/\Delta V$). Examples of the plots used for ECSA measurements are shown in Figure 3-4. Figure 3-4A is a plot of q vs. $\nu^{-1/2}$. By applying a linear fit to the data, the y-intercept ($\nu = \infty$) gives a value for q_{DL}. The total charge passed was determined in a similar way from Figure 3-4B; the data is extrapolated to $\nu = 0$. The double layer charge was then subtracted from the total charge, giving the faradaic contribution.

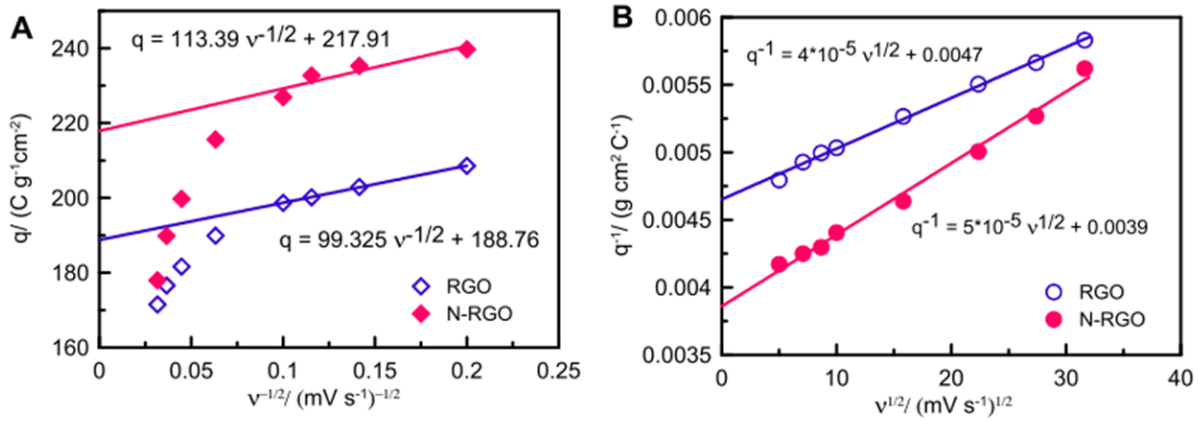

Figure 3-4: Plots used to determine ECSA. [111]

Since double layer capacitance is directly proportional to the surface area of an electrode, this technique can be used to compare the relative surface areas of electrodes. However, this technique is not very reliable for quantifying surface area. In order to convert the double layer capacitance (C_{DL}) to a surface area, the capacitance per unit area for the film must be known. Capacitance per unit are is difficult to determine and is dependent on the electrode material. In order to simplify analysis in this work, C_{DL} was used to compare ECSA for various electrodes.

3.2.2 Full Cell Testing

Full cell Zn-air battery (ZAB) tests were performed using an electrolyte of 6 M KOH + 0.25 M ZnO. ALD coated GDL was used as the air electrode, with an exposed area of 1 cm^2. A Zn plate was used as the Zn electrode. ZAB tests were performed using a horizontal cell, shown schematically in Figure 3-5. The horizontal configuration was chosen over a vertical design because the horizontal orientation greatly reduces electrolyte leakage and electrode flooding. ZAB tests were performed using a tri-electrode configuration as well as a bifunctional configuration. The tri-electrode configuration, shown in Figure 3-5A, utilizes separate electrodes for charge and discharge. This allows each electrode to be optimized for a single reaction, improving battery efficiency and stability. The charge electrode used in tri-electrode tests was a CoFe alloy electrodeposited on Ni foam. Bifunctional electrodes were tested using the configuration shown in Figure 3-5B.

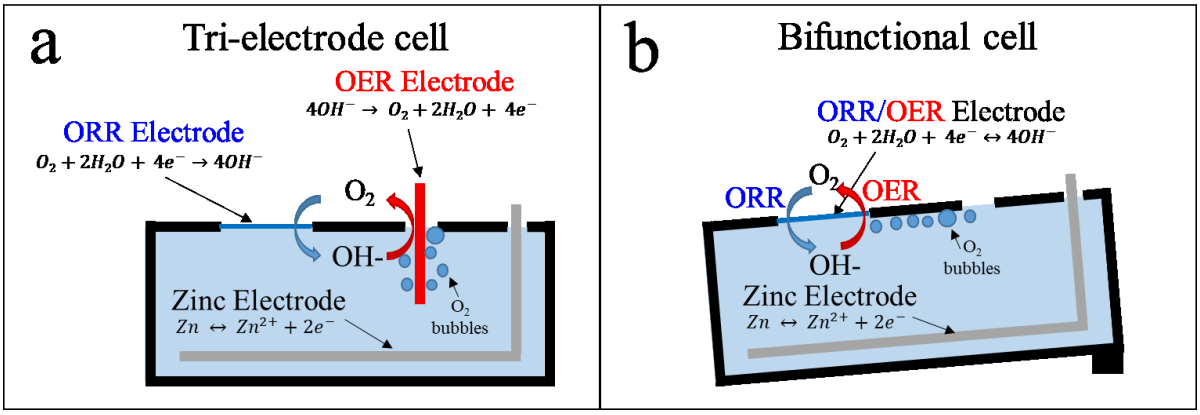

Figure 3-5: Schematics of ZAB configurations used for full cell testing.

Polarization tests were performed at a sweep rate of 1 mA $cm^{-2}s^{-1}$ and were performed from 0 to either 100 or 400 mA cm^{-2}. Rate capability tests were performed at current densities of 2, 5, 10,

20, and 50 mA cm^{-2}; holding each current for 10 min. Electrochemical impedance spectroscopy was performed at a cell voltage of 1.2 V with an amplitude of 10 mV within the frequency range of 100 mHz to 1 MHz.

Cycling stability tests were performed with a timing scheme of 10/5/10/5 min (discharge/ rest/ charge/ rest). Tri-electrode cycling was done at a current density of 20 mA cm^{-2} for 200 cycles (100 h), while bifunctional cycling was done at 10 mA cm^{-2} for 100 cycles (50 h). EIS and polarization were performed before and after cycling in order to quantify changes in electrode performance.

3.2.2.1 Electrodeposition of CoFe

A CoFe alloy was electrodeposited onto Ni foam for use as the charge electrode in tri-electrode ZAB tests. The electrodeposition procedure was developed previously by our group. [27], [112], [113] CoFe was cathodically electrodeposited onto pieces of Ni foam (4.2 cm^2) at a constant current of 300 mA under ultrasonic agitation. Two pieces of Pt mesh (2.5 x 2.5 cm) were used as the counter electrode, with the Ni foam placed between them. The electrolyte for Co-Fe deposition contained 0.1 M $CoSO_4$, 0.1 M $FeSO_4$, 0.2 M sodium citrate, 0.2 M boric acid, 0.05 M L-ascorbic acid, and 400 mg L^{-1} of sodium dodecyl sulfate.

3.3 Materials Characterization

3.3.1 Scanning Electron Microscopy

Scanning electron microscopy (SEM) was performed using a Zeiss Sigma field emission SEM. The microscope is equipped with a number of detectors including backscatter electron, secondary electron, in-lens, and two x-ray detectors. The SEM was operated at accelerating voltages from 10 – 20 kV. EDX spectra were taken at 20 kV, and images was generally collected at 10 kV.

3.3.2 Transmission Electron Microscopy/ Scanning Transmission Electron Microscopy

Transmission electron microscopy (TEM) and scanning transmission electron microscopy (STEM) were performed using a JOEL JEM-ARM200CF at an accelerating voltage of 200 kV. This microscope is equipped with an aberration corrector for STEM mode, enabling resolutions

on the order of 50 pm. In addition to bright field and annular dark field detectors, the JOEL JEM-ARM200CF has a large solid angle EDX detector, enabling fast collection of high resolution elemental maps. TEM/ STEM samples were prepared by scraping the ALD coating from the microporous layer of the GDL. The residue was sonicated in ethanol and dropped onto a lacey carbon TEM grid. Select films were also deposited directly onto SiO_2 membranes (18 nm SiO_2, Ted Pella) for plan-view imaging.

3.3.3 X-ray Photoelectron Spectroscopy

X-ray photoelectron spectroscopy (XPS) was conducted with a Kratos AXIS Supra instrument using monochromatic Al-K_α x-rays and a pass energy of 20 eV. Prior to analysis, samples were sputtered for 15 s using an Ar ion gun at an energy of 500 eV. All XPS spectra were calibrated using the C 1s C-H peak at 284.8 eV.

Chapter 4: Saturation Behaviour of Atomic Layer Deposition MnO_x from Bis(Ethylcyclopentadienyl) Manganese and Water: Saturation Effect on Coverage of Porous Oxygen Reduction Electrodes for Metal-Air Batteries

A version of this chapter has been published in the journal ACS Applied Nano Materials:

M. P. Clark, T. Muneshwar, M. Xiong, K. Cadien, and D. G. Ivey, "Saturation Behavior of Atomic Layer Deposition MnOx from Bis(Ethylcyclopentadienyl) Manganese and Water: Saturation Effect on Coverage of Porous Oxygen Reduction Electrodes for Metal−Air Batteries", *ACS Appl. Nano Mater.*, vol. 2, pp. 267-277, 2018

4.1 Introduction

Atomic layer deposition (ALD) is a thin film technique capable of producing highly conformal thin films with thickness control on the order of Ångstroms. ALD is achieved by the use of gas phase species which undergo self-limiting reactions on the substrate surface. [11], [66] ALD of a compound AB is achieved by repetitive exposures of reactants AL_m and BX_n, where A is the metal species, B is the non-metal species and L and X are sacrificial ligands. The metal containing species is commonly referred to as the precursor and the non-metal species is called the reactant. [114] A typical ALD cycle is composed of four steps: 1) precursor dose, 2) post-precursor purge, 3) reactant dose, and 4) post-reactant purge. This sequence is repeated until the desired film thickness is achieved. The purge steps are required in order to remove reaction by-products and avoid overlap between the precursor and reactant species within the reactor. Growth rate of an ALD process is commonly reported as growth per cycle (GPC). The theoretical maximum GPC for an ALD material is one monolayer. The monolayer thickness can be calculated using Equation (1), where d_{ML} is the monolayer thickness, M is the molar mass of the material, ρ is the density, and N_A is Avogadro's number. Typical GPC values range from ~7% – 40% of the monolayer thickness due to limited surface active sites and/ or adsorbed ligands blocking neighboring adsorption sites. [73]

$$d_{ML} = \left(\frac{M}{\rho N_A}\right)^{\frac{1}{3}} \quad (1)$$

Precursor selection is an important factor in the development of an ALD process. The selected precursor must meet a number of requirements in order to achieve the desired reaction mechanisms. Some of the considerations in selecting a precursor are vapour pressure, stability,

reactivity, and composition. Bis(ethylcyclopentadienyl) manganese, $(EtCp)_2Mn$, is regarded as a good precursor for the preparation of Mn oxide because it is liquid and has a relatively high decomposition temperature of 500 °C. [115], [116] The vapour pressure of $(EtCp)_2Mn$ is among the highest of the Mn precursors, but is still comparatively low relative to commonly used ALD precursors such as trimethyl aluminum[117] or diethyl zinc[118]. Due to the low vapour pressure of $(EtCp)_2Mn$, a bubbler is commonly used to aid in the delivery of $(EtCp)_2Mn$ molecules.

Lu *et al.* [96] were the first group to prepare MnO_x using the $(EtCp)_2Mn$ precursor, but provided little analysis on the deposition mechanism. Burton *et al.* [80] reported on the ALD mechanism of MnO_x utilizing $(EtCp)_2Mn$ and H_2O, providing saturation data and extensive in-situ and ex-situ characterization of films. Multiple groups have since prepared MnO_x using a similar procedure to Burton *et al.*, using substrate temperatures of ~150 °C. In order to achieve sufficient precursor dose, groups utilizing $(EtCp)_2Mn$ have held the precursor at 75-100 °C, many in conjunction with a bubbler. Films prepared using $(EtCp)_2Mn$ and H_2O have a stoichiometry of MnO and a reported growth rate of ~1 Å/cy. [12], [76], [80], [87], [90]–[93], [96], [100], [119], [120]

Manganese oxide has a wide range of practical applications including energy storage technologies, such as supercapacitors and batteries. [9], [17], [84], [85], [97], [121]–[123] MnO_x has been extensively studied as a catalyst for the oxygen reduction reaction (ORR) because of its good activity, low cost, and environmentally friendly nature. The catalytic activity of ALD MnO_x has been previously investigated by Pickrahn *et al.* [12], [76] and Fan *et al.* [49]. Pickrahn *et al.* prepared MnO_x on glassy carbon electrodes. In their work Pickrahn *et al.* showed that annealed MnO_x films provide catalytic activity towards ORR, with an onset potential 120 mV less than Pt/C. Fan *et al.* deposited ALD MnO_x onto carbon nanotubes, demonstrating that their MnO_x followed a 4-electron mechanism with ORR activity on par with Pt/C. Metal-air batteries are an emerging application for MnO_x-based catalysts, with the potential to replace Li-ion batteries in many cases. [19] The air electrodes used in metal-air batteries are composed of high surface area carbon, which commonly have catalyst loaded directly onto the electrode surface. Through the use of ALD to prepare air electrodes for metal-air batteries, the high surface area structure of the carbon electrode can be coated with a conformal layer of MnO_x, improving MnO_x dispersion and surface area.

The purpose of this work is to investigate the saturation behaviour of ALD MnO_x from $(EtCp)_2Mn$ plus water for the preparation of electrodes for metal-air batteries. Growth behaviour is examined using in-situ spectroscopic ellipsometry on Si wafers. Reported within are a complete set of saturation plots for all dose and purge steps, with the $(EtCp)_2Mn$ dose step examined within a range of substrate temperatures. Depositions utilizing $(EtCp)_2Mn$ plus water exhibited anomalous saturation behaviour in disagreement with prior literature. [76], [80] A saturating deposition mechanism has been achieved using $(EtCp)_2Mn$ through the use of a forming gas (95% N_2/5% H_2) plasma step. Porous carbon oxygen reduction electrodes were coated with ALD MnO_x to examine the effect of saturation behaviour on catalyst distribution and ORR performance. The saturating behaviour of ALD reactions allow for MnO_x to penetrate into the depth of the electrode, increasing effective surface area and ORR performance.

4.2 Experimental

A Kurt J. Lesker ALD 150LX reactor (continuous flow) operated at a pressure of ~1 Torr was used for all depositions. High purity Ar (99.999%, Praxair) was used as the carrier gas. $(EtCp)_2Mn$ (98%, STREM Chemicals, Inc.) was used as the Mn precursor and was maintained at a temperature of 80 °C. Bis(cyclopentadienyl) manganese (manganocene, $(Cp)_2Mn$, a powdered precursor) was also examined as a potential precursor, but condensed in the valve and lines, causing blockage. The valve and line used to transport the precursor vapours were held at 100 and 110 °C, respectively. Distilled water was used as the reactant and was maintained at a room temperature (~22 °C). Films prepared using $(EtCp)_2Mn$ and H_2O will be referred to as W-MnO_x. The effect of a forming gas (FG - 95% N_2, 5% H_2) plasma step between the $(EtCp)_2Mn$ and H_2O doses was also examined; these films are referred to as FG-MnO_x. Si (100) substrates with the native SiO_x layer were used to investigate deposition saturation behaviour. Depositions were performed at substrate temperatures ranging from 40 to 250 °C. Substrates were cleaned using 30 s of O_2 plasma immediately prior to deposition. For depositions utilizing forming gas, 30 s of FG plasma was used for the pre-deposition clean. Film thickness was monitored using in-situ spectroscopic ellipsometry (Woollam M-2000DI). Select films were annealed in air for 30 minutes at 300 °C in order to further oxidize the MnO_x films. Annealed W-MnO_x and FG-MnO_x films have the designations W-MnO_x-Ann, and FG-MnO_x-Ann, respectively.

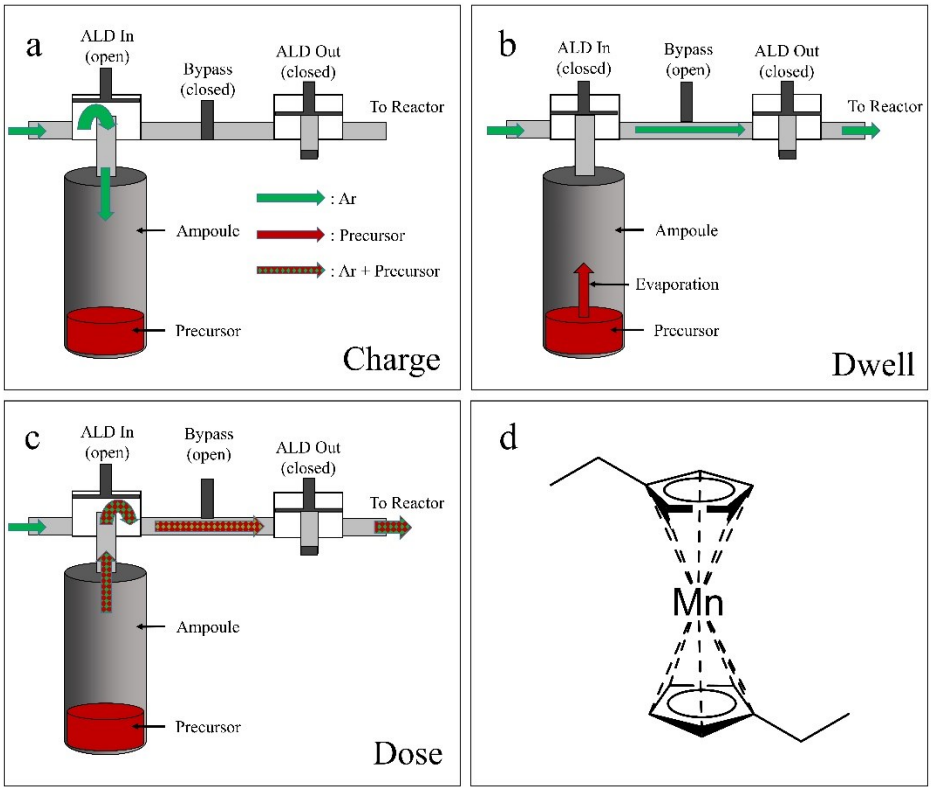

Figure 4-1: (a-c) Schematic of the pressurized precursor delivery method. (a) Charge, (b) dwell, and (c) dose. (d) Molecular structure of $(EtCp)_2Mn$.

Due to the low volatility of the $(EtCp)_2Mn$ precursor (0.1 Torr at 50 - 65 °C)[116], delivery of an adequate amount of precursor vapour to the substrate is difficult using conventional effusion methods. In order to achieve sufficient precursor dose without the use of a bubbler, an alternate method, similar to the so-called "Boost" method developed by Picosun^{TM}, was used. A precursor pulse using this method is broken into three steps: charge, dwell, and discharge (summarized schematically in Figure 4-1). During the charge step the ALD bypass valve is closed, allowing Ar to flow into the ampule, increasing the pressure relative to the ALD reactor. Once pressurized, the ampule is isolated (ALD in valve closed) and given some time to allow for the precursor partial pressure to equilibrate. This is the dwell step and it occurs in conjunction with the precursor purge, H_2O dose, and H_2O purge. The dwell step is an important consideration when using low vapour pressure precursors, because these precursors tend to have slow evaporation rates and require some time to regenerate gas phase precursor molecules within the ampule. When it is time for the precursor dose, the ampule is discharged. The ampule is opened

to the reactor, allowing the positive pressure inside the ampule to carry precursor molecules to the substrate.

X-ray photoelectron spectroscopy (XPS) analysis was conducted using a Kratos AXIS Supra instrument using a monochromatic Al-K_α x-ray source and a pass energy of 20 eV. Prior to XPS analysis samples were sputter cleaned using an Ar ion gun for 15 s with an energy of 500 eV to remove contamination and surface oxides due to exposure to atmosphere. XPS spectra were calibrated using the C 1s C-H peak at 284.8 eV. A Zeiss Sigma scanning electron microscope (SEM) was used for imaging and energy dispersive x-ray (EDX) analysis. Sample cross sections were prepared by fracturing electrodes after cooling in liquid nitrogen. Transmission electron microscopy (TEM) and scanning transmission electron microscopy energy dispersive x-ray (STEM EDX) analysis were conducted using a JEOL JEM-ARM200CF at an accelerating voltage of 200 kV. Samples for TEM/ STEM analysis were prepared by depositing films directly onto 18 nm thick SiO_2 membranes supported by a SiN grid (Ted Pella).

Electrochemical measurements were performed using a Biologic SP-300 potentiostat in Ar or O_2 saturated 1 M KOH. The reference electrode used was Hg/HgO and a Pt coil was used as the counter electrode. All reported potentials are versus Hg/HgO (0.098 V vs. SHE) and all measurements were IR-corrected. The working electrodes were porous carbon gas diffusion layers (GDL, Sigracet 39BC), coated with 40 nm of MnO_x (measured on a Si wafer placed in the reactor beside the electrodes) following the optimized deposition parameters. Prior to deposition, the GDL was exposed to 60 s of oxygen plasma. Pt-C (40% Pt- Alfa Aesar) was used as a baseline reference for ORR activity. A Pt-C ink containing Pt-C, Nafion, Teflon, ethanol, and water was spray coated onto GDL at a mass loading for 500 μg cm^{-2} (200 μg(Pt) cm^{-2}).

4.3 Results and Discussion

4.3.1 ALD of MnO_x from $(EtCp)_2Mn$ and H_2O

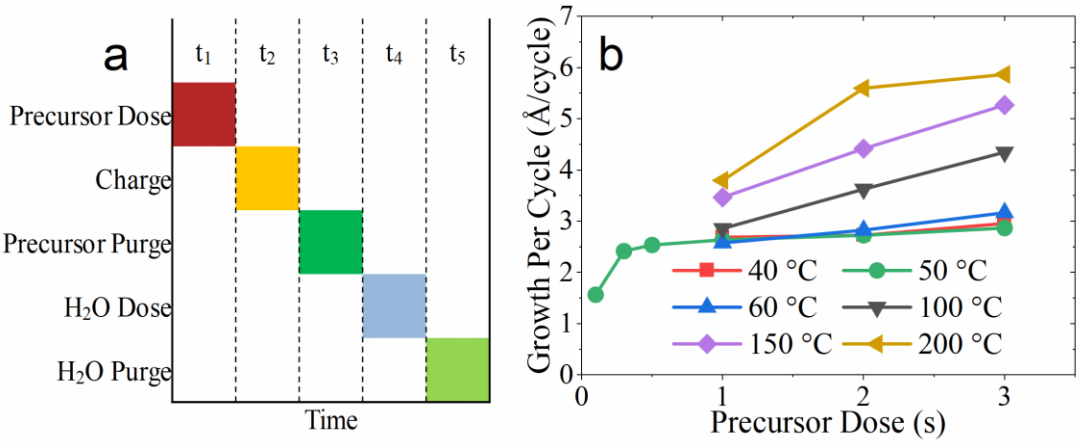

Figure 4-2: (a) Pulse timing scheme for a single $(EtCp)_2Mn + H_2O$ ALD cycle. (b) GPC vs. precursor dose (t_1) at various substrate temperatures for W-MnO_x. All depositions had a timing scheme of x/2 s/20 s/2 s/30 s.

Optimization for the $(EtCp)_2Mn + H_2O$ process was done at T_{sub} = 50 °C. The optimized timing scheme for MnO_x deposition using $(EtCp)_2Mn$ and H_2O (W-MnO_x) is 3 s/2 s/20 s/2 s/30 s ($t_1/t_2/t_3/t_4/t_5$), where t_1 is the precursor dose time, t_2 is the charge time, t_3 is the precursor purge, t_4 is the H_2O dose, and t_5 is the post H_2O purge time. A schematic diagram of the timing scheme is shown in Figure 4-2a. Film thickness was measured using in-situ spectroscopic ellipsometry. After the first few cycles of each deposition, thickness vs. cycle number became linear. GPC values were taken as the slope of this linear region. Precursor saturation was investigated by plotting GPC vs. precursor dose time (t_1) at substrate temperatures (T_{sub}) ranging from 40 to 200 °C. Precursor saturation results are shown in Figure 4-2b. A timing scheme of x/2 s/20 s/2 s/30 s was used for all precursor saturation tests, where x is the precursor dose time and was varied from 0.1 s to 3 s. This timing scheme was determined from the saturation plots shown in Figure 4-3, ensuring that purge times (t_3 and t_5) and H_2O dose times (t_4) are adequately long. A reaction is said to be saturating if the GPC remains constant with increasing precursor and/ or reactant dose, indicating a limit to the number of molecules that can be adsorbed to the surface. Of the substrate temperatures investigated, precursor saturation was only observed at T_{sub} = 40 and 50 °C. The saturated GPC was 2.85 Å/cy, which is about the same as the theoretical maximum of 2.8 Å/cy for MnO, as calculated from Equation (1). As the theoretical maximum for ALD

reactions is rarely achieved due to steric hindrance effects, this high GPC suggests that the film is likely not composed purely of MnO and/ or that the reactions are not following a self-limiting mechanism. [73] This observed saturation behaviour conflicts with works published in literature, these conflicts are discussed in Appendix C. As shown in the subsequent characterization sections, the deposited films contain a large amount of carbon, which explains the high GPC observed at T_{sub} = 40 - 50 °C. At $T_{sub} \geq 60$ °C GPC continuously increases with increasing precursor dose, indicating the presence of non-saturating reactions. The mechanism of deposition leading to non-saturating reactions is currently not clear. It is suspected that incomplete ligand removal plays a roll in the non-saturating behaviour.

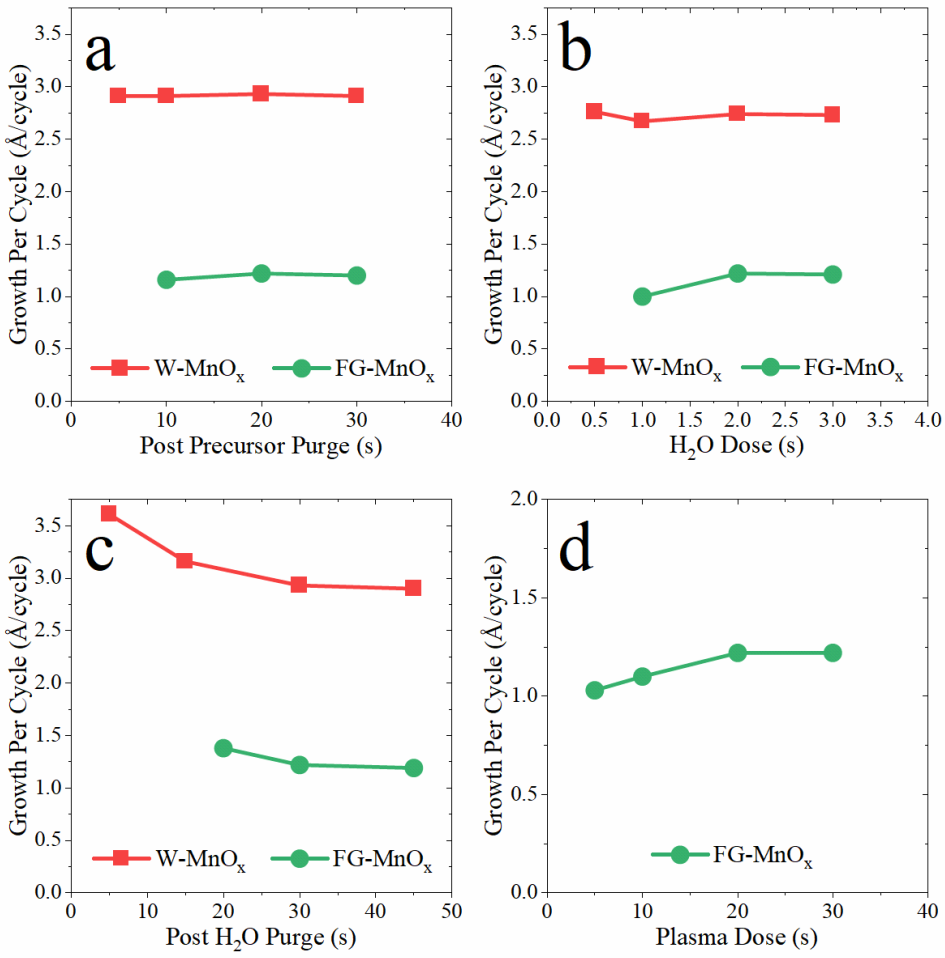

Figure 4-3: GPC versus dose and purge times for W-MnO_x (squares, Tsub =50 °C) and FG-MnO_x (circles, Tsub = 100 °C) systems. For all plots, the optimized tims are 3 s/2 s/20 s/2 s/30 s for $(EtCp)_2Mn$ + H_2O and 3 s/2 s/20 s/20 s/2 s/30 s for $(EtCp)_2Mn$ + FG plasma + H_2O. For each plot, only one time is varied while all other times are held constant, following the standard timing. (a) Post precursor purge, (b) H_2O dose, (c) post H_2O purge, and (d) FG plasma dose.

4.3.2 ALD of MnO_x from $(EtCp)_2Mn$, FG plasma, and H_2O

In order to obtain self-saturating surface reactions for the ALD system of $(EtCp)_2Mn$ and H_2O, a FG plasma step was introduced between the $(EtCp)_2Mn$ and water exposures. The radical species present in the FG plasma can be highly reactive and are known to be effective at dissociating carbon-metal bonds. [124], [125] Optimization of the timing scheme was done at T_{sub} = 100 °C. The optimized timing was found to be 3 s/2 s/20 s/20 s/2 s/30 s ($t_1/t_2/t_3/t_4/t_5/t_6$), where t_1 is the precursor dose time, t_2 is the charge time, t_3 is the precursor purge, t_4 is the FG plasma exposure, t_5 is the H_2O dose, and t_6 is the post H_2O purge time. Figure 4-4a shows a schematic of the timing scheme used. Precursor saturation was investigated at T_{sub} temperatures in the range of 50 – 250 °C; results are shown in Figure 4-4b. Saturation curves used for timing optimization are shown in Figure 4-3. A saturated GPC of 1.15 Å/cy was observed in the temperature range of 100 – 200 °C, indicating that deposition under these conditions does not experience any non-ALD type reactions like those observed for the W-MnO_x system. The use of a FG plasma step clearly promotes a saturating deposition mechanism, which is desirable for the coating of porous electrodes.

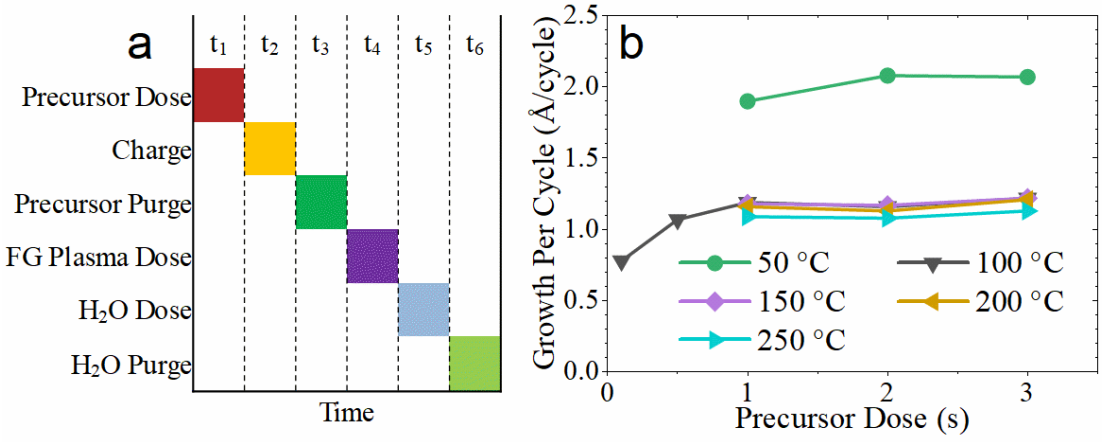

Figure 4-4: (a) Pulse timing scheme for a single $(EtCp)_2Mn$ + FG plasma + H_2O ALD cycle. (b) GPC vs. precursor dose (t_1) at various substrate temperatures for FG-MnO_x. All depositions had a timing scheme of x/2 s/20 s/20 s/2 s/30 s.

The GPC for T_{sub} = 50 °C deviates from the saturated GPC between 100 and 200 °C, reaching a value of 2.10 Å/cy. This deviation is attributed to inadequate purge steps causing gas phase reactions. Since the recipe was optimized at 100 °C, the purge steps would need to be increased in duration to avoid non-ALD reactions at T_{sub} = 50 °C due to reduced desorption rates at lower

temperatures. The measured GPC for T_{sub} = 250 °C was 1.10 Å/cy, which is slightly lower than the GPC at 100 – 200 °C. This slight decrease in GPC is due to insufficient water dose at T_{sub} = 250 °C caused by fast desorption rates at elevated temperatures.

4.3.3 Transmission Electron Microscopy

W-MnO_x and FG-MnO_x films were deposited directly onto SiO_2 membranes to a thickness of 20 nm using the respective optimized recipes. High resolution (HR) TEM images are shown in Figure 4-5. The films are mostly amorphous with some small crystalline regions. The crystal size for the W-MnO_x film is 3 – 5 nm. The crystalline regions for the FG-MnO_x are larger and better defined than for the W-MnO_x sample, with a crystal size of 5 – 10 nm. Since the W-MnO_x and FG-MnO_x films were prepared at 50 and 100 °C respectively, at present it is not clear whether the difference in grain size is due to the difference in T_{sub} or a consequence of the FG plasma.

STEM EDX spectra were collected from the W-MnO_x and FG-MnO_x films as well as a bare SiO_2 membrane. Representative EDX spectra are shown in Figure 4-5c. All spectra contain a large amount of Si and O due to the SiO_2 support under the deposited films. For the W-MnO_x and FG-MnO_x films, the Mn Kα and Kβ signals are clearly visible, as well as a number of peaks at energies <1 keV. Figure 4-5d shows the low energy region of the EDX spectra. Both deposited films contain a significant amount of C. The FG-MnO_x film shows a significant N K peak, indicating that N from the FG plasma was incorporated into the film.

The diffraction pattern obtained from the W-MnO_x film is very diffuse with no clear rings, consistent with the amorphous/ nanocrystalline structure. Patterns taken from the bare SiO_2 membrane showed no diffracted intensity. The diffraction pattern from the FG-MnO_x film shows mostly diffuse intensity with four faintly defined rings. The diffracted rings correspond to planar spacings of 4.76 Å, 2.72 Å, 2.10 Å, and 1.65 Å. These planar spacings are consistent with a number of different MnN_x, MnO_x, and MnO_xN_y structures, making identification of the crystal structure difficult.

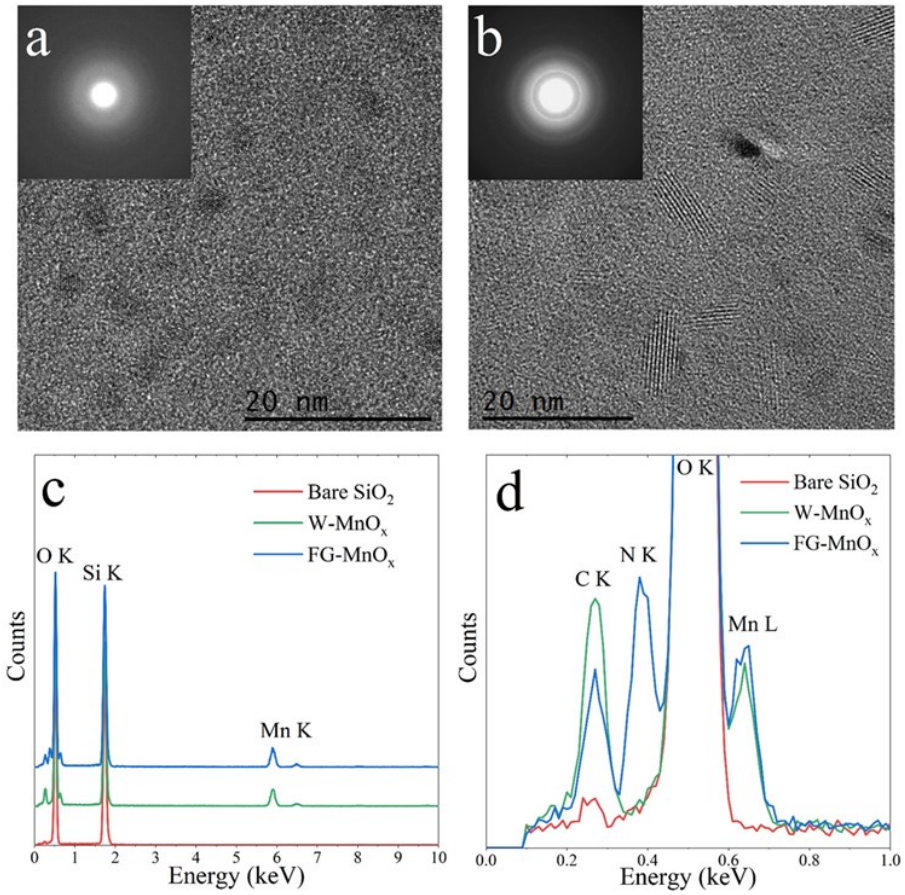

Figure 4-5: HR-TEM images of (a) W-MnO_x, and (b) FG-MnO_x films (20 nm thick) deposited on 18 nm SiO_2 membranes. Diffraction patterns are inset. (c, d) STEM EDX spectra from the W-MnO_x and FG-MnO_x films as well as the bare SiO_2 membrane.

4.3.4 X-ray Photoelectron Spectroscopy

XPS spectra were collected for as deposited and annealed films. The obtained spectra for Mn 2p, and Mn 3s are shown in Figure 4-6. O 1s, N 1s, and C 1s spectra are shown in Figure 4-7; results of peak deconvolution are shown in Table 4-1. [52], [126]–[129] The Mn oxidation state is determined from the Mn 3s and Mn 2p spectra as described by Gorlin et al. [52] The as deposited W-MnO_x and FG-MnO_x films show very similar Mn spectra. The as deposited samples exhibit peak splittings of 6.0 eV and 5.9 eV for the Mn 3s and Mn 2p spectra respectively, corresponding to an Mn oxidation state of 2.0 for both samples. The Mn 3s peak splitting reduces slightly after annealing, dropping to 5.7 eV and 5.6 eV for annealed W-MnO_x and FG-MnO_x films, respectively. Assuming a linear relation between Mn 3s splitting and oxidation state, the Mn 3s peak splitting for annealed W-MnO_x and FG-MnO_x films corresponds to average Mn

oxidation states of 2.2 and 2.4, respectively. The Mn 2p splitting for both annealed films is ~10 eV, which is in agreement with the Mn 3s results. [52], [130] The as deposited FG-MnO_x film contains significantly more N than O, suggesting that the H_2O exposure after the FG plasma step is not able to effectively remove N in favour of O. The N 1s spectrum for the FG-MnO_x sample shows that N is incorporated into the film as a combination of Mn-N, O-Mn-N, and C-N species. After annealing, most of the N and C are removed from the films as indicated by the quantification results. The only significant difference in the XPS analysis between W-MnO_x-Ann and FG-MnO_x-Ann films is the slightly elevated carbon content for W-MnO_x-Ann and slightly higher Mn oxidation state for FG-MnO_x-Ann.

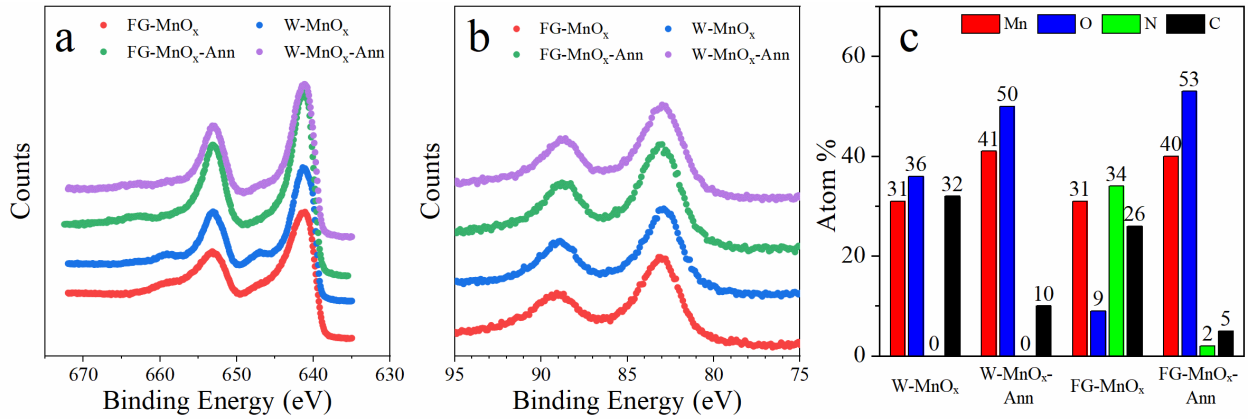

Figure 4-6: XPS results for W-MnO_x, FG-MnO_x, W-MnO_x-Ann, and FG-MnO_x-Ann films. (a) Mn 2p, (b) Mn 3s, (c) quantification results.

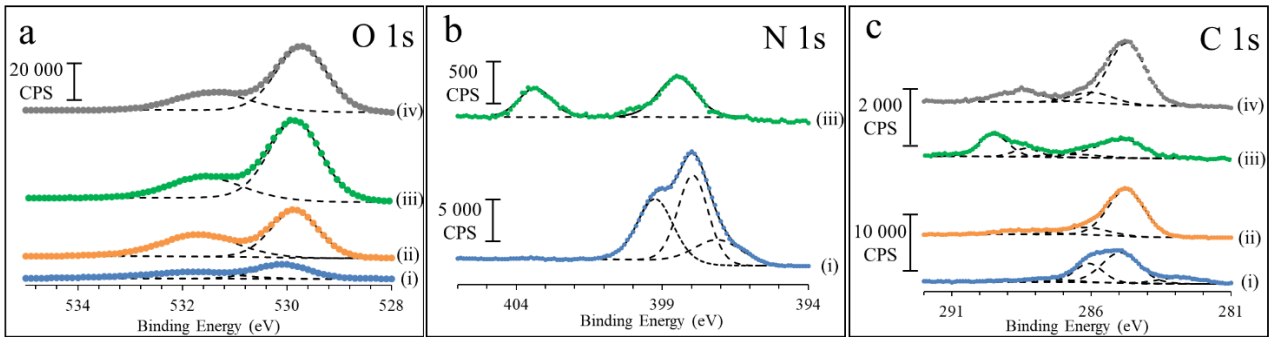

Figure 4-7: XPS results for W-MnO_x (i), FG-MnO_x (ii), W-MnO_x-Ann (iii), and FG-MnO_x-Ann (iv) films. (a) O 1s, (b) N 1s, (c) C 1s.

Table 4-1: XPS deconvolution results [52], [126]–[129]

	W-MnO_x		FG-MnO_x		W-MnO_x-Ann		FG-MnO_x-Ann		
	Position (eV)	% Area	Position (eV)	% Area	Position (eV)	% Area	Position (eV)	% Area	Assignment
O 1s	529.9	57.4	530.1	56.4	529.7	71.8	529.9	73.8	Mn-O
	531.7	41.8	531.8	39.6	531.4	28.2	531.6	26.2	C-O, Mn-OH
	533.6	0.8	533.4	4.0	-	-	-	-	C=O, H-O-H
N 1s	-	-	397.1	20.1	-	-	-	-	O-Mn-N
	-	-	397.9	43.9	-	-	-	-	Mn-N
	-	-	399.2	36.0	-	-	398.8	61.6	C-N
	-	-	-	-	-	-	403.6	38.4	NO_2^-
C 1s	-	-	282.9	14.2	-	-	-	-	Mn-C
	284.8	75.8	284.8	39.1	284.8	70.4	284.8	45.5	C-C, C-H
	286.2	14.5	285.9	40.7	286.1	13.6	286.7	9.9	C-N, C-O
	288.4	9.7	287.9	6.0	288.6	15.9	288.3	11.3	C=O
	-	-	-	-	-	-	289.5	33.4	CO_3^{-2}

4.3.5 Scanning Electron Microscopy

Plan view images of coated electrodes are shown in Figure 4-8. The uncoated GDL is composed of carbon particles 50 – 100 nm in diameter. All films were deposited to a thickness of 40 nm; this thickness was measured on a Si wafer placed beside the GDL in the reactor. The effect of deposition conditions on catalyst distribution was examined by coating electrodes under different conditions. Figure 4-8b shows a GDL coated with FG-MnO_x; this deposit coated the carbon particles, causing an increase in particle size. Coating the GDL with W-MnO_x at 50 °C (50C-W-MnO_x) results in a greater increase in particle size than for the FG-MnO_x deposition. Figure 4-8c shows that the 50C-W-MnO_x deposit is thick enough to cause fusing of the particles; reducing the effective surface area. The GDLs coated with W-MnO_x at 100 - 200 °C (100C-W-MnO_x, 150C-W-MnO_x, and 200C-W-MnO_x) are very similar to the 50C-W-MnO_x, with relatively large, fused particles. These observations are consistent with the saturation behavior of these films. The W-MnO_x depositions are not saturating and lead to excessive deposition on the surface where the precursor vapours have easy access. The FG-MnO_x depositions follow a saturating mechanism, allowing for more uniform deposition into the GDL porosity.

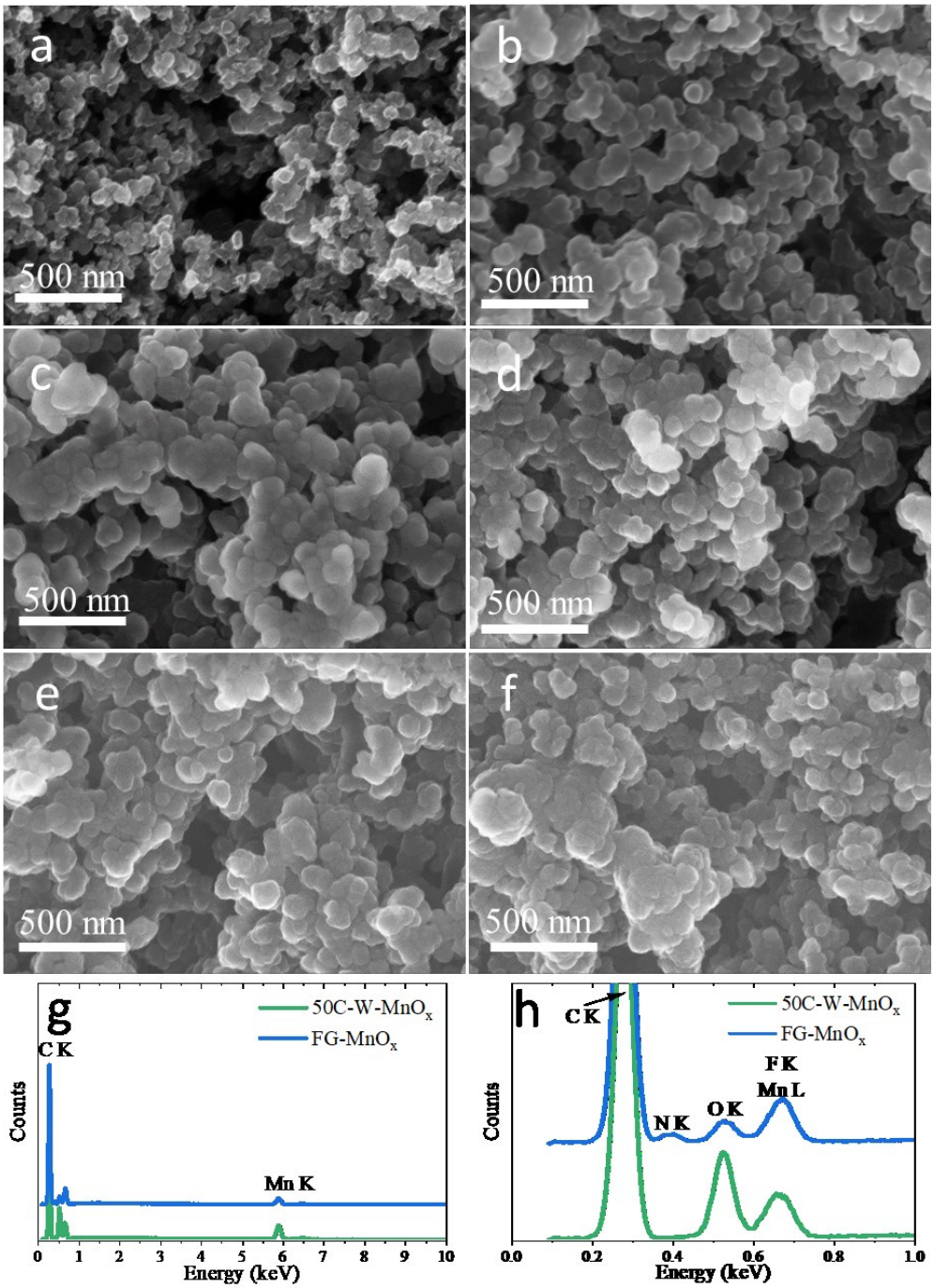

Figure 4-8: Plan view SEM secondary electron images of GDLs coated with ALD Mn oxide. (a) uncoated electrode, (b) FG-MnO_x, (c) 50C-W-MnO_x, (d) 100C-W-MnO_x, (e) 150C-W-MnO_x, (f) 200C-W-MnO_x. (g, h) EDX spectra from 50C-W-MnO_x and FG-MnO_x coated GDL.

EDX results from 50C-W-MnO_x and FG-MnO_x coated electrodes are shown in Figure 4-8g, h. The EDX spectra confirm the presence of Mn and O in both films. The FG-MnO_x film also contains some N. The large C peak is due to the C particles that compose the GDL. It should be

noted that the Mn L peak overlaps with the F K peak. Fluorine is present in the GDL as polytetrafluoroethylene (Teflon), which is used as a binder and to increase electrode hydrophobicity.

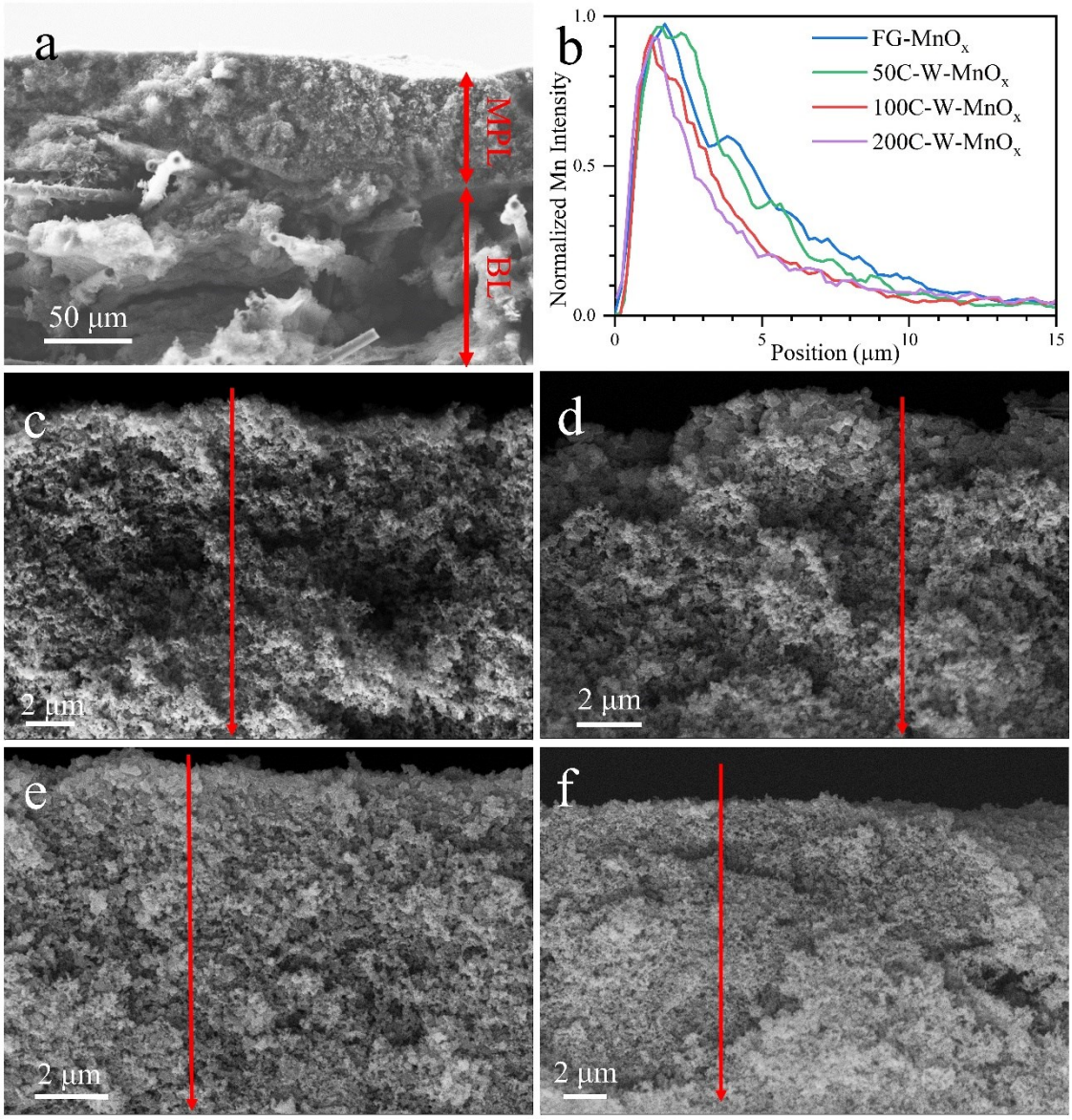

Figure 4-9: Cross sectional SEM results. (a) Structure of the GDL showing the microporous layer (MPL) and the backing layer (BL). (b) EDX line scan results from the regions shown in c, e, and g. (c) FG-MnO_x, (d) 50C-W-MnO_x, (e) 100C-W-MnO_x, (f) 200C-W-MnO_x.

Figure 4-9a shows a cross section view of the structure of the GDL; it is composed of the high surface area microporous layer (MPL) and the supportive backing layer (BL). The top surface of the MPL experiences direct exposure to the reactant gases during the ALD process and

experiences significant deposition. For Mn oxide to deposit within the porosity of the GDL, reactant gases need to diffuse into the porosity. The distribution of Mn oxide within the microporous layer of the GDL was investigated using cross sectional SEM and EDX line scans. EDX line scans were taken from the surface of the MPL into the bulk (Figure 4-9c, e, and g). Five line scans were taken from different areas on each sample, the results shown in Figure 4-9b are representative for each deposit. The three electrodes show similar distributions of Mn within the porosity of the GDL, with some minor differences. Mn is distributed deeper within the GDL for the FG-MnO_x sample relative to the W-MnO_x samples, as evident from the higher Mn intensity at depths between 5 – 10 μm. For these samples, the vast majority of Mn oxide is deposited within the top 5 – 10 μm of the MPL, which is still significantly deeper than deposits produced by other methods such as electrodeposition and spray coating. In order to reach regions deeper within the MPL, precursor molecules require time to diffuse into the porosity. With exceedingly long precursor doses, it may be possible to coat GDL through its entire depth. [131]

4.3.6 Electrochemical Measurements

Figure 4-10 shows the electrochemical behaviour of MnO_x films deposited on GDL. Additional electrochemical data is given in Figure 4-10. Cyclic voltammetry (CV) in Ar saturated 1 M KOH (Figure 4-10a) shows that annealed films undergo redox reactions. All annealed films had very similar voltammograms, with decreasing peak height with increasing deposition temperature. The differences in peak height are attributed to differences in MnO_x surface area. All annealed MnO_x films show a redox couple with anodic and cathodic peaks at 0.03 and -0.06 V vs. Hg/HgO, respectively. This redox couple is consistent with the $Mn^{3+} \leftrightarrow Mn^{4+}$ redox transition. [36], [50], [132]

The activity of the coated electrodes towards ORR was determined by LSV in 1 M KOH. LSV measurements in Ar-saturated 1 M KOH (Figure 4-10b) show very little reduction current. With the O_2-saturated electrolyte, the reduction current is vastly increased, confirming that this current is due to ORR. The performance of the electrodes was compared using the onset potential (V_{onset}). The onset potential is defined as the potential at which a current of -10 mA cm^{-2} is reached. The V_{onset} for the bare GDL is -260 mV. The as deposited films out-performed the uncoated electrode. After annealing V_{onset} was further improved; V_{onset} results are summarized in Table 4-2. Upon annealing, the carbon content of the films is reduced and the Mn oxidation state

increases; both of these changes improve the ORR activity of the electrode. Mn oxide has been widely studied as an ORR catalyst and is known to catalyze ORR via a 4-electron (or serial 2 x 2 electron) mechanism. Most carbon materials follow a kinetically inferior 2-electron mechanism, so removing carbon from the films improves V_{onset}. [9], [17] The Pt-C reference had a V_{onset} of -50 mV, which is 57 mV better than the best ALD sample (FG-MnO_x-Ann). The anomaly in the Pt-C LSV curve at -0.18 V is due to O_2 diffusion limitations. The stability of ALD MnO_x electrodes under ORR conditions was investigated using chronopotentiometry at a current density of 10 mA cm^{-2} (Figure 4-10c). FG-MnO_x-Ann and 50C-W-MnO_x-Ann both exhibit good stability after 12 h, with potential drops of 30 and 50 mV, respectively.

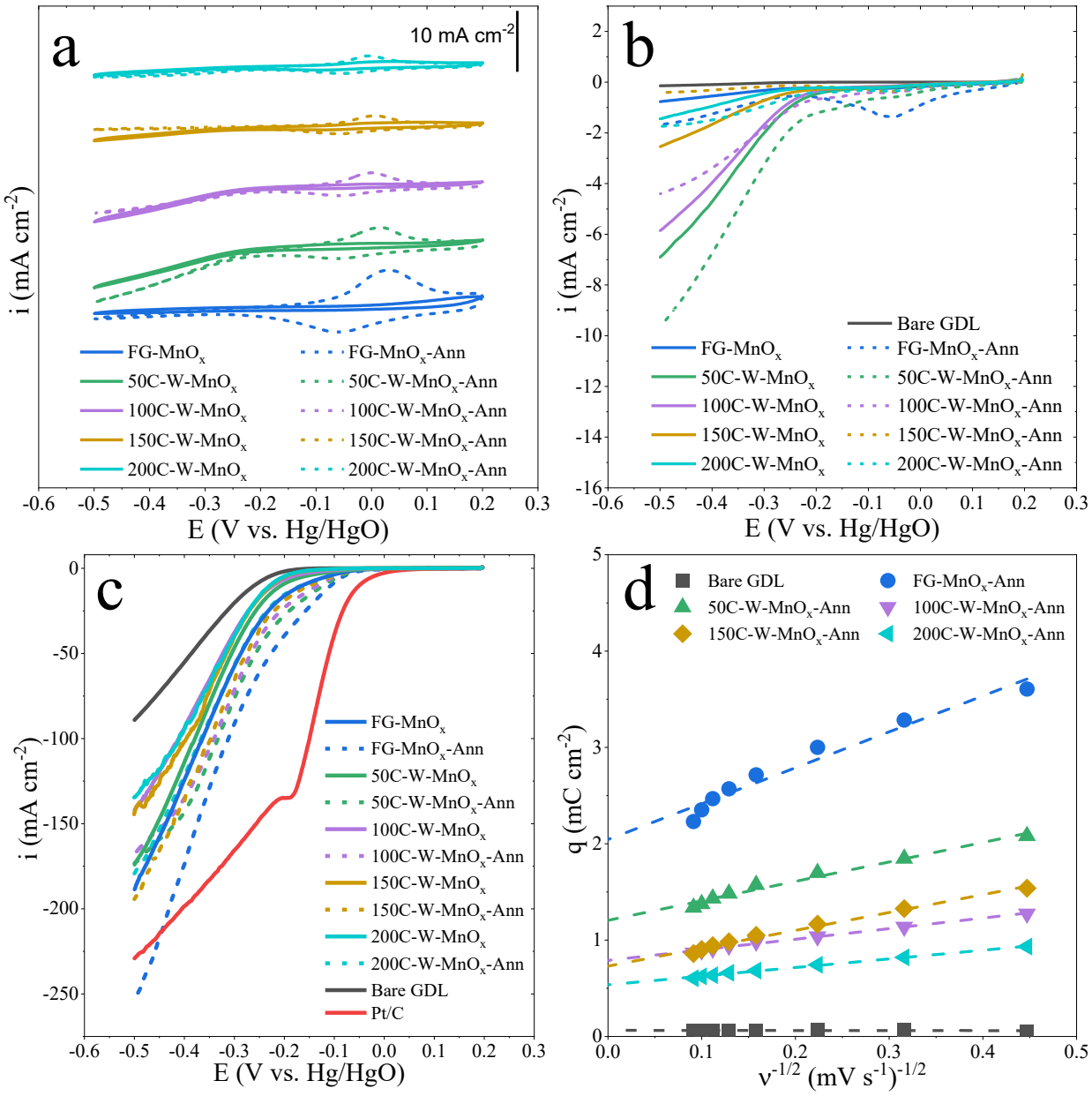

Figure 4-10: (a) Cyclic voltammograms performed at a scan rate of 20 mV s^{-1} in Ar saturated 1 M KOH. The vertical line in the upper right of the plot gives the current density scale. (b, c) Linear sweep voltammetry results performed at 5 mV s^{-1} in Ar and O_2 saturated 1 M KOH, respectively. (d) Double layer capacitance (C_{DL}) measurement results.

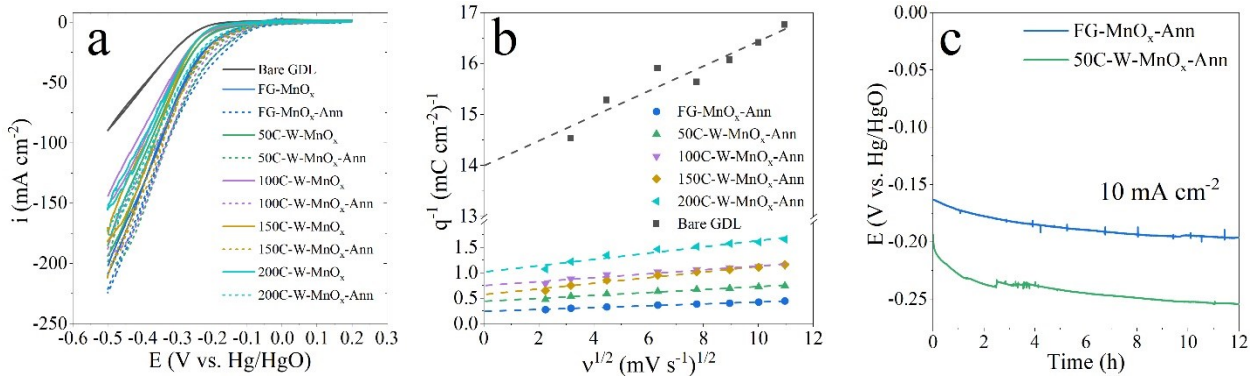

Figure 4-11: (A) CV results performed in O_2 saturated 1 M KOH (20mV s^{-1} scan rate). (B) q^{-1} vs. $\nu^{1/2}$ plot used for calculating total electrode capacitance. (c) Chronopotentiometry results in 1 M KOH at a current of 10 mA cm^{-2}.

To compare the surface areas of deposits, the double layer capacitances of the films was measured by performing cyclic voltammetry in the potential range of 0.1 – 0.2 V, as described by Lee *et al.* [111]. Using this method, the double layer capacitance (C_{DL}) can be differentiated from the pseudocapacitance (C_P). The double layer capacitance is directly related to the surface area and is used to compare the electrochemically active surface area of the electrodes. Double layer charge (q_{DL}) is determined by extrapolating ν to infinity on a plot of q vs. $\nu^{-1/2}$ (Figure 4-10d), where q is the charge of one half-cycle and ν is the scan speed. The total charge (q_T) is determined by extrapolating ν to 0 on a plot of q^{-1} vs. $\nu^{1/2}$ (Figure 4-11b). Capacitance can then be determined by dividing q by the potential window (0.1 V). Pseudocapacitance was determined by subtracting C_{DL} from C_T. The results of these measurements are shown in Table 4-2. The FG-MnO_x film has the highest double layer capacitance. The C_{DL} for W-MnO_x-Ann films showed a continuous decrease with increasing deposition temperature. This trend in surface area is the same trend as observed for V_{onset}. Since these films have nearly identical chemical compositions, any differences in catalytic activity can be attributed to overall surface area. The capacitance results also confirm the trend in catalyst distribution observed via EDX line scans. The differences in distribution for these films arises from the saturation behavior of the ALD process. The FG-MnO_x deposition is saturating and allows for better MnO_x distribution throughout the MPL porosity. On the other hand, the W-MnO_x depositions are not saturating and cause MnO_x to be concentrated near the surface of the electrode.

Table 4-2: Capacitance and V_{onset} measurement results

	q_T (mC cm^{-2})	q_{DL} (mC cm^{-2})	C_T (mF cm^{-2})	C_{DL} (mF cm^{-2})	C_P (mF cm^{-2})	V_{onset} (mV vs. Hg/HgO)
Bare GDL	0.06	0.06	0.6	0.6	0.0	-260
FG-MnO_x-Ann	4.09	2.04	40.8	20.4	20.4	-107
50C-W-MnO_x-Ann	2.26	1.20	22.6	12.0	10.6	-121
100C-W-MnO_x-Ann	1.33	0.79	13.2	7.8	5.4	-132
150C-W-MnO_x-Ann	1.74	0.73	17.4	7.3	10.1	-147
200C-W-MnO_x-Ann	0.98	0.54	9.8	5.4	4.4	-165

4.4 Conclusions

The deposition behaviour of the bis(ethylcyclopentadienyl) manganese ($(EtCp)_2Mn$) and H_2O system (W-MnO_x) has been investigated over a range of substrate temperatures (T_{sub}). The films are composed of MnO, with a large amount of C impurities. The reactions do not reach saturation at $T_{sub} \geq 60$ °C, indicating that these depositions do not follow an ALD mechanism. In an effort to generate saturating reactions, the use of a forming gas (FG- 95% N_2, 5% H_2) plasma step was investigated. Films prepared using the $(EtCp)_2Mn$ + FG + H_2O chemistry (FG-MnO_x) showed a saturated growth rate of 1.15 Å/cy in the T_{sub} range of 100 – 200 °C. The addition of a FG plasma step promotes precursor saturation by modifying the surface via N and/ or H radicals. The exact mechanism behind the change in deposition behaviour with the addition of the FG plasma step is currently under investigation. After annealing, FG-MnO_x and W-MnO_x films had nearly identical chemical composition as measured by XPS. Annealed films contained a combination of Mn^{2+} and Mn^{3+}.

Porous carbon oxygen reduction electrodes for metal-air batteries were coated with ALD MnO_x. Mn distribution through the porous electrodes was examined using SEM EDX line scans of electrode cross sections. The EDX line scans were consistent with double layer capacitance measurements, showing that FG-MnO_x electrodes achieved better coverage and surface area than W-MnO_x electrodes. The superior coverage of the FG-MnO_x film resulted in improved onset potential for the oxygen reduction reaction.

Chapter 5: High Performance Oxygen Reduction/ Evolution Electrodes for Zinc-Air Batteries Prepared by Atomic Layer Deposition of MnO_x

A version of this chapter has been published in the journal ACS Applied Energy Materials:

M. P. Clark, M. Xiong, K. Cadien, and D. G. Ivey, "High Performance Oxygen Reduction/ Evolution Electrodes for Zinc-Air Batteries Prepared by Atomic Layer Deposition of MnOx", *ACS Appl. Energy Mater.,* vol. 3, pp. 603-613, 2020

5.1 Introduction

As society reduces its reliance on fossil fuels and moves towards wide-spread implementation of renewable energy technologies, there is the need for safe and inexpensive energy storage solutions. Due to the intermittent nature of wind and solar power, energy needs to be stored during periods of high output and released when it is needed. Zinc-air batteries (ZABs) provide high energy density and are composed of safe and inexpensive materials, making them well suited for grid-scale energy storage. [17], [19]

ZABs are composed of a metallic Zn electrode and a porous carbon air electrode, with a typical electrolyte of 6 M KOH and ~0.25 M Zn^{2+} (e.g., ZnO, $ZnCl_2$ or $Zn(CH_3COO)_2$). The air electrode, also referred to as the gas diffusion layer (GDL), is composed of a high surface area microporous layer (MPL) and a backing layer that provides structural support. The MPL is composed of carbon nanoparticles bound together with polytetrafluoroethylene (PTFE). PTFE is present in both the MPL and the backing layer and increases the hydrophobicity of the GDL. The porosity of the MPL increases the surface area available for reaction and enables oxygen diffusion into the cell. Equation (1) shows the oxygen reduction reaction (ORR), which is the discharge reaction at the air electrode. The oxygen evolution reaction (OER) is the charge reaction, and is Equation (1) in reverse (right to left). [17], [19], [60], [133]

$$O_2 + 2H_2O + 4e^- \leftrightarrow 4OH^- \quad (1)$$

ORR relies on three-phase boundaries between the electrolyte, oxygen and catalyst. [19], [133] The GDL must be hydrophobic enough to prevent electrolyte flooding through the catalyst layer, which can limit oxygen access. However, if the GDL is too hydrophobic, the electrolyte is unable to wet the surface. The flooding problem can be minimized by using a horizontal configuration for the ORR electrode, and/ or by distributing catalysts throughout the thickness of

the GDL. [27], [31], [32] Figure 5-1 shows a schematic of how catalyst can be distributed on the GDL and how flooding affects three phase boundary area. Figure 5-1a shows catalyst loaded on the surface of the GDL; this loading is typical of techniques such as electrodeposition and spray coating. If the GDL begins to flood (Figure 5-1b), electrolyte will soak past the catalyst layer eliminating three-phase boundaries between electrolyte, catalyst and air. Figure 5-1c shows a structure where catalyst is distributed throughout the MPL. If flooding occurs for this structure (Figure 5-1Figure 5-d), three-phase boundaries are maintained. By distributing catalyst through the MPL, the detrimental effects of electrolyte flooding can be minimized.

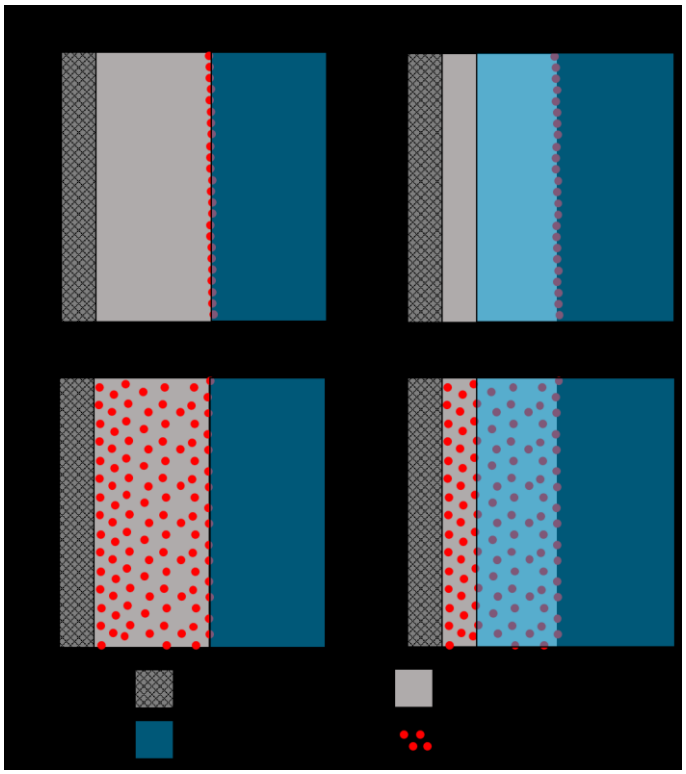

Figure 5-1: GDL schematic showing catalyst distribution and the effect of electrolyte flooding. (a, b) Catalyst loaded on the surface of the GDL: (a) before flooding, (b) after flooding. (c, d) Catalyst distributed throughout the MPL: (c) before flooding, (d) after flooding.

Currently, widespread application of ZABs is hindered by their low discharge-charge efficiency and short cycle life. [17], [19], [60] The air electrode is exposed to large potential changes during charge and discharge cycles. These potential changes, in conjunction with the pH 14 electrolyte, produce harsh conditions under which very few catalysts are stable. Using separate electrodes for the charge and discharge reactions limits the potential window to which each electrode is exposed, greatly improving battery cycle life. In addition to improved cyclability, a tri-electrode

configuration allows for the ORR and OER electrodes to be independently optimized for their individual reaction, thereby improving battery efficiency. For example, high surface area carbon based electrodes are very good for ORR but suffer from dissolution and mechanical damage during OER. Ni foam is much better suited for OER electrodes, since the large porosity allows O_2 bubbles to easily escape and the native NiO layer provides OER activity. [29]–[31], [134], [135]

There has been much effort in recent years in the development of inexpensive, efficient, and stable catalysts for ORR and OER. Transition metal oxide catalysts have been demonstrated as promising alternatives to highly active, but expensive noble metals. Of the transition metal oxides examined as metal-air battery catalysts, Co oxide and Mn oxide (CoO_x and MnO_x) have received the most attention because of their cost, activity, and stability. Most transition metals form a range of oxides with varying stoichiometry and crystal structure; catalytic activity depends on the phase type and morphology. Because of their poor conductivity, transition metal oxide catalysts need to be effectively distributed on/ with conductive supports. Catalysts with feature sizes on the order of nanometers have been shown to improve performance because of the reduced path length for electron conduction and the increase in specific surface area. Electronic conductivity and catalyst surface area can be enhanced through the development of nanostructured oxides in combination with conductive carbon-based supports. [58], [60], [136]–[139]

Atomic layer deposition (ALD) is a thin film technique that is capable of depositing uniform thin films of a variety of materials. [11] A number of ALD films have been investigated for their activity towards ORR and OER, with many utilizing high surface area supports. [12], [49], [76], [84], [120], [123], [140]–[143] Li *et al.* prepared a ZAB using carbon nanotubes coated with ALD Co_9S_8 as a bifunctional catalyst. Full cell testing at 10 mA cm^{-2} showed excellent catalyst stability over 100 h with charge and discharge potentials of 2.0 and 1.25 V, respectively. Their work demonstrates the excellent performance of ALD films in a full cell ZAB configuration. [123]

In this work, oxygen reduction electrodes are prepared by depositing MnO_x (in some cases CoO_x as well) directly onto GDL using ALD. The GDL structure provides a conductive, high surface area support for the conformal catalyst layer. ALD allows MnO_x to be deposited within the bulk

of the microporous layer, increasing catalyst surface area, conductivity, and oxygen access for ORR. [144] Horizontal ZABs are assembled with separate ORR and OER electrodes (tri-electrode cell) as described previously [27], as well as in a bifunctional configuration. Full cell battery tests show excellent performance and demonstrate the importance of maintaining three phase boundaries.

5.2 Experimental

ALD films were deposited using a Kurt J. Lesker ALD 150LX system at a pressure of ~1 Torr. The ALD system is equipped with an inductively coupled plasma system, operated at a power of 600 W. Ultrahigh purity Ar (99.999%) was used as the carrier gas. Bis(ethylcyclopentadienyl) Mn ($(EtCp)_2Mn$) was used as the Mn precursor and was maintained at a temperature of 80 °C. To prevent precursor condensation, the valve and line used to transport precursor vapors to the reactor were maintained at 100 and 110 °C, respectively. The reactants were forming gas (FG-95% N_2, 5% H_2), oxygen (99.999%) and distilled water. CoO_x was deposited using cyclopentadienyl cobalt dicarbonyl ($(Cp)Co(CO)_2$) as the Co precursor and oxygen plasma as the reactant. $(Cp)Co(CO)_2$ was held at 70 °C, while the valve and line were held at 95 °C and 110 °C, respectively. CoO_x was deposited at a substrate temperature of 100 °C and a timing scheme of 0.02/ 10/ 20/ 10 s (Co dose/ purge/ O_2 plasma/ purge) for 200 cycles (~15 nm). The electrodes were Sigracet 35 BC GDL (Fuel Cell Store). Prior to deposition, electrodes were treated with 60 s of O_2 plasma in order to clean the surface and promote film nucleation. MnO_x films were deposited to a thickness of 40 nm, measured using in-situ ellipsometry (Woollam M-2000DI) on a Si wafer placed beside the electrodes in the reactor. The mass loading of MnO_x on the electrodes was ~50 μg cm^{-2}.

MnO_x films were prepared using two deposition chemistries; detailed analysis on deposition behaviour has been reported previously. [144] Films deposited using FG plasma followed a pulsing sequence of $(EtCp)_2Mn$ dose/ purge/ FG plasma/ H_2O dose/ purge; these films are referred to as FG-MnO_x. The second deposition chemistry utilized an O_2 plasma, following a modified version of the deposition reported in our previous work. [144] The supercycle for O_2-MnO_x films was 5 cycles of $(EtCp)_2Mn$/ purge/ H_2O dose/ purge followed by 60 s of O_2 plasma. These films are designated as O_2-MnO_x. To improve the bifunctional activity of ALD MnO_x, CoO_x was deposited directly on top of FG-MnO_x; this sample is denoted as FG-MnO_x + CoO_x.

Deposited films were annealed at 300 °C for 30 min in air. As deposited films (not annealed) have the postfix "AD" (e.g., O_2-MnO_x: AD). Annealing was performed in order to partially oxidize and crystallize the ALD films. Annealed films have no postfix designation (e.g., O_2-MnO_x).

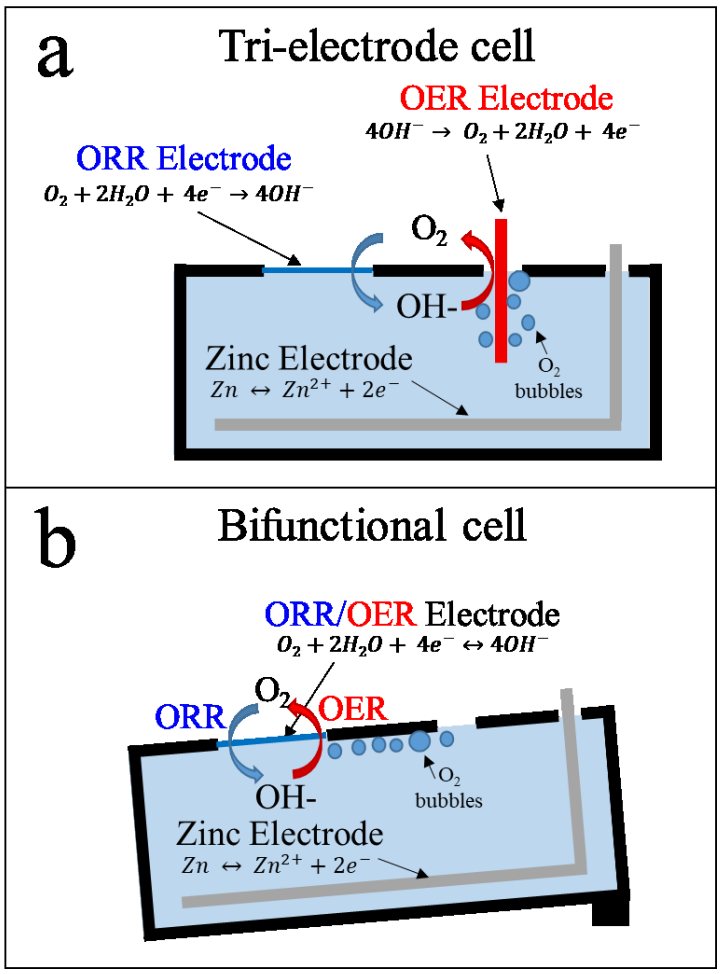

Figure 5-2: Zn-air battery schematics for full cell tests. (a) Tri-electrode configuration and (b) bifunctional configuration. The bifunctional cell is tilted to allow O_2 bubbles to escape during OER.

Electrochemical measurements were performed using Biologic SP-300 and VSP-300 potentiostats. Half cell tests were performed in 1 M KOH using a Pt coil counter electrode and a Hg/HgO reference electrode (0.098 V vs. SHE). Chronopotentiometry was performed at a current of -20 mA cm^{-2} in O_2-saturated 1 M KOH, utilizing a graphite counter electrode. All half cell measurements were IR-corrected. Full cell experiments were conducted using an electrolyte of 6 M KOH + 0.25 M ZnO, with the horizontal configuration reported previously. [27] Cell

schematics for tri-electrode and bifunctional ZAB tests are shown in Figure 5-2. Electrochemical impedance spectroscopy (EIS) measurements were done at a cell potential of 1.2 V with an amplitude of 10 mV within the frequency range of 100 mHz to 1 MHz. The OER electrode used in tri-electrode cyclability tests was a Co-Fe alloy electrodeposited onto Ni foam. Detailed descriptions of the Co-Fe deposition have been reported previously. [27], [112], [113] Briefly, Co-Fe was cathodically electrodeposited onto Ni foam pieces (4.2 cm^2) at a constant current of 300 mA under ultrasonic agitation. The electrolyte for Co-Fe deposition contained 0.1 M $CoSO_4$, 0.1 M $FeSO_4$, 0.2 M sodium citrate, 0.2 M boric acid, 0.05 M L-ascorbic acid and 400 mg L^{-1} of sodium dodecyl sulfate. Tri-electrode cycling tests were conducted at a current density of 20 mA cm^{-2} for 200 cycles with a discharge/ rest/ charge/ rest timing of 10/ 5/ 10/ 5 min. Bifunctional cycling, using the ALD catalysts for both ORR and OER, was also done and was performed at 10 mA cm^{-2} for 100 cycles, following the same timing scheme as the tri-electrode tests. A baseline catalyst, consisting of 40% Pt and 20% Ru on carbon black (Alfa Aesar), was used for comparison. The Pt/Ru-C powder was mixed with PTFE and Nafion binders and spray coated onto pieces of GDL with a loading of ~600 μg cm^{-2} (240 μg(Pt) cm^{-2} and 120 μg(Ru) cm^{-2}). Zn foil (99.98%, Alfa Aeasar - 0.5 mm thick) was used as the Zn electrode. Charge-discharge efficiency (ε) was calculated by dividing the discharge potential by the charge potential.

A Zeiss Sigma scanning electron microscope (SEM) was used for imaging and energy dispersive x-ray (EDX) analysis. Imaging was done at either 10 kV or 20 kV, while EDX analysis was done at 20 kV. Transmission electron microscopy (TEM) and scanning transmission electron microscopy (STEM) analysis were conducted using a JEOL JEM-ARM200CF at an accelerating voltage of 200 kV. TEM/ STEM samples were prepared by scraping the ALD coating from the microporous layer of the GDL. The residue was sonicated in ethanol and dropped onto a lacey carbon TEM grid. X-ray photoelectron spectroscopy (XPS) analysis was performed using a Kratos AXIS Supra instrument with a monochromatic Al-K_α x-ray source and a pass energy of 20 eV. Prior to XPS analysis, samples were sputter cleaned using an Ar ion gun for 15 s with an energy of 500 eV to remove contamination and surface oxides due to exposure to the atmosphere. XPS spectra were calibrated using the C 1s C-H peak at 284.8 eV.

5.3 Results & Discussion

5.3.1 Electrode Characterization

Images of O_2-MnO_x, FG-MnO_x and FG-MnO_x + CoO_x coated electrodes are shown in Figure 5-3. A plan view image of bare GDL is shown in Figure 5-3a. Comparing the coated and uncoated electrodes (Figure 5-3a, b, c and d) clearly shows that the ALD coating increases the particle size of the GDL, confirming the presence of a uniform catalyst layer. Figure 5-3e presents representative EDX line scan results taken from GDL cross sections, showing the Mn distribution from the surface of the MPL into the bulk. Figure 5-3f shows an example of a GDL cross section used for EDX line scans. Because of the topography associated with the GDL cross section surfaces, there can be some variability in the measured Mn distribution. Therefore, multiple line scans were taken from different regions of the cross-sections and compared. Results were considered to be representative if three or more EDX profiles overlapped, i.e., were essentially the same. Mn content is highest near the surface, with a gradual drop in intensity into the bulk of the porous structure. During deposition, precursor molecules can readily access the top surface of the electrode, leading to significant deposition. For deposition to occur within the porosity of the electrode, precursor molecules need to diffuse through the porous structure, which reduces the amount of material deposited deeper within the electrode. The EDX line scan results show that the FG-MnO_x deposition has a better Mn distribution through the GDL depth than O_2-MnO_x. The FG-MnO_x deposition follows a true saturating ALD mechanism, which was confirmed in our previous work with depositions on Si wafers. It is assumed that the saturation behaviour is not greatly affected by the underlying substrate. Once a few monolayers of material have been deposited, the substrate surface is effectively replaced by MnO_x and the deposition behaviour of MnO_x on MnO_x is believed to be independent of the underlying substrate. Deposition reactions for O_2-MnO_x, however, do not exhibit the same saturating behaviour characteristic of ALD processes. [144] A more accurate description for the O_2-MnO_x process would be pulsed chemical vapour deposition. In the interest of simplicity and conciseness, the O_2-MnO_x process will be referred to as ALD in this paper. The differing saturation behaviour of the two types of depositions results in improved deposition within the depth of the MPL for the FG-MnO_x films. This effect is further demonstrated by the Co distribution in the FG-MnO_x + CoO_x film. The CoO_x deposition is not saturating, resulting in poorer penetration into the MPL. [145]

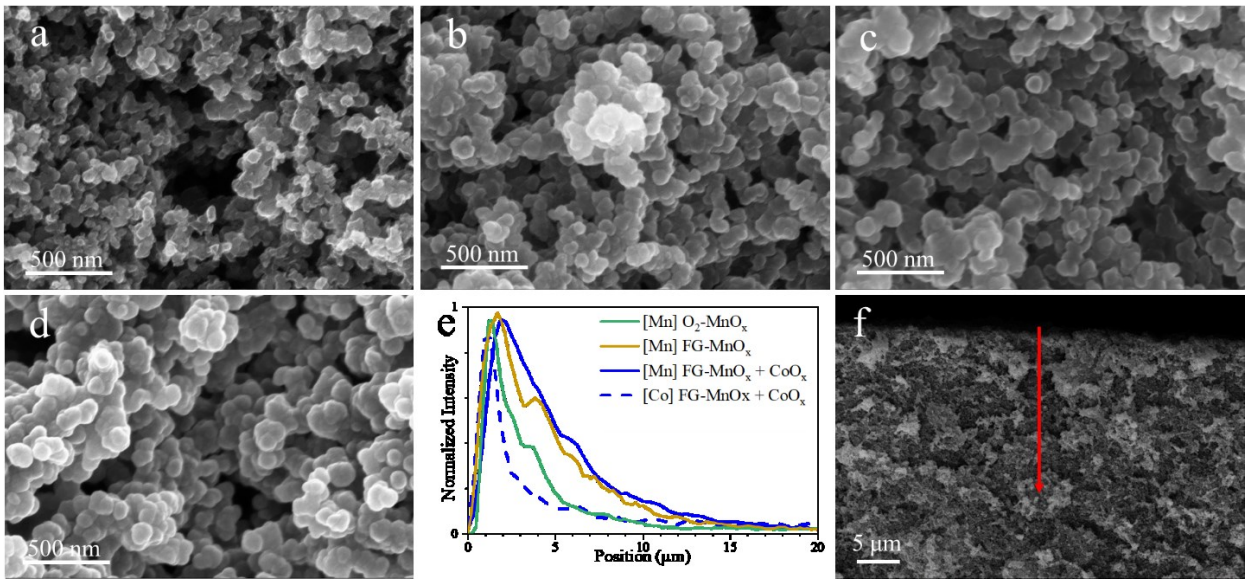

Figure 5-3: (a-d) Plan view SEM SE images of (a) bare GDL, (b) O_2-MnO_x, (c) FG-MnO_x and (d) FG-MnO_x + CoO_x samples. (e) EDX line scan results from GDL cross sections. (f) Cross-section image of O_2-MnO_x on GDL; the red arrow indicates where the EDX line scan was taken. Plan view images (a-d) were taken at 10 kV; cross section images and EDX line scans were taken at 20 kV.

Coated GDL particles were examined using STEM EDX mapping and electron diffraction. Results for O_2-MnO_x are shown in Figure 5-4. TEM/ STEM results for FG-MnO_x and FG-MnO_x + CoO_x are shown in Figure 5-5 and Figure 5-6, respectively. Mapping results for all three films show that the GDL particles received a conformal coating of MnO_x (and CoO_x). Note that for the FG-MnO_x + CoO_x sample, separate unmixed layers of MnO_x and CoO_x are clearly visible (Figure 5-6g). Particle to particle variation in film thickness was observed. Because of the nature of the TEM sample preparation process, the original location within the GDL depth of the imaged particles is not known. However, it is reasonable to assume that particles with thicker MnO_x films originated from regions closer to the surface while thinner MnO_x films are on particles from deeper within the MPL. Film thickness varied significantly for the O_2-MnO_x sample. Many observed particles had no coating, while some particles had a film thickness of up to 35 nm. The FG-MnO_x sample displayed much less variation in film thickness. Most particles had a film thickness of 10 – 25 nm; very few particles with no coating were observed. The variation in film thickness is consistent with the SEM EDX line scan results. The O_2-MnO_x deposit is concentrated near the surface of the GDL, so that the surface particles have thicker films, while most particles within the bulk of the GDL substrate received little to no deposition.

The FG-MnO_x deposition is much more uniform through the GDL, resulting in more consistent film thickness from particle to particle in the TEM. For the FG-MnO_x + CoO_x sample, most particles had no CoO_x layer present. When CoO_x is detected on a GDL particle, it is typically present in relatively large quantities. As discussed above, CoO_x is not deposited via ALD, but rather by pulsed chemical vapour deposition. The non-saturating reactions result in significant deposition on the surface of the MPL, but little deposition within the porosity.

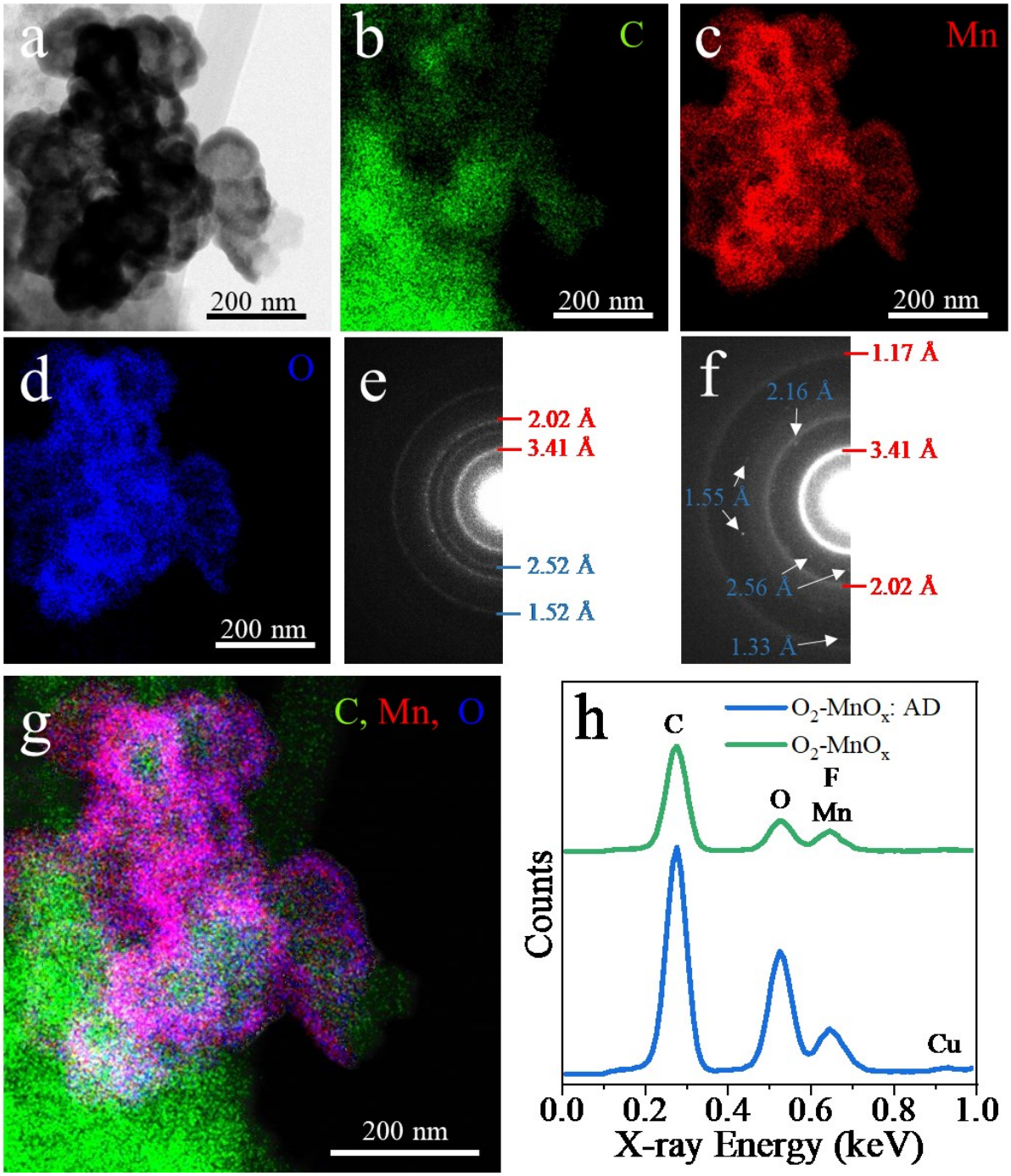

Figure 5-4: STEM results from O_2-MnO_x on GDL. (a) STEM bright field (BF) image. (b, c, d, g) STEM EDX maps for the region shown in (a). (b) C map, (c) Mn map, (d) O map and (g) overlain mapping results. (e) SAD pattern from O_2-MnO_x: AD. (f) SAD pattern from O_2-MnO_x after annealing. Diffracted intensity associated with GDL is marked in red, while the O_2-MnO_x film is marked in blue. (h) STEM EDX spectra from O_2-MnO_x films on GDL.

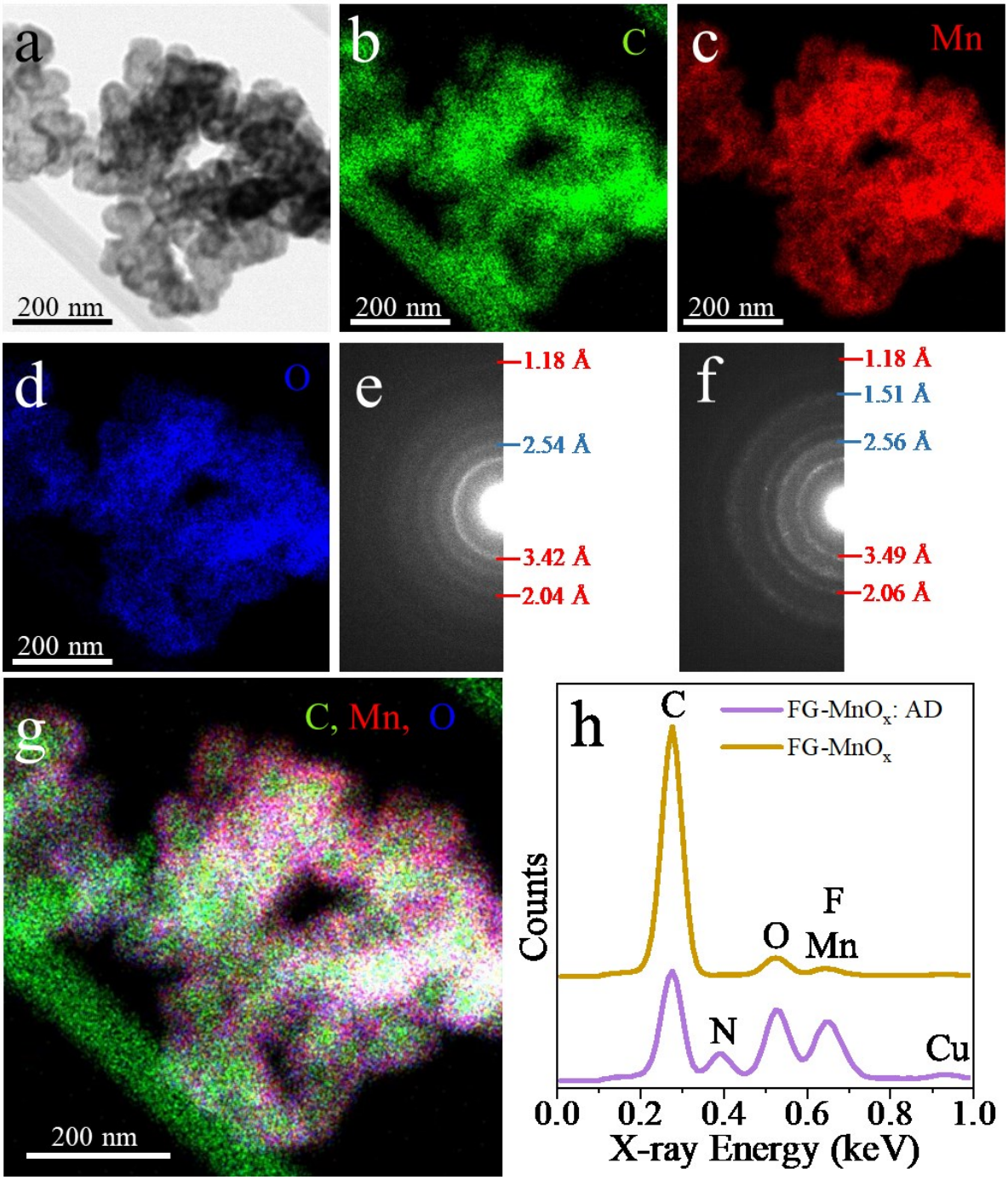

Figure 5-5: STEM results for FG-MnO_x on GDL. (a) STEM BF image. (b, c, d, g) STEM EDX maps for the region shown in (a). (b) C map, (c) Mn map, (d) O map and (g) overlain mapping results. (e) SAD pattern from FG-MnO_x: AD. (f) SAD pattern from FG-MnO_x after annealing. Diffracted intensity associated with GDL is marked in red, while diffracted intensity from the FG-MnO_x film is marked in blue. (h) STEM EDX spectra from FG-MnO_x film on GDL.

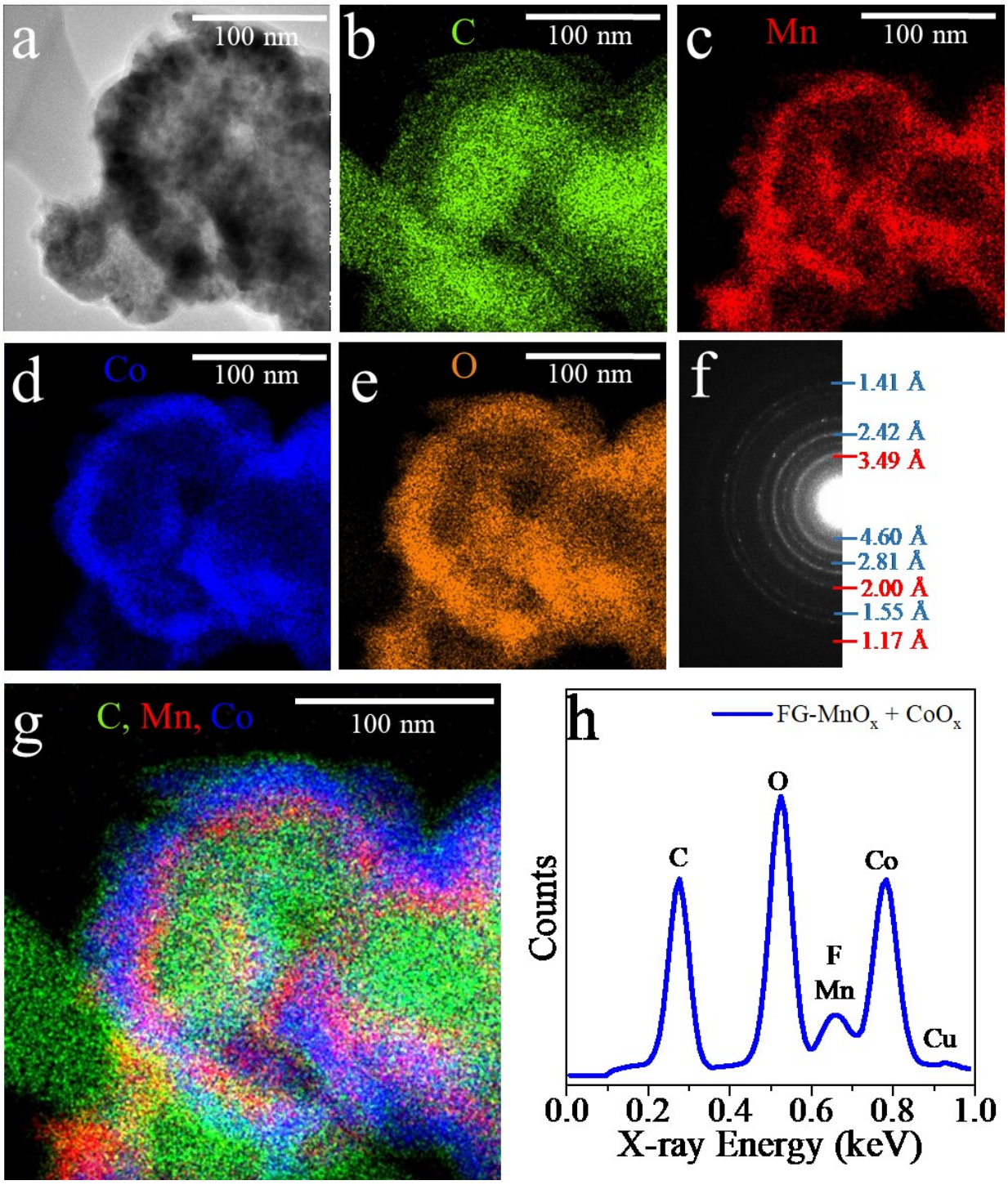

Figure 5-6: STEM results for FG-MnO_x + CoO_x on GDL after annealing. (a) STEM BF image. (b, c, d, g) STEM EDX maps for the region shown in (a). (b) C map, (c) Mn map, (d) Co, (e) O map and (g) overlain mapping results. (f) SAD pattern from FG-MnO_x + CoO_x. Diffracted intensity associated with GDL is marked in red, while the diffracted intensity for the FG-MnO_x + CoO_x film is marked in blue. (h) STEM EDX spectrum from the overall area.

EDX spectra from O_2-MnO_x coated GDL particles show the presence of C, Mn, F and O (Figure 5-4h); the small Cu peak is from the TEM grid. The large C is peak is due to the GDL particles. The GDL contains F from the PTFE binder and the F K peak overlaps with the Mn L peak. After annealing, the composition of O_2-MnO_x appears unchanged. The as deposited FG-MnO_x film contains a significant amount of N, in addition to C, F, Mn and O (Figure 5-5h). The N peak is absent after annealing, suggesting that N is liberated from the film.

The selected area diffraction (SAD) patterns for all MnO_x films are dominated by contributions from the GDL particles at ~3.48, 2.02 and 1.17 Å (Figure 5-4e and f, Figure 5-5e and f). Before annealing, O_2-MnO_x: AD exhibits weak and diffuse rings at 2.52 and 1.52 Å (Figure 5-4e), indicating that the film has an amorphous structure. After annealing, a number of faint spots appear in the diffraction pattern indicative of nanocrystalline grains (Figure 5-4f). These spots correspond to planar spacings of 2.56, 2.16, 1.55, and 1.33 Å, which is consistent with a number of MnO_x crystal structures including Mn_3O_4 and MnO. The FG-MnO_x: AD sample has a single weakly diffracted ring at 2.54 Å, while the FG-MnO_x sample shows diffuse rings at 1.51 and 2.56 Å. These rings are consistent with the most intense rings observed for the O_2-MnO_x samples. However, the diffraction patterns from the FG-MnO_x samples do not contain enough information to confidently identify the phase or phases present, as the rings match with a large number of MnN_x, MnO_xN_y, and MnO_x crystal structures. The SAD pattern from annealed FG-MnO_x + CoO_x (Figure 5-6f) shows rings at 4.60, 2.81, 2.42, 1.55, and 1.41 Å. This pattern can be indexed to both cubic and tetragonal M_3O_4 (M = Mn or Co) structures. The overlapping layers of CoO_x and MnO_x (Figure 5-6g) results in a diffraction pattern that contains intensity from both layers. Because Mn and Co have similar ionic radii, separate Mn_3O_4 and Co_3O_4 diffraction rings cannot be distinguished from the SAD pattern shown in Figure 5-6f. All diffraction results are summarized in Table 5-1. Diffraction data for relevant crystal structures are shown in Table 5-2.

Table 5-1: Summary of TEM electron diffraction results for cycled/ uncycled electrodes

Uncycled O_2-MnO_x	Uncycled FG-MnO_x	Uncycled FG-MnO_x + CoO_x	Tri-Electrode FG-MnO_x	Tri-Electrode FG-MnO_x + CoO_x	Bifunctional FG-MnO_x + CoO_x	M_3O_4 Tetragonal- I41/amd		M_3O_4 Cubic- Fd-3m	
d (Å)	d (Å)	d (Å)	d (Å)	d (Å)	d (Å)	d (Å)	hkl	d (Å)	hkl
		4.60		4.67	4.78	4.87 - 4.91	(101)	4.67 - 4.86	(111)
3.41	3.49	3.49	3.36	3.50	3.56				
		2.81	3.00	2.82	2.96	3.04 - 3.08 2.86 - 2.89	(112) (200)	2.86 - 2.98	(220)
2.56	2.56	2.42	2.48	2.41	2.54	2.47 - 2.49	(211)	2.44 - 2.54	(311)
2.16			2.15	2.02	2.14	2.02 - 2.05	(220)	2.02 - 2.10	(400)
2.02	2.06	2.00							
				1.66	1.59	1.62 - 1.64	(303)	1.65 - 1.72	(422)
1.55	1.51	1.55	1.51	1.53	1.48	1.52 - 1.54	(224)	1.56 - 1.62	(511)
		1.41		1.42		1.43 - 1.47	(400)	1.43 - 1.49	(440)

Values highlighted in red are attributed to GDL.

The range of d values given for cubic and tetragonal M_3O_4 are the largest and smallest values for M_3O_4 structures where M = Mn, Co, and/ or Zn.

Table 5-2: Diffraction data for relevant M_3O_4 structures

$ZnMn_2O_4$			Mn_3O_4			Mn_3O_4			$CoMn_2O_4$			$MnCo_2O_4$			Co_3O_4			$Zn_{0.58}Co_{2.42}O_4$		
PDF#24-1133			PDF#71-6262			PDF#13-0162			PDF#77-0471			PDF#23-1237			PDF#43-1003			PDF#81-2295		
Tetragonal- I41/amd			Tetragonal- I41/amd			Cubic- Fd-3m			Tetragonal- I41/amd			Cubic- Fd-3m			Cubic- Fd-3m			Cubic- Fd-3m		
a = 5.720 Å c = 9.245 Å			a = 5.757 Å c = 9.424 Å			a = 8.42 Å			a = 5.784 Å c = 9.091 Å			a = 8.269 Å			a = 8.084 Å			a = 8.088 Å		
d (Å)	I	hkl	d (Å)	I	hkl	d (Å)	I	hkl	d (Å)	I	hkl	d (Å)	I	hkl	d (Å)	I	hkl	d (Å)	I	hkl
4.870	10	(101)	4.913	27	(101)	4.860	26	(111)	4.880	24	(101)	4.780	14	(111)	4.667	16	(111)	4.670	13	(111)
3.047	45	(112)	3.081	38	(112)				3.040	36	(112)									
2.862	19	(200)	2.879	16	(200)	2.980	42	(220)	2.892	15	(200)	2.925	35	(220)	2.858	33	(220)	2.860	36	(220)
2.715	65	(103)	2.758	76	(103)				2.684	58	(103)									
2.466	100	(211)	2.484	100	(211)	2.540	98	(311)	2.488	100	(211)	2.493	100	(311)	2.437	100	(311)	2.439	100	(311)
2.432	12	(202)	2.457	15	(202)	2.430	10	(222)	2.440	13	(202)									
2.311	10	(004)	2.356	18	(004)				2.273	14	(004)	2.388	10	(222)	2.334	9	(222)	2.335	8	(222)
2.022	16	(220)	2.036	20	(220)	2.100	59	(400)	2.045	19	(220)	2.067	20	(400)	2.021	20	(400)	2.022	16	(400)
1.798	7	(204)	1.823	6	(204)				1.787	5	(204)									
1.760	15	(105)	1.791	22	(105)				1.735	18	(105)									
1.684	12	(312)	1.698	9	(312)	1.718	29	(422)	1.697	8	(312)	1.687	9	(422)	1.650	9	(422)	1.651	9	(422)
1.621	9	(303)	1.638	8	(303)				1.627	7	(303)									
1.564	25	(321)	1.574	28	(321)	1.620	77	(511)	1.580	23	(321)	1.591	30	(511)	1.556	21	(511)	1.557	29	(511)
1.522	40	(224)	1.540	50	(224)	1.488	100	(440)	1.520	39	(224)	1.461	35	(440)	1.429	38	(440)	1.430	31	(440)
1.439	4	(116)	1.465	2	(116)				1.421	2	(116)									
1.430	17	(400)	1.439	18	(400)/ (314)				1.466	1	(400)/ (314)									

Diffraction data taken from: ICSD (2014), Eggenstein-Leopoldshafen, Germany (Accessed January 2019)

XPS results for annealed films are shown in Figure 5-7; XPS results for as deposited films are shown in Figure 5-8. The Mn oxidation state was determined by using the splitting of the Mn 3s orbital and the separation between the Mn $2p_{1/2}$ peak and its satellite. [52] The Mn oxidation states for O_2-MnO_x: AD and O_2-MnO_x are approximately +2.6 and +2.8, respectively. The oxidation states of Mn_3O_4 (+2.67) and Mn_2O_3 (+3) are within the experimental error for the XPS measurements. The measured oxidation states in combination with TEM diffraction indicate that O_2-MnO_x is likely Mn_3O_4. Since cubic Mn_3O_4 is thermodynamically unstable at temperatures below 1160 °C, O_2-MnO_x was indexed to hausmannite. Tetragonal Mn_3O_4 (hausmannite) (PDF#071-6262) and γ-Mn_2O_3 are isostructural and it is possible that the O_2-MnO_x: AD and O_2-MnO_x films contain some combination of these phases. [146], [147] XPS quantification results (Figure 5-7d) show a small amount of carbon for the O_2-MnO_x films. The origin of this carbon is not certain; it is possible that carbon is present in the film or that the carbon signal originated from the GDL substrate. The FG-MnO_x: AD and FG-MnO_x films have Mn oxidation states of +2.0 and +2.4, respectively, which suggests that FG-MnO_x is deposited as MnO and further oxidizes on annealing. The FG-MnO_x: AD film contains a significant amount of C and N impurities. A large fraction of the C and almost all of the N are removed upon annealing. The annealed FG-MnO_x sample has an oxidation state of +2.4 and d spacings of 1.51 and 2.56 Å from the electron diffraction pattern (Figure 5-5f), suggesting that MnO_x is present as tetragonal Mn_3O_4. The Co 2p spectra are in agreement with the FG-MnO_x + CoO_x TEM analysis; i.e., CoO_x is present as Co_3O_4 (+2.67 for Co). [148] Due to fact that CoO_x coats the MnO_x layer and the surface sensitivity of XPS, the quantification results for FG-MnO_x + CoO_x show very little Mn content.

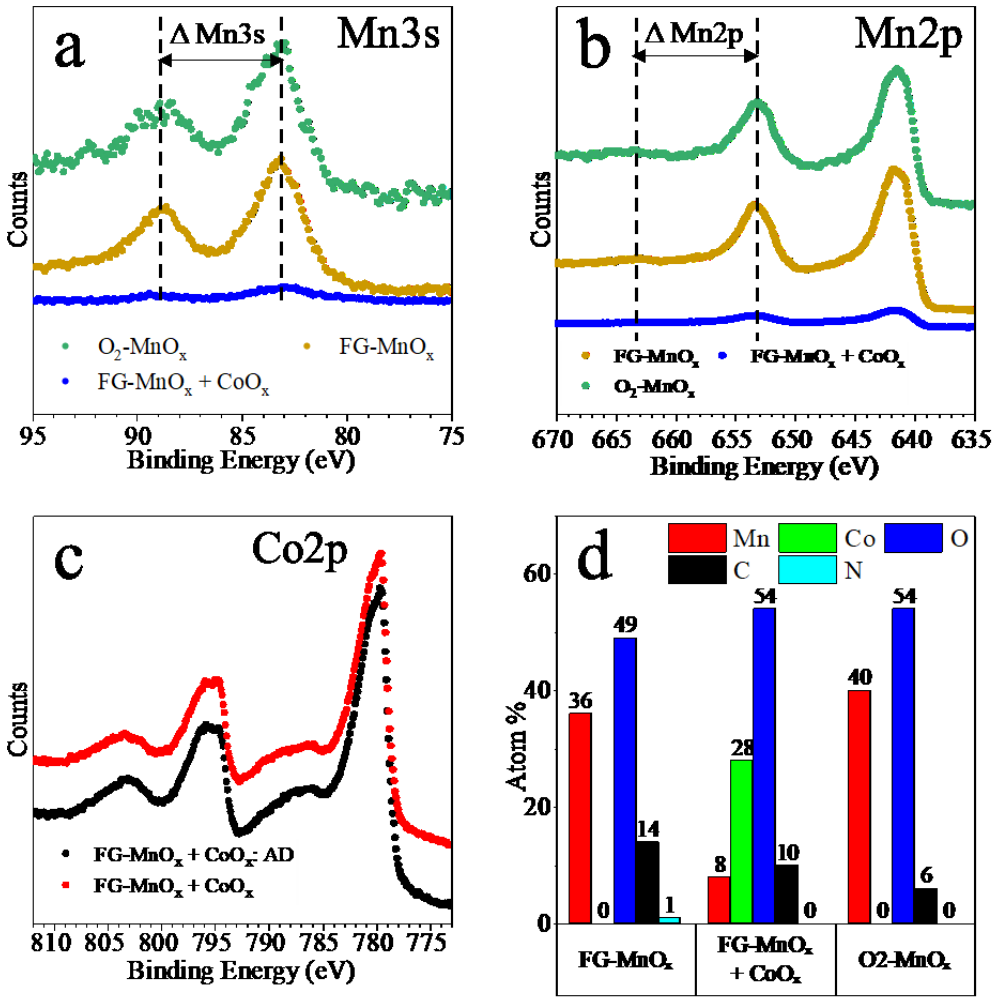

Figure 5-7: XPS results from coated electrodes after annealing. (a) Mn 3s, (b) Mn 2p, (c) Co 2p, and (d) quantification results.

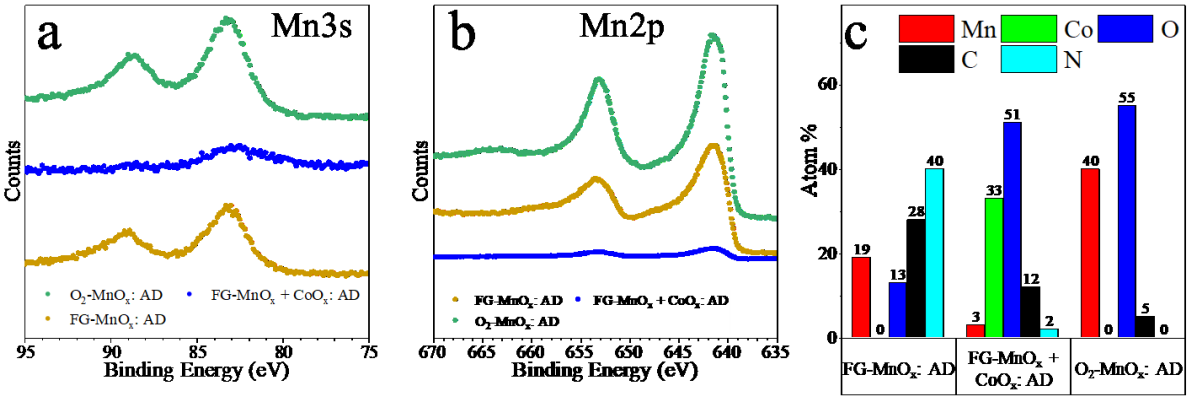

Figure 5-8: XPS results from coated electrodes before annealing (as deposited). (a) Mn 3s, (b) Mn 2p and (d) quantification results.

5.3.2 Electrochemical Characterization

The electrochemical behaviour of coated electrodes was examined using a number of half-cell techniques, shown in Figure 5-9 and Figure 5-10. FG-MnO_x and O_2-MnO_x both showed improved catalytic activity after annealing, due to the higher oxidation state and increased crystallinity of the annealed films (Figure 5-9b). Because of their relatively low activity, the as deposited films were not investigated further. Cyclic voltammetry (CV) curves in Ar-saturated, 1 M KOH (Figure 5-9a) show that the electrochemical behaviour differs for the three tested films. FG-MnO_x shows anodic and cathodic redox peaks associated with the $Mn^{3+} \leftrightarrow Mn^{4+}$ redox transition. The voltammogram for FG-MnO_x matches well with Mn_3O_4 data previously reported in the literature. [36], [45], [50], [132] CV results in conjunction with TEM and XPS measurements confirm that FG-MnO_x has a tetragonal Mn_3O_4 structure. The O_2-MnO_x sample shows the same $Mn^{3+} \leftrightarrow Mn^{4+}$ redox peaks as the FG-MnO_x, albeit with lower intensities. These redox peaks indicate that some amount of Mn_3O_4 is present in the O_2-MnO_x sample. [36], [45], [50], [132] FG-MnO_x + CoO_x has large broad redox peaks shifted slightly relative to the FG-MnO_x and O_2-MnO_x samples. The addition of CoO_x to the FG-MnO_x introduces the $Co^{2+} \leftrightarrow Co^{3+}$ redox transition, which overlaps and broadens the $Mn^{3+} \leftrightarrow Mn^{4+}$ peaks. O_2-MnO_x coated electrodes show relatively large cathodic currents at potentials <-0.2 V vs. Hg/HgO, which have previously been observed for Mn_2O_3 and MnO_2. The large current below -0.2 V vs. Hg/HgO is due to the formation of $Mn(OH)_2$. $Mn(OH)_2$ is soluble in the electrolyte, causing loss of Mn during cycling. [36][50] The FG-MnO_x sample does not exhibit the same reduction behaviour as the O_2-MnO_x sample, indicating that the formation of $Mn(OH)_2$ is kinetically limited for the FG-MnO_x film. [36] It is proposed that the difference in cathodic behaviour can be attributed to the higher Mn^{3+} content in the O_2-MnO_x deposit. Messaoudi *et al.* claim that Mn_2O_3 dissolves chemically in alkaline electrolytes and that reduction of Mn_2O_3 into Mn_3O_4 results in release of Mn^{2+} into solution. [50]

Mn dissolution was confirmed by chronopotentiometry followed by SEM and EDX analysis. Electrodes were discharged at 20 mA cm^{-2} for 12 h in O_2-saturated, 1 M KOH; results are shown in Figure 5-10c. After an initial conditioning period, the FG-MnO_x and FG-MnO_x + CoO_x samples show relatively stable potentials up to 12 h. The O_2-MnO_x sample experiences a drastic drop in potential after ~6 h, indicating catastrophic failure of the electrode. SEM EDX analysis

was performed on plan-view samples of the tested electrodes (Figure 5-10d). The EDX results show that significant amounts of Mn remain for the FG-MnO_x and FG-MnO_x + CoO_x samples, while the O_2-MnO_x sample has no Mn. This confirms that Mn dissolves from the O_2-MnO_x during discharge.

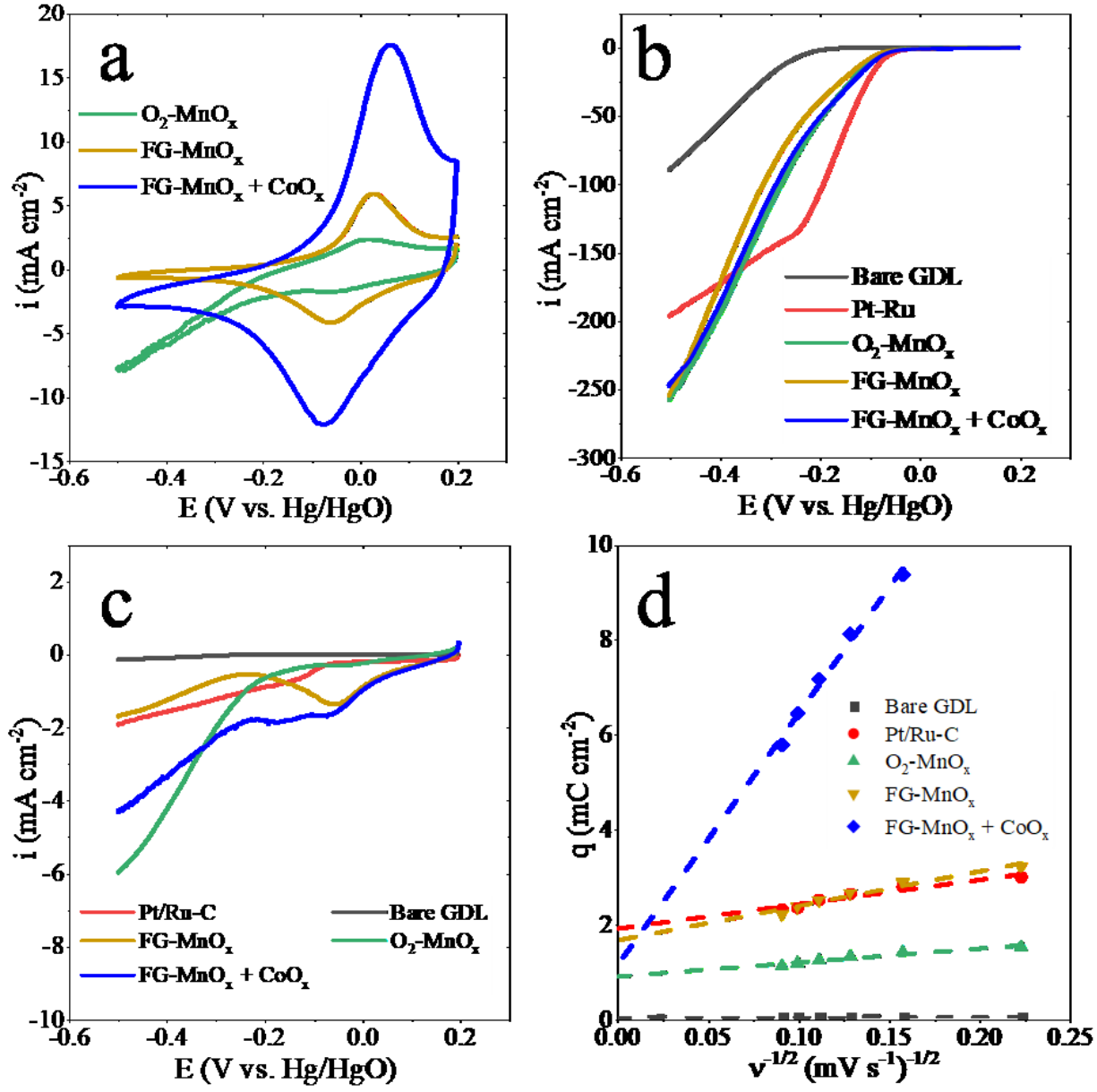

Figure 5-9: Half-cell testing results. (a) 10th CV cycle in Ar-saturated 1 M KOH. LSV results at a scan rate of 5 mV s^{-1} in (b) O_2-saturated and (c) Ar-saturated 1 M KOH. (d) CV results used for capacitance measurements (C_{DL}), performed between 0.1 and 0.2 V vs. Hg/HgO at varying scan rates.

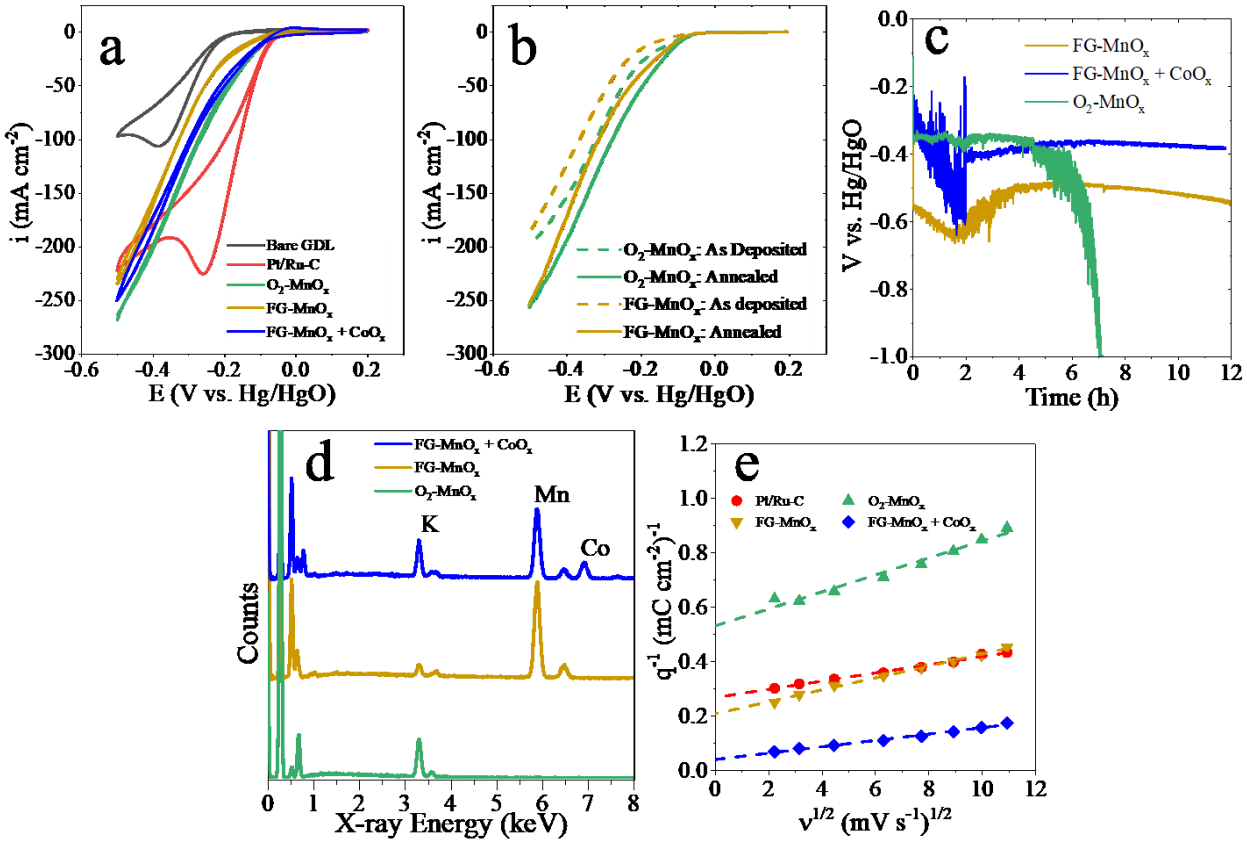

Figure 5-10: (a) CV results at a scan rate of 20 mV s^{-1} in O_2-saturated 1 M KOH. (b) LSV results in O_2-saturated 1 M KOH. (c) Chronopotentiometry performed at -20 mA cm^{-2} in O_2-saturated KOH. (d) EDX results from samples tested in (c). (e) CV results used for capacitance measurements (C_T), performed between 0.1 and 0.2 V vs. Hg/HgO at varying scan rates.

LSV curves in O_2-saturated 1 M KOH (Figure 5-9b) show drastically increased current densities compared with Ar-saturated tests (Figure 5-9c), confirming the activity of the coated electrodes towards ORR. The O_2-MnO_x films show significant cathodic current during Ar-saturated LSV testing (Figure 5-9c), associated with Mn dissolution via the formation of $Mn(OH)_2$. [50] FG-MnO_x and FG-MnO_x + CoO_x samples also exhibit cathodic currents which are attributed to the formation of Co^{2+} and/ or Mn^{2+}. However, the formation of these species on the FG-MnO_x + CoO_x sample does not result in significant dissolution of the catalyst, as confirmed in Figure 5-10d.

The LSV curves in O_2-saturated 1 M KOH (Figure 5-9b) were used to quantitatively compare the ORR activity (V_{onset}) of electrodes. V_{onset} in this work is defined as the potential at which a current of -10 mA cm^{-2} is reached. Data for Pt/Ru-C is presented as a benchmark in order to show the relative performance of the ALD MnO_x electrodes; bare GDL data is also shown. FG-

MnO_x and O_2-MnO_x films show good catalytic activity towards ORR with V_{onset} values of -107 mV and -95 mV (vs. Hg/HgO), respectively. The addition of CoO_x to FG-MnO_x enhances the activity; FG-MnO_x + CoO_x has a V_{onset} of -92 mV vs. Hg/HgO. These values are close to that of spray coated Pt/Ru-C on GDL, which has a V_{onset} of -75 mV vs. Hg/HgO.

Cyclic voltammetry (CV) was used to measure the double layer capacitance of coated electrodes, as described by Lee *et al*. [111] CV was performed between 0.1 and 0.2 V vs. Hg/HgO at a range of scan speeds (ν). The charge transferred (q) per half cycle was measured and plotted in order to calculate the double layer capacitance (C_{DL}) and the total capacitance (C_T). C_{DL} was determined by plotting q vs. $\nu^{-1/2}$ (Figure 5-9d) and extrapolating to $\nu = \infty$. C_T was determined by plotting q^{-1} vs. $\nu^{1/2}$ (Figure 5-10c) and extrapolating to $\nu = 0$. C_{DL} is directly related to electrode surface area and can be used to compare the electrochemically active surface area of the deposits. The capacitance measurement results are shown in Table 5-3. O_2-MnO_x films have lower C_{DL} than FG-MnO_x films, indicating that the FG-MnO_x sample has superior surface area. This observation is consistent with the Mn distribution observed in the SEM EDX line scans and STEM analysis. The FG-MnO_x deposition allows for better coverage within the porosity, enhancing the effective surface area. Despite having higher surface area, the FG-MnO_x electrode has a lower V_{onset} than the O_2-MnO_x film (Figure 5-9b). This is because of the higher oxidation state of the O_2-MnO_x film (2.8+) compared with the FG-MnO_x film (2.4+), as measured by XPS. The catalytic activity of MnO_x is largely determined by the presence of Mn^{3+} species on the catalyst surface. The higher Mn oxidation state of the O_2-MnO_x film compared with the FG-MnO_x film leads to a higher V_{onset} despite its lower surface area because of the relative abundance of Mn^{3+} species. [36], [149], [150] The addition of CoO_x to FG-MnO_x appears to have reduced the surface area of the electrode. This discrepancy can be attributed to blocked porosity and/ or calculation error due to the large pseudocapacitance. FG-MnO_x + CoO_x exhibited a high pseudocapacitance due to the $Co^{2+} \leftrightarrow Co^{3+}$ redox peak being within the potential range used during CV. The C_{DL} of Pt/Ru-C is comparable to that for the FG-MnO_x film. However, the Pt particles are only distributed on the surface of the GDL, which may restrict catalyst access to O_2 in a full cell battery configuration. Also, much of the surface area for Pt/Ru-C is from the carbon support, as opposed to the catalytically active Pt. The bare GDL has a comparatively low C_{DL} due to the PTFE binder preventing wetting of the electrode.

Table 5-3: Capacitance measurement results

	q_T (mC cm^{-2})	q_{DL} (mC cm^{-2})	C_T (mF cm^{-2})	C_{DL} (mF cm^{-2})	C_P (mF cm^{-2})
Bare GDL	0.06	0.06	0.6	0.6	0.0
FG-MnO_x	4.86	1.66	48.6	16.6	32.0
O_2-MnO_x	1.89	0.90	19.5	9.0	9.8
Pt/Ru-C	3.76	1.91	37.6	19.2	18.4
FG-MnO_x + CoO_x	26.46	1.12	265	11.2	254

* q_T is the total capacitive charge, q_{DL} is the double layer charge, C_T is the total capacitance, C_{DL} is the double layer capacitance and C_P is the pseudocapacitance.

The performance of ALD MnO_x electrodes was examined in a full cell ZAB configuration. Full cell battery test results are shown in Figure 5-11. ZAB test results are summarized and compared with results from the literature in Table 5-4. Although O_2-MnO_x performed better than FG-MnO_x in half-cell LSV experiments, the full-cell discharge potential for the two films is nearly identical up to 20 mA cm^{-2} (Figure 5-11a and b). Despite the superior intrinsic activity for O_2-MnO_x, FG-MnO_x is distributed deeper within the GDL resulting in greater surface area and similar full-cell discharge potential for the two electrodes up to 20 mA cm^{-2} (Figure 5-11a). The higher oxidation state and subsequent intrinsic activity of the O_2-MnO_x film facilitate higher discharge potentials at discharge rates greater than 20 mA cm^{-2}. [36], [149] FG-MnO_x + CoO_x had the best discharge performance of the samples tested, approaching that of Pt/Ru-C. The FG-MnO_x deposition provides high surface area and good catalyst distribution, while the addition of CoO_x enhances the intrinsic activity of the electrode. Co_3O_4 is well known as an effective ORR catalyst. [150] The addition of CoO_x to the FG-MnO_x film results in discharge performance exceeding that of both FG-MnO_x and O_2-MnO_x. Figure 5-11b shows that the ALD MnO_x electrodes have similar discharge polarization as Pt/Ru-C at low current densities. At high current densities, O_2 is consumed rapidly and discharge potential is determined largely by the availability of O_2. The MnO_x coated electrodes have catalyst distributed within the depth of the MPL, facilitating O_2 access to the catalyst surface. The Pt/Ru-C electrode, despite having excellent intrinsic activity, was prepared by spray coating which ultimately limits the availability of diffused O_2. O_2-MnO_x and FG-MnO_x have improved polarization behaviour over Pt/Ru-C at current densities exceeding 100 and 200 mA cm^{-2}, respectively. It is interesting to note that despite its superior performance at current densities less than 100 mA cm^{-2}, FG-MnO_x + CoO_x is out performed by the other films

at current densities exceeding 200 mA cm^{-2}. The additional film thickness added by the CoO_x to the FG-MnO_x reduces the porosity size at the surface of the MPL. Smaller pores reduce the rate at which reaction products (OH^-) diffuse away from the electrode, degrading performance at high current densities. FG-MnO_x and O_2-MnO_x films exhibited high maximum power densities of 170 and 184 mW cm^{-2}, respectively, out performing Pt/Ru-C (158 mW cm^{-2}).

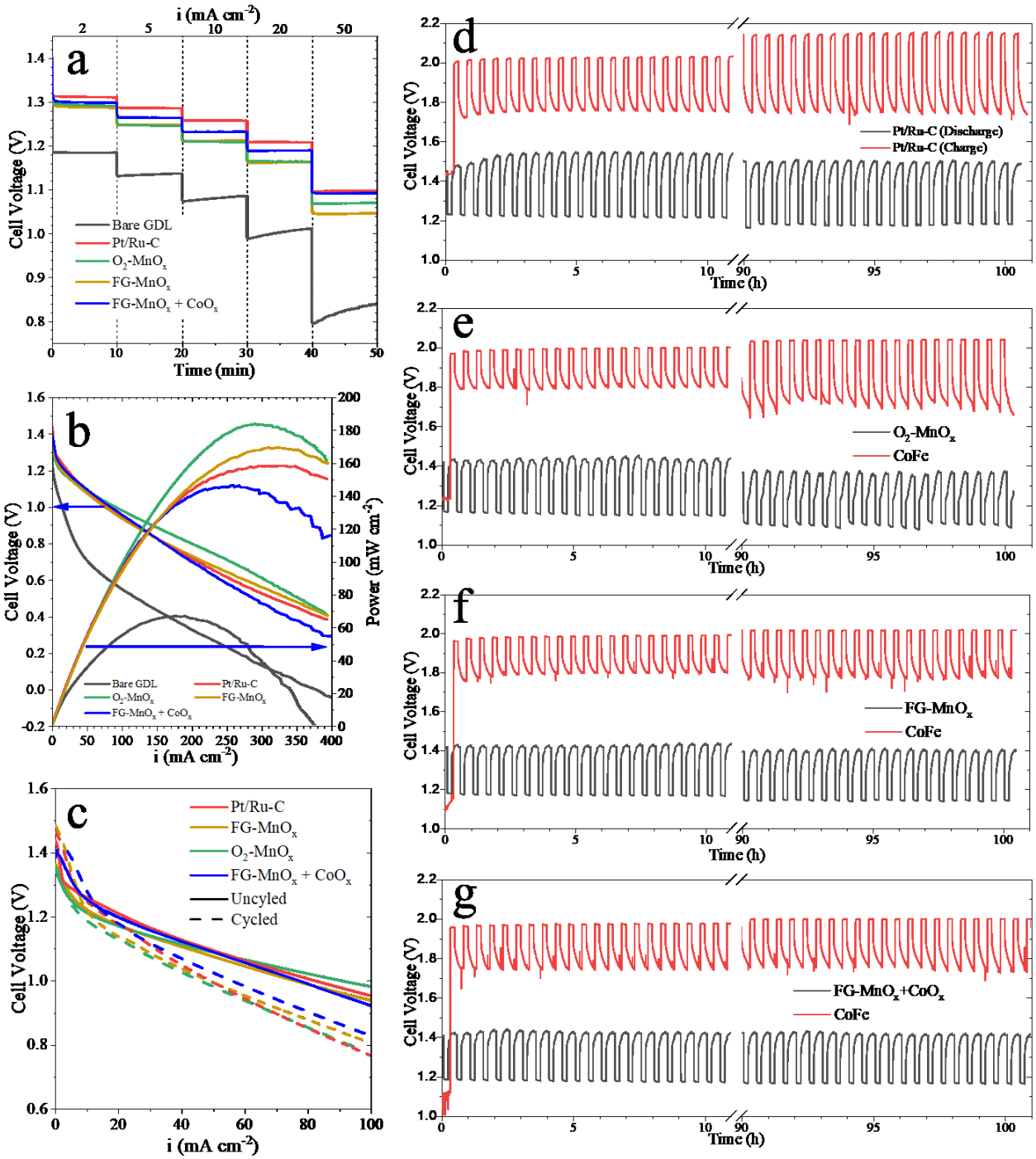

Figure 5-11: Full cell battery test results, performed in 6 M KOH + 0.25 M ZnO. (a) Discharge voltage at various discharge rates. (b) Electrode polarization (left axis) and power (right axis) curves (1 mA s^{-1} scan rate). (c) Electrode polarization at 1 mA s^{-1} before and after 200 cycles. (d, e, f, and g) Tri-electrode cycling results at 20 mA cm^{-2}: (d) Pt/Ru-C (ORR) and Pt/Ru-C (OER), (e) O_2-MnO_x (ORR) and CoFe (OER), (f) FG-MnO_x and CoFe, (g) FG-MnO_x + CoO_x (ORR) and CoFe (OER).

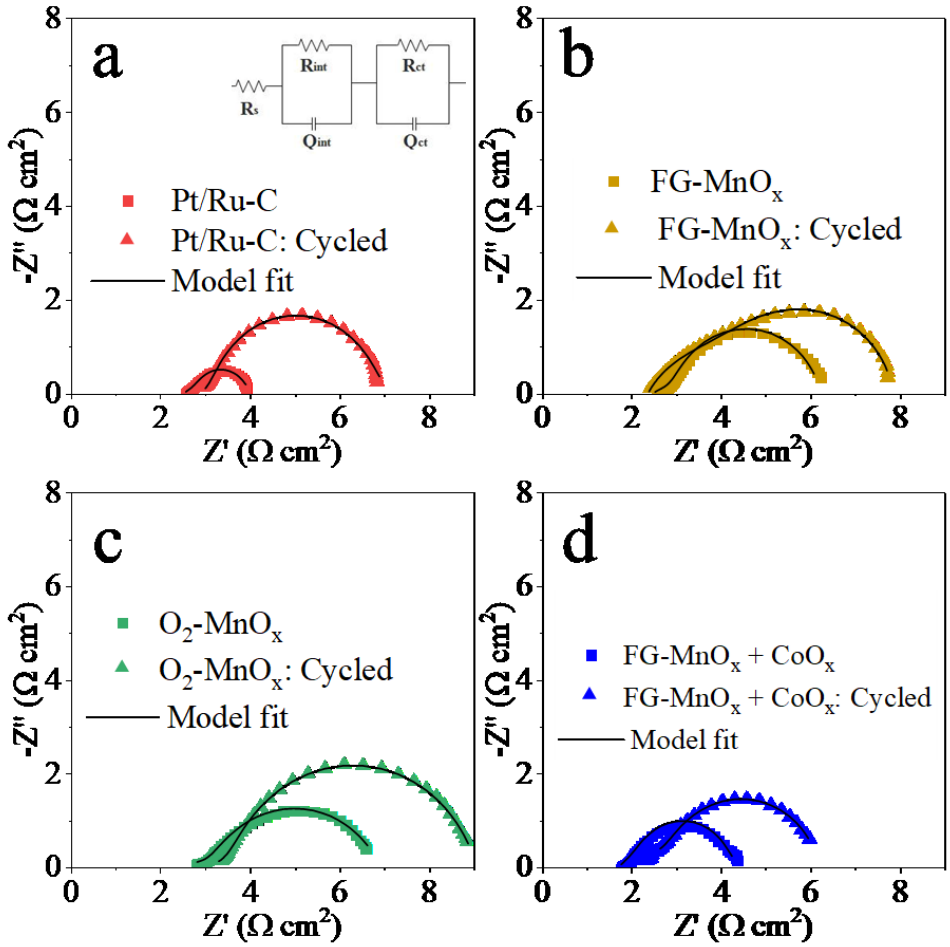

Figure 5-12: EIS results for cycled and uncycled electrodes performed at a cell potential of 1.2 V. (a) Pt/Ru-C, (b) FG-MnO_x, (c) O_2-MnO_x and (d) FG-MnO_x + CoO_x. Cycling was performed at 20 mA cm^{-2} for 200 cycles in a tri-electrode configuration.

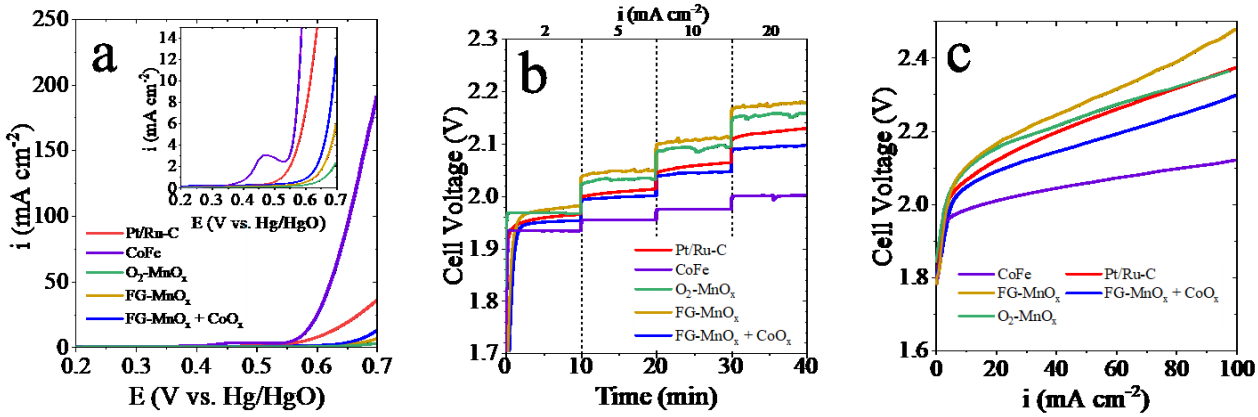

Figure 5-13: OER performance comparison. (a) LSV in 1 M KOH at 5 mV s^{-1}. (b) Charge rate in 6 M KOH + 0.25 M ZnO. (c) Charge polarization (1 mA s^{-1}), measured after rate test shown in (b).

Table 5-4: Comparison of ZAB results

ORR Catalyst	OER Catalyst	Catalyst Preparation	Electrode Preparation	Maximum Power	Configuration	Cycling Conditions	Initial ε	Final ε	Ref.
MnO_x	CoFe	Electrodeposition	Direct	ND	Tri-Electrode	100 cy (50 h), 10 mA cm^{-2}	60%	56%	[27]
Bare GDL	RuO_2/Ti	None	None	105 mW cm^{-2}	Tri-Electrode	1000 cy (1920 h), 20 mA cm^{-2}	54%	42%	[31]
MnO_2-Co_3O_4/ Ni foam	MnO_2-Co_3O_4/ Ni foam	Hydrogel Mediated Electrodeposition	Direct	ND	Tri-Electrode	96 cy (400 h), 1 mA cm^{-2}	62%	57%	[135]
MnO_2-Co_3O_4/ Ni foam		Hydrogel Mediated Electrodeposition	Direct	ND	Bifunctional	96 cy (400 h), 1 mA cm^{-2}	60%	59%	[135]
Fe-N_x /CNT	NiFe LDH	Hydrothermal	Ink	ND	Tri-Electrode	300 cy (300 h), 1 mA cm^{-2}	70%	68%	[29]
N-doped Hollow Mesoporous Carbon		Templated Solution Based	Ink	ND	Bifunctional	30 cy (17 h), 2 mA cm^{-2}	61%	56%	[136]
MnO_x-CoFe		Electrodeposition	Direct	ND	Bifunctional	80 cy (40 h), 5 mA cm^{-2}	63%	56%	[138]
Co_9S_8/CNT		ALD	Direct	198 mW cm^{-2}	Bifunctional	576 cy (96 h), 10 mA cm^{-2}	63%	62%	[123]
O_2-MnO_x	CoFe/ Ni foam	ALD/ Electrodeposition	Direct	184 mW cm^{-2}	Tri-Electrode	200 cy (100 h), 20 mA cm^{-2}	58%	55%	This Work
FG-MnO_x	CoFe/ Ni foam	ALD/ Electrodeposition	Direct	170 mW cm^{-2}	Tri-Electrode	200 cy (100 h), 20 mA cm^{-2}	59%	57%	This Work
FG-MnO_x +CoO_x	CoFe/ Ni foam	ALD/ Electrodeposition	Direct	148 mW cm^{-2}	Tri-Electrode	200 cy (100 h), 20 mA cm^{-2}	59%	57%	This Work
FG-MnO_x+CoO_x		ALD	Direct	148 mW cm^{-2}	Bifunctional	100 cy (50 h), 10 mA cm^{-2}	60%	53%	This Work

LDH- layered double hydroxide, CNT- carbon nanotubes, ND- not determined.
For electrode preparation, direct indicates that the catalyst was deposited directly onto the electrode and ink indicates that the catalyst was dispersed in an ink before depositing onto the electrode.

The cycling stability of ALD coated electrodes and Pt/Ru-C was examined by cycling at 20 mA cm^{-2} for 200 cycles (100 h) (Figure 5-11d-g) using separate electrodes for ORR and OER in a tri-electrode configuration. EIS results before and after cycling are shown in Figure 5-12. The tri-electrode configuration allows assessment of ORR cyclability without the interference of OER potentials. The OER electrodes used in conjunction with the ALD MnO_x ORR electrodes were electrodeposited Co-Fe on Ni foam. [27], [112], [113] The OER performance of Co-Fe, Pt/Ru-C, and the ALD films is shown in Figure 5-13. For the Pt/Ru-C benchmark catalyst, separate spray coated Pt/Ru-C GDL electrodes were used for ORR and OER. Cycling results are summarized in Table 5-5 and compared with results from the literature in Table 5-4. TEM/ STEM analysis was conducted on cycled electrodes; results are shown in Figure 5-14, Figure 5-15, Figure 5-16, and Figure 5-17. After 100 h, the Pt/Ru-C, O_2-MnO_x, FG-MnO_x and FG-MnO_x + CoO_x electrodes experienced discharge potential drops of 40, 60, 30 and 30 mV, respectively. The relatively poor stability of O_2-MnO_x is attributed to two factors. One factor is the formation of soluble $Mn(OH)_2$ during discharge, as confirmed in Figure 5-10. Figure 5-14 shows that only very small amounts of MnO_x are present on the cycled O_2-MnO_x sample; most of the MnO_x coating has dissolved during cycling. Secondly, the O_2 plasma used during deposition etches PTFE and carbon from the GDL, resulting in severe electrode flooding during long term testing. Electrolyte was observed on the reverse side of the GDL, meaning it had passed through the backing layer of the GDL. The cycling results for O_2-MnO_x demonstrate the importance of maintaining three phase boundaries within the electrode. The electrodeposited CoFe on Ni foam showed excellent OER cycling stability compared with Pt/Ru-C on GDL. The CoFe electrodes experienced a 20 mV potential increase for charging after cycling, while the Pt/Ru-C charge potential increased by 130 mV. FG-MnO_x + CoFe showed the best cycling stability, with only a 2% drop in efficiency from 59% to 57% after 100 h. Efficiency (ε) is defined as the discharge potential divided by the charge potential. The effect of cycling was further investigated by comparing polarization and EIS measurements before and after cycling (Figure 5-11c and Figure 5-12). The polarization curves show that all samples experienced a decrease in discharge potential after cycling, with FG-MnO_x + CoO_x experiencing the smallest drop and O_2-MnO_x the largest drop.

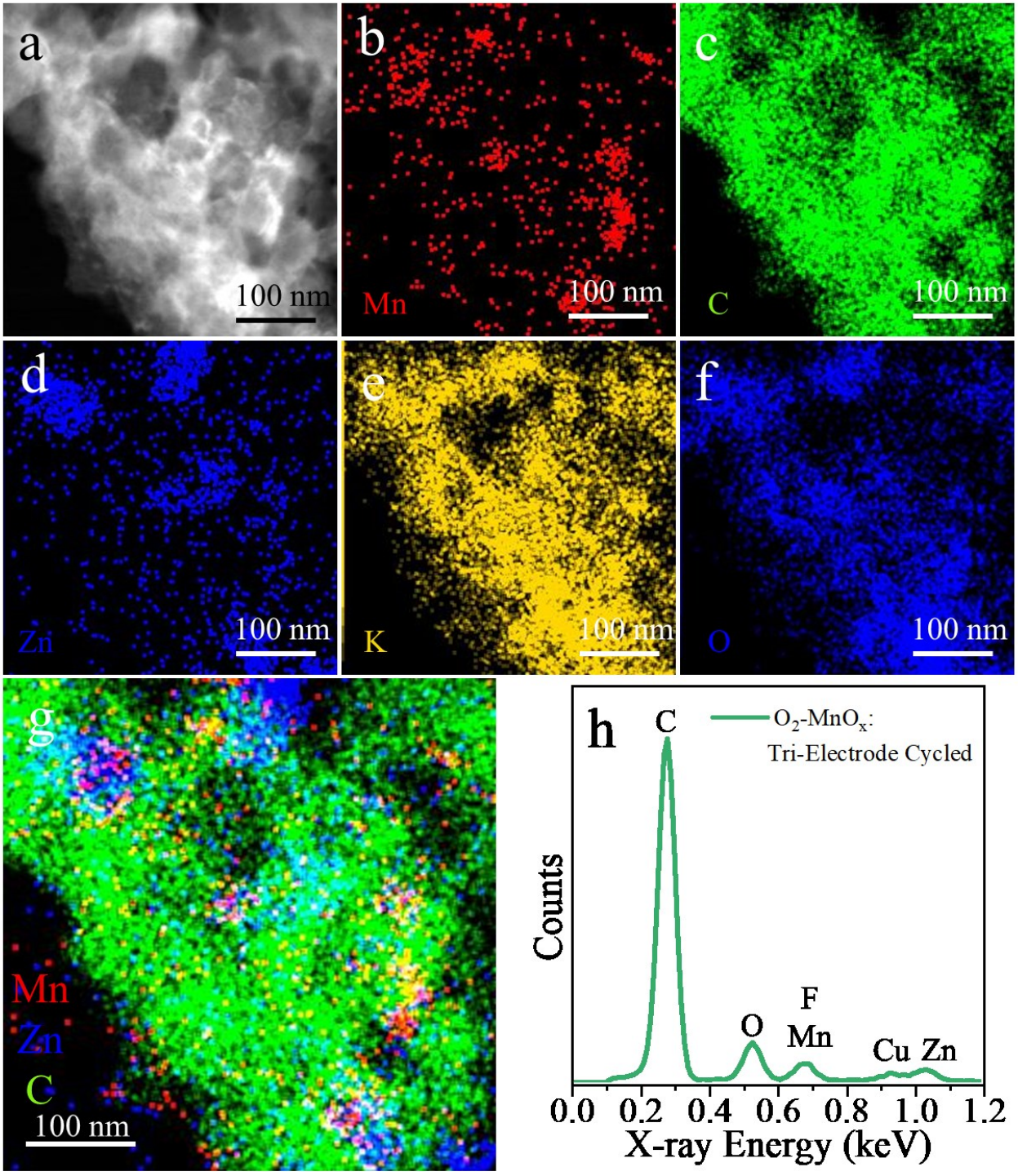

Figure 5-14: STEM results for O_2-MnO_x cycled as the ORR electrode in a tri-electrode configuration (200 cycles, 100 h at 20 mA cm^{-2}). (a) STEM annular dark field (ADF) image. (b-g) STEM EDX mapping results: (b) Mn map, (c) C map, (d) Zn map, (e) K map, (f) O map and (g) overlain Mn, Zn and C map. (h) STEM EDX spectrum from the overall area.

EIS fitting results in Table 5-5 show how solution resistance (R_s), interfacial resistance (R_{Int}) and charge transfer resistance (R_{CT}) change after cycling for the tested electrodes. [138], [151] FG-MnO_x and FG-MnO_x + CoO_x experienced negligible changes in R_S with cycling. R_S increased by 0.4 and 0.5 Ω for Pt/Ru-C and O_2-MnO_x, respectively. This increase in R_S is attributed to the instability of these electrodes. During cycling, Pt is known to agglomerate and O_2-MnO_x experiences dissolution. R_{CT} is related to the catalytic activity of the electrode. A small R_{CT} indicates that an electrode has good activity towards ORR. As shown in Table 5-5, electrodes with a larger discharge voltage have lower R_{CT} values. The introduction of CoO_x to the FG-MnO_x electrode causes a drop in R_{CT}. This is because nanostructured CoO_x, in addition to its OER activity, has good activity towards ORR. [150], [152], [153] The activity of a pure CoO_x film could not be investigated in this work because the O_2 plasma used as the co-reactant during CoO_x deposition causes extreme carbon corrosion without an underlying MnO_x layer to protect the GDL. Changes in R_{CT} during cycling are consistent with the cycling performance of the catalysts. Pt/Ru-C and O_2-MnO_x experienced significant increases in R_{CT}, whereas the FG-MnO_x and FG-MnO_x + CoO_x electrodes had relatively small increases in R_{CT}.

TEM/ STEM analysis of FG-MnO_x and FG-MnO_x + CoO_x films cycled in a tri-electrode configuration are shown in Figure 5-15 and Figure 5-16, respectively. Imaging and EDX mapping show that the morphology of the ALD films is virtually unchanged, confirming that these films are stable during cycling. STEM EDX mapping of FG-MnO_x and FG-MnO_x + CoO_x reveals that Zn (and K) from the electrolyte are present on the electrode after cycling. It is not clear whether Zn is incorporated into the films or if it is present as salt residue on the electrode surface. SAD patterns from cycled samples show greater intensity and more spots than for the uncycled samples, indicating an increase in crystallinity. Since Mn_3O_4, $ZnMn_2O_4$, Co_3O_4, and $Zn_xCo_{3-x}O_4$ have very similar crystal structures, it is difficult to confidently identify the exact phase(s) present after cycling (Table 5-1 and Table 5-2). Ternary oxides of Mn-Zn and Co-Zn have been shown to have activity towards ORR, which could explain the cycling stability of FG-MnO_x and FG-MnO_x + CoO_x. [154] The SAD pattern for the cycled tri-electrode FG-MnO_x sample can be indexed best with Mn_3O_4/$ZnMn_2O_4$. The FG-MnO_x + CoO_x sample has separate MnO_x and CoO_x layers, which results in overlapping diffraction patterns from the layers (Figure 5-16c). The SAD pattern for cycled FG-MnO_x + CoO_x is consistent with M_3O_4 structures where M = Mn, Co, and/ or Zn.

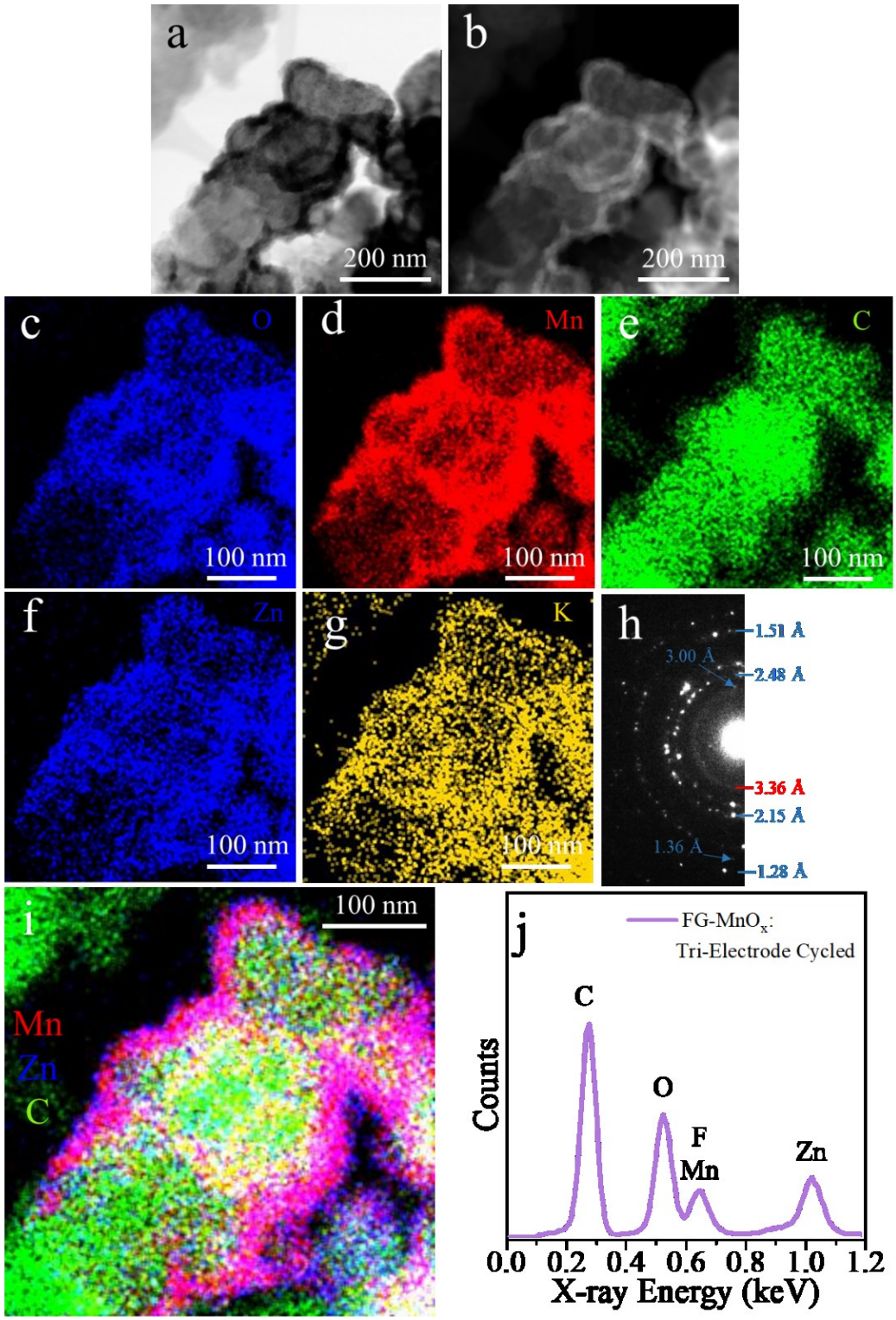

Figure 5-15: STEM results from FG-MnO_x cycled as the ORR electrode in a tri-electrode configuration (200 cycles, 100 h at 20 mA cm^{-2}). (a) STEM BF image. (b) STEM ADF image. (c-g, i) STEM EDX mapping results: (c) O map, (d) Mn map, (e) C map, (f) Zn map, (g) K map, (i) overlain Mn, Zn and C map. (h) SAD pattern. (j) STEM EDX spectrum from overall area.

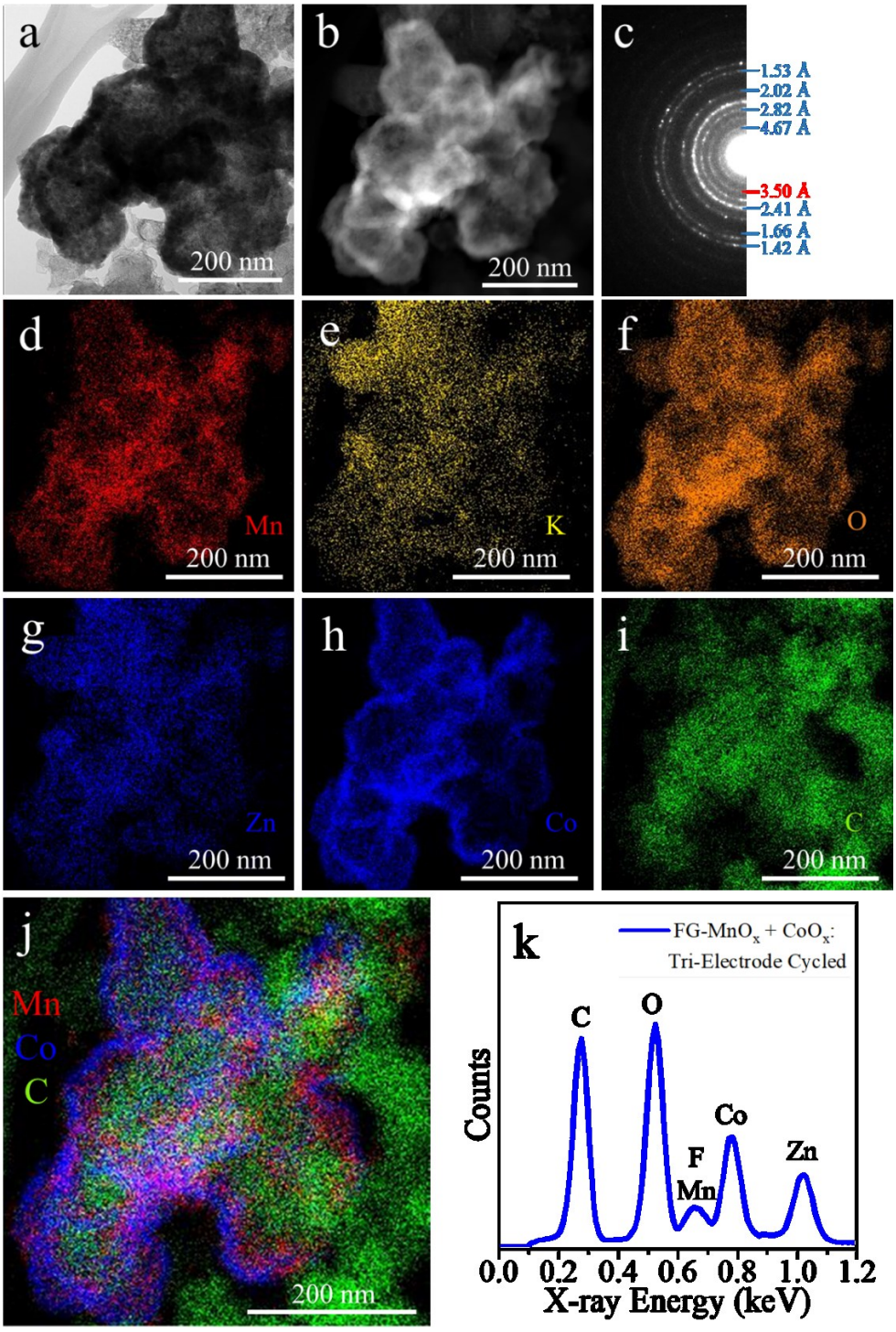

Figure 5-16: TEM/ STEM results from FG-MnO_x + CoO_x cycled as the ORR electrode in a tri-electrode configuration (200 cycles, 100 h at 20 mA cm^{-2}). (a) TEM BF image. (b) STEM ADF image. (c) SAD pattern. Diffracted intensity associated with GDL is marked in red, while the diffracted intensity for the FG-MnO_x + CoO_x film is marked in blue. (d-j) STEM EDX mapping results: (d) Mn map, (e) K map, (f) O map, (g) Zn map, (h) Co map, (i) C map and (j) overlain Mn, Co and C maps. (k) STEM EDX spectrum from the overall area.

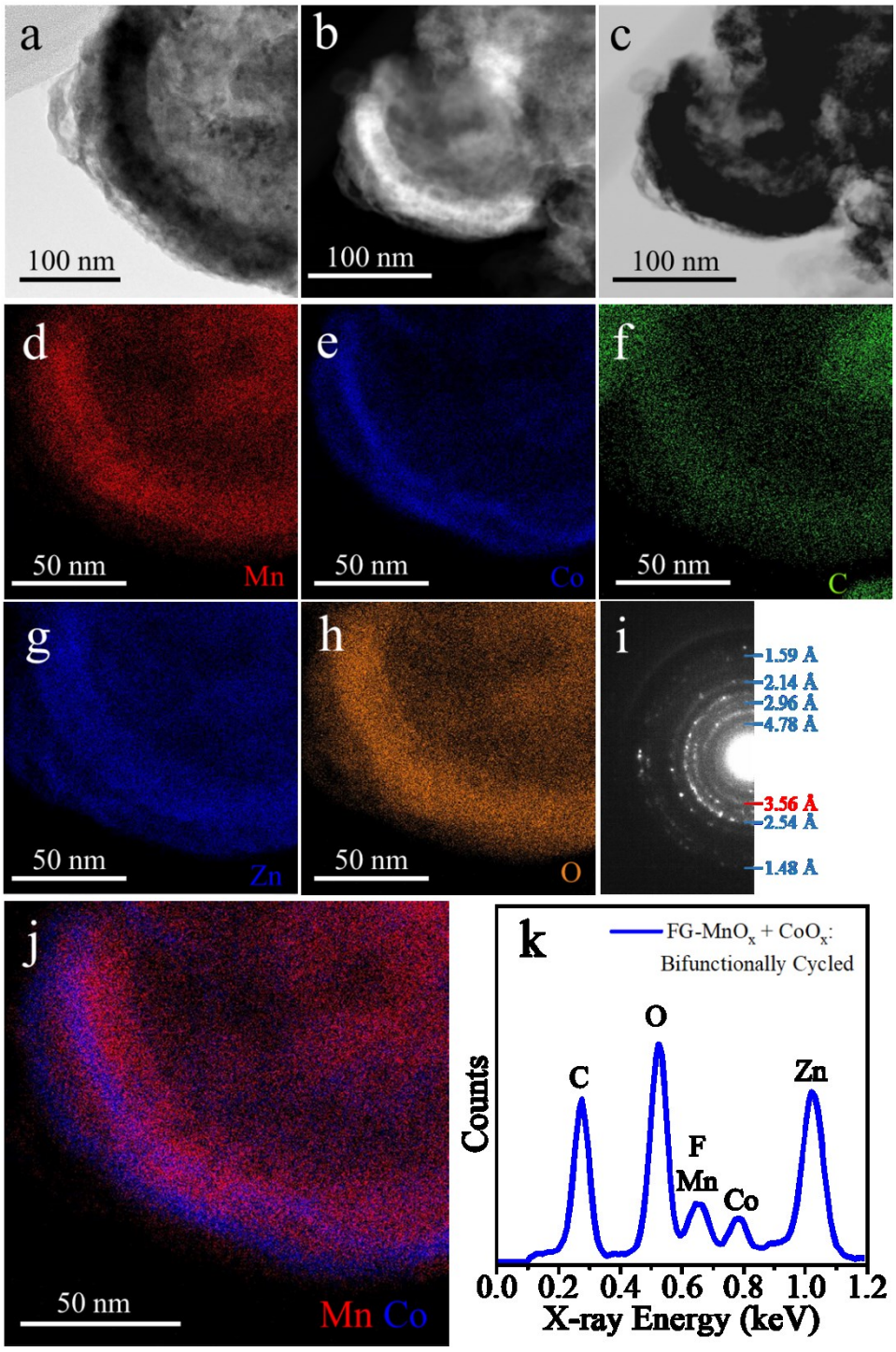

Figure 5-17: TEM/ STEM results for FG-MnO_x + CoO_x cycled in a bifunctional configuration (100 cycles, 50 h at 10 mA cm^{-2}). (a) TEM BF image. (b) STEM ADF image. (c) STEM BF image. (d-h, j) STEM EDX mapping results: (d) Mn map, (e) Co map, (f) C map, (g) Zn map, (h) O map, (j) overlain Co and Mn maps. (i) SAD pattern. Diffracted intensity associated with GDL is marked in red, while the diffracted intensity for the FG-MnO_x + CoO_x film is marked in blue. (k) STEM EDX spectrum of the overall area.

Table 5-5: Cycling stability results - 100 h (200 cycles) tri-electrode test at 20 mA cm^{-2}

		E_{ORR} (V)	E_{OER} (V)	ε	R_S (Ω cm^2)	R_{Int} (Ω cm^2)	R_{CT} (Ω cm^2)
Pt/Ru-C	Initial	1.22	2.02	60%	2.57	0.69	0.83
	Final	1.18	2.15	55%	2.93	1.21	3.04
FG-MnO_x + CoFe	Initial	1.17	1.99	59%	2.56	0.93	2.90
	Final	1.14	2.01	57%	2.43	2.19	3.30
O_2-MnO_x + CoFe	Initial	1.16	1.99	58%	2.67	0.92	3.42
	Final	1.10	2.01	55%	3.20	0.97	4.99
FG-MnO_x + CoO_x + CoFe	Initial	1.18	1.99	59%	1.74	0.81	2.15
	Final	1.15	2.01	57%	1.95	0.93	3.45

* Initial and final potentials were taken as an average of the first 5 cycles and last 5 cycles, respectively.

Bifunctional stabilities of Pt/Ru-C and FG-MnO_x + CoO_x were tested by cycling for 100 cycles (50 h) at 10 mA cm^{-2}; results are shown in Figure 5-18 and Table 5-6. In this case, the respective electrodes are used for both the ORR and OER processes, exposing them to a larger potential range than the tri-electrode configuration. Both systems showed a gradual degradation for both charge and discharge. The Pt/Ru-C electrode experienced problems with bubble formation and electrolyte flooding through to the backside of the GDL. The FG-MnO_x + CoO_x electrode did not experience these problems. After 100 cycles, the efficiency of Pt/Ru-C dropped 11%, from 62% to 51%. The FG-MnO_x + CoO_x electrode showed superior stability, dropping only 7% from 60% to 53%. Polarization curves (Figure 5-18a) show that the performance of Pt/Ru-C dropped more significantly than that for the FG-MnO_x + CoO_x sample, particularly for the charge process (OER). The EIS data before and after cycling is more difficult to interpret, since the Pt/Ru-C sample shows an additional semicircle at low frequencies (< 500 mHz). No appropriate model could be found to fit the data for the cycled Pt/Ru-C sample. Since this feature was not present during the tri-electrode tests, it is believed to be caused by the charge cycles. During charging, in addition to film oxidation, O_2 bubbles can form within the porosity causing mechanical damage to the spray-coated Pt/Ru-C layer. TEM/ STEM analysis of the bifunctionally cycled FG-MnO_x + CoO_x sample is shown in Figure 5-17. STEM EDX mapping shows that like the uncycled sample, distinct layers of MnO_x and CoO_x are present on the GDL particles. However, the amount of CoO_x present has been reduced. This is clearly indicated by the thicknesses of the

cycled and uncycled films, as well as the intensities of their respective EDX spectra. As with tri-electrode cycling, the bifunctionally cycled sample shows Zn present on the sample surface. The SAD pattern for bifunctionally cycled FG-MnO_x + CoO_x exhibits increased crystallinity over the uncycled sample and can be indexed to M_3O_4 structures where M = Mn, Co, and/ or Zn.

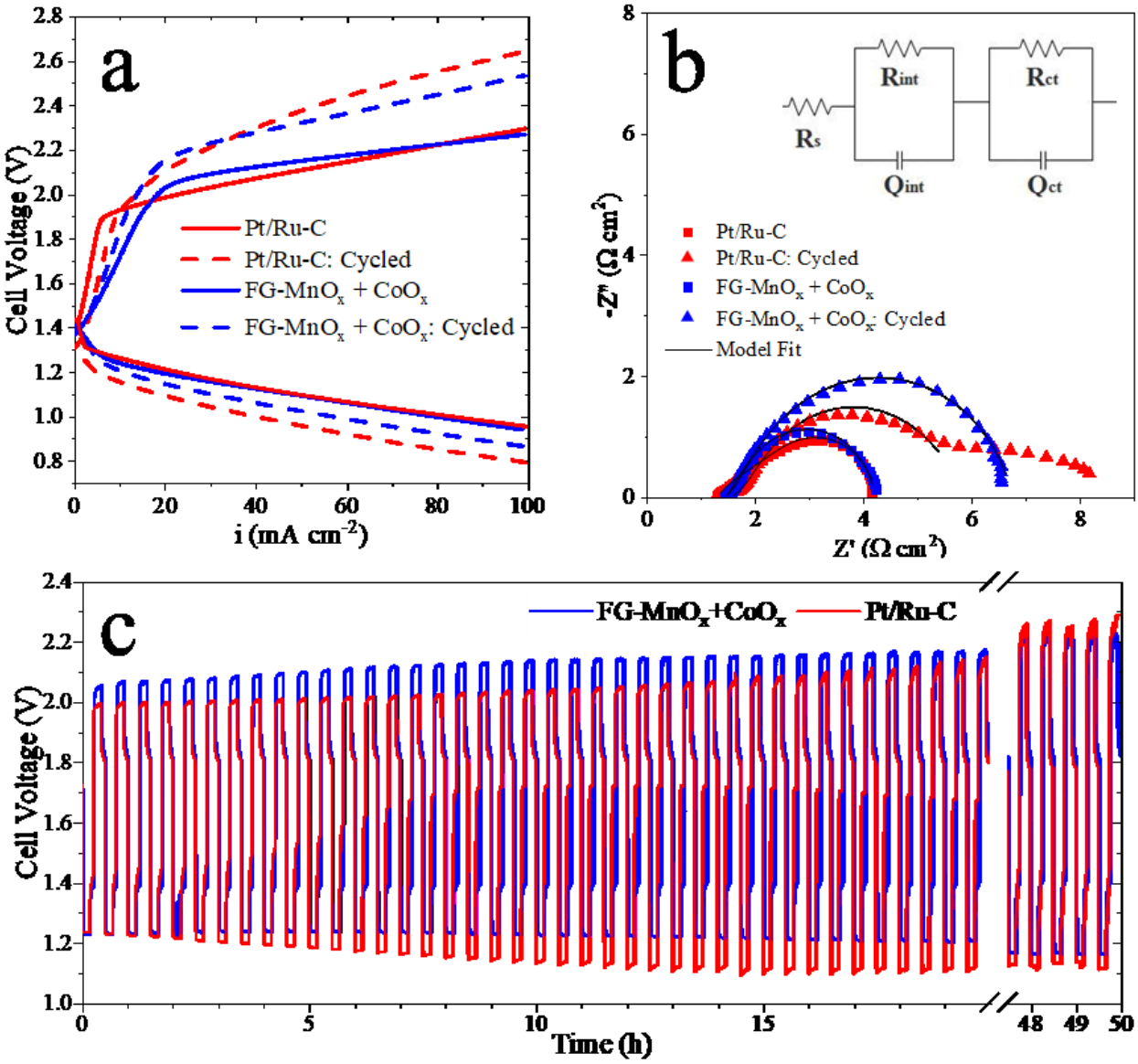

Figure 5-18: Bifunctional cycling results. (a) Charge and discharge polarization before and after cycling. (b) EIS before and after cycling. (c) Bifunctional cycling test for 100 cycles (50 h) at 10 mA cm^{-2}.

Table 5-6: Bifunctional cycling results – 50 h test at 10 mA cm^{-2}.

		E_{ORR} (V)	E_{OER} (V)	ε	R_S (Ω cm^2)	R_{Int} (Ω cm^2)	R_{CT} (Ω cm^2)
Pt/Ru-C	Initial	1.23	2.00	62%	1.32	1.61	1.36
	Final	1.13	2.23	51%	1.44	0.25	4.10
FG-MnO_x + CoO_x	Initial	1.23	2.06	60%	1.47	0.52	2.25
	Final	1.16	2.20	53%	1.46	0.47	4.89

5.4 Conclusions

Porous carbon gas diffusion layers (GDL) were successfully coated with catalytic MnO_x, using novel atomic layer deposition (ALD) procedures, for use in Zn-air batteries (ZABs). MnO_x films were deposited using two ALD recipes, one utilizing forming gas plasma (FG-MnO_x) and one using oxygen plasma (O_2-MnO_x). A bifunctional electrode, FG-MnO_x + CoO_x was also prepared and examined. All samples were annealed prior to electrochemical testing. Electron microscopy and x-ray microanalysis confirmed that MnO_x deposited conformally around the GDL particles and successfully penetrated into the depth of the GDL. FG-MnO_x films had improved coverage and surface area compared with O_2-MnO_x films. X-ray photoelectron spectroscopy (XPS), electron diffraction, and electrochemical testing indicated that annealed FG-MnO_x is composed of Mn_3O_4, while annealed O_2-MnO_x contains a combination of γ-Mn_2O_3 and Mn_3O_4. Full-cell battery tests of coated electrodes showed performance comparable with Pt/Ru-C at lower current densities and with performance exceeding Pt/Ru-C at current densities larger than 100 mA cm^{-2}. Annealed FG-MnO_x and O_2-MnO_x exhibited high maximum power densities of 170 and 184 mW cm^{-2}, respectively. Cycling stability was tested at 20 mA cm^{-2} for 100 h (200 cycles) using separate charge and discharge electrodes. Nickel foam coated with electrodeposited CoFe was used as the charge electrode. FG-MnO_x, FG-MnO_x + CoO_x, and O_2-MnO_x electrodes experienced 30, 30, and 60 mV drops in discharge potential after 100 h, respectively. Post cycling STEM analysis showed that the O_2-MnO_x sample experienced severe dissolution, whereas the FG-MnO_x and FG-MnO_x + CoO_x samples remained intact. During bifunctional cycling tests FG-MnO_x + CoO_x had superior cyclability compared with Pt/Ru-C with better stability for 100 cycles (50 h) at 10 mA cm^{-2}. This work demonstrates how the effective distribution of catalyst through the GDL can improve the performance of ZAB discharge electrodes, particularly at high current densities.

Chapter 6: Conclusions and Future Work

6.1 Conclusions

In summary, this work has reported the development of ALD procedures to prepare high performance air electrodes for Zn-air batteries (ZABs). ALD has been demonstrated as being able to conformally deposit catalytic films into the porosity of the gas diffusion layer (GDL), enhancing catalyst distribution and subsequent performance.

6.1.1 Chapter 4 - Conclusions

- Deposition data for the $(EtCp)_2Mn + H_2O$ ALD system revealed non-saturating behaviour. This is in direct disagreement with previous reports in literature.
- Saturating deposition of MnO_x was achieved through the use of a forming gas (95% N_2, 5% H_2) plasma step between the $(EtCp)_2Mn$ and H_2O doses, giving a stable growth per cycle of 1.15 Å/cy across a wide temperature range (100 – 200 °C).
- Scanning electron microscopy of GDL cross sections demonstrated that ALD was able to deposit MnO_x within the porosity of the electrode. Saturating depositions using a forming gas plasma reached deeper within the GDL than the non-saturating depositions utilizing only $(EtCp)_2Mn$ and H_2O.
- Electrochemical testing demonstrated that MnO_x deposition utilizing a forming gas plasma have good catalytic activity and are stable during the oxygen reduction reaction.

6.1.2 Chapter 5 - Conclusions

- Air electrodes for ZABs were prepared by ALD following three different recipes. O_2-MnO_x was deposited using an oxygen plasma, FG-MnO_x was deposited using a forming gas plasma, and FG-MnO_x + CoO_x was deposited in the same manner as FG-MnO_x but with a layer of CoO_x deposited on top.
- Scanning transmission electron microscopy revealed that the C particles composing the GDL were conformally coated with MnO_x. The saturating behaviour of the FG-MnO_x deposition resulted in greater uniformity than the non-saturating O_2-MnO_x deposition.
- X-ray photoelectron spectroscopy and electron diffraction identified the O_2-MnO_x and FG-MnO_x films as hausmannite (Mn_3O_4). Despite their similar crystal structures, O_2-

MnO_x had a Mn oxidation state of $Mn^{2.8+}$, while the oxidation state for FG-MnO_x was $Mn^{2.4+}$. The difference in oxidation state occurs because of the highly oxidizing species present in the O_2 plasma. The difference in oxidation state resulted in differences in electrochemical behaviour, most notably the O_2-MnO_x experienced catastrophic dissolution while the FG-MnO_x film was very stable.

- Full cell ZAB testing revealed the excellent performance of the ALD coated electrodes, comparable to Pt/Ru-C. FG-MnO_x and O_2-MnO_x demonstrated large maximum power densities of 170 and 184 mW cm^{-2}, respectively. FG-MnO_x + CoO_x exhibited the best cycling performance with initial and final efficiencies of 59% and 57% respectively, after 200 cycles at 20 mA cm^{-2} in a tri-electrode configuration. FG-MnO_x + CoO_x out performed Pt/Ru-C in bifunctional cycling tests at 10 mA cm^{-2} for 100 cycles. Pt/Ru-C experienced an 11% drop in efficiency whereas FG-MnO_x + CoO_x experienced only a 7% drop in efficiency.

6.2 Future Work

- Incorporation of one or more additional transition metal elements into an ALD MnO_x film could help to improve catalyst properties. Ternary and higher order oxides containing Mn, Fe, Co, and/ or, Ni have been demonstrated to enhance ORR and OER performance, as well as improve catalyst stability. However, deposition of higher order oxide films is not trivial. The deposition chemistry and conditions must be compatible in order to achieve the desired mixed oxide film.
- Perovskite oxides (e.g., $LaMnO_3$, $LaCoO_3$, $LaNiO_3$) have great potential as highly active and stable bifunctional catalysts. However, as with mixed transition metal oxides, deposition of perovskites is not trivial. Deposition of perovskites is further complicated by the need for the specific perovskite crystal structure.
- An exposure-type ALD reactor could be used to achieve catalyst deposition throughout the entirety of the GDL. The flow-type design of the ALD reactor used for this work limits exposure time and, as such, precursor diffusion into the GDL. In an exposure reactor, the reactor is isolated from pumping during precursor dose, permitting precursor diffusion into highly porous structures.

- Alternative thermal ALD reactants could be used such as O_3 or H_2O_2. Due to the high reactivity and short lifetime of plasma species, films prepared via plasma enhanced ALD tend to have worse uniformity and conformity than thermal ALD films. It is expected that better coverage throughout the GDL structure could be achieved using thermal ALD. In this work, H_2O and O_2 were examined as thermal reactants, but did not produce high quality films. Highly oxidizing species such as O_3 or H_2O_2 may be able to prepare high quality MnO_x via thermal ALD.

References

[1] World Resources Institute, "CAIT Climate Data Explorer." [Online]. Available: http://cait.wri.org/.

[2] IRENA International Renewable Energy Agency, *Renewable Power Generation Costs in 2017*. 2018.

[3] Argyrou, M. C., Christodoulides, P., and Kalogirou, S. A., "Energy storage for electricity generation and related processes : Technologies appraisal and grid scale applications," *Renew. Sustain. Energy Rev.*, vol. 94, no. June, pp. 804–821, 2018.

[4] Xiong, M., "Electrodeposited Electrocatalysts For Rechargeable Zinc-air Batteries," University of Alberta, 2018.

[5] Hannan, M. A., Hoque, M. M., Mohamed, A., and Ayob, A., "Review of energy storage systems for electric vehicle applications: Issues and challenges," *Renew. Sustain. Energy Rev.*, vol. 69, no. August 2016, pp. 771–789, 2017.

[6] Akinyele, D. O. and Rayudu, R. K., "Review of energy storage technologies for sustainable power networks," *Sustain. Energy Technol. Assessments*, vol. 8, pp. 74–91, 2014.

[7] Guarnieri, M., Mattavelli, P., Petrone, G., and Spagnuolo, G., "Vanadium redox flow batteries: Potentials and challenges of an emerging storage technology," *IEEE Ind. Electron. Mag.*, vol. 10, no. 4, pp. 20–31, 2016.

[8] Fu, J., Cano, Z. P., Park, M. G., Yu, A., Fowler, M., and Chen, Z., "Electrically Rechargeable Zinc-Air Batteries : Progress , Challenges , and Perspectives," *Adv. Mater.*, vol. 29, no. 7, 2016.

[9] Cheng, F. and Chen, J., "Metal – air batteries : from oxygen reduction electrochemistry to cathode catalysts," *Chem. Soc. Rev.*, vol. 41, pp. 2172–2192, 2012.

[10] Osgood, H., Devaguptapu, S. V., Xu, H., Cho, J., and Wu, G., "Transition metal (Fe, Co, Ni, and Mn) oxides for oxygen reduction and evolution bifunctional catalysts in alkaline media," *Nano Today*, vol. 11, no. 5, pp. 601–625, 2016.

[11] George, S. M., "Atomic Layer Deposition: An Overview," *Chem. Rev.*, vol. 110, p. 111, 2010.

[12] Pickrahn, K. L., Gorlin, Y., Seitz, L. C., Garg, A., Nordlund, D., Jaramillo, F., and Bent, S. F., "Applications of ALD MnO to electrochemical water splitting," *Phys. Chem. Chem. Phys.*, vol. 17, pp. 14003–14011, 2015.

[13] Cook, T. R., Dogutan, D. K., Reece, S. Y., Surendranath, Y., Teets, T. S., and Nocera, D. G., "Solar energy supply and storage for the legacy and nonlegacy worlds," *Chem. Rev.*, vol. 110, no. 11, pp. 6474–6502, 2010.

[14] Lee, J., Kim, S. T., Cao, R., Choi, N., Liu, M., and Lee, K. T., "Metal – Air Batteries with

High Energy Density : Li – Air versus Zn – Air," *Adv. Energy Mater.*, vol. 1, pp. 34–50, 2011.

[15] Zhang, T., Tao, Z., and Chen, J., "Magnesium-air batteries: From principle to application," *Mater. Horizons*, vol. 1, no. 2, pp. 196–206, 2014.

[16] Mokhtar, M., Talib, M. Z. M., Majlan, E. H., Tasirin, S. M., Ramli, W. M. F. W., Daud, W. R. W., and Sahari, J., "Recent developments in materials for aluminum-air batteries: A review," *J. Ind. Eng. Chem.*, vol. 32, pp. 1–20, 2015.

[17] Davari, E. and Ivey, D., "Bifunctional Electrocatalysts for Zn-air Batteries," *Sustain. Energy Fuels*, vol. 2, pp. 39–67, 2017.

[18] Ross, P. N. and Sattler, M., "The Corrosion of Carbon Black Anodes in Alkaline Electrolyte," *J. Electrochem. Soc.*, vol. 135, no. 6, pp. 1464–1470, 1988.

[19] Li, Y. and Dai, H., "Recent advances in zinc–air batteries," *Chem. Soc. Rev.*, vol. 43, no. 15, p. 5257, 2014.

[20] Fu, J., Cano, Z. P., Park, M. G., Yu, A., Fowler, M., and Chen, Z., "Electrically Rechargeable Zinc–Air Batteries: Progress, Challenges, and Perspectives," *Adv. Mater.*, vol. 29, no. 7, 2016.

[21] Zhang, X., Li, B., Liu, C., Chu, Q., Liu, F., Wang, X., Chen, H., and Liu, X., "Rapid microwave-assisted hydrothermal synthesis of morphology-tuned MnO 2 nanocrystals and their electrocatalytic activities for oxygen reduction," *Mater. Res. Bull.*, vol. 48, no. 7, pp. 2696–2701, 2013.

[22] Lee, D. U., Park, M. G., Park, H. W., Seo, M. H., Ismayilov, V., Ahmed, R., and Chen, Z., "Electrochemistry Communications Highly active Co-doped LaMnO 3 perovskite oxide and N-doped carbon nanotube hybrid bi-functional catalyst for rechargeable zinc – air batteries," *Electrochem. commun.*, vol. 60, pp. 38–41, 2015.

[23] Wang, H., Tang, C., and Zhang, Q., "A Review of Precious-Metal-Free Bifunctional Oxygen Electrocatalysts : Rational Design and Applications in Zn − Air Batteries," *Adv. Energy Mater.*, vol. 28, p. 1803329, 2018.

[24] Kim, H., Jeong, G., Kim, Y. U., Kim, J. H., Park, C. M., and Sohn, H. J., "Metallic anodes for next generation secondary batteries," *Chem. Soc. Rev.*, no. 42, pp. 9011–9034, 2013.

[25] Sherman, S. B., Cano, Z. P., Fowler, M., and Chen, Z., "Range-extending Zinc-air battery for electric vehicle," vol. 6, no. January, pp. 121–145, 2018.

[26] Reddy, T. B., *Linden's Handbook of Batteries*, Fourth Edi. New York: McGraw-Hill Education, 2011.

[27] Xiong, M., Clark, M. P., Labbe, M., and Ivey, D. G., "A horizontal zinc-air battery with physically decoupled oxygen evolution/reduction reaction electrodes," *J. Power Sources*, vol. 393, no. May, pp. 108–118, 2018.

[28] Zhang, J., Zhao, Z., Xia, Z., and Dai, L., "A metal-free bifunctional electrocatalyst for oxygen reduction and oxygen evolution reactions," *Nat. Nanotechnol.*, vol. 10, no. 5, pp. 444–452, 2015.

[29] Ahn, S. H., Yu, X., and Manthiram, A., "'Wiring' Fe-Nx-Embedded Porous Carbon Framework onto 1D Nanotubes for Efficient Oxygen Reduction Reaction in Alkaline and Acidic Media," *Adv. Mater.*, vol. 29, no. 26, pp. 1–10, 2017.

[30] Yan, Z., Wang, E., Gao, J., Yang, J., Wu, C., Jiang, L., Zhu, M., and Sun, G., "An Exceptionally Facile Synthesis of Highly Efficient Oxygen Evolution Electrodes for Zinc-Oxygen Batteries," *ChemElectroChem*, vol. 4, no. 9, pp. 2190–2195, 2017.

[31] Hong, W., Li, H., and Wang, B., "A horizontal three-electrode structure for zinc-air batteries with long-term cycle life and high performance," *Int. J. Electrochem. Sci.*, vol. 11, no. 5, pp. 3843–3851, 2016.

[32] Pei, P., Wang, K., and Ma, Z., "Technologies for extending zinc-air battery's cyclelife: A review," *Applied Energy*, vol. 128. pp. 315–324, 2014.

[33] Huang, Z.-F., Wang, J., Peng, Y., Jung, C.-Y., Fisher, A., and Wang, X., "Design of Efficient Bifunctional Oxygen Reduction/Evolution Electrocatalyst: Recent Advances and Perspectives," *Adv. Energy Mater.*, vol. 1700544, p. 1700544, 2017.

[34] Suntivich, J., Gasteiger, H. A., Yabuuchi, N., Nakanishi, H., Goodenough, J. B., and Shao-Horn, Y., "Design principles for oxygen-reduction activity on perovskite oxide catalysts for fuel cells and metal–air batteries," *Nat. Chem.*, vol. 3, no. 8, pp. 647–647, 2011.

[35] Hong, W. T., Risch, M., Stoerzinger, K. A., Grimaud, A., Suntivich, J., and Shao-Horn, Y., "Toward the rational design of non-precious transition metal oxides for oxygen electrocatalysis," *Energy Environ. Sci.*, vol. 8, no. 5, pp. 1404–1427, 2015.

[36] Ryabova, A. S., Napolskiy, F. S., Poux, T., Istomin, S. Y., Bonnefont, A., Antipin, D. M., Baranchikov, A. Y., Levin, E. E., Abakumov, A. M., Kéranguéven, G., Antipov, E. V., Tsirlina, G. A., and Savinova, E. R., "Rationalizing the Influence of the Mn(IV)/Mn(III) Red-Ox Transition on the Electrocatalytic Activity of Manganese Oxides in the Oxygen Reduction Reaction," *Electrochim. Acta*, vol. 187, pp. 161–172, 2016.

[37] Kuznetsov, D. A., Han, B., Yu, Y., Rao, R. R., and Hwang, J., "Tuning Redox Transitions via Inductive Effect in Metal Oxides and Complexes , and Implications in Oxygen Electrocatalysis," *Joule*, vol. 2, pp. 225–244, 2018.

[38] Lima, F. H. B., Zhang, J., Shao, M. H., Sasaki, K., Vukmirovic, M. B., Ticianelli, E. A., and Adzic, R. R., "Catalytic activity - d-band center correlation for the O2 reduction reaction on platinum in alkaline solutions," *J. Phys. Chem. C*, vol. 111, no. 1, pp. 404–410, 2007.

[39] Nørskov, J. K., Rossmeisl, J., Logadottir, A., Lindqvist, L., Kitchin, J. R., Bligaard, T., and Jónsson, H., "Origin of the overpotential for oxygen reduction at a fuel-cell cathode,"

J. Phys. Chem. B, vol. 108, no. 46, pp. 17886–17892, 2004.

[40] Busch, M., Halck, N. B., Kramm, U. I., Siahrostami, S., Krtil, P., and Rossmeisl, J., "Beyond the top of the volcano?- A unified approach to electrocatalytic oxygen reduction and oxygen evolution," *Nano Energy*, vol. 29, pp. 126–135, 2016.

[41] Ludwig, J., "Bifunctional oxygen / air electrodes," *J. Power Sources*, vol. 155, pp. 23–32, 2006.

[42] Stoerzinger, K. A., Risch, M., Han, B., and Shao-horn, Y., "Recent Insights into Manganese Oxides in Catalyzing Oxygen Reduction Kinetics," *ACS Catal.*, vol. 5, pp. 6021–6031, 2015.

[43] Shao, M., Chang, Q., Dodelet, J., and Chenitz, R., "Recent Advances in Electrocatalysts for Oxygen Reduction Reaction," *Chem. Rev.*, vol. 116, pp. 3594–3657, 2016.

[44] Wei, W., Cui, X., Chen, W., and Ivey, D. G., "Manganese oxide-based materials as electrochemical supercapacitor electrodes.," *Chem. Soc. Rev.*, vol. 40, no. 3, pp. 1697–721, Mar. 2011.

[45] Lima, F. H. B., Calegaro, M. L., and Ticianelli, E. A., "Investigations of the catalytic properties of manganese oxides for the oxygen reduction reaction in alkaline media," *J. Electroanal. Chem.*, vol. 590, no. 2, pp. 152–160, 2006.

[46] Toh, R. J., Sofer, Z., and Pumera, M., "Transition Metal Oxides for the Oxygen Reduction Reaction: Influence of the Oxidation States of the Metal and its Position on the Periodic Table," *ChemPhysChem*, vol. 16, no. 16, pp. 3527–3531, 2015.

[47] Gorlin, Y., Chung, C., Nordlund, D., Clemens, B. M., and Jaramillo, T. F., "Mn 3 O 4 Supported on Glassy Carbon: An Active Non-Precious Metal Catalyst for the Oxygen Reduction Reaction," *ACS Catal.*, vol. 2, pp. 2687–2694, 2012.

[48] Duan, J., Zheng, Y., Chen, S., Tang, Y., Jaroniec, M., and Shizhang, Q., "Mesoporous hybrid material composed of Mn 3 O 4 nanoparticles on nitrogen-doped graphene for highly efficient oxygen reduction reaction †," *Chem. Commun.*, vol. 49, p. 7705, 2013.

[49] Fan, Y., Wu, Y., Huang, X., Clavel, G., Amsalem, P., Koch, N., and Pinna, N., "Polarization Resistance-Free Mn3O4-Based Electrocatalysts for the Oxygen Reduction Reaction," *ChemElectroChem*, vol. 5, pp. 1–10, 2018.

[50] Messaoudi, B., Joiret, S., Keddam, M., and Takenouti, H., "Anodic behaviour of manganese in alkaline medium," *Electrochim. Acta*, vol. 46, no. 16, pp. 2487–2498, 2001.

[51] McBreen, J., "The electrochemistry of β-MnO2 and γ-MnO2 in alkaline electrolyte," *Electrochim. Acta*, vol. 20, no. 3, pp. 221–225, 1975.

[52] Gorlin, Y., Lassalle-Kaiser, B., Benck, J. D., Gul, S., Webb, S. M., Yachandra, V. K., Yano, J., and Jaramillo, T. F., "In Situ X-ray Absorption Spectroscopy Investigation of a Bifunctional Manganese Oxide Catalyst with High Activity for Electrochemical Water Oxidation and Oxygen Reduction," *J. Am. Chem. Soc.*, vol. 135, no. 23, p. 8525, 2013.

[53] Rios, E., Gautier, J., Poillerat, G., and Chartier, P., "Mixed valency spinel oxides of transition metals and electrocatalysis : case of the MnxCo3-xO4 system," *Electrochim. Acta*, vol. 44, pp. 1491–1497, 1998.

[54] Pike, J., Hanson, J., Zhang, L., Chan, S., and York, N., "Synthesis and Redox Behavior of Nanocrystalline Hausmannite," *Chem. Mater.*, vol. 19, pp. 5609–5616, 2007.

[55] Matsumoto, Y., Yoneyama, H., and Tamura, H., "Catalytic activity for electrochemical reduction of oxygen of lanthanum nickel oxide and related oxides," *J. Electroanal. Chem.*, vol. 79, no. 2, pp. 319–326, 1977.

[56] Matsumoto, Y., Yoneyama, H., and Tamura, H., "Influence of the nature of the conduction band of transition metal oxides on catalytic activity for oxygen reduction," *J. Electroanal. Chem. Interfacial Electrochem.*, vol. 83, no. 2, pp. 237–243, 1977.

[57] Dai, L., Xue, Y., Qu, L., Choi, H.-J., and Baek, J.-B., "Metal-Free Catalysts for Oxygen Reduction Reaction," *Chem. Rev.*, vol. 115, no. 11, pp. 4823–4892, 2015.

[58] Li, Q., Cao, R., Cho, J., and Wu, G., "Nanocarbon electrocatalysts for oxygen reduction in alkaline media for advanced energy conversion and storage," *Adv. Energy Mater.*, vol. 4, no. 6, 2014.

[59] Wei, Q., Fu, Y., Zhang, G., and Sun, S., "Rational design of carbon-based oxygen electrocatalysts for zinc – air batteries," *Curr. Opin. Electrochem.*, vol. 4, no. 1, pp. 45–59, 2017.

[60] Pan, J., Xu, Y. Y., Yang, H., Dong, Z., Liu, H., and Xia, B. Y., "Advanced Architectures and Relatives of Air Electrodes in Zn-Air Batteries," *Adv. Sci.*, vol. 5, p. 1700691, 2018.

[61] Qian, Y., Khan, I. A., and Zhao, D., "Electrocatalysts Derived from Metal – Organic Frameworks for Oxygen Reduction and Evolution Reactions in Aqueous Media," *Small*, vol. 13, p. 1701143, 2017.

[62] Liu, B., Shioyama, H., Akita, T., and Xu, Q., "Metal-Organic Framework as a Template for Porous Carbon," *J. Am. Chem. Soc.*, vol. 130, pp. 5390–5391, 2008.

[63] Fu, S., Zhu, C., Song, J., Du, D., and Lin, Y., "Metal-Organic Framework-Derived Non-Precious Metal Nanocatalysts for Oxygen Reduction Reaction," *Adv. Energy Mater.*, vol. 7, p. 1700363, 2017.

[64] Puurunen, R. L., "A short history of atomic layer deposition: Tuomo Suntola's atomic layer epitaxy," *Chem. Vap. Depos.*, vol. 20, no. 10–12, pp. 332–344, 2014.

[65] Aleskovskii, V. B. and Kol'tsov, S. I., "Some characteristics of molecularlayering reactions," in *Abstract of Scientific and Technical Conference,Goskhimizdat*, 1965, p. 67.

[66] Johnson, R. W., Hultqvist, A., and Bent, S. F., "A brief review of atomic layer deposition: from fundamentals to applications," *Mater. Today*, vol. 17, no. 5, pp. 236–246, 2014.

[67] Marichy, C., Bechelany, M., and Pinna, N., "Atomic layer deposition of nanostructured

materials for energy and environmental applications," *Adv. Mater.*, vol. 24, no. 8, pp. 1017–1032, 2012.

[68] Ma, L., Nuwayhid, R. B., Wu, T., Lei, Y., Amine, K., and Lu, J., "Atomic Layer Deposition for Lithium-Based Batteries," *Adv. Mater. Interfaces*, vol. 3, no. 21, 2016.

[69] Guan, C. and Wang, J., "Recent Development of Advanced Electrode Materials by Atomic Layer Deposition for Electrochemical Energy Storage," *Adv. Sci.*, vol. 3, no. 10, pp. 1–23, 2016.

[70] Elam, J. W., Dasgupta, N. P., and Prinz, F. B., "ALD for clean energy conversion, utilization, and storage," *MRS Bull.*, vol. 36, no. 11, pp. 899–906, 2011.

[71] Muneshwar, T. and Cadien, K., "AxBAxB … pulsed atomic layer deposition : Numerical growth model and experiments," *J. Appl. Phys.*, vol. 119, 2016.

[72] Knisley, T. J., Kalutarage, L. C., and Winter, C. H., "Precursors and chemistry for the atomic layer deposition of metallic first row transition metal films," *Coordination Chemistry Reviews*, vol. 257, no. 23–24. pp. 3222–3231, 2013.

[73] Puurunen, R. L., "Growth Per Cycle in Atomic Layer Deposition: A Theoretical Model," *Chem. Vap. Depos.*, vol. 9, no. 5, pp. 249–257, 2003.

[74] Sell, B., Sanger, A., Pomplun, K., and Krautschneider, W., "Chemical vapor deposition of tungsten silicide (WSi x) for high aspect ratio applications," *Thin Solid Films*, vol. 443, no. 03, pp. 97–107, 2003.

[75] Qin, X. and Zaera, F., "Oxidizing versus Reducing Co-Reactants in Manganese Atomic Layer Deposition (ALD) on Silicon Oxide Surfaces," *ECS J. Solid State Sci. Technol.*, vol. 3, no. 5, pp. 89–94, 2014.

[76] Pickrahn, K. L., Park, S. W., Gorlin, Y., Lee, H. B. R., Jaramillo, T. F., and Bent, S. F., "Active MnO x electrocatalysts prepared by atomic layer deposition for oxygen evolution and oxygen reduction reactions," *Adv. Energy Mater.*, vol. 2, no. 10, pp. 1269–1277, 2012.

[77] Singh, T., Lehnen, T., Leuning, T., and Mathur, S., "Atomic layer deposition grown MO x thin films for solar water splitting: Prospects and challenges," *J. Vac. Sci. Technol. A*, vol. 33, no. 1, 2015.

[78] Meng, X., Wang, X., Geng, D., Ozgit-Akgun, C., Schneider, N., and Elam, J. W., "Atomic layer deposition for nanomaterial synthesis and functionalization in energy technology," *Mater. Horiz.*, vol. 4, no. 2, pp. 133–154, 2017.

[79] Guo, Z. and Tan, L., *Fundamentals and Applications of Nanomaterials*. Norwood: Artech House, 2009.

[80] Burton, B. B., Fabreguette, F. H., and George, S. M., "Atomic layer deposition of MnO using Bis (ethylcyclopentadienyl) manganese and H 2 O," *Thin Solid Films*, vol. 517, no. 19, pp. 5658–5665, 2009.

[81] Marichy, C. and Pinna, N., "Carbon-nanostructures coated / decorated by atomic layer deposition : Growth and applications," *Coord. Chem. Rev.*, vol. 257, no. 23–24, pp. 3232–3253, 2013.

[82] Harris, P. J. F., "Structure of non-graphitising carbons," *Int. Mater. Rev.*, vol. 42, no. 5, pp. 206–218, 1997.

[83] Jin, H., Hagen, D., and Karppinen, M., "Low-temperature atomic layer deposition of crystalline manganese oxide thin films," *Dalt. Trans.*, vol. 45, pp. 18737–18741, 2016.

[84] Mattelaer, F., Bosserez, T., Rongé, J., Martens, J. A., Dendooven, J., and Detavernier, C., "Manganese oxide films with controlled oxidation state for water splitting devices through a combination of atomic layer deposition and post-deposition annealing," *RSC Adv.*, vol. 6, no. 6, pp. 98337–98343, 2016.

[85] Strandwitz, N. C., Comstock, D. J., Grimm, R. L., Nichols-Nielander, A. C., Elam, J., and Lewis, N. S., "Photoelectrochemical behavior of n-type Si(100) electrodes coated with thin films of manganese oxide grown by atomic layer deposition," *J. Phys. Chem. C*, vol. 117, no. 10, pp. 4931–4936, 2013.

[86] Silva, R. M., Clavel, G., Fan, Y., Amsalem, P., Koch, N., Silva, R. F., and Pinna, N., "Coating of Vertically Aligned Carbon Nanotubes by a Novel Manganese Oxide Atomic Layer Deposition Process for Binder-Free Hybrid Capacitors," *Adv. Mater. Interfaces*, vol. 3, no. 21, 2016.

[87] Lipson, A. L., Puntambekar, K., Comstock, D. J., Meng, X., Geier, M. L., Elam, J. W., and Hersam, M. C., "Nanoscale investigation of solid electrolyte interphase inhibition on li-ion battery MnO electrodes via atomic layer deposition of Al 2O3," *Chem. Mater.*, vol. 26, no. 2, pp. 935–940, 2014.

[88] Wójcik, A., Kopalko, K., Godlewski, M., Guziewicz, E., Jakieła, R., Minikayev, R., and Paszkowicz, W., "Magnetic properties of ZnMnO films grown at low temperature by atomic layer deposition," *Appl. Phys. Lett.*, vol. 89, no. 5, pp. 1–4, 2006.

[89] Wojcik, A., Kiecana, M., Kopalko, K., Godlewski, M., Guziewicz, E., Yatsunenko, S., Lusakowska, E., Minikayev, R., Paszkowicz, W., Swiatek, K., Wilamowski, Z., Sawicki, M., and Dietl, T., "Magnetic , Structural , and Optical Properties of Low Temperature ZnMnO Grown by Atomic Layer Epitaxy," *Acta Phys. Pol. A*, vol. 108, no. 5, pp. 915–921, 2005.

[90] Miikkulainen, V., Ruud, A., Østreng, E., Nilsen, O., Laitinen, M., Sajavaara, T., and Fjellvaìšg, H., "Atomic layer deposition of spinel lithium manganese oxide by film-body-controlled lithium incorporation for thin-film lithium-ion batteries," *J. Phys. Chem. C*, vol. 118, no. 2, pp. 1258–1268, 2014.

[91] Matsumoto, K., Maekawa, K., Nagai, H., and Koike, J., "Deposition behavior and substrate dependency of ALD MnOx diffusion barrier layer," *Proc. 2013 IEEE Int. Interconnect Technol. Conf. IITC 2013*, pp. 1–3, 2013.

[92] Yang, X., Du, C., Liu, R., Xie, J., and Wang, D., "Balancing photovoltage generation and charge-transfer enhancement for catalyst-decorated photoelectrochemical water splitting: A case study of the hematite/MnOx combination," *J. Catal.*, vol. 304, pp. 86–91, 2013.

[93] Yang, N., Yoo, J. S., Schumann, J., Bothra, P., Singh, J. A., Valle, E., Abild-Pedersen, F., Nørskov, J. K., and Bent, S. F., "Rh-MnO Interface Sites Formed by Atomic Layer Deposition Promote Syngas Conversion to Higher Oxygenates," *ACS Catal.*, vol. 25, pp. 5746–5757, 2017.

[94] Young, M. J., Neuber, M., Cavanagh, A. C., Sun, H., Musgrave, C. B., and George, S. M., "Sodium Charge Storage in Thin Films of MnO 2 Derived by Electrochemical Oxidation of MnO Atomic Layer Deposition Films," *J. Electrochem. Soc.*, vol. 162, no. 14, pp. A2753–A2761, 2015.

[95] Du, L., Yu, S., Liu, X., and Ding, Y., "An efficient atomic layer deposition process of MnOx films using bis(N,N′-di-tert-butylacetamidinato)manganese-(II) and H2O as reactants," *Appl. Surf. Sci.*, vol. 486, no. January, pp. 460–465, 2019.

[96] Lu, H. L., Scarel, G., Li, X. L., and Fanciulli, M., "Thin MnO and NiO films grown using atomic layer deposition from ethylcyclopentadienyl type of precursors," *J. Cryst. Growth*, vol. 310, no. 24, pp. 5464–5468, 2008.

[97] Mattelaer, F., Vereecken, P. M., Dendooven, J., and Detavernier, C., "Deposition of MnO Anode and MnO 2 Cathode Thin Films by Plasma Enhanced Atomic Layer Deposition Using the Mn(thd) 3 Precursor," *Chem. Mater.*, vol. 27, no. 10, pp. 3628–3635, 2015.

[98] Nilsen, O., Fjellvåg, H., and Kjekshus, A., "Growth of manganese oxide thin films by atomic layer deposition," *Thin Solid Films*, vol. 444, no. 1–2, pp. 44–51, 2003.

[99] Nilsen, O., Foss, S., Fjellvåg, H., and Kjekshus, A., "Effect of substrate on the characteristics of manganese(IV) oxide thin films prepared by atomic layer deposition," *Thin Solid Films*, vol. 468, no. 1–2, pp. 65–74, 2004.

[100] Young, M. J., Hare, C. D., Cavanagh, A. S., Musgrave, C. B., and George, S. M., "Rapid Growth of Crystalline Mn5O8 by Self-Limited Multilayer Deposition using Mn(EtCp)2 and O3," *ACS Appl. Mater. Interfaces*, vol. 8, no. 28, pp. 18560–18569, 2016.

[101] Xiong, M. and Ivey, D. G., "Electrodeposited MnOX-CoFe as Bifunctional Electrocatalysts for Rechargeable Zinc-air Batteries," *ECS Trans.*, vol. 75, no. 36, pp. 1–7, 2017.

[102] Gauvin, R., "Casino v2.48." Université de Sherbrooke, Sherbrook, Quebec, Canada.

[103] Kohno, Y., Okunishi, E., Tomita, T., Ishikawa, I., Kaneyama, T., Ohkura, Y., and Kondo, Y., "Development of a Cold Field-Emission Gun for a 200kVAtomic Resolution Electron Microscope," vol. 24, no. 7, pp. 1–3, 2010.

[104] Williams, D. B. and Carter, C. B., *The Transmission electron microscope*. 2009.

[105] Yamashita, S., Kikkawa, J., Yanagisawa, K., Nagai, T., and Ishizuka, K., "Atomic number

dependence of Z contrast in scanning transmission electron microscopy," *Sci. Rep.*, vol. 8, p. 12325, 2018.

[106] Yücelen, E., Lazić, I., and Bosch, E. G. T., "Phase contrast scanning transmission electron microscopy imaging of light and heavy atoms at the limit of contrast and resolution," *Sci. Rep.*, vol. 8, p. 2676, 2018.

[107] Isabell, T., Brink, J., Kawasaki, M., and Armbruster, B., "Development of a 200kV Atomic Resolution Analytical Electron Microscope Development of a 200kV Atomic Resolution Analytical Electron," *Micros. Today*, no. May, 2009.

[108] Lu, P., Zhou, L., Kramer, M. J., and Smith, D. J., "Atomic-scale chemical imaging and quantification of metallic alloy structures by energy-dispersive x-ray spectroscopy," *Sci. Rep.*, vol. 4, pp. 1–5, 2014.

[109] Fujiwara, H., *Spectroscopic Ellipsometry- Principals and Applications*. West Sussex, England: Wiley, 2007.

[110] Liu, G., Bertuch, A., Deguns, E. W., Dalberth, M. J., Sundaram, G. M., and Becker, J. S., "Method and Apparatus for Precursor Delivery- US 2011/0311726 A1," 2011.

[111] Lee, Y. H., Chang, K. H., and Hu, C. C., "Differentiate the pseudocapacitance and double-layer capacitance contributions for nitrogen-doped reduced graphene oxide in acidic and alkaline electrolytes," *J. Power Sources*, vol. 227, pp. 300–308, 2013.

[112] Xiong, M. and Ivey, D. G., "Composition effects of electrodeposited Co-Fe as electrocatalysts for the oxygen evolution reaction," *Electrochim. Acta*, vol. 260, pp. 872–881, 2018.

[113] Xiong, M. and Ivey, D. G., "Electrodeposited Co-Fe as an oxygen evolution catalyst for rechargeable zinc-air batteries," *Electrochem. commun.*, vol. 75, pp. 73–77, 2017.

[114] Muneshwar, T., Shoute, G., Barlage, D., and Cadien, K., "Plasma enhanced atomic layer deposition of ZnO with diethyl zinc and oxygen plasma: Effect of precursor decomposition," *J. Vac. Sci. Technol. A*, vol. 34, no. 5, 2016.

[115] Neishi, K., Aki, S., Matsumoto, K., Sato, H., Itoh, H., Hosaka, S., and Koike, J., "Formation of a manganese oxide barrier layer with thermal chemical vapor deposition for advanced large-scale integrated interconnect structure," *Appl. Phys. Lett.*, vol. 93, no. 3, pp. 1–4, 2008.

[116] Dixit, V. K., Neishi, K., Akao, N., and Koike, J., "Structural and Electronic Properties of a Mn Oxide Diffusion Barrier Layer Formed by Chemical Vapor Deposition," *Ieee Trans. Device Mater. Reliab.*, vol. 11, no. 2, pp. 295–302, 2011.

[117] Strem Chemicals, "Safety Data Sheet- Trimethylaluminum." 2016.

[118] Strem Chemicals, "Safety Data Sheet- Diethylzinc," 2016.

[119] Young, M. J., Holder, A. M., George, S. M., and Musgrave, C. B., "Charge Storage in

Cation Incorporated α-MnO 2," *Chem. Mater.*, vol. 27, pp. 1172–1180, 2015.

[120] Siddiqi, G., Luo, Z., Xie, Y., Pan, Z., Zhu, Q., Röhr, J. A., Cha, J. J., and Hu, S., "Stable Water Oxidation in Acid Using Manganese-Modified TiO 2 Protective Coatings," *ACS Appl. Mater. Interfaces*, vol. 10, pp. 18805–18815, 2018.

[121] Wei, W., Cui, X., Chen, W., and Ivey, D. G., "Manganese oxide-based materials as electrochemical supercapacitor electrodes," *Chem. Soc. Rev.*, vol. 40, no. 3, pp. 1697–1721, 2011.

[122] Dalili, N., Clark, M. P., Davari, E., and Ivey, D. G., "Microstructural characterization of the cycling behavior of electrodeposited manganese oxide supercapacitors using 3D electron tomography," *J. Power Sources*, vol. 328, pp. 318–328, 2016.

[123] Li, H., Guo, Z., and Wang, X., "Atomic-layer-deposited ultrathin Co9S8on carbon nanotubes: An efficient bifunctional electrocatalyst for oxygen evolution/reduction reactions and rechargeable Zn-air batteries," *J. Mater. Chem. A*, vol. 5, no. 40, pp. 21353–21361, 2017.

[124] Nagai, H., Takashima, S., Hiramatsu, M., Hori, M., and Goto, T., "Behavior of atomic radicals and their effects on organic low dielectric constant film etching in high density N2/H2and N2/NH3plasmas," *J. Appl. Phys.*, vol. 91, no. 5, pp. 2615–2621, 2002.

[125] Shimizu, H., Sakoda, K., Momose, T., Koshi, M., and Shimogaki, Y., "Hot-wire-assisted atomic layer deposition of a high quality cobalt film using cobaltocene: Elementary reaction analysis on NH x radical formation," *J. Vac. Sci. Technol. A*, vol. 30, 2012.

[126] Chigane, M. and Ishikawa, M., "Manganese oxide thin film preparation by potentiostatic electrolyses and electrochromism," *J. Electrochem. Soc.*, vol. 147, no. May 2010, pp. 2246–2251, 2000.

[127] Moulder, J. F., Stickle, W. F., Sobol, P. E., and Bomben, K. D., *Handbook of X-ray photoelectron spectroscopy: a reference book of standard spectra for identification and interpretation of XPS data*. Eden Prairie, 1992.

[128] Hueso, J. L., Espinós, J. P., Caballero, A., Cotrino, J., and González-Elipe, A. R., "XPS investigation of the reaction of carbon with NO, O2, N2and H2O plasmas," *Carbon N. Y.*, vol. 45, pp. 89–96, 2007.

[129] Takeuchi, K., Yamamoto, S., Hamamoto, Y., Shiozawa, Y., Tashima, K., Fukidome, H., Koitaya, T., Mukai, K., Yoshimoto, S., Suemitsu, M., Morikawa, Y., Yoshinobu, J., and Matsuda, I., "Adsorption of CO2on Graphene: A Combined TPD, XPS, and vdW-DF Study," *J. Phys. Chem. C*, vol. 121, no. 5, pp. 2807–2814, 2017.

[130] Clark, M. and Ivey, D. G., "Nucleation and growth of electrodeposited Mn oxide rods for supercapacitor electrodes," *Nanotechnology*, vol. 26, no. 38, 2015.

[131] Elam, J. W., Routkevitch, D., Mardilovich, P. P., and George, S. M., "Conformal coating on ultrahigh-aspect-ratio nanopores of anodic alumina by atomic layer deposition," *Chem. Mater.*, vol. 15, no. 18, pp. 3507–3517, 2003.

[132] Lima, F. H. B., Calegaro, M. L., and Ticianelli, E. A., "Electrocatalytic activity of manganese oxides prepared by thermal decomposition for oxygen reduction," *Electrochim. Acta*, vol. 52, no. 11, pp. 3732–3738, 2007.

[133] Neburchilov, V., Wang, H., Martin, J. J., and Qu, W., "A review on air cathodes for zinc-air fuel cells," *J. Power Sources*, vol. 195, no. 5, pp. 1271–1291, 2010.

[134] Li, Y. and Lu, J., "Metal-Air Batteries: Will They Be the Future Electrochemical Energy Storage Device of Choice?," *ACS Energy Lett.*, vol. 2, no. 6, pp. 1370–1377, 2017.

[135] Kim, G. P., Sun, H. H., and Manthiram, A., "Design of a sectionalized MnO2-Co3O4electrode via selective electrodeposition of metal ions in hydrogel for enhanced electrocatalytic activity in metal-air batteries," *Nano Energy*, vol. 30, no. September, pp. 130–137, 2016.

[136] Hadidi, L., Davari, E., Iqbal, M., Purkait, T. K., Ivey, D. G., and Veinot, J. G. C., "Spherical nitrogen-doped hollow mesoporous carbon as an efficient bifunctional electrocatalyst for Zn-air batteries," *Nanoscale*, vol. 7, pp. 20547–20556, 2015.

[137] Hadidi, L., Davari, E., Ivey, D. G., and Veinot, J. G. C., "Microwave-assisted synthesis and prototype oxygen reduction electrocatalyst application of N-doped carbon-coated Fe3O4nanorods," *Nanotechnology*, vol. 28, no. 9, 2017.

[138] Xiong, M. and Ivey, D. G., "Sequentially Electrodeposited MnO X /Co-Fe as Bifunctional Electrocatalysts for Rechargeable Zinc-Air Batteries," *J. Electrochem. Soc.*, vol. 164, no. 6, pp. A1012–A1021, 2017.

[139] Li, Y., Gong, M., Liang, Y., Feng, J., Kim, J.-E., Wang, H., Hong, G., Zhang, B., and Dai, H., "Advanced zinc-air batteries based on high-performance hybrid electrocatalysts," *Nat. Commun.*, vol. 4, no. May, p. 1805, 2013.

[140] Pickrahn, K. L., Garg, A., and Bent, S. F., "ALD of ultrathin ternary oxide electrocatalysts for water splitting," *ACS Catal.*, vol. 5, no. 3, pp. 1609–1616, 2015.

[141] Hsu, I. J., Hansgen, D. A., Mccandless, B. E., Willis, B. G., and Chen, J. G., "Atomic layer deposition of Pt on tungsten monocarbide (WC) for the oxygen reduction reaction," *J. Phys. Chem. C*, vol. 115, no. 9, pp. 3709–3715, 2011.

[142] Jukk, K., Kongi, N., Tarre, A., Rosental, A., Treshchalov, A. B., Kozlova, J., Ritslaid, P., Matisen, L., Sammelselg, V., and Tammeveski, K., "Electrochemical oxygen reduction behaviour of platinum nanoparticles supported on multi-walled carbon nanotube/titanium dioxide composites," *J. Electroanal. Chem.*, vol. 735, pp. 68–76, 2014.

[143] Su, C.-Y., Liu, B.-H., Lin, T.-J., Chi, Y.-M., Kei, C.-C., Wang, K.-W., and Perng, T.-P., "Carbon nanotube-supported Cu $_3$ N nanocrystals as a highly active catalyst for oxygen reduction reaction," *J. Mater. Chem. A*, vol. 3, no. 37, pp. 18983–18990, 2015.

[144] Clark, M. P., Muneshwar, T., Xiong, M., Cadien, K., and Ivey, D. G., "Saturation Behavior of Atomic Layer Deposition MnOx from Bis(Ethylcyclopentadienyl) Manganese and Water: Saturation Effect on Coverage of Porous Oxygen Reduction Electrodes for

Metal–Air Batteries," *ACS Appl. Nano Mater.*, vol. 2, pp. 267–277, 2018.

[145] Lee, H.-B.-R. and Kim, H., "High-Quality Cobalt Thin Films by Plasma-Enhanced Atomic Layer Deposition," *Electrochem. Solid-State Lett.*, vol. 9, no. 11, p. G323, 2006.

[146] Moore, T., Ellis, M., and Selwood, P. W., "Solid Oxides and Hydroxides of Manganese," *J. Am. Chem. Soc.*, vol. 72, p. 856, 1950.

[147] Kim, S. H., Choi, B. J., Lee, G. H., and Kim, B., "Ferrimagnetism in γ -Manganese Sesquioxide (γ − Mn 2 O 3) Nanoparticles," *J. Korean Phys. Soc.*, vol. 46, no. 4, pp. 941–944, 2005.

[148] Petitto, S. C. and Langell, M. A., "Surface composition and structure of Surface composition and structure of Co 3 O 4 „ 110 … and the effect of impurity segregation," *J. Vac. Sci. Technol. A*, vol. 22, no. 4, pp. 1690–1696, 2004.

[149] Tang, Q., Jiang, L., Liu, J., Wang, S., and Sun, G., "Effect of surface manganese valence of manganese oxides on the activity of the oxygen reduction reaction in alkaline media," *ACS Catal.*, vol. 4, no. 2, pp. 457–463, 2014.

[150] Pan, J., Tian, L., Zaman, S., Dong, Z., and Liu, H., "Recent Progress on Transition Metal Oxides as Bifunctional Catalysts for Lithium-Air and Zinc-Air Batteries," *Batter. Supercaps*, no. 1, pp. 1–13, 2018.

[151] Zhuang, S., Huang, K., Huang, C., Huang, H., Liu, S., and Fan, M., "Preparation of silver-modified La0.6Ca0.4CoO 3 binary electrocatalyst for bi-functional air electrodes in alkaline medium," *J. Power Sources*, vol. 196, no. 8, pp. 4019–4025, 2011.

[152] Al-Hakemy, A. Z., Nassr, A. B. A. A., Naggar, A. H., Salaheldin Elnouby, M., Soliman, H. M. A. E.-F., and Taher, M. A., "Electrodeposited cobalt oxide nanoparticles modified carbon nanotubes as a non-precious catalyst electrode for oxygen reduction reaction," *J. Appl. Electrochem.*, vol. 47, no. 2, pp. 183–195, 2017.

[153] Zhong, H., Campos-Roldán, C. A., Zhao, Y., Zhang, S., Feng, Y., and Alonso-vante, N., "Recent Advances of Cobalt-Based Electrocatalysts for Oxygen Electrode Reactions and Hydrogen Evolution Reaction," *Catalysts*, vol. 8, p. 559, 2018.

[154] Toh, R. J., Sheng, Y., Sofer, Z., Sedmidubsky, D., and Pumera, M., "Ternary Transition Metal Oxide Nanoparticles with Spinel Structure for the Oxygen Reduction Reaction **," *ChemElectroChem*, vol. 2, pp. 982–987, 2015.

[155] Shao, M., Chang, Q., Dodelet, J.-P., and Chenitz, R., "Recent Advances in Electrocatalysts for Oxygen Reduction Reaction.," *Chem. Rev.*, vol. 116, no. 6, pp. 3594–3657, 2016.

[156] Liu, Y., Ishihara, A., Mitsushima, S., Kamiya, N., and Ota, K., "Transition metal oxides as DMFC cathodes without platinum," *J. Electrochem. Soc.*, vol. 154, no. 7, pp. B664–B669, 2007.

[157] Liu, Y., Ishihara, A., Mitsushima, S., and Ota, K. ichiro, "Influence of sputtering power on

oxygen reduction reaction activity of zirconium oxides prepared by radio frequency reactive sputtering," *Electrochim. Acta*, vol. 55, no. 3, pp. 1239–1244, 2010.

[158] Descorme, C., Madier, Y., and Duprez, D., "Infrared Study of Oxygen Adsorption and Activation on Cerium–Zirconium Mixed Oxides," *J. Catal.*, vol. 196, no. 1, pp. 167–173, 2000.

[159] Bonakdarpour, A., Tucker, R. T., Fleischauer, M. D., Beckers, N. A., Brett, M. J., and Wilkinson, D. P., "Nanopillar niobium oxides as support structures for oxygen reduction electrocatalysts," *Electrochim. Acta*, vol. 85, pp. 492–500, 2012.

[160] Huang, K., Li, Y., Yan, L., and Xing, Y., "Nanoscale conductive niobium oxides made through low temperature phase transformation for electrocatalyst support," *RSC Adv.*, vol. 4, no. 19, p. 9701, 2014.

[161] Bothe, K. M., Hauff, P. A. Von, Afshar, A., Foroughi-abari, A., Cadien, K. C., and Barlage, D. W., "Electrical Comparison of HfO 2 and ZrO 2 Gate Dielectrics on GaN," *IEEE Trans. Electron Devices*, vol. 60, no. 12, pp. 4119–4124, 2013.

[162] Hausmann, D. M. and Gordon, R. G., "Surface morphology and crystallinity control in the atomic layer deposition (ALD) of hafnium and zirconium oxide thin films," *J. Cryst. Growth*, vol. 249, no. 1–2, pp. 251–261, 2003.

[163] Kim, W. S., Park, S. K., Moon, D. Y., Kang, B. W., Kim, H. Do, and Park, J. W., "Characteristics of high-k dielectric ECR-ALD lanthanum hafnium oxide (LHO) films," *Thin Solid Films*, vol. 517, no. 14, pp. 3900–3903, 2009.

[164] He, W., Schuetz, S., Solanki, R., Belot, J., and McAndrew, J., "Atomic Layer Deposition of Lanthanum Oxide Films for High-κ Gate Dielectrics," *Electrochem. Solid-State Lett.*, vol. 7, no. 7, p. G131, 2004.

[165] Suzuki, T., Kouda, M., Ahmet, P., Iwai, H., Kakushima, K., and Yasuda, T., "La $_2$ O $_3$ gate insulators prepared by atomic layer deposition: Optimal growth conditions and MgO/La $_2$ O $_3$ stacks for improved metal-oxide-semiconductor characteristics," *J. Vac. Sci. Technol. A Vacuum, Surfaces, Film.*, vol. 30, no. 5, p. 051507, 2012.

[166] Kim, W.-H., Maeng, W. J., Moon, K.-J., Myoung, J.-M., and Kim, H., "Growth characteristics and electrical properties of La2O3 gate oxides grown by thermal and plasma-enhanced atomic layer deposition," *Thin Solid Films*, vol. 519, no. 1, pp. 362–366, 2010.

[167] Maeng, W. J., Kim, W. H., and Kim, H., "Flat band voltage (VFB) modulation by controlling compositional depth profile in La2 O3 / HfO2 nanolaminate gate oxide," *J. Appl. Phys.*, vol. 107, no. 7, pp. 3–8, 2010.

[168] Wiemer, C., Lamagna, L., and Fanciulli, M., "Atomic layer deposition of rare-earth-based binary and ternary oxides for microelectronic applications," *Semicond. Sci. Technol.*, vol. 27, no. 7, p. 074013, 2012.

[169] Seim, H., Mölsä, H., Nieminen, M., Fjellvåg, H., and Niinistö, L., "Deposition of LaNiO3

thin films in an atomic layer epitaxy reactor," *J. Mater. Chem.*, vol. 7, no. 3, pp. 449–454, 1997.

[170] Nilsen, O., Peussa, M., Fjellvåg, H., Niinistö, L., and Kjekshus, A., "Thin film deposition of lanthanum manganite perovskite by the ALE process," *J. Mater. Chem.*, vol. 9, no. 8, pp. 1781–1784, 1999.

[171] Uusi-Esko, K. and Karppinen, M., "Extensive series of hexagonal and orthorhombic RMnO 3 (R = Y, La, Sm, Tb, Yb, Lu) thin films by atomic layer deposition," *Chem. Mater.*, vol. 23, no. 7, pp. 1835–1840, 2011.

[172] Seim, H., Nieminen, M., Niinistö, L., Fjellvåg, H., and Johansson, L.-S., "Growth of LaCoO3 thin films from β-diketonate precursors," *Appl. Surf. Sci.*, vol. 112, pp. 243–250, 1997.

[173] Nilsen, O., Rauwel, E., Fjellvaga, H., and Kjekshusa, A., "Growth of La1-xCaxMnO3 thin films by atomic layer deposition," *J. Mater. Chem.*, no. 17, pp. 1466–1475, 2006.

[174] Lie, M., Nilsen, O., Fjellvåg, H., and Kjekshus, A., "Growth of La 1−x Sr x FeO 3 thin films by atomic layer deposition," *Dalt. Trans.*, no. 3, pp. 481–489, 2009.

[175] Nieminen, M., Sajavaara, T., Rauhala, E., Putkonen, M., and Niinistö, L., "Surface-controlled growth of LaAlO3 thin films by atomic layer epitaxy," *J. Mater. Chem.*, vol. 11, no. 9, pp. 2340–2345, 2001.

[176] Nieminen, M., Lehto, S., and Niinistö, L., "Atomic layer epitaxy growth of LaGaO3 thin films," *J. Mater. Chem.*, vol. 11, no. 12, pp. 3148–3153, 2001.

[177] Ahvenniemi, E., Matvejeff, M., and Karppinen, M., "Atomic layer deposition of quaternary oxide (La,Sr)CoO 3−δ thin films," *Dalt. Trans.*, vol. 44, no. 17, pp. 8001–8006, 2015.

[178] Myllymäki, P., Roeckerath, M., Lopes, J. M., Schubert, J., Mizohata, K., Putkonen, M., and Niinistö, L., "Rare earth scandate thin films by atomic layer deposition: effect of the rare earth cation size," *J. Mater. Chem.*, vol. 20, no. 20, p. 4207, 2010.

[179] Lim, B. S., Rahtu, A., De Rouffignac, P., and Gordon, R. G., "Atomic layer deposition of lanthanum aluminum oxide nano-laminates for electrical applications," *Appl. Phys. Lett.*, vol. 84, no. 20, pp. 3957–3959, 2004.

[180] Kwon, J., Dai, M., Halls, M. D., Langereis, E., Chabal, Y. J., and Gordon, R. G., "In Situ Infrared Characterization during Atomic Layer Deposition of Lanthanum Oxide," *J. Phys. Chem. C*, vol. 113, no. 2, pp. 654–660, 2009.

[181] Triyoso, D. H., Hegde, R. I., Grant, J. M., Schaeffer, J. K., Roan, D., B. E. White, J., and Tobin, P. J., "Evaluation of lanthanum based gate dielectrics deposited by atomic layer deposition," *J. Vac. Sci. Technol. B Microelectron. Nanom. Struct.*, vol. 23, no. 1, pp. 288–297, 2005.

[182] Kukli, K., Ritala, M., Pore, V., Leskelä, M., Sajavaara, T., Hegde, R. I., Gilmer, D. C.,

Tobin, P. J., Jones, A. C., and Aspinall, H. C., “Atomic layer deposition and properties of lanthanum oxide and lanthanum-aluminum oxide films,” *Chem. Vap. Depos.*, vol. 12, no. 2–3, pp. 158–164, 2006.

[183] Wang, T. and Ekerdt, J. G., “Atomic layer deposition of lanthanum stabilized amorphous hafnium oxide thin films,” *Chem. Mater.*, vol. 21, no. 14, pp. 3096–3101, 2009.

[184] Lim, D., Jung, W. S., Kim, Y. J., and Choi, C., “Electrical characteristics of ALD La2O3 capping layers using different lanthanum precursors in MOS devices with ALD HfO2, HfSiOx, and HfSiON gate dielectrics,” *Microelectron. Eng.*, vol. 147, pp. 206–209, 2015.

[185] Chiang, C. K., Wu, C. H., Liu, C. C., Lin, J. F., Yang, C. L., Wu, J. Y., and Wang, S. J., “Effects of La2O3 Capping Layers Prepared by Different ALD Lanthanum Precursors on Flatband Voltage Tuning and EOT Scaling in TiN/HfO2/SiO2/Si MOS Structures,” *J. Electrochem. Soc.*, vol. 158, no. 4, p. H447, 2011.

[186] Ragnarsson, L. Å., Chang, V. S., Yu, H. Y., Cho, H. J., Conard, T., Yin, K. M., Delabie, A., Swerts, J., Schram, T., De Gendt, S., and Biesemans, S., “Achieving conduction band-edge effective work functions by La2O3 capping of hafnium silicates,” *IEEE Electron Device Lett.*, vol. 28, no. 6, pp. 486–488, 2007.

[187] Nieminen, M., Putkonen, M., and Niinistö, L., “Formation and stability of lanthanum oxide thin films deposited from β-diketonate precursor,” *Appl. Surf. Sci.*, vol. 174, no. 2, pp. 155–165, 2001.

[188] Kim, B., Ko, M., Lee, E., Hong, M., Jeon, Y., and Park, J., “Atomic Layer Deposition of La 2 O 3 Thin Films by Using an Electron Cyclotron Resonance Plasma Source,” *J. Korean Phys. Soc.*, vol. 49, no. 3, pp. 1303–1306, 2006.

[189] Tsoutsou, D., Scarel, G., Debernardi, A., Capelli, S. C., Volkos, S. N., Lamagna, L., Schamm, S., Coulon, P. E., and Fanciulli, M., “Infrared spectroscopy and X-ray diffraction studies on the crystallographic evolution of La2O3 films upon annealing,” *Microelectron. Eng.*, vol. 85, no. 12, pp. 2411–2413, 2008.

[190] Kim, H., Lee, H.-B.-R., and Maeng, W.-J., “Applications of atomic layer deposition to nanofabrication and emerging nanodevices,” *Thin Solid Films*, vol. 517, no. 8, pp. 2563–2580, 2009.

[191] No, S. Y., Eom, D., Hwang, C. S., and Kim, H. J., “Properties of lanthanum oxide thin films deposited by cyclic chemical vapor deposition using tris(isopropyl-cyclopentadienyl)lanthanum precursor,” *J. Appl. Phys.*, vol. 100, no. 2, 2006.

[192] Oh, I. K., Kim, M. K., Lee, J. S., Lee, C. W., Lansalot-Matras, C., Noh, W., Park, J., Noori, A., Thompson, D., Chu, S., Maeng, W. J., and Kim, H., “The effect of La2O3-incorporation in HfO2 dielectrics on Ge substrate by atomic layer deposition,” *Appl. Surf. Sci.*, vol. 287, pp. 349–354, 2013.

[193] Eom, D., No, S. Y., Hwang, C. S., and Kim, H. J., “Deposition Characteristics and Annealing Effect of La[sub 2]O[sub 3] Films Prepared Using La(iPrCp)[sub 3]

Precursor," *J. Electrochem. Soc.*, vol. 154, no. 3, p. G49, 2007.

[194] He, W., Chan, D. S. H., Kim, S.-J., Kim, Y.-S., Kim, S.-T., and Cho, B. J., "Process and Material Properties of HfLaO[sub x] Prepared by Atomic Layer Deposition," *J. Electrochem. Soc.*, vol. 155, no. 10, p. G189, 2008.

[195] Kamiyama, S., Kurosawa, E., and Nara, Y., "Improving Threshold Voltage and Device Performance of Gate-First HfSiON/Metal Gate n-MOSFETs by an ALD La[sub 2]O[sub 3] Capping Layer," *J. Electrochem. Soc.*, vol. 155, no. 6, p. H373, 2008.

[196] Congedo, G., Spiga, S., Lamagna, L., Lamperti, A., Lebedinskii, Y., Matveyev, Y., Zenkevich, A., Chernykh, P., and Fanciulli, M., "Effect of high-temperature annealing on lanthanum aluminate thin films grown by ALD on Si(1 0 0)," *Microelectron. Eng.*, vol. 86, no. 7–9, pp. 1696–1699, 2009.

[197] Moon, J. H., Eom, D. Il, No, S. Y., Song, H. K., Yim, J. H., Na, H. J., Lee, J. Bin, and Kim, H. J., "Electrical Properties of the La_2O_3/4H-SiC Interface Prepared by Atomic Layer Deposition Using $La(iPrCp)_3$ and H_2O," *Mater. Sci. Forum*, vol. 527–529, pp. 1083–1086, 2006.

[198] Fei, C., Liu, H., Wang, X., Zhao, L., Zhao, D., and Feng, X., "Effects of Rapid Thermal Annealing and Different Oxidants on the Properties of LaxAlyO Nanolaminate Films Deposited by Atomic Layer Deposition," *Nanoscale Res. Lett.*, vol. 12, no. 1, p. 218, 2017.

Appendix A: ORR activity of Zr-, Hf-, Nb-, and Ta-based thin films

A.1 Introduction

The main challenge in the development of Zn-air batteries (ZABs) is the poor kinetics of the oxygen reduction reaction (ORR) which necessitates high overpotentials and subsequently reduces the effective voltage of the battery. In addition to having good activity towards ORR, another requirement of the catalyst is stability. The electrolyte used in ZABs is 6 M KOH, which has a pH of 14, which is a very harsh environment for most materials. One commonly used catalyst for ORR is finely dispersed Pt particles. Pt shows very good activity towards ORR and is used as the benchmark for comparison of different ORR catalysts. However, Pt is far too sparse and expensive for many applications. In order to achieve widespread use of ZABs, an effective, abundant, stable, and inexpensive electrocatalyst is needed.

The main factors governing ORR performance of an electrocatalyst are the surface area, conductivity, and catalytic mechanism. Increasing surface area improves performance by simply supplying more active sites for catalysis to occur. Higher conductivity catalysts will have better performance by allowing for easier electron transfer. The ORR mechanism of a catalyst can be quite complex and depends on the binding energies of multiple reaction intermediates including OOH*, OH*, and O* (* denotes a surface adsorbed species). The surface must bind to oxygen or oxygen containing species strongly enough to adsorb, but weakly enough to allow for desorption after the ORR has completed. The binding energy of the surface needs to be intermediate between these two effects. The catalytic activity is further complicated by the fact that the ORR has multiple intermediates, each of which has its own binding energy for the specific catalyst surface. Due to the presence of these multiple intermediates and non-ideal scaling of their binding energies, the theoretical optimum overpotential for ORR is in the range of 0.3 to 0.4 V.

One group of candidate materials that has received much attention is transition metal oxides, many of which exhibit good activity towards ORR and stability is alkaline solutions. Of the transition metal oxides, MnO_x and CoO_x have received the most attention due largely to their high theoretical performance. These oxides were the subject of the main portion of this thesis. Some transition metal oxides that have been sparsely investigated are ZrO_x, HfO_x, NbO_x, and TaO_x. These materials do not exhibit high theoretical activity, but there has been evidence that their activity can be improved though structure modification. [155]–[157] These materials are

also known to have excellent stability in alkaline solutions. Liu et al. showed that the activity of ZrO_x varied with oxygen content for films prepared by reactive sputtering. The presence of oxygen vacancies in the ZrO_x structure increases the number of surface active sites while also improving the conductivity of the material. [158] The addition of another element, to yield a ternary oxide, has also been shown to improve the activity of some oxides; the mechanism behind this effect is not currently understood. The addition of nitrogen to form an oxynitride has also been shown to yield some ORR activity; the improvement to activity is attributed to surface defects. [157]

NbO_x has been used as a support for Pt catalysts, [159], [160] but has not received much attention as a catalyst on its own. NbO_x is utilized as a Pt support because of its stability in harsh environments and its good electronic conductivity. Nb_2O_5 is an insulator, while NbO_2 and NbO have conductivities of $\sim 10^{-4}$ S cm^{-1} and $\sim 10^{4}$ S cm^{-1}, respectively. [159]

The purpose of this work was to investigate the feasibility of ALD to prepare catalyst coated GDL substrates. This work also examined how deposition conditions can be used to modify film structures and improve their catalytic activity. Zr- and Hf-based films were deposited using ALD. These films included oxides, nitrides, oxynitrides, oxygen deficient oxides, and ternary oxides. Nb- and Ta-based films were prepared by sputtering followed by an oxygen or forming gas plasma step. The Nb- and Ta-based films were metals, oxides, and nitrides. Despite the efforts made to modify the film structures, the films prepared in this work all had poor catalytic performance especially when compared with the MnO_x films prepared in Chapters 4 and 5 (Table A-1). For this reason, most films presented were not thoroughly investigated. This study represents some of the initial work done during the PhD program and also provided an opportunity to learn various fabrication and characterization techniques, such as TEM, STEM, STEM EDX mapping, ALD, sputtering, and electrochemical testing.

A.2 Experimental

The transition metal oxide films were deposited on gas diffusion layers (GDL, Sigracet 35/39 BC) composed of carbon held together by a Teflon™ binder. Zr and Hf films were prepared via atomic layer deposition (ALD) from precursors of tetrakis-dimethyl-amido zirconium (TDMAZr) and tetrakis-dimethyl-amido hafnium (TDMAHf), respectively. Deposition

procedures used for ZrO_2 and HfO_2 followed well established procedures developed by the Cadien ALD group. [161] The ALD reactor was a viscous flow design utilizing a continuous flow of Ar and maintained at a pressure of 1 Torr. ZrO_x and HfO_x films were prepared using the same deposition conditions. The precursor ampules were held at 75°C and the substrate temperature was 150°C. A single deposition cycle was broken into four sections: precursor dose (t_1), precursor purge (t_2), reactant pulse (t_3), and reactant purge (t_4). For ZrO_x and HfO_x films, the reactant was O_2 plasma and the pulse timing (t_1-t_2-t_3-t_4) was 0.06-8-5-5 s unless otherwise specified. ZrO_xN_y and HfO_xN_y films were prepared by depositing 30 cycles of the respective nitride, followed by 10 cycles of oxide as per the above pulse sequence. The Zr and Hf nitrides were preparing using forming gas plasma (95% N_2 + 5% H_2) as the reactant with a pulse timing of 0.1-12-9-9 s. Plasma exposures were conducted using an inductively coupled plasma system at a power of 600 W with a continuous flow of 100 sccm Ar and 60 sccm reactant gas (O_2 or forming gas).

Ta- and Nb-based films were prepared on GDL using DC magnetron sputtering with a plasma power of 200 W. Depositions were done at a temperature of 20°C in an Ar atmosphere at a pressure of 2.1 mTorr. The estimated deposition rate for sputtered films is about 0.2 nm s^{-1}. Three thicknesses of each Nb- and Ta-based films were prepared, with sputter times of 50, 100, and 250 s yielding films of approximately 10, 20, and 50 nm, respectively. To prepare oxides from the sputtered films, samples were exposed to oxygen plasma for 2 min. Ta and Nb nitride films were prepared by exposing 100 s sputtered films to 5 min of forming gas plasma. The plasma steps were performed using an inductively coupled plasma in the ALD reactor as described above. Nb and Ta metal films were also tested without any post deposition plasma treatment.

Electrochemical characterization was performed using a Biologic SP-300 potentiostat. A Pt coil was used as the counter electrode and the electrolyte used for all measurements was oxygen saturated 1 M KOH. During testing oxygen was continuously bubbled into the solution at a rate of 20 sccm. Hg/HgO was used as the reference electrode and all reported potentials are relative to Hg/HgO. Linear sweep voltammetry (LSV) measurements were conducted between 0.2 to -0.5 V at a scan rate of 5 mV s^{-1}. Prior to LSV measurement, electrodes were cycled using cyclic voltammetry between 0.2 and -0.5 V at a scan rate of 20 mV s^{-1} to remove any surface

contamination and ensure reproducible results. To make determination of ORR onset potential consistent (V_{ORR}) between samples, onset potential was defined as the potential at which a current of 10 mA cm^{-2} is reached. For further comparison of catalysts, the current at -0.5 V ($i_{-0.5}$) was also tabulated.

A.3 Results and Discussion

A.3.1 ZrO_2 and HfO_2

ZrO_2 and HfO_2 films of varying thicknesses were prepared via ALD. Thickness of the films was varied by changing the cycle count for the ALD depositions. Samples were prepared using 25, 50, and 100 cycles for each oxide. TEM analysis was conducted on the 25, 50 and 100 cycle ZrO_2 deposits. TEM results for ZrO_2 films are shown in Figure A-1. The bright field images show agglomerated carbon particles from the GDL, coated with a film of ZrO_2; from these images it was possible to estimate the film thicknesses. The film thicknesses varied slightly and were approximately 3 ± 1, 6 ± 2, and 15 ± 3 nm, respectively, for 25, 50 and 100 cycle films. The variations in film thickness can be attributed to the original location of the carbon particles within the GDL. Particles near the GDL surface have good access to gaseous precursors whereas particles from deeper within the GDL rely on diffusion, resulting in fewer precursor molecules reaching the particle surface and slower film growth. The GPC values for the films are all ~0.12 nm, which is consistent with the recorded GPC value for ZrO_2 films on planar silicon.

Dark field imaging (Figure A-1B) of the 25 cycle deposit shows bright areas scattered throughout the GDL particles. These bright areas are due to small crystalline areas within the GDL and are not due to the ZrO_2 film; images of bare GDL have this structure as well in dark field images. The structure of the 25 cycle film is completely amorphous, as shown by the dark field image as well as the diffraction pattern in Figure A-1C. The diffraction pattern collected from the 25 cycle sample matches with the bare GDL pattern; there is no intensity from the ZrO_2 film. Dark field imaging of the 50 and 100 cycle samples on GDL reveal a mostly amorphous structure with some nanocrystals (Figure A-1E, H); the 100 cycle sample has a larger degree of crystallinity than the 25 cycle sample (Figure A-1B). The crystalline regions in the 50 cycle sample are 2-8 nm in size, while for the 100 cycle sample they are mostly in the 5-20 nm range. Diffraction patterns from these samples confirm a mixture of amorphous and nanocrystalline structures, showing a combination of diffuse rings and bright spots. The diffuse rings are due to

the amorphous regions of the ZrO_2 film as well as the underlying carbon support. The bright spots come from the crystalline regions of the ZrO_2 film and match well with the cubic ZrO_2 structure (PDF PDF#89-9096). The increasing degree of crystallinity with increasing ALD cycles for ZrO_2 and HfO_2 has been previously reported by Hausmann *et al.* [162]. The mechanism behind the increasing crystallinity is as follows: At the beginning of the deposition, most material will be deposited amorphously, with some small chance of a region being deposited as crystalline. With successive cycles, the material deposited on crystalline regions will grow epitaxially, increasing the size of the crystal vertically as well as laterally. As the crystals deposited at early cycle numbers grow, new crystals also have a chance to nucleate. [162] This mechanism explains the observations of the ZrO_2 film crystallinity changing with cycle number.

Table A-1: LSV results for various thin films

	V_{ORR} (V vs. Hg/HgO)	$i_{-0.5}$ (mA cm^{-2})		V_{ORR} (V vs. Hg/HgO)	$i_{-0.5}$ (mA cm^{-2})
Bare GDL	-0.260	-89	ZrON	-0.244	-97
Pt/C	-0.050	-229	HfON	-0.236	-106
FG-MnO_x	-0.107	-255	$ZrHfO_x$	-0.220	-159
FG-MnO_x + CoO_x	-0.095	-248	$HfZrO_x$	-0.215	-177
25cy ZrO_2	-0.222	-170	100s Nb	-0.365	-22
50cy ZrO_2	-0.228	-140	50s NbO_x	-0.219	-150
100cy ZrO_2	-0.229	-137	100s NbO_x	-0.210	-181
25cy HfO_2	-0.228	-126	250s NbO_x	-0.211	-179
50cy HfO_2	-0.226	-113	100s NbN	-0.416	-15
100cy HfO_2	-0.229	-116	100s Ta	-0.331	-28
10cy ZrN	-0.242	-135	50s TaO_x	-0.210	-210
25cy ZrN	-0.239	-144	100s TaO_x	-0.207	-242
50cy ZrN	-0.231	-124	250s TaO_x	-0.212	-207
ZrO_x(Ar1sO_2)	-0.329	-22	100s TaN	-0.399	-15
ZrO_x(Ar2sO_2)	-0.299	-30			
ZrO_x(2sO_2)	-0.229	-150			
ZrO_x(3.5sO_2)	-0.229	-136			

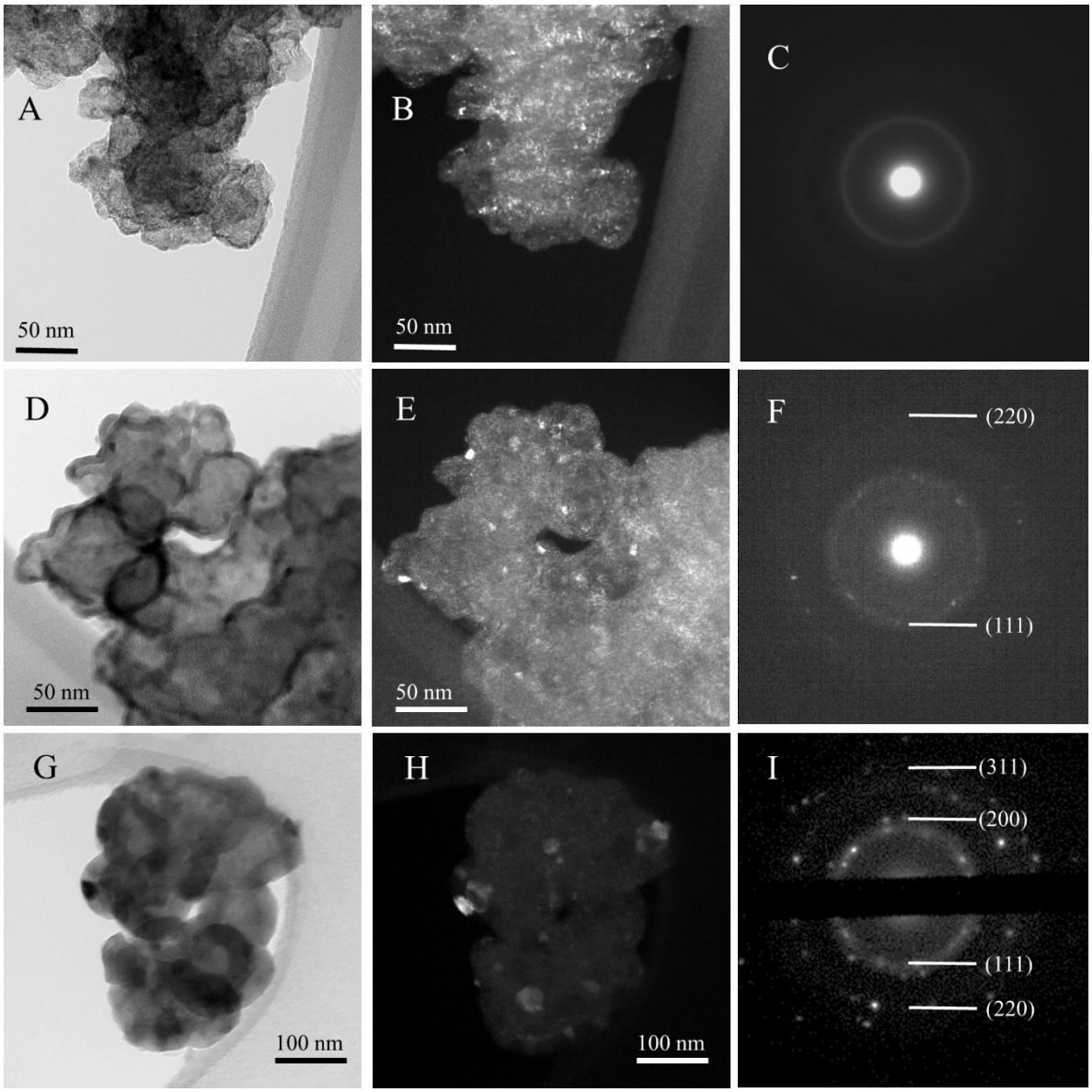

Figure A-1: TEM results for ZrO_2 films deposited on GDL. A), B), and C) are for the 25 cycle deposit; D), E), and F) are for the 50 cycle deposit; G), H), and I) are for the 100 cycle deposit. A) D) and G) are bright field images; B), E) and H) are dark field images; C), F), and I) are selected area diffraction (SAD) patterns.

LSV results for ZrO_2 and HfO_2 films are shown in Figure A-2 and all LSV results are tabulated in Table A-1. Table A-1 also presents data for Pt/Ru-C, FG-MnO_x, and FG-MnO_x + CoO_x for comparison. All ZrO_2 and HfO_2 films out performed bare GDL (V_{ORR} = -0.260 V). Of the ZrO_2 films, the 25 cycle sample showed the best performance with an onset potential of -0.222 V. The V_{ORR} for the 25, 50, and 100 cycle HfO_2 films were nearly identical. In a similar trend to the ZrO_2 films, the thicker deposits showed reduced performance.

For both the ZrO_2 and HfO_2 films, the 50 and 100 cycle films showed reduced performance. This reduction in performance can be attributed to two main factors: crystallinity and conductivity. An amorphous structure will have a higher density of defects on the surface than a highly crystalline film; these defects act as active sites for ORR. As shown in the TEM results, the 25 cycle sample is completely amorphous while the 50 and 100 cycle samples show some crystallinity. Film thickness and the resulting conductivity also greatly affect catalyst performance. ZrO_2 and HfO_2 are both insulating materials. Thicker films have a higher electronic resistance, hindering effective electron transfer for the ORR reaction at the surface. Because of the conformal nature of ALD films, the mass of active material deposited has little effect on performance. The surface areas for 25, 50, and 100 cycle samples are nearly identical because the starting substrates are identical. Increasing cycle number may also cause the porosity of the GDL to become blocked, limiting electrolyte access and effective surface area.

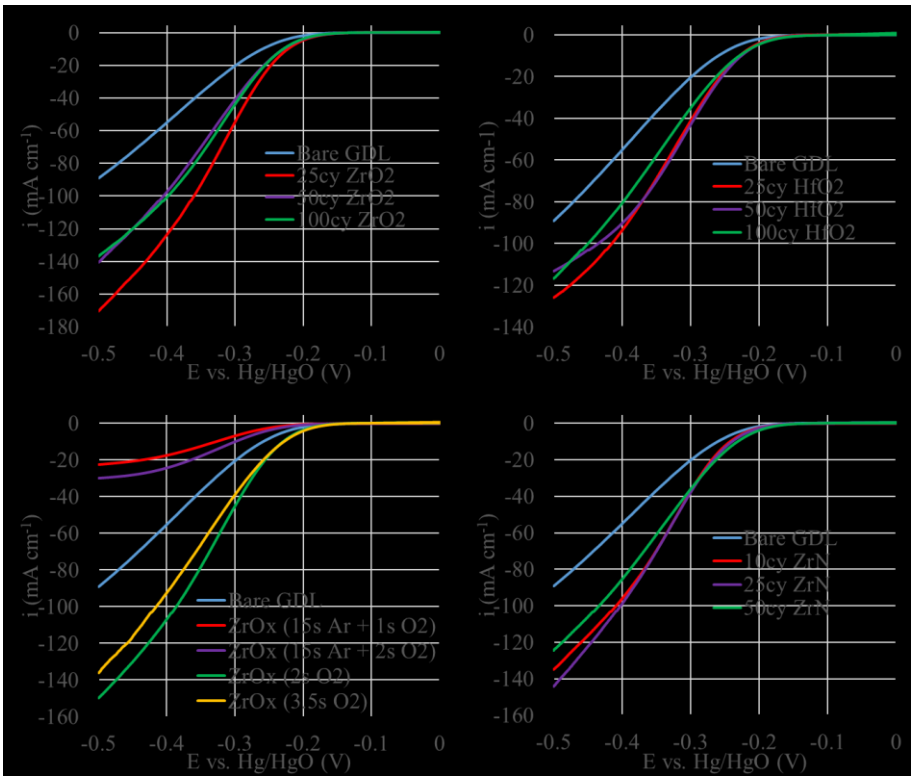

Figure A-2: LSV results for various ALD films prepared on GDL: A) ZrO_2, B) HfO_2, C) reduced oxygen content ZrO_x, and C) ZrN.

A.3.2 Reduced Oxygen Content ZrO_2

In an attempt to introduce oxygen vacancies into the ZrO_2 structure, films were prepared with reduced oxygen plasma doses. Instead of the standard dose time of 5 s, 50 cycle films were prepared using 2 s and 3.5 s plasma doses; these samples are denoted as $ZrO_x(2sO_2)$ and $ZrO_x(3.5sO_2)$, respectively. In the standard recipe, the oxygen plasma serves two purposes. The oxygen plasma introduces oxygen into the film, but it is also used to remove precursor ligands that are attached to the surface after the precursor dose. With reduced oxygen plasma time, it was suspected that there may be insufficient time for all precursor ligands to be removed. To investigate this behavior, films were deposited using an additional argon plasma step. The intended purpose of the argon plasma was to remove the precursor ligands from the surface before the oxygen plasma step. These films were prepared using 50 cycles with the following sequence: precursor dose (0.06 s), precursor purge (8 s), argon plasma (15 s), oxygen plasma (1 or 2 s), and reactant purge (5 s). The samples are denoted as $ZrO_x(Ar\text{-}1sO_2)$ and $ZrO_x(Ar\text{-}2sO_2)$.

The $ZrO_x(3.5sO_2)$ sample on GDL was investigated using TEM (Figure A-3). The TEM sample was prepared in the same manner as the ZrO_2 samples described previously. Figure A-3A shows a bright field image of GDL particles coated with ZrO_2. Film thickness varied between 5 and 10 nm, with a GPC of 0.1-0.2 nm. A GPC of 0.2 nm is much larger than the standard GPC for this material, which is a further indication that the thickness measurements from GDL are an over estimation. The variation in thickness across the sample is much larger than for the 100 cycle sample prepared with the standard oxygen plasma time. This variation may be due to the inaccuracy of the thickness measurements causing larger variations at smaller thicknesses. The thickness variation may also be attributed to the reduced oxygen plasma dose. With reduced plasma time, it is likely that the surface reaction during each cycle does not have sufficient time to reach completion. Some parts of the sample may not have good access to the plasma due to GDL porosity. These areas would require longer a longer plasma dose to ensure that the reaction completion. With reduced plasma time, the GPC would be reduced. Dark field imaging (Figure A-3B) shows that the film is mostly amorphous with some regions consisting of very small crystals (< 1 nm). The SAD diffraction pattern confirms that the film is mostly amorphous with some crystalline regions. The spots in the diffraction pattern match with cubic ZrO_2.

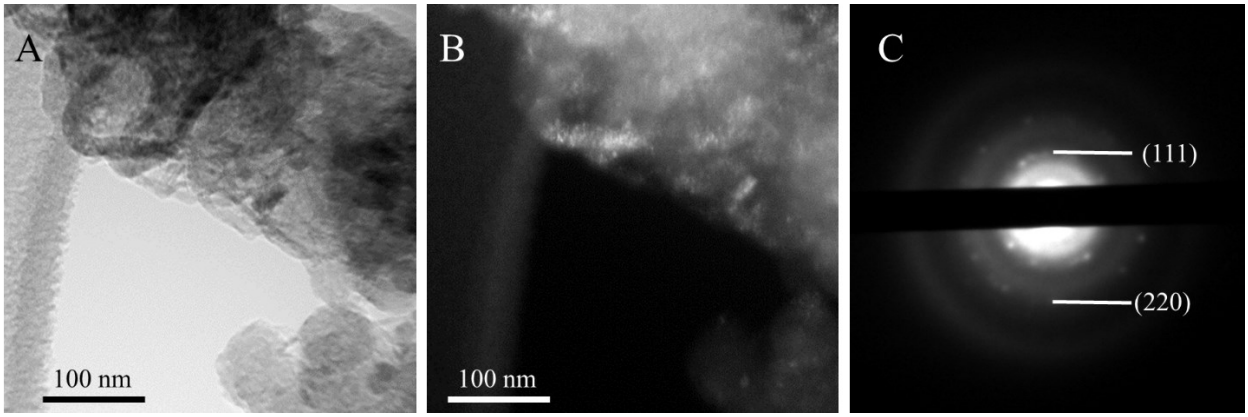

Figure A-3: TEM results from 50 cycles ZrO_x(3.5sO2). A) Bright field image, B) dark field image, and C) SAD pattern.

LSV results for the reduced oxygen content sample are shown in Figure A-2C. The $ZrO_x(2sO_2)$ and $ZrO_x(3.5sO_2)$ samples both had a V_{ORR} = -0.229 V, while the standard recipe 50 cycle ZrO_2 had a V_{ORR} = -0.228 V. These results are effectively the same which suggests that the reduced plasma time did not result in reduced oxygen content. $ZrO_x(2sO_2)$ had a slightly improved $i_{-0.5}$ (-150 mA cm^{-2}) compared with the 50 cycle ZrO_2 ($i_{-0.5}$ = -140 mA cm^{-2}). The improved $i_{-0.5}$ is likely due to $ZrO_x(2sO_2)$ having a slightly reduced thickness compared with the 50 cycle ZrO_2 sample, caused by the reduced oxygen plasma time lower the GPC.

The samples utilizing argon plasma showed very poor results. The argon plasma step had an unexpected effect on the deposition. It is unclear how the argon plasma changed the depositions. It is possible that small amounts of contamination present in the ALD reactor were incorporated into the film during the argon plasma step. Argon also may have been incorporated into the film during deposition.

A.3.3 ZrN

ZrN samples were prepared using 10, 25, and 50 ALD cycles. LSV results are shown in Figure A-2D. In order to investigate the growth behaviour and facilitate TEM analysis, ZrN films were deposited directly onto lacey carbon TEM grids. TEM analysis of the 50 cycle ZrN sample deposited directly onto a lacey carbon grid (Figure A-4) showed that the film had completely oxidized in contact with air. Oxidation happened quickly, as the sample was imaged less than 24 h after being prepared. EDX analysis of the film confirmed the presence of oxygen and zirconium, with no nitrogen peak detected. The film was nanocrystalline, with a grain size of 2-

10 nm, as shown in the dark field image (Figure A-4B). The diffraction pattern has four rings (Figure A-4C), each composed of many individual spots, due to the nanocrystalline nature of the sample. The ring pattern was indexed to cubic ZrO_2.

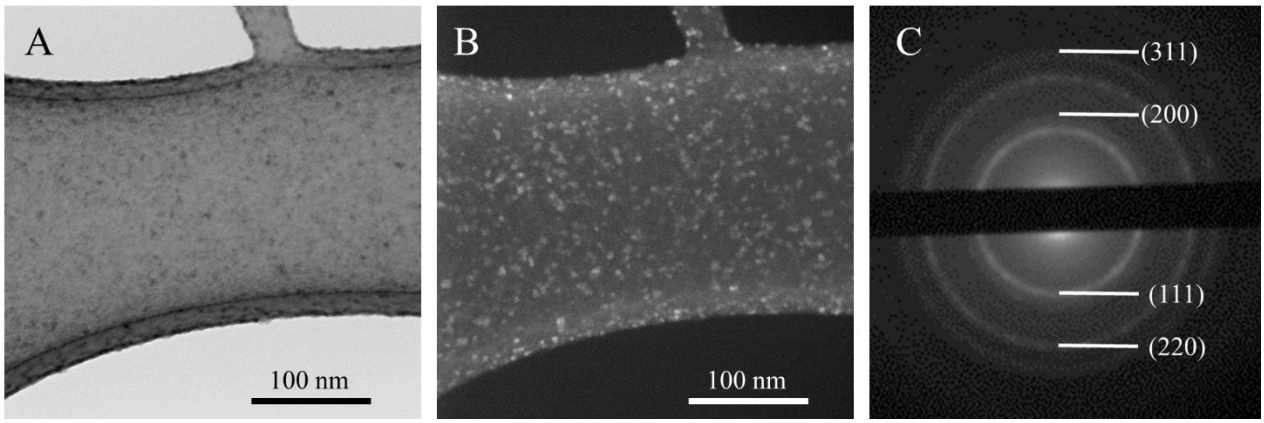

Figure A-4: TEM results from 50 cycle ZrN on holey carbon. A) Bright field image, B) dark field image, C) SAD pattern.

ZrN films had comparable performance to the ZrO_2 coatings, but with slightly poorer results. The difference in performance between the ZrN and ZrO_2 samples may be related to the higher degree of crystallinity for the ZrN films. The amorphous structure of the ZrO_2 films provides more active sites for ORR catalysis. Since the degree of crystallinity is only marginally better for the films deposited as nitrides, the reduction in performance is also marginal.

A.3.4 ZrON and HfON

ZrON and HfON samples were fabricated by depositing 30 cycles of nitride followed by 10 cycles of oxide. It was anticipated that during the oxygen plasma step, energetic oxygen radicals would be able to penetrate into the nitride structure, forming an oxynitride. However, due to the very poor ORR performance of these films, no further characterization was performed to confirm the structure or composition of the deposits. LSV results for the oxynitride films are shown in Figure A-5A. Both ZrON and HfON improved upon the activity of the bare GDL only slightly, with onset potentials of -0.244 and -0.236 V for ZrON and HfON, respectively.

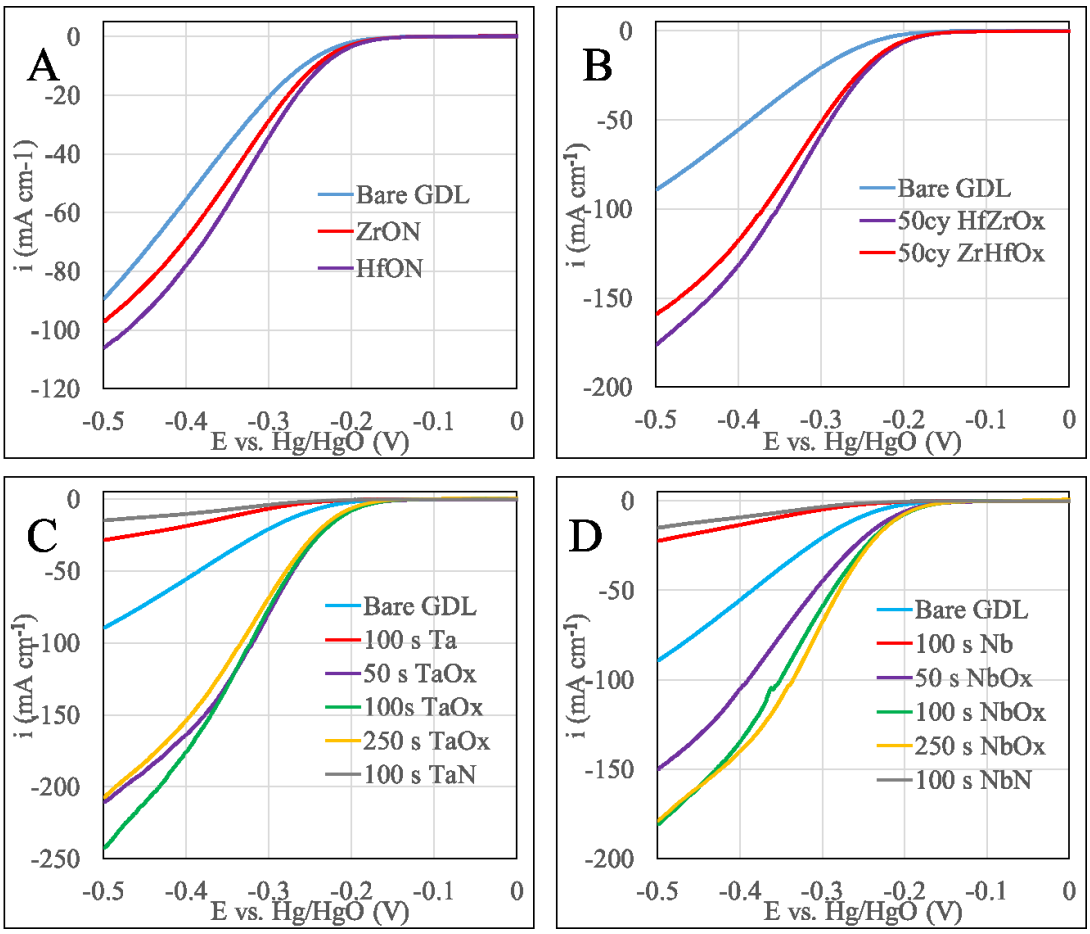

Figure A-5: LSV curves for various ALD and sputtered films. A) ALD oxynitrides, B) ALD ternary oxides, C) sputtered Ta-based films, and D) sputtered Nb-based films.

A.3.5 Ternary Oxides

Ternary oxides of Zr and Hf were prepared by performing a second precursor dose before the plasma step with each cycle. $ZrHfO_x$ was prepared by using 50 cycles of the following sequence: Zr dose (0.06 s), purge (8 s), Hf dose (0.06 s), purge (8 s), oxygen plasma (5 s), and purge (5 s). $HfZrO_x$ was prepared in a similar manner, with 50 cycles as well: Hf dose (0.06 s), purge (8 s), Zr dose (0.06 s), purge (8 s), oxygen plasma (5 s), and purge (5 s). When precursor molecules are introduced to the surface, they quickly physisorb to active sites. The density of physisorbed molecules is governed by the size of the precursor molecule. A physisorbed molecule will then either desorb from the surface or chemisorb to the surface. During chemisorption, the precursor molecule will lose one or more ligands, reducing the size of the molecule and the steric hindrance. Both chemisorption and desorption occur during the purge step and reveal active sites that were previously blocked by physisorbed molecules. These newly revealed active sites are

then available for precursor molecules introduced during the second precursor dose within the same cycle. This mechanism suggests that the $ZrHfO_x$ sample will have a higher Zr content, while the $HfZrO_x$ sample will have a larger Hf content.

LSV results for the ternary oxide films are shown in Figure A-5B. Both $ZrHfO_x$ and $HfZrO_x$ films out perform all the other Zr and Hf films with onset potentials of -0.220 and -0.215 V, respectively. As mentioned in Section 2.3.1.1, ternary oxides have shown some enhanced catalytic activity; these results support this observation. However, the mechanism behind this enhance activity is currently not understood.

Since $HfZrO_x$ showed the best performance of the Zr and Hf based films, it was chosen for investigation using TEM as well as STEM EDX mapping. TEM results from the 50 cycles $HfZrO_x$ sample are shown in Figure A-6. Bright field imaging (Figure A-6A) shows a film thickness of approximately 7 ± 2 nm which is about the same as the 50 cycle ZrO_2 sample (6 ± 2 nm). Dark field imaging (Figure A-6B) and the diffraction pattern (Figure A-6C) show that the film is entirely amorphous. The rings in the diffraction pattern are due to the bare GDL and the bright areas in Figure A-6B can also be attributed to the GDL.

STEM EDX maps of the $HfZrO_x$ deposit are shown in Figure A-7. Figure A-7A is an annular dark field (ADF) image of the area mapped by EDX spectroscopy. The contrast shown in ADF images is almost entirely due to atomic number differences. Areas with relatively high atomic number appear as bright, while low atomic number areas will appear darker. Since Zr and Hf are much heavier elements than the C particles of the GDL, the areas containing Zr and/ or Hf will appear bright. The ADF image in Figure A-7A indicates that the film surrounding the C particles is composed of Zr and Hf. The EDX maps confirm this; the maps show that the bulk of the particles are composed of C, with high concentrations of Zr, Hf, and O around the edges of the particles. From these maps, Zr and Hf are shown to be evenly distributed throughout the film as expected. The GDL particles are uniformly coated.

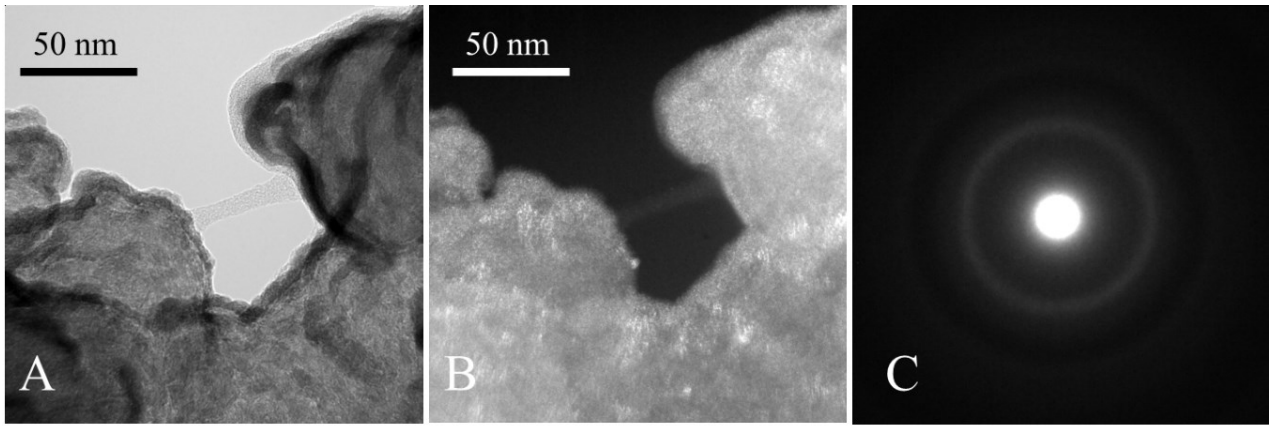

Figure A-6: TEM results from 50 cycles $HfZrO_x$ on GDL. A) Bright field image, B) dark field image, and C) SAD diffraction pattern.

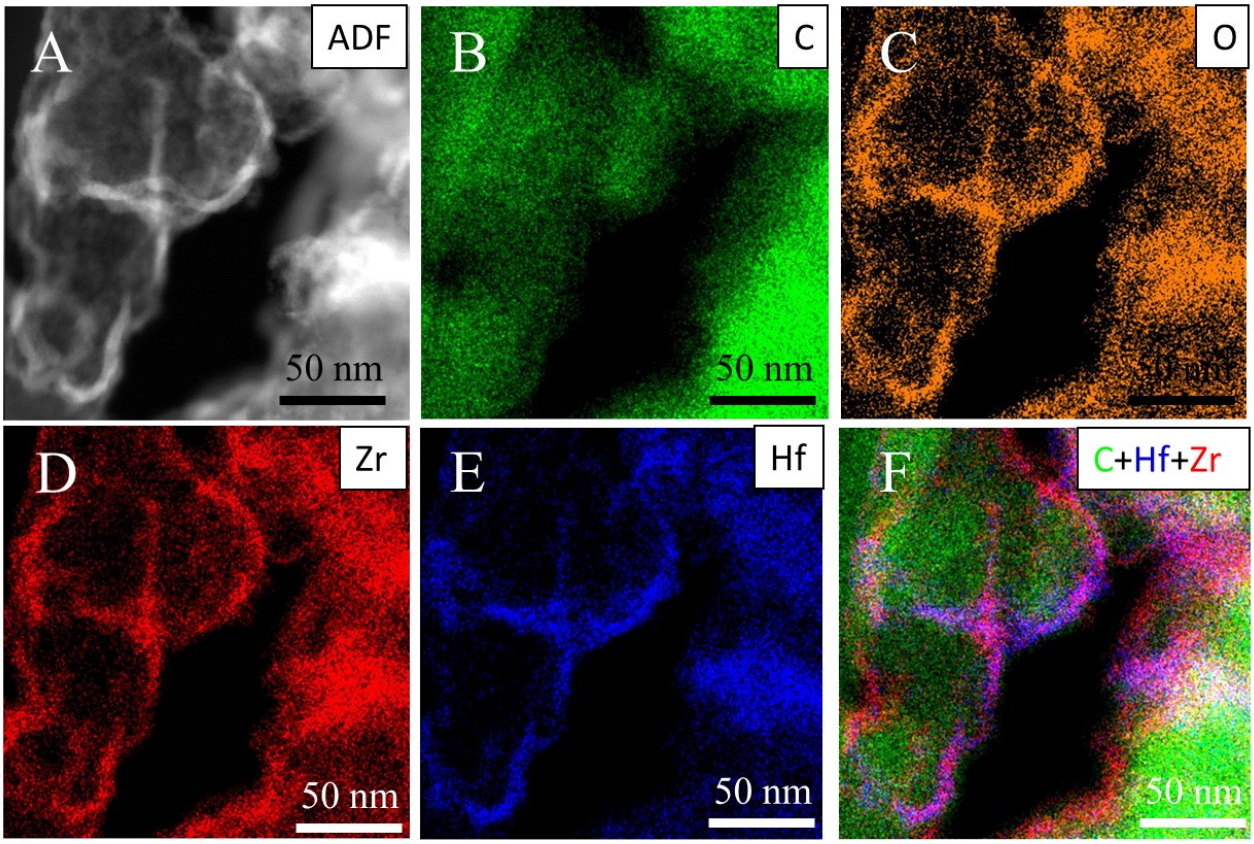

Figure A-7: STEM EDX mapping results for the 50 cycle $HfZrO_x$ on GDL sample. A) ADF image, B) C-K map, C) O-K map, D) Zr-L map, E) Hf-M map, and F) overlain C, Hf, and Zr map.

A.3.6 TaO_x and NbO_x

TEM results for 100 s TaO_x and 100 s NbO_x films are shown in Figure A-8. For both samples, bright field imaging (Figure A-8A, C) shows a thin film of material on one side of the carbon particles. This is in contrast to the Zr- and Hf-based films prepared by ALD which uniformly cover the entire surface of the particles. The directional nature of the TaO_x and NbO_x films is due to nature of the sputtering process. Sputtering deposits material only in areas that are in 'line of sight' from the sputtering source, i.e., the very top surface of the GDL structure. The 100 s TaO_x film was approximately 35 nm thick, while the 100 s NbO_x film was approximately 20 nm thick. This observation is the opposite of what was expected. These films were prepared under identical sputtering conditions and the heavier element (Ta) was expected to have a lower sputtering rate than the lighter element (Nb). It is possible that this discrepancy was caused by the geometry of the Ta target. The Ta target had been used extensively previously, so that a large amount of material removed in a ring shape from the target. The ring shape is due to the geometry of the magnetic field produced by the magnetron. The presence of the trench increased the surface area of the target exposed to the plasma, likely increasing the total sputter rate. The Nb target on the other hand had only been used sparingly and had very little trench formation.

Dark field imaging and diffraction of the TaO_x and NbO_x samples (Figure A-8B, D) reveal that the films are completely amorphous, making determination of their structure and/ or oxidation state difficult without additional analysis (e.g., XPS). The diffraction patterns from TaO_x (Figure A-8E) and NbO_x (Figure A-8G) are compared directly with a diffraction pattern taken from the bare GDL (Figure A-8F). This comparison shows that the rings present in the TaO_x and NbO_x diffraction patterns are due to the GDL and not the deposited films. It is apparent that the patterns from the metal oxide films do have some increased intensity, particularly around the 2.15 Å ring; however, this intensity is far too diffuse to obtain any meaningful data. TEM EDX spectra (not shown) of the NbO_x films confirm the presence of Nb and O, with a small amount of Ca contamination.

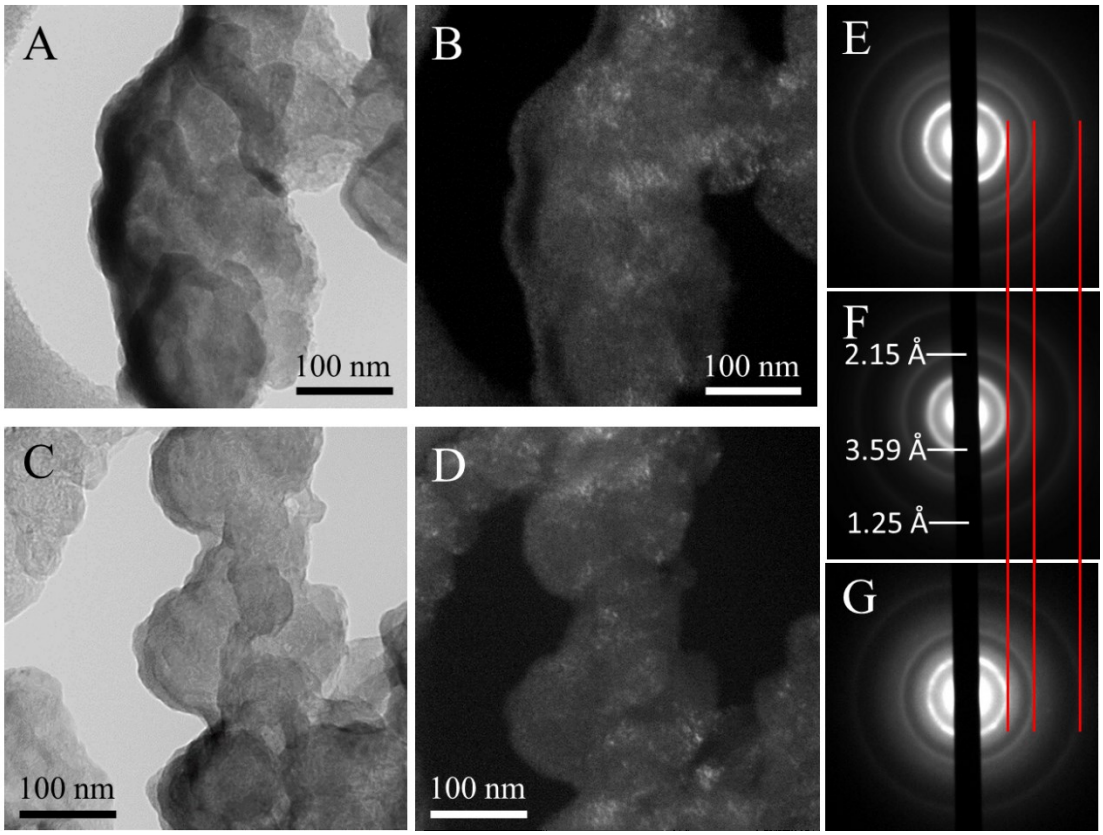

Figure A-8: TEM results for the TaO_x (A, B, E) and NbO_x films (C, D, G). A and C are bright field images, while B and D are dark field images. E, F, and G are SAD patterns. F is a diffraction pattern taken from a sample of bare GDL and is shown for comparison.

The LSV curves for Ta and Nb based films are shown in Figure A-5. The oxidized films show good activity towards ORR, while the pure metal and nitride films show very poor performance. The pure metal films were not expected to have good performance; the only pure metals to show catalytic activity are noble metals. The nitride films were expected to have some catalytic activity, but Figure A-5 shows that they were outperformed even by the pure Nb film. Without further characterization it is not clear why the nitride film had such poor performance. It is not clear whether a nitride phase was actually formed. Of the oxide films, the 100 s depositions showed the best performance with V_{ORR} values of -0.210 V and -0.207 V for 100 s NbO_x and TaO_x films, respectively. All three thicknesses of the TaO_x films showed quite similar performance, but the 50 s sample was significantly out performed by the 100 s and 250 s films. The thickness of the 50 s NbO_x film was estimated from TEM observations to be only 10 nm. It is believed that the small amount of catalyst loading was responsible for the 50 s sample's relatively poor performance.

Appendix B: Atomic Layer Deposition of La Oxide Using Pressurized Precursor Delivery

B.1 Introduction

Atomic layer deposition (ALD) is a vapor phase deposition technique capable of producing very thin films with a number of desirable properties. ALD films are high purity, conformal, uniform, and have thickness control on the order of Ångstroms. ALD is performed by sequentially introducing vapor phase reactants to the substrate where they undergo self-limiting reactions. The self-limiting behavior of the deposition provides ALD films with many of their useful properties. For the deposition of oxide films, the reactants are typically an organometallic compound and an oxygen source such as H_2O, O_3, or O_2 plasma. One major challenge in developing ALD processes is the selection and use of organometallic precursors (see Section 2.2.4). Many of the organometallic precursors used in ALD have low vapor pressures, making delivery of vapor phase molecules to the substrate difficult. [11] Figure B-1 shows two common methods of precursor delivery. Conventional precursor delivery (Figure B-1A) relies on the vapor pressure of the precursor to push precursor vapors into the carrier gas stream. For this method to be used effectively, the precursor must have a vapor pressure above the pressure in the ALD system (typically ~1 Torr). For low vapor pressure precursors, bubblers are commonly used (Figure B-1B). A bubbler allows the carrier gas to flow through the head space above the precursor within the ampule. This permits precursor vapors to be carried through the system towards the substrate regardless of the vapor pressure.

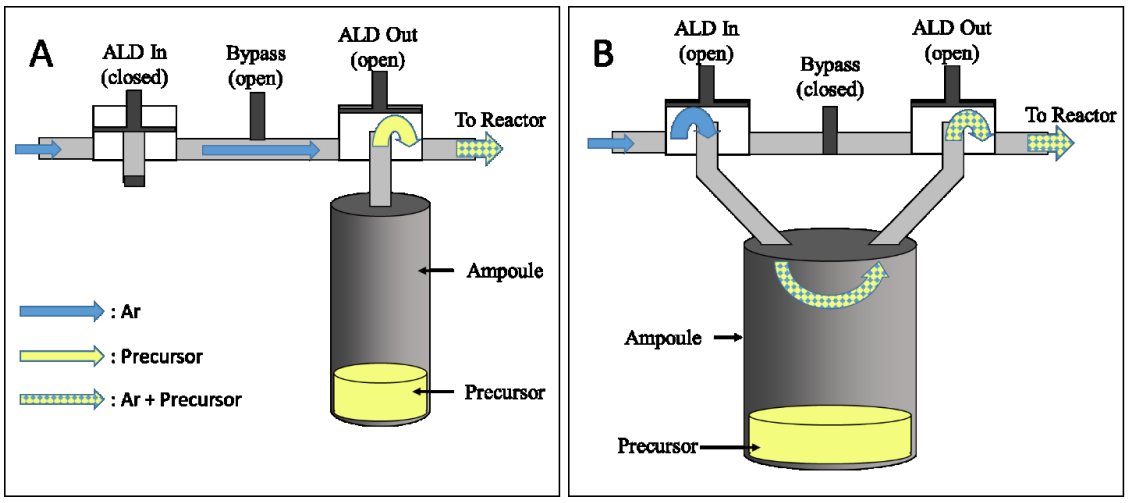

Figure B-1: Schematics of A) conventional precursor delivery and B) precursor delivery using a bubbler.

As trends in the semiconductor industry move towards smaller and smaller feature sizes, the materials requirements become stricter. One such material requirement is the thickness of the gate oxide in transistor devices. The physical limit for SiO_2 thickness (~2 nm) has been reached; at this limit quantum tunneling becomes significant enough to affect the reliability of devices. In order to avoid the problem of tunneling, materials with high dielectric constants (known as high-k dielectrics) such as HfO_2 are now commonly used in transistor devices. However, HfO_2 has a relatively low crystallization temperature (~400 °C) which can cause high leakage currents. La_2O_3 has started to be investigated as a material for high-k gate dielectrics because of its high dielectric constant and good interfacial properties. Ternary oxides containing La are also of interest, particularly $LaAlO_3$ and La-doped HfO_2. Most of the development of La_2O_3 ALD processes has been used for preparation of gate oxides. [163]–[168]

Another application of La ALD is the preparation of perovskites. Perovskites are oxides containing two or more cations with the formula ABO_3, where A and B are transition metals. The crystal structure of perovskites allows for useful material properties such as ferroelectricity, piezoelectricity, catalytic activity, superconductivity, and many others. The properties of perovskite materials arise from the atomic configuration of the cations and oxygen within the crystal structure; the degree of crystallinity is crucial to the performance of perovskites. A variety of La containing perovskites have been deposited using ALD: $LaNiO_3$,[169] $LaMnO_3$,[170], [171] $LaCoO_3$,[172], $La_{1-x}Ca_xMnO_3$,[173] $La_{1-x}Sr_xFeO_3$,[174] $LaAlO_3$,[175] $LaGaO_3$,[176] $La_{1-x}Sr_xCoO_3$,[177] and $LaScO_3$. [178] All metal precursors used to prepare La containing perovskites have been of the β-diketonate type. Nearly all precursors utilized so far have (2,2,6,6-tetramethyl-3,5-heptane-dione) ligands, with the exception of the use of cobalt acetylacetonate ($Co(acac)_3$) by Ahvennieni *et al*. [177] All groups use O_3 as the oxygen source. A group from the University of Oslo has published a number of papers on the ALD deposition of lanthanum containing perovskites; $LaNiO_3$,[169] $LaMnO_3$,[170] $LaCoO_3$,[172], $La_{1-x}Ca_xO_3$,[173] and $La_{1-x}Sr_xFeO_3$. [174] Most films prepared in these studies were deposited amorphously below deposition temperatures of 350 °C; the films showed varying degrees of crystallinity at temperatures greater than 350 °C. Annealing at 600 °C in an air or O_2 environment provided a dramatic increase in crystallinity for most films. Seim *et al.* [169], [172] claim that an O_2 atmosphere during annealing is critical to obtaining the perovskite structure. Nilsen *et al.* and Seim *et al.* also investigated the effect of pulsing ratio on film composition in

order to obtain stoichiometric films. [169], [170], [172], [173] Uusi-Esko and Karppinen [171] investigated ALD of a variety of Mn containing perovskites of the form $RMnO_3$ (R = Y, La, Sm, Tb, Yb, and Lu). In their work, most films were deposited amorphously, probably due to the relatively low deposition temperature of 275 °C. Uusi-Esko and Karppinen annealed deposits at 600-1000 °C in nitrogen, obtaining improved film crystallinity. $LaMnO_3$ films annealed in N_2 showed a shift in lattice parameter compared with films annealed in O_2, indicating a sub-stoichiometric composition for films annealed in N_2. Uusi-Esko and Karppinen deposited films on Si, $LaAlO_3$, and $SrTiO_3$ and showed that the crystal structure of deposited films was dependent on substrate crystallinity. [171] Of the work on ALD of La containing perovskites, none have investigated their films for use as a catalyst. [169]–[178]

A number of La precursors have been used in literature for ALD of La_2O_3 including tris(N,N'-diisopropylformamidinato) lanthanum [$La(^iPrAMD)_3$], [179] tris(N,N′-diisopropylacetamidinate) lanthanum [$La(^iPr\text{-}MeAMD)_3$], [180] tris(bis(trimethylsilyl)amide) lanthanum [$La(N(SiMe_3)_2)_3$] [164], [181]–[183], (2,2,6,6-tetramethyl-3,5-heptane-dione)$_3$ lanthanum [$La(thd_3)$] [169]–[178], [184]–[187] tris(N,N'-diisopropylformamidinato) lanthanum [$La(fAMD)_3$] [184], [185], tris(ethylcyclopentadienyl) lanthanum [$La(EtCp)_3$],[188] tris(cyclopentadienyl) lanthanum [$La(Cp)_3$],[189] and tris(isopropylcyclopentadienyl) lanthanum [$La(^iPrCp)_3$] [165]–[167], [190]–[198]. Many of these precursors provide challenges to development of effective ALD processes. La_2O_3 prepared by $La(N(SiMe_3)_2)_3$ contains high amounts (~10 at%) of Si. [181] Films prepared with $La(^iPrAMD)_3$, $La(^iPr\text{-}MeAMD)_3$, $La(fAMD)_3$, and $La(thd)_3$ contain large amounts (~10 at%) of carbon impurities. [179], [180], [184], [187] Lanthanum precursors also have poor volatility, requiring high temperatures in order to achieve sufficient vapor pressure; most precursors require temperatures in excess of 150 °C.

Of the precursors investigated in literature, $La(^iPrCp)_3$ appears to be the most promising. $La(^iPrCp)_3$ has a low melting point of 38 °C, which is desirable for ALD processes. Although $La(^iPrCp)_3$ does not have the highest vapor pressure of the La precursors, the purity of films prepared with this precursor is significantly better than those with higher vapor pressure precursors. Films prepared with $La(^iPrCp)_3$ have a carbon content of only 1-2 at%. [191], [194] A summary of ALD literature on La_2O_3 prepared from $La(iPrCp)_3$ is shown in Table B-1. Table B-1 does not include all work published on La_2O_3 from $La(iPrCp)_3$, as some papers do not provide

much information on their ALD process. [196]–[198] Table B-1 shows that most groups chose to use a bubbler and a precursor temperature ≥150 °C. Suzuki *et al.* [165] used a lower precursor temperature of 135 °C without a bubbler. In their work, Suzuki *et al.* claim that saturation only occurs at a substrate temperature of 150 – 175 °C. However, upon deeper investigation of their data it appears they did not achieve saturation at all. At 135 °C, the precursor has insufficient vapor pressure to saturate the surface in 10 s (the maximum dose time used by Suzuki *et al.*). This conclusion is supported by their low GPC of 0.1 Å/cy. [165] La_2O_3 is hydroscopic and readily forms $La(OH)_3$ upon exposure to water vapor. Some groups using H_2O as the oxygen source have reported anomalous deposition behaviour that they have attributed to the formation of La-OH groups on the surface. He *et al.* [194] observed a decrease in GPC with increasing length of the H_2O pulse, claiming that the formation of strongly bonded La-OH surface groups inhibited further La deposition. Kim *et al.* [166] propose an opposing La-OH mechanism to explain their observed GPC behaviour at lower substrate temperatures. Kim *et al*. state that an increase in La-OH surface species at lower temperatures promotes adsorption of La, increasing the GPC. [166] Kim *et al.*'s interpretation is likely incorrect, as it does not explain the observed increase in GPC for low temperature depositions using oxygen plasma. The GPC increase could be attributed to precursor condensation.

The purpose of this work was to develop an ALD procedure for the deposition of La_2O_3 from $La(^{i}PrCp)_3$, with the intent of adapting the procedure to prepare catalytic perovskite films. This work also involved the development of the pulsed precursor delivery method which was utilized for the $(EtCp)_2Mn$ precursor in Chapters 4 and 5. Despite the successful development of an ALD procedure for the deposition of La_2O_3, attempts at preparing perovskite films were unsuccessful. This study represents some of the initial work done during the PhD program and also provided an opportunity to learn about the development of a new ALD process from scratch.

Table B-1: Literature summary of ALD La oxide using $La(^{i}PrCp)_3$

Reference	Oxygen Source	Precursor Temperature	Deposition Temperature	Substrate	Growth Per Cycle	Characterization	Notes
[191], [193]	H_2O, O_2, NH_3	150 °C (bubbler)	170-380 °C	H-Si	< 0.2 Å/cy	SE, AES, AFM, XPS, TEM, electrical measurements	H_2O yielded the highest quality films. Did not claim an ALD mechanism; called it "cyclic CVD".
[165]	H_2O	135 °C	135-300 °C	SiO_2	0.1 Å/cy	SE, TEM, electrical measurements	Claimed only to get saturation at 150-175 °C. However, their data appears to indicate that they do not get saturation at any temperature.
[194]	H_2O	180 °C (bubbler)	280-480 °C	HfO_2, Al_2O_3, SiO_2	0.2 Å/cy	SE, SIMS, XPS	Claimed formation of La-OH groups, which hinder reaction.
[166], [167], [192]	H_2O	160 °C (bubbler)	200-400 °C	H-Si, H-Ge	0.8 Å/cy	SE, XPS, electrical measurements	Fairly good ALD data; saturation curves and temperature window data.
	O_2*				1.4 Å/cy		
[163]	O_2*	150 °C	150-350 °C	H-Si	0.6 Å/cy	SE, XPS, electrical measurements	Fairly good ALD data; saturation curves and temperature window data.
[195]	O_3	150 °C (bubbler)	250 °C	HfSiON	0.4 Å/cy	SE, SIMS, electrical measurements	Not much ALD data; focused on electronic properties.

Abbreviations: **O_2*** is oxygen plasma, **H-Si** is hydrogen terminated silicon, **H-Ge** is hydrogen terminated germanium, **SE** is spectroscopic ellipsometry, **AES** is Auger electron spectroscopy, **AFM** is atomic force microscopy, **XPS** is x-ray photoelectron spectroscopy, **TEM** is transmission electron microscopy, **SIMS** is secondary ion mass spectroscopy.

B.2 Experimental

A Kurt J. Lesker ALD 150LX reactor operated at a pressure of ~1 Torr was used for all depositions. High purity Ar was used as the carrier gas. Tris(isopropylcyclopentadienyl) lanthanum ($La(^{i}PrCp)_3$) (STREM Chemicals, Inc.) was used as the La source and the ampule was maintained at a temperature of 130 °C unless otherwise stated. The valve and line used to transport the precursor vapors were held at 15 and 25 °C, respectively, above the ampule temperature in order to prevent condensation. O_2 plasma was used as the oxygen source and was generated by an inductively coupled plasma system operated at a power of 600 W. Si (100) wafers, with the native SiO_x layer intact, were used as substrates for deposition. Depositions were performed at substrate temperatures ranging from 150 to 400 °C. Substrates were cleaned using 30 s of O_2 plasma immediately prior to deposition. Film thickness was monitored using in-situ spectroscopic ellipsometry.

Due to the low volatility of the $La(^{i}PrCp)_3$ precursor, high ampule temperatures are required to achieve sufficient vapor pressure. However, because of equipment limitations, the ALD system was unable to maintain ampule temperatures much higher than 130 °C. In order to achieve sufficient precursor dose without the use of a bubbler, a method referred to here as "pressurized precursor delivery" was used. A precursor pulse using this method was separated into three steps: charge, dwell, and discharge (summarized schematically in Figure B-2). During the charge step, Ar was flowed into the ampule, increasing the pressure relative to the ALD reactor. Once pressurized, the ampule was isolated and given some time to allow for precursor molecules to evaporate into the vapor phase. This was the dwell step and it occurred in conjunction with the plasma exposure and post plasma purge steps. When it was time for the precursor dose, the ampule was discharged. The ampule was opened to the reactor, allowing the positive pressure inside the ampule to carry precursor molecules to the substrate. The typical timing scheme for La oxide deposition was 10 s–10 s–20 s–10 s (t_1-t_2-t_3-t_4). A diagram of the pulsing scheme is shown in Figure B-2D. t_1 is the precursor dose/ discharge time, t_2 is both the precursor purge step and the charge time, t_3 is the O_2 plasma dose, and t_4 is the post plasma purge. The dwell time is t_3 + t_4.

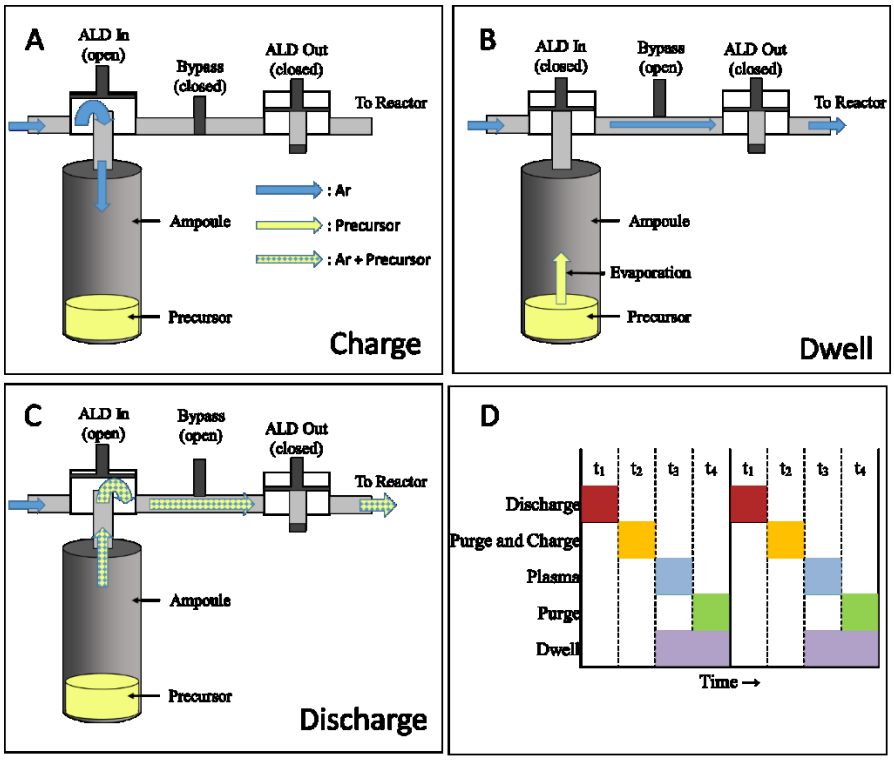

Figure B-2: Schematic of pressurized precursor delivery steps. A) Charge, B) dwell, and C) discharge. D) Pulse timing scheme.

B.3 Results and Discussion

Development of the ALD recipe for La oxide took a significant amount of trial and error. Initial depositions using conventional precursor delivery (Figure B-1A) yielded very slow and inconsistent growth even at an ampule temperature of 130 °C. This is why the pressurized precursor delivery method was chosen. A number of deposition parameters were tried including varying the ampule temperature, substrate temperature, as well as charge and discharge times. During the refinement of the pressurized precursor delivery parameters depositions had a fairly consistent growth per cycle (GPC) of 0.3 Å/cy. Once the parameters were finalized and testing was started to determine the ALD window, the GPC suddenly changed from 0.3 to 0.6 Å/cy. After additional testing, the GPC stabilized at 0.7 Å/cy. From our group's experience with ALD precursors, it is very common for a newly purchased precursor to have anomalous and inconsistent deposition behavior for several hundred cycles. It is believed that this behavior is due to impurities in the precursor which contaminate the vapors that reach the substrate. After pulsing for some time, the impurities are removed and the precursor becomes stabilized. The behavior of the La(^{i}PrCp)$_3$ precursor is somewhat different than the behavior observed with other

precursors. La(^{i}PrCp)$_3$ took a very long time to stabilize; it was pulsed ~2000 times over the course of a month before growth stabilized. The length of time for stabilization is likely because of its low vapor pressure; each pulse removed only a very small amount of the impurities from the ampule.

The temperature window for ALD growth (Figure B-3) was determined by performing depositions at substrate temperatures ranging from 150 to 400 °C. Depositions were performed using a timing scheme of 10 s–10 s–20 s–10 s for 50-100 cycles. Thickness was measured in-situ using spectroscopic ellipsometry. Growth during the first 10 cycles was relatively fast, indicating substrate enhanced growth. After the first 10 cycles growth became linear; the GPC was taken as the slope of the linear region. At temperatures below 250 °C, the GPC increases dramatically due to precursor condensation. The GPC from 250-400 °C has a fairly constant value of 0.7 Å/cy indicating that this temperature range represents the window for ALD growth. The GPC within the ALD window has a small negative slope with increasing temperature, which is due to precursor desorption. At higher temperatures a larger fraction of physisorbed molecules will desorb before they are able to chemisorb to the surface.

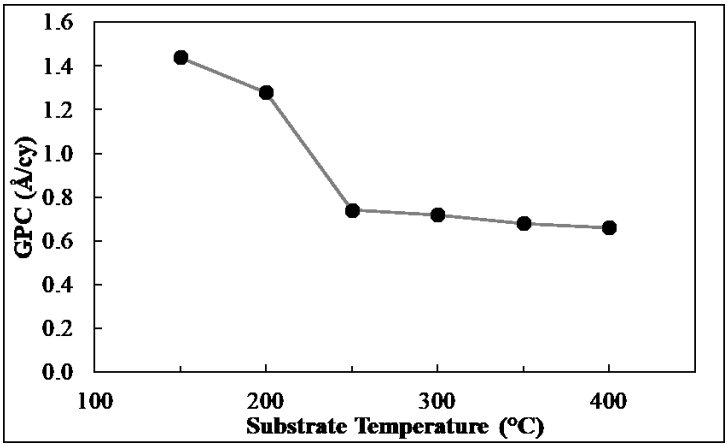

Figure B-3: ALD temperature window; depositions were performed with a pulse timing of 10 s–10 s–20 s–10 s.

Figure B-4A and Figure B-4B show saturation curves for precursor and plasma exposures respectively. Typically precursor saturation curves are obtained by varying the precursor dose time (t_1). However, since pressurized precursor delivery was used for this work, increasing t_1 has a very small effect on total precursor dose. In order to obtain the precursor saturation curve for the pressurized precursor delivery method, the GPC was plotted vs. ampule temperature. With

increasing ampule temperature, more vapor phase precursor molecules are present in the ampule before the pressurized Ar transports them to the substrate. Figure B-4A shows that saturation is nearly complete at 125 °C. At a set point of 125 °C, slight variations in precursor temperature cause significant changes in the GPC. 130 °C was selected as the ampule temperature because this temperature allows for stable and repeatable growth behavior.

The plasma saturation curve was also determined in a slightly unconventional way. Typically, the plasma saturation curve is determined simply by varying t_3, the plasma exposure. However, with pressurized precursor delivery, the dwell time needs to be considered when changing the timing scheme. In order to keep a constant dwell time between experiments, t_3 and t_4 were both varied. The timing scheme used to generate the plasma saturation curve was 10 s–10 s– x – (30 s-x). t_4 was varied such that $t_3 + t_4 = 30$ s in order to maintain a constant dwell time of 30 s. t_4 is the plasma purge step and is used to remove excess plasma reactant (O_2) and reaction by-products from the chamber. Increasing the duration of this step should have no effect on the growth behavior. As shown in Figure B-4B, the GPC increases from 3 to 5 s, then decreases and levels off at 0.7 Å/cy at $t_3 = 15$ s. At $t_3 = 3$ s, the plasma dose is very small and most of the (^{i}PrCp) ligands remain bonded to the surface, limiting precursor adsorption during subsequent cycles and causing a significant amount of carbon incorporation. At a plasma time of 5 s, an intermediate amount of (^{i}PrCp) ligands remains on the surface. Enough ligands are removed such that there are sufficient adsorption sites for more precursor to adsorb with the next cycle, but there are also many ligands remaining that become incorporated into the film. This incorporation of adsorbed ligands causes an increase in GPC. It is suspected that films prepared with $t_3 = 3$ s and 5 s would have a high carbon content. At t_3 times greater than 15 s, there has been sufficient plasma dose to remove most or all of the adsorbed ligands and the surface becomes saturated with oxygen. 20 s was chosen as the optimum plasma time to ensure complete ligand removal.

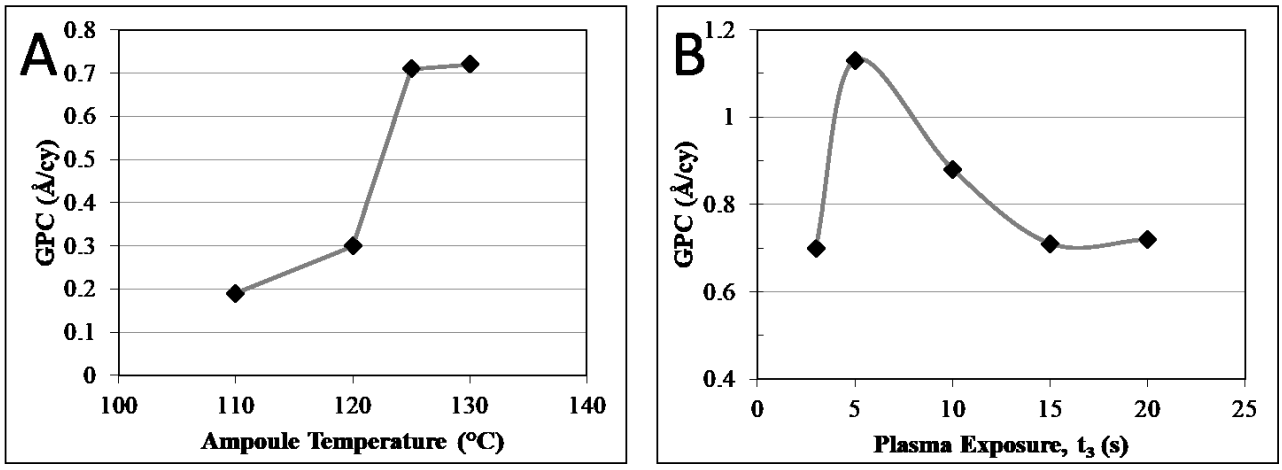

Figure B-4: Saturation curves. A) Precursor saturation curve, prepared with timing scheme: 10 s–10 s–20 s–10 s. B) Plasma dose saturation curve, prepared with timing scheme 10 s–10 s– x – (30 s-x).

B.4 Deposition of La-based Perovskites

Attempts were made to prepare several different La-based perovskite films via ALD. These films were $LaMnO_3$, $LaCoO_3$, and $LaNiO_3$. However, this work was not successful due to a number of issues including negligible growth rates, incompatible deposition conditions between precursors, and etching of GDL during high temperature plasma exposures. The appeal of using ALD perovskites as catalysts still exists, since perovskites have been shown to have excellent bifunctional performance and stability. It is believed that with additional work and perhaps some clever engineering solutions, the problems associated with perovskite depositions can be overcome using this preliminary work as a starting point.

Appendix C: Discussion of Saturation Results Conflicting With the Literature

The saturation data presented in Chapter 4[144] is in disagreement with results previously published in the literature. Saturation plots from the literature are shown in Figure C-1. The authors of these works claim that their depositions follow a saturating mechanism. Upon close inspection of the plots given in Figure C-1, it is apparent that there may have been experimental errors and/or misinterpretation of the data. Firstly, Burton *et al.*'s saturation plot has four data points that result in nearly identical growth. This would typically indicate a saturating mechanism. However, since there was no variation at all in the growth, it is suspected that Burton *et al.* did not truly achieve variable precursor doses. All four points in Figure C-1 experienced the same precursor dose. Pickrahn *et al.* and Siddiqi *et al.*'s saturation curves have a slightly positive slope, indicating that saturation has not been achieved. Both Pickrahn *et al.* and Siddiqi *et al.* misinterpreted the small slope as a plateaux in growth.

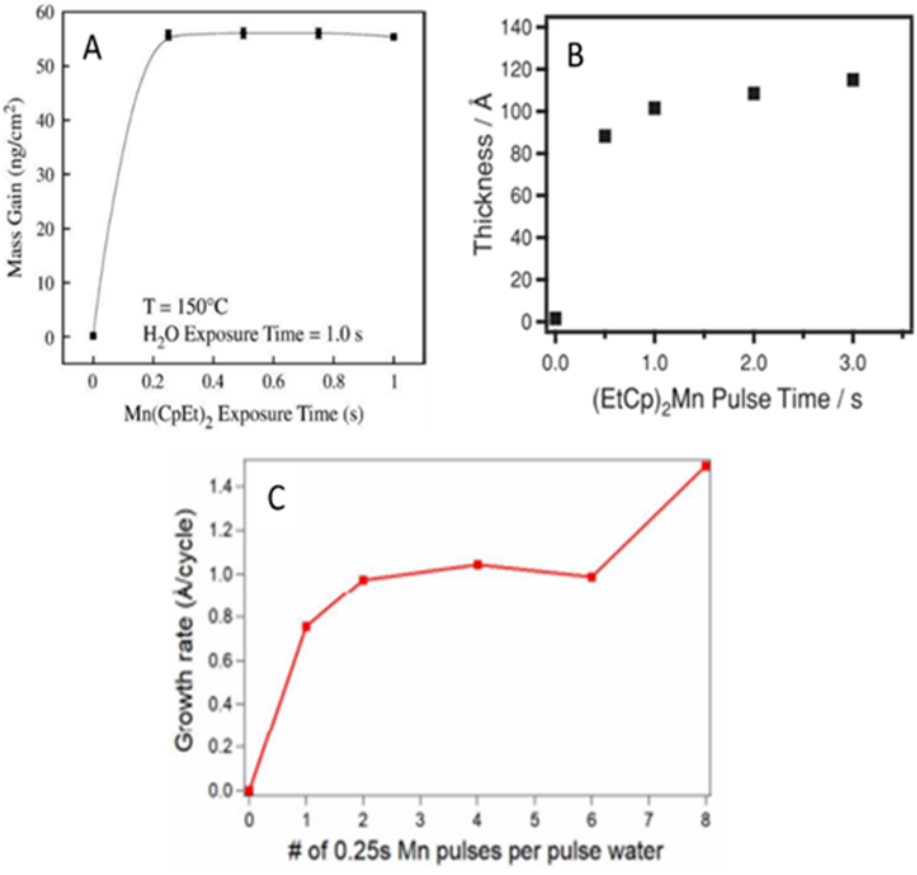

Figure C-1: Saturation plots for the $(EtCp)_2Mn + H_2O$ ALD system presented in literature. (A) Burton *et al.*[80], (B) Pickrahn *et al.*,[76] (C) Siddiqi *et al.*[120]